

# Advances in tomographic PIV

Matteo Novara



# Advances in tomographic PIV

PROEFSCHRIFT

ter verkrijging van de graad van doctor  
aan de Technische Universiteit Delft,  
op gezag van de Rector Magnificus Prof. ir. K. Ch. A. M. Luyben,  
voorzitter van het College voor Promoties,  
in het openbaar te verdedigen op vrijdag 22 februari 2013 om 12.30 uur

door

Matteo NOVARA  
Master in aerospace engineering  
geboren te Cuneo, Italy

Dit proefschrift is goedgekeurd door de promotor  
Prof. dr.-Ing F. Scarano

Samenstelling promotiecommissie:

Rector Magnificus	Technische Universiteit Delft	voorzitter
Prof. dr.-Ing. F. Scarano	Technische Universiteit Delft	promotor
Prof. dr. Ir. J. Westerweel	Technische Universiteit Delft	
Prof. dr.-Ing. T. Astarita	Universita' degli studi di Napoli, Federico II	
Prof. dr. C. Schnörr	Universität Heidelberg	
Prof. dr.-Ing. J. Soria	Monash University, Melbourne	
Dr. ir. G. Elsinga	Technische Universiteit Delft	
B. Wieneke, M.Sc.	LaVision, Göttingen	

Copyright © 2013 M. Novara

Cover image: painting by Silvio Novara (1978), editing by Matteo Enrici

All rights reserved.

# Summary

This research deals with advanced developments in 3D particle image velocimetry based on the tomographic PIV technique (Tomo-PIV). The latter is a relatively recent measurement technique introduced by Elsinga et al. in 2005, which is based on the tomographic reconstruction of particle tracers in three-dimensional space from a small number of its projections obtained with digital cameras. Tomography is widely known in the medical diagnostics (e.g. computerized axial tomography) to inspect the human body. For PIV applications the problem is formulated as that of reconstructing the spatial distribution of sparse emitters (illuminated tracers).

The present work initially surveys the state of advancement of the research conducted on this new measurement technique and the main bottlenecks and aspects to be improved are identified. The two major elements covered in this research are the 3D object reconstruction and the advanced analysis of the tracers motion.

Concerning the first aspect, one of the recognized limitations is the exponential increase of *ghost particles* when a higher particle concentration is desired for high-resolution measurements (e.g. in turbulence studies). Although Tomo-PIV already outperforms other volumetric 3D techniques in terms of allowed particle tracers concentration, many efforts are constantly devoted to find ways to further increase the particle density.

A novel concept is presented in this work that makes use for the first time of more than a single recording to increase the accuracy of tomographic reconstruction. This method considers that the moving particle field can be regarded as a solid object recorded from a moving imaging system. That is why the author refers to the concept of *fluid tomography*, whereby the two recordings of the same set of particles are “deformed back” to the same time instant when the particle tracers come to coincide and the *ghost particles* do not. The Motion Tracking Enhancement reconstruction technique (MTE) is described in Chapter 4 of this thesis. The validity of the MTE working principle is verified both numerically and by experiments. Its application in turbulent shear flows shows that the seeding density can be increased by a factor 4 ( $ppp=0.2$ ) with respect to that currently practiced ( $ppp=0.05$ ) without loss of accuracy.

The focus is then set on techniques to increase the spatial resolution of velocity fields measured by tomographic PIV. The approach followed is that of locally adaptive interrogation volume, following the concept of non-isotropic resolution in PIV (Scarano 2003). The study shows a novel technique that exploits the additional degrees of freedom when adapting window shape and orientation in a 3D domain based on velocity gradient tensor invariants analysis (Chapter 5). It is shown that the measurement spatial resolution can be increased by a factor 2.5 and 1.5 across shear layers and in the core of a vortex respectively.

The present work deals also with the advanced treatment of time-resolved Tomo-PIV experimental data (Chapter 6), where the accurate measurement of the velocity material derivative is of paramount importance to extract the instantaneous flow field pressure (pressure from PIV, van Oudheusden, 2013). The approach investigated here is based on the use of particle-tracking for a time-resolved sequence of 3D particle fields. Adopting a high-

## *Summary*

order polynomial basis for the particle trajectory reconstruction allows the reconstruction of long trajectories with a strong reduction of random error and nearly the complete elimination of the truncation error. The application to a 3D measurement of a transitional jet demonstrates the higher accuracy obtained for the estimate of fluid parcels acceleration and in turn of the instantaneous pressure field.

The work is concluded with a synthesis of the advances obtained in this field, followed by a perspective towards the most significant upcoming developments for the tomographic PIV technique.

# Samenvatting

Deze thesis beschrijft geavanceerde ontwikkelingen in 3D particle image velocimetry, gebruikmakende van de tomografische PIV techniek (Tomo-PIV). Dit is een recente meettechniek geïntroduceerd door Elsinga et al. in 2005, gebaseerd op de tomografische reconstructie van deeltjes in een drie-dimensionale ruimte van een klein aantal projecties verkregen met digitale camera's. Tomografie is wijdverbreid in de medische diagnostiek (bijv. computerized axial tomografie) ter inspectie van het menselijke lichaam. Voor PIV applicaties is het probleem geformuleerd in termen van de reconstructie van een ruimtelijke verdeling van belichte deeltjes.

Het huidige werk richt zich eerst op het in kaart brengen van het onderzoek dat al is uitgevoerd aan deze nieuwe meettechniek en identificeert vervolgens de belangrijkste knelpunten en verbeteringspunten. De twee belangrijkste elementen die behandeld worden in dit onderzoek zijn 3D object reconstructie technieken en een geavanceerde analyse van de manier waarop de deeltjes bewegen.

Een eerste limiet wordt gevormd door de exponentiele toename in het aantal *ghost particles*, wanneer een hogere deeltjes concentratie vereist is voor hoge-resolutie metingen, bijvoorbeeld voor turbulentie studies. Alhoewel Tomo-PIV al beter presteert dan andere 3D volumetrische technieken in termen van de toelaatbare deeltjes concentratie, wordt er nog steeds veel energie gestoken in het verder verhogen van de deeltjes dichtheid.

In dit werk wordt er innovatieve methode geïntroduceerd welke gebruik maakt van meer dan een opname om zodoende de nauwkeurigheid van de tomografische reconstructie te verbeteren. Deze methode gaat er vanuit dat het bewegende deeltjesveld gezien kan worden als een solide object waargenomen vanaf een bewegend opnamesysteem. Daarom spreekt de auteur ook wel van het concept "fluid tomografie", waarbij twee opnames van dezelfde deeltjesvelden "terug getransformeerd" worden naar dezelfde tijd. Hierbij zullen de echte deeltjes samenvallen, terwijl de *ghost particles* geen overlap zullen tonen. De Motion Tracking Enhancement reconstruction technique (MTE) wordt beschreven in hoofdstuk 4 van deze thesis. De validiteit van MTE is geverifieerd door middel van zowel experimenten en numerieke simulaties. De techniek is toegepast op data van een turbulent grenslaag experiment, waaruit blijkt dat de deeltjesdichtheid met een factor 4 ( $ppp=0.2$ ) verhoogd kan worden ten opzichte van de huidige standaard (0.05), zonder daarbij nauwkeurigheid te verliezen.

De aandacht wordt daarna verlegd naar technieken om de ruimtelijke resolutie van de snelheidsvelden te verhogen. De aanpak die gevolgd wordt, is gebaseerd op adaptieve correlatie (in vorm en oriëntatie), gevolgd door het concept van anisotrope resolutie in PIV (Scarano 2003). Deze techniek maakt gebruik van de extra vrijheidsgraden die geboden worden door de drie-dimensionaliteit van het domein (Hoofdstuk 5). De ruimtelijke resolutie kan verhoogd worden met een factor van 2.5 en 1.5 in shear layers en vortex cores, respectievelijk.

Deze thesis gaat ook in op de geavanceerde behandeling van experimentele time-resolved Tomo-PIV data (Hoofdstuk 6), waarbij een nauwkeurige bepaling van de acceleraties van groot belang is om het instantane drukveld te berekenen (pressure from PIV, van

Oudheusden, 2013). Deze aanpak is gebaseerd op particle-tracking voor een set time-resolved 3D deeltjes velden. Door gebruik te maken van een set hoge order polynomen voor traject reconstructie is het mogelijk om lange deeltjes trajecten te voorspellen met een sterke reductie in de random fout en een vrijwel complete reductie in de truncatie fout. Toepassing op een 3D meting van een jet in transitie demonstreert dat een hogere nauwkeurigheid bereikt wordt in het acceleratieveld en als gevolg daarvan ook in het instantane drukveld.

Deze thesis wordt afgerond met een beschouwing van de belangrijkste ontwikkelingen in dit veld, gevolgd door een vooruitzicht op de belangrijkste ontwikkelingen die in de planning staan voor de tomografische PIV techniek.

# Contents

<b>Summary</b> .....	<b>v</b>
<b>Samenvatting</b> .....	<b>vii</b>
<b>Contents</b> .....	<b>ix</b>
<b>Introduction</b> .....	<b>13</b>
1.1 From planar to 3D measurements .....	13
1.2 The tomographic approach .....	15
1.3 Limitations and developments .....	17
1.3.1 Illumination.....	17
1.3.2 Imaging system calibration .....	18
1.3.3 Computational costs.....	18
1.3.4 Limitations of processing techniques .....	19
1.4 Objectives of the thesis .....	21
1.4.1 Reduction of ghost intensity.....	21
1.4.2 Adaptive motion analysis .....	22
1.4.3 Accurate acceleration measurement.....	23
1.5 Research framework .....	24
1.6 Outline of the thesis .....	26
<b>Fundamentals of tomographic PIV</b> .....	<b>27</b>
2.1 Working principle.....	27
2.2 Experimental setup .....	29
2.2.1 Volume illumination .....	29
2.2.2 Seeding particles .....	31
2.2.3 Configuration of the imaging system.....	36
2.2.4 Calibration.....	38
2.3 Data processing.....	41
2.3.1 Image pre-processing .....	41
2.3.2 Tomographic reconstruction .....	42
2.3.3 Motion analysis.....	49
<b>Assessment methodology</b> .....	<b>57</b>
3.1 Introduction.....	57
3.2 Imaged seeding density.....	58
3.2.1 The TomoPIV Design Tool.....	58

3.2.2	Thinning the illuminated domain .....	63
3.2.3	Average image intensity .....	63
3.3	Tomographic reconstruction accuracy .....	64
3.3.1	Reconstructed intensity profile .....	64
3.3.2	Relative quality factor .....	66
3.3.3	Reconstructed intensity variance .....	66
3.3.4	Consistency of particle trajectories .....	68
3.4	Accuracy of the velocity measurement .....	69
3.4.1	Spatial and temporal coherence .....	70
3.4.2	Cross-correlation signal-to-noise .....	71
3.4.3	Compliance with physical laws .....	73
	<b>Motion tracking enhancement .....</b>	<b>77</b>
4.1	Background .....	77
4.2	The ghost particles .....	79
4.3	Theoretical model for MTE .....	82
4.3.1	Geometrical analogy for MART solution representation .....	82
4.3.2	Iterative first guess evaluation .....	83
4.4	MTE algorithm .....	85
4.4.1	Suppression of incoherent ghost intensity .....	85
4.4.2	MART first guess and iterative evaluation .....	87
4.4.3	Numerical evaluation .....	89
4.5	Numerical performance assessment .....	90
4.5.1	Double-frame recordings .....	91
4.5.2	Time-resolved recordings .....	95
4.6	Multiplicative variant of the MTE algorithm .....	97
4.7	Computational cost of MTE .....	99
4.8	Effective volume for MTE .....	100
4.9	Experimental assessment of MTE .....	101
4.9.1	Time-resolved measurements of a transitional jet .....	101
4.9.2	Turbulent boundary layer .....	108
4.10	Conclusions .....	117
	<b>Adaptive 3D correlation .....</b>	<b>119</b>
5.1	Adaptivity in planar PIV .....	119
5.2	Working principle .....	122
5.2.1	Adaptive criterion .....	125

5.2.2	Numerical implementation of shaped cross-correlation.....	128
5.3	Numerical assessment.....	130
5.4	Transitional jet experiment.....	134
5.5	Turbulent boundary layer experiment.....	136
5.6	Conclusions.....	138
<b>A particle-tracking approach for accurate acceleration measurements.....</b>		<b>141</b>
6.1	Acceleration and pressure from PIV.....	141
6.2	Theoretical background.....	144
6.2.1	Fluid parcel trajectory reconstruction from PIV data.....	145
6.3	The Tomo-3D-PT approach.....	147
6.3.1	Trajectory reconstruction.....	148
6.4	Numerical assessment.....	149
6.4.1	Particle tracking.....	150
6.4.2	Evaluation of Lagrangian acceleration.....	150
6.4.3	Evaluation of dense information onto regular grid.....	153
6.5	Experimental results.....	156
6.5.1	Lagrangian derivative evaluation.....	156
6.5.2	Pressure field evaluation.....	159
6.6	Conclusions.....	160
<b>Conclusions.....</b>		<b>161</b>
7.1	Motion Tracking Enhancement.....	161
7.2	Adaptive cross-correlation.....	162
7.3	Acceleration evaluation by Tomo-3D-PT.....	162
7.4	Perspectives.....	163
<b>Bibliography.....</b>		<b>165</b>
	References.....	165
	List of journal publications.....	173
	Conferences.....	173
<b>Acknowledgements.....</b>		<b>175</b>
<b>Curriculum vitae.....</b>		<b>177</b>



# Chapter 1

## Introduction

This chapter traces the development of particle image velocimetry towards three dimensional measurements through the introduction of tomography. The path from the appearance of tomographic PIV in 2005 to the present days is depicted and the main advances achieved are discussed. Particular attention is given to the main limitations and bottlenecks of Tomo-PIV, as they represent the main drive for the development of the advanced processing techniques presented in this work. The objectives of the thesis are stated and the framework of the research work is presented. In conclusion a brief outline of the thesis is given.

### 1.1 From planar to 3D measurements

Particle image velocimetry (PIV) is a quantitative field velocimetry technique (Adrian 1991; Raffel et al. 1998) capable of measuring two components of the velocity vector in a planar domain. Particle tracers immersed in the flow are illuminated twice by a pulsed laser over a light-sheet and the light scattered by the particles is captured by a camera on two separate frames. Correlation analysis of the two recordings provides the displacement field of the tracers, which, in the hypothesis that the particles move with the flow, leads to the velocity vector field in the illuminated plane.

The use of digital cameras (Willert and Gharib 1991) and high-power pulsed lasers largely contributed to the development of the technique which is now a well-established tool for industrial applications (Willert 1997) and for turbulent flows investigation (Adrian 2007). Results from PIV significantly improved the understanding of turbulence and of the spatially coherent structures which could not be measured by previous point-wise techniques (e.g. the hairpins in a turbulent boundary layer shown in Figure 1.1).

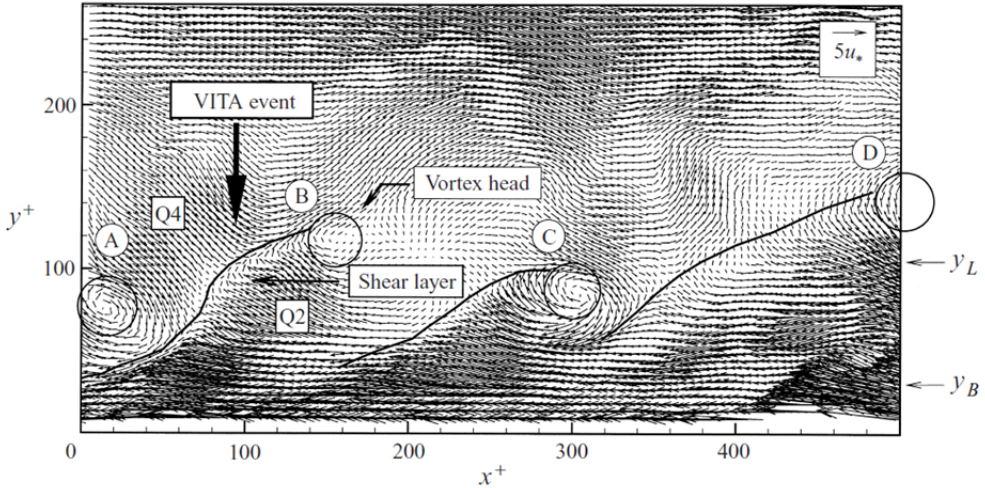


Figure 1.1 Velocity field by PIV in a turbulent boundary layer ( $x^+$  and  $y^+$  indicate the streamwise and wall-normal directions respectively). Hairpin heads and inclined shear-layers are indicated by the circles and solid lines (Adrian et al. 2000).

On the other hand, given the three-dimensional nature of turbulence, the planar PIV approach fails to provide a full description of the flow structure. In order to overcome this limitation, Stereoscopic PIV was introduced (Arroyo and Greated 1991; Willert 1997; Prasad 2000) where the use of two cameras having different viewing directions with respect to the illuminated plane made it possible to measure the third component of velocity, Figure 1.2. Nevertheless, the measurement domain was still limited to two-dimensions.

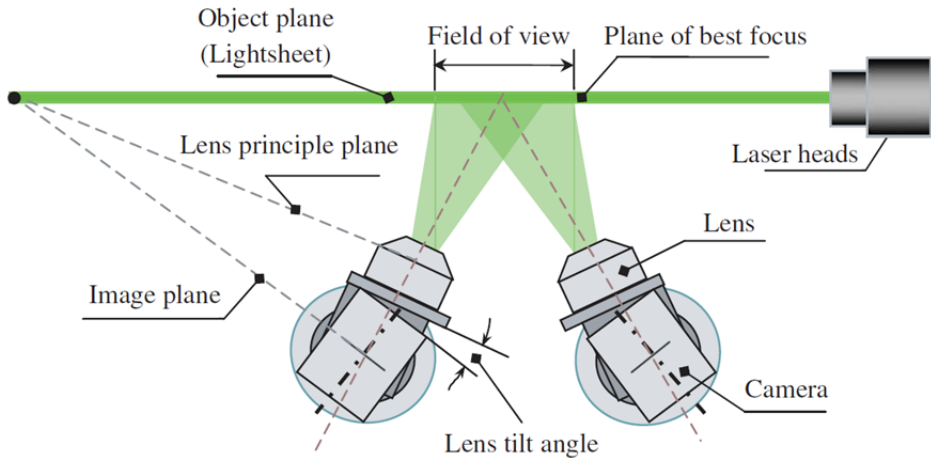


Figure 1.2 Sketch of stereoscopic PIV experimental setup, Liu et al. (2006).

The need of a fully three-dimensional description of turbulent phenomena combined with the one to validate results from 3D numerical simulation, led to the development of 3D-PIV techniques such as scanning light-sheet PIV (Brücker 1995; Hori and Sakakibara 2004),

holographic PIV (Zhang et al. 1997; Hinsch 2002) and digital holographic PIV (Coëtmelec et al. 2001), defocusing PIV (Pereira and Gharib 2001), 3D particle tracking (Maas et al. 1993) and tomographic PIV (Tomo-PIV, Elsinga et al. 2005). For a review of the above mentioned techniques the author refers to the work from Arroyo and Hinsch (2008).

The most recently developed is tomographic PIV, which is the main subject of this study. In particular, since its appearance, Tomo-PIV, compared to the other 3D techniques, has attracted much attention in the scientific community. The particular features that make it an attractive technique are its high spatial resolution and the versatility of the measurement configuration. A recent review on the subject is due to Scarano (2013).

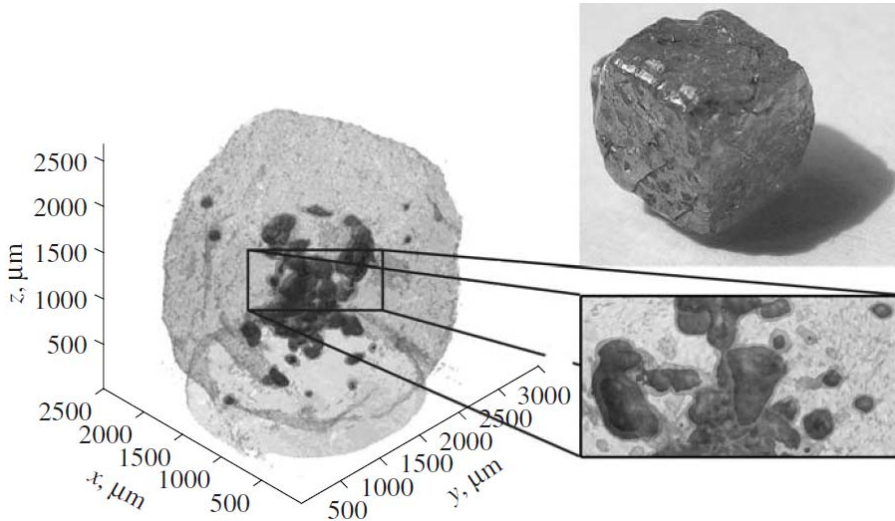


Figure 1.3 X-ray tomographic reconstruction of a diamond; dark gray areas indicate inclusions (Zolotov et al. 2009).

## 1.2 The tomographic approach

Tomographic PIV has been introduced by Elsinga et al. in 2005 at the International Symposium on PIV held in Caltech (Pasadena, USA), as a three-dimensional three-components (3D-3C) velocimetry technique. The technique exploits tomographic reconstruction, which consists in the reconstruction of a three-dimensional objects from a set of its two-dimensional projections. The concept of tomography is well known in the medical field or for the analysis of precious stones (e.g. diamonds, see Figure 1.3), where the reconstruction is carried out based on X-ray images captured by a moving sensor.

For PIV applications, the object is the distribution of light scattered by the particle tracers illuminated by a laser beam which is expanded in order to illuminate a three-dimensional region. As the object moves following the flow pattern, the single moving sensor used for solid object tomography is replaced by a multiple-sensors imaging system, typically formed by 3 to 6 digital cameras having different viewing directions with respect to the investigated domain, Figure 1.4-top. Three-dimensional cross-correlation between two subsequent

reconstructed objects is used to obtain the vector fields, similarly to planar or stereoscopic PIV.

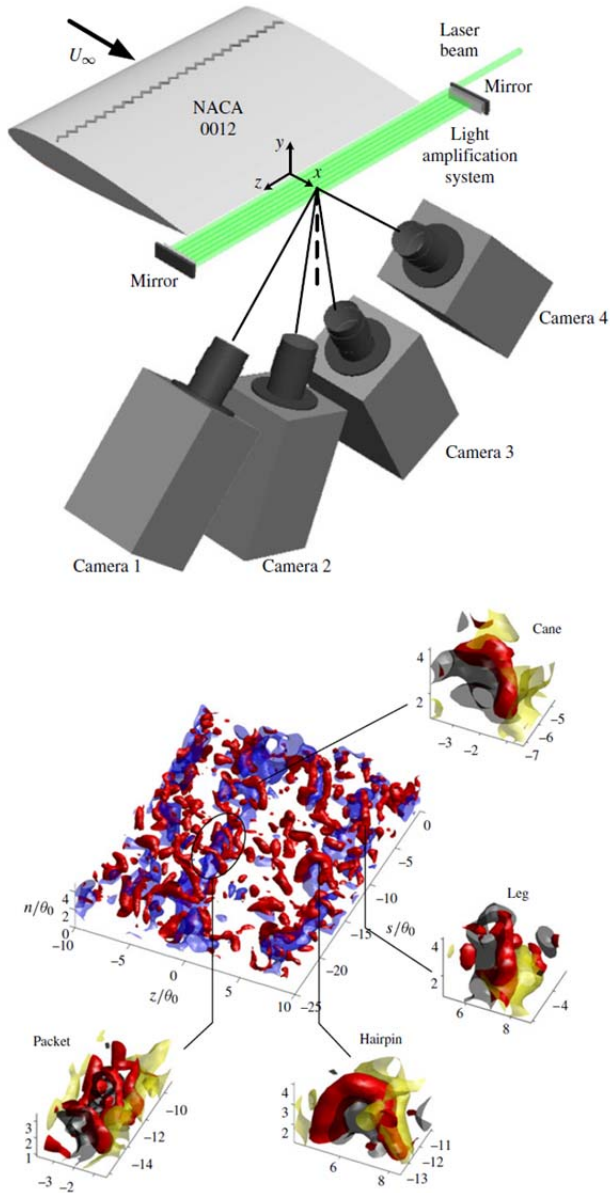


Figure 1.4 Top: sketch of experimental setup of a tomographic PIV investigation of a turbulent wake behind an airfoil. Bottom: iso-surfaces of streamwise velocity in blue (low-speed streaks) and vortical structures identified by iso-surfaces of  $Q$  criterion (Hunt 1988). Magnified details of a hairpin packet, a full hairpin and leg and cane vortices (Ghaemi and Scarano 2011).

Given its capability in providing instantaneous 3D velocity fields with a relatively high spatial resolution, Tomo-PIV candidates as a powerful tool to investigate complex fluid dynamic problems such as in turbulent, transitional and separated flows, Figure 1.4-bottom. Moreover, the availability of high-speed cameras led, in recent years, to the development of time-resolved Tomo-PIV (Schröder et al. 2008b), a major advantage when dealing with unsteady flows.

For these reasons, since its introduction, a number of Tomo-PIV experiments have been conducted to investigate several fluid dynamic problems ranging from jets (Violato and Scarano 2011; Thomas et al. 2009), to turbulent boundary layers (Schröder et al. 2008b; Humble et al. 2009; Ghaemi et al. 2012), turbulent wakes (Ghaemi and Scarano 2011, see Figure 1.4), cylinder flows (Scarano and Poelma 2009; Hain et al. 2008) and multiphase flows (Ortiz-Dueñas et al. 2009). As a consequence, the number of scientific publications has grown substantially in the last 5 years (Scarano 2013), contributing to the spread of the technique among the PIV community.

## 1.3 Limitations and developments

As tomographic PIV is used in different fields and applications, new challenges are faced which motivate the efforts in developing both the experimental equipment and the processing techniques. Since the introduction of Tomo-PIV, the novel aspects of volumetric illumination, imaging system calibration, computational costs and accuracy of the data processing have been the subject of several studies. This section presents the milestones of the technique development. A detailed description of the experimental setup parameters and of the processing technique can be found in Chapter 2.

### 1.3.1 Illumination

In tomographic PIV the laser light illuminates a three-dimensional volume; as the laser beam needs to be expanded, the light budget is significantly reduced if compared to the planar or stereoscopic cases. This aspect has been addressed by the multi-pass light amplification system proposed by Ghaemi and Scarano (2010), after first use reported by Schröder et al. (2008b). The system makes use of reflecting mirrors which guide the laser light to reflect and overlap inside the investigated volume increasing the amount of light scattered by particle tracers up to a factor 5. This result is particularly important when dealing with high-speed tomographic PIV measurements in air flows, where small particles need to be used.

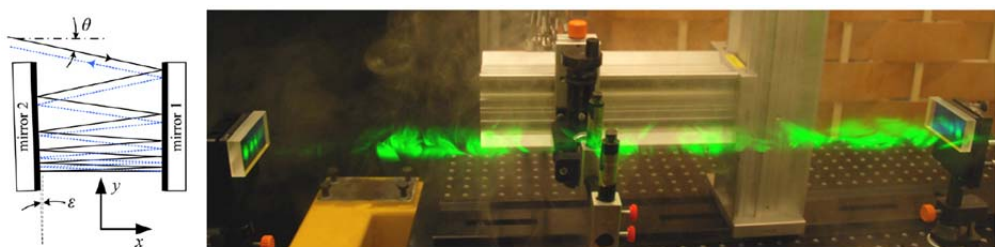


Figure 1.5 Left: scheme of the multi-pass light amplification system (light beam in black, reflected beam in blue). Right: light amplification setup (Ghaemi and Scarano 2010).

### 1.3.2 Imaging system calibration

Another milestone in the tomographic PIV development is undoubtedly represented by the introduction of the Volume self-calibration procedure (Wieneke 2008). This technique allows to correct the physical calibration, obtained by translating a target across the reconstructed volume, based on individual particle detection in the camera images and on their triangulation. After the target calibration is performed, depending on the mechanical stability of the camera support and the presence of vibrations, errors of the order of a few pixels can be observed in the position of the lines-of-sight, Figure 1.6. Since the MART algorithm is based on triangulation between lines-of-sight, such errors lead to cancellation of particles (Elsinga et al. 2006), which rapidly compromises the accuracy and the spatial resolution of the measurement. To date, this is the sole technique available to reduce calibration errors from the pixel range to less than a fraction of a pixel. Such a triangulation precision is required to obtain an accurate tomographic PIV reconstruction.

### 1.3.3 Computational costs

Ever since its introduction, Tomo-PIV developers have been focusing their efforts in reducing the computational burden associated to the processing of tomographic PIV data. The high computational cost, whereby one hour or more were needed in the early times (2005-2007) to analyze one tomographic snapshot returning the instantaneous 3D velocity vector field, justifies the number of studies devoted to increase the computational efficiency of the reconstruction and of the particle motion analysis. In fact, when a long time is needed to obtain a single velocity vector field, not only the data processing is affected, but also the process of optimizing the experimental setup becomes significantly more complicated as no feedback is rapidly available to guide the experimentalist in the choice of different configurations (e.g. illumination strength, seeding concentration, calibration verification).

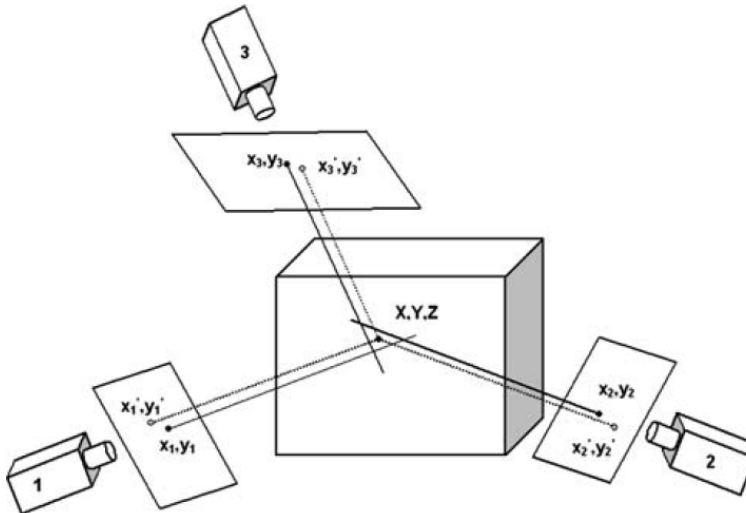


Figure 1.6 Residual triangulation disparities caused by calibration errors;  $x', y'$  indicate the actual particle projection on the image,  $x, y$  the position defined by target calibration (Wieneke 2008).

### *Tomographic reconstruction*

Particular attention has been given to the innovative step of tomographic reconstruction. The reconstruction of the 3D particle intensity fields is carried out by means of the MART algorithm (multiplicative algebraic reconstruction technique) introduced by Herman and Lent in 1976. Based on the iterative structure of the tomographic reconstruction algorithm, Worth and Nickels (2008) achieved a reduction of the computational efforts using a multiplicative first guess (MFG) instead of the uniform first guess. This approach has been brought forward by a sparse object reconstruction and cross-correlation technique recently proposed by Atkinson and Soria (2009). An acceleration over more than one order of magnitude is obtained introducing a new initial guess estimate based on multiplicative line-of-sight (MLOS) matched with a simultaneous correction of the solution (simultaneous algebraic reconstruction technique, SMART) without compromising the reconstruction accuracy in comparison to MART.

### *Motion analysis*

Regarding the 3D particle motion analysis performed by cross-correlation of reconstructed objects, the sparsity of the reconstructed intensity field can be exploited to accelerate the cross-correlation avoiding redundant operations (Atkinson and Soria 2009; Discetti and Astarita 2012b) and voxel binning can be used to reduce the size of the volume in the first step of the iterative interrogation (Discetti and Astarita 2012a).

Thanks to the advances in the hardware (multi-core processors) and in the processing algorithms, the computational cost to obtain a single velocity field from images by a 4 camera system (1 Mpixel), could be reduced from approximately 1 hour to a few minutes.

### 1.3.4 Limitations of processing techniques

The developments in the illumination system and accurate calibration procedures significantly improved the quality of tomographic PIV measurements. On the other hand, the introduction of fast reconstruction and interrogation algorithms largely contributed to the diffusion of the technique and to its application to even more challenging problems (e.g. large format camera sensors, time-resolved data).

Nevertheless, since the year of its introduction, both the reconstruction and interrogation techniques have not improved significantly in terms of accuracy, leaving room for further research and development.

### *The ghost particles*

The accuracy of the reconstruction is strongly dependent upon the particle tracers concentration and the number of cameras (see Figure 1.7) and it remains one of the major bottlenecks to increase the spatial resolution of tomographic PIV measurements.

Among the sources of error in tomographic reconstruction (e.g. discretization effects, limited aperture of the imaging system) the most severe is represented by the presence of the so called *ghost particles* (Maas et al. 1993). The *ghost particles* are spurious intensity blobs, which are erroneously reconstructed at the intersection of lines-of-sight corresponding to non-zero intensity on the camera pixel. As a consequence they appear in the reconstructed objects together with the actual tracers. As discussed in the work by Elsinga et al. (2011), the presence of the *ghosts* affects the reconstruction and motion analysis accuracy.

In fact, the intensity that contributes to the formation of the spurious particles is subtracted from the actual particles affecting the signal-to-noise ratio of the reconstruction and the robustness of the motion analysis. Moreover their presence can produce a modulation of the velocity fluctuations associated to the displacement gradient over the investigated volume thickness (Elsinga et al. 2011). Since the number of *ghost particles* strongly depends upon that of the real particles, they represent a limitation in the achievable spatial resolution of the Tomo-PIV technique.

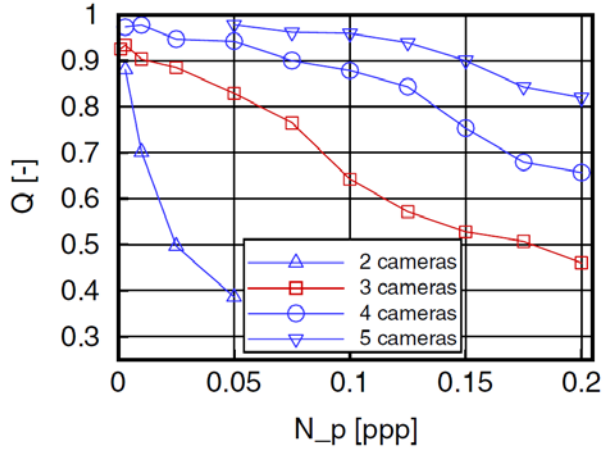


Figure 1.7 Reconstruction quality ( $Q$ ) as a function of the number of particles  $N_p$  (particles per pixels) and of the number of cameras in the tomographic system (Elsinga et al. 2006).

Based on the above discussion it is clear that any technique able to increase the maximum number of tracer particles in the measurement domain has a strong impact on the measurement spatial resolution.

Only a few studies are available which deal with different reconstruction approaches aimed to address this issue. Petra et al. (2009) investigated an algorithm based on sparsity maximization, which strongly outperformed MART according to numerical simulations, however applications in real experiments are yet to come. Gesemann et al. (2010) proposed an algorithm based on constrained least squares and  $L1$ -regularization which showed benefits from the computational point of view and allows the inclusion of more realistic imaging model to increase the reconstruction accuracy. Also in this case, further studies are needed to verify the applicability to real experimental conditions of optimization methods, where good a priori knowledge of the object to be reconstructed is required. As a consequence, the reconstruction technique commonly used in real tomographic experiments is still based on the MART algorithm initially proposed by Elsinga et al. (2005).

### *Dynamic spatial and velocity range*

Regarding the motion analysis, the main limitation consists in the spatial resolution and measurement precision. The choice of the interrogation volume size depends on the particle concentration; interrogation volumes typically feature a cube of voxels. Despite the use of the volume deformation technique (VODIM, Scarano and Poelma, 2009), the spatial modulation of the velocity fluctuations is still present when length-scales in the flow are

equal or smaller than the interrogation box size. Following Adrian (1997), the *dynamic spatial range* of the measurement is defined as the ratio between the object size and the smallest resolvable spatial variation. On the other hand, the *dynamic velocity range* indicates the ratio between the maximum and minimum measurable velocity, therefore inversely proportional to the measurement error. Reducing the interrogation volume size would lead to a higher *dynamic spatial range*, in turn providing higher spatial resolution. Moreover, due to the lower signal modulation, the accuracy of the velocity measurement would improve. Nevertheless, the reduction of the volume size affects the correlation signal-to-noise ratio (lower image density  $N_i$ , Adrian 1991), which results in higher precision error.

## 1.4 Objectives of the thesis

The objective of this thesis is the development of advanced processing techniques for Tomo-PIV data to address the issues described in section 1.3.4. The focus is set on the accuracy of the reconstruction with particular attention to the problem of the *ghost particles*, on the spatial resolution of the velocity and vorticity measurements and on the measurement accuracy of quantities, such as acceleration and pressure, that can be inferred from tomographic PIV results.

### 1.4.1 Reduction of ghost intensity

The introduction of the novel reconstruction method Motion Tracking Enhancement (MTE) is among the main advances presented in the present thesis. The MTE technique aims to increase the accuracy of the reconstruction with higher seeding density conditions; the main objective is to increase the amount of information within the measurement domain, therefore extending the *dynamic spatial range* of the measurement. The validity of the principle has been also confirmed by the number of other independent research groups who have devoted further studies to the subject (Atkinson et al. 2010, Discetti et al. 2012). The novel aspect of MTE is the combination of multiple recordings (two or more in case of time resolved PIV) to achieve a cancellation of particles that move not coherently with the flow pattern, which correspond to *ghost intensity*.

The working principle of the technique is briefly illustrated in Figure 1.8. In this two dimensional example, two particles are imaged by a two-camera system at subsequent time instants ('1' and '2'). Tomographic reconstruction by MART produces, along with the actual tracers, *ghost particles* in both the exposures, Figure 1.8-left. Assuming the displacement field, or an estimate of it, is known, the second exposure can be deformed to the first time instant by means of volume deformation technique, Figure 1.8-right. As the *ghosts* do not follow the flow field, they do not overlap after the deformation, unlike actual particles. These behavior allows for the identification of the *ghost intensity* from the actual one; averaging the two reconstructed fields (field '1' and the deformed field '2') retains the actual intensity and reduces the *ghost* one by a factor 2.

A detailed description of the MTE technique and the assessment of its performances is given in Chapter 4 of this thesis.

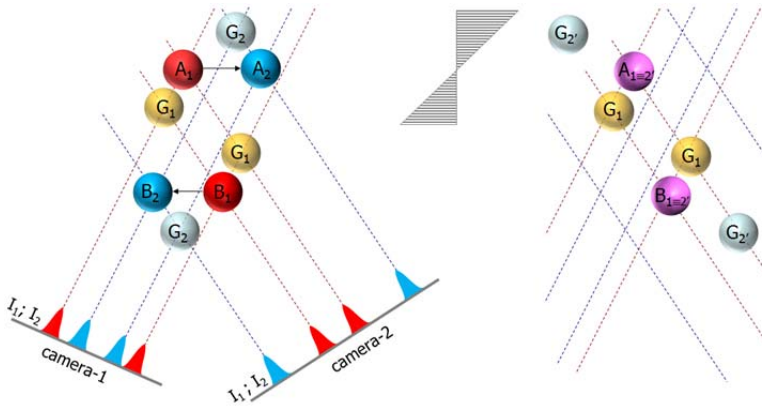


Figure 1.8 Left: particles A and B imaged from two cameras exposed twice (first exposure field ‘1’ in red and second exposure field ‘2’ in blue). Particle move accordingly to the flow pattern in gray. *Ghost particles* produced by MART reconstruction are represented in lighter colors. Right: superimposed reconstructed fields after the second exposure field is tracked back to the first exposure time considering the displacement field as known.

### 1.4.2 Adaptive motion analysis.

Inspired by the adaptive non-isotropic approaches proposed for interrogation of planar PIV images (Scarano 2003; Theunissen et al. 2007 see Figure 1.9; Astarita, 2009), a criterion to adapt the 3D interrogation volumes according to the local feature of the velocity gradient tensor is proposed in this thesis (Chapter 5). The basic principle consists in reducing the interrogation volume size in the direction of the strongest flow fluctuation and increase it in the other direction to maintain constant the interrogation volume on one hand and reduce the modulation of the signal due to the finite size of the interrogation region on the other. As a consequence the spatial resolution can be locally increased and the effect of velocity gradient within the correlation volume reduced, leading to more accurate velocity and vorticity measurement.

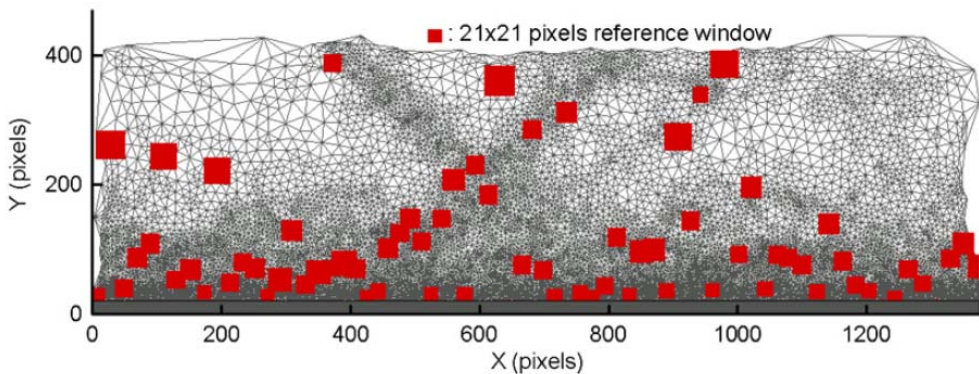


Figure 1.9 Adaptive mesh and interrogation window size for an instantaneous velocity fields from a shock-wave-boundary layer interaction (Theunissen et al. 2007).

### 1.4.3 Accurate acceleration measurement

A further development is investigated to add a significant increase of dynamic range in the measurement of acceleration (material derivative of the velocity) from Tomo-PIV data. This part of the work is justified by the increased interest in the use of PIV as a non-intrusive method to measure the pressure field in the flow. A recent review on the topic has been provided by van Oudheusden (2013). With the widespread use of high-speed PIV systems, time-resolved PIV measurements became possible and a number of studies have been devoted to extract pressure information from the measured velocity fields, Figure 1.10. Instantaneous pressure fields are obtained integrating across the domain the pressure gradient computed making use of the Navier-Stokes equations. A milestone in this method is the accurate evaluation of the fluid velocity material derivative.

Recently, pressure fields from PIV have been used to infer aerodynamic loads (van Oudheusden et al. 2007) and aeroacoustic predictions (Haigermoser 2009). The accuracy of the pressure measurement strongly depends on the accuracy of material acceleration. The latter can be obtained from time-resolved PIV data both in a Eulerian and Lagrangian frame. The latter option allows the use of larger time separation therefore lower precision error (Violato et al. 2011); the fluid parcel trajectory is reconstructed by numerical integration of the velocity vector time history. Finally, the acceleration is approximated by means of finite differences. Depending on the time separation along which the trajectories are reconstructed, precision and truncation errors are introduced and an optimal choice of the time separation needs to be made depending on the investigated flow.

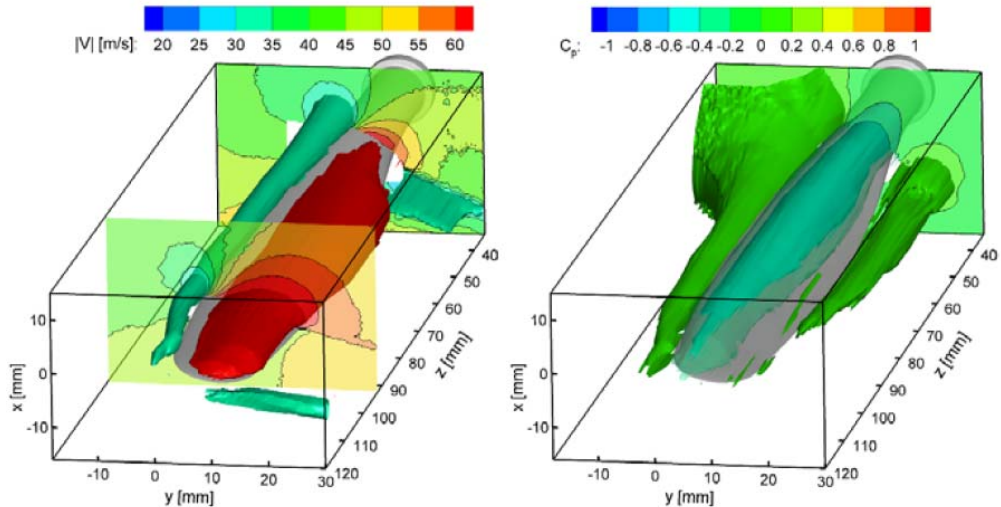


Figure 1.10 Analysis of propeller blade flow by means of phase-locked stereoscopic PIV. Left: iso-surfaces of absolute velocity. Right: iso-surfaces of pressure coefficient (Ragni et al. 2012).

In order to increase the acceleration dynamic range measured by tomographic PIV, a method inspired to the concept of particle tracking is proposed in this thesis (Tomo-3D-PT, see Chapter 6). Particle tracking is performed on reconstructed objects from tomographic PIV

and trajectories are accurately described over long sequences. The use of a polynomial fit of the trajectories provides a reduction of the precision error, while the value of acceleration is obtained analytically from the fitting curve therefore avoiding the introduction of truncation error, which modulates the acceleration signal. The sparsity of the reconstructed object in the three-dimensional space largely simplifies the tracking procedure, as the probability of overlapping particles is significantly lower when compared with the particle density in the recorded images.

## **1.5 Research framework**

The research documented in the present thesis has been carried out in the framework of the FLOVIST project (Flow Visualization Inspired Aeroacoustics with time-resolved tomographic PIV) partly funded by the European Research Council (ERC) grant n° 202887 and by the AFDAR project (Advanced Flow Diagnostics for Aeronautical Research) within the Seventh Framework program of the European Community grant n° 265695.

The aim of the FLOVIST project is to exploit the quantitative flow visualization approach of Tomo-PIV to perform aeroacoustic predictions and understand the fluid dynamic mechanisms at the origin of the acoustic noise. If compared to other experimental approaches such as surface pressure transducers and microphones arrays, the PIV technique has the advantage of being non-intrusive and capable of time-resolved measurements. Moreover the visualization of the flow, coupled with the aeroacoustic prediction, allows the identification of flow mechanisms that are responsible for the noise generation. Such information is not provided by other experimental techniques.

The investigation of aeroacoustic phenomena by means of tomographic PIV relies on the possibility to extract accurate instantaneous pressure information from the measured velocity fields; in this crucial step spatial and temporal derivatives of the velocity are needed. The sensitivity of this quantities to discretization effects and errors in the measured particle displacement motivates the effort in developing advanced techniques oriented to increase spatial resolution and accuracy of the tomographic PIV measurement.

A tool based on instantaneous 3D flow visualization for accurate pressure measurements and aeroacoustic predictions can be used to investigate a wide range of flows relevant for applications in aerodynamics (e.g. turbulent boundary layers, see Figure 1.11).

In this respect, the further development of tomographic PIV as a technique more affordable in terms of computational costs is a necessary step to progress from a method used mainly for fundamental studies to a reliable measurement tool for industrial applications. Along with the computational efficiency, issues such as robustness, spatial resolution and accuracy are important to allow the measurement of the spatial and temporal velocity derivatives and in turn the time-dependent flow pressure. The impact in aeronautical research can be significant, with applications ranging from increasing the aerodynamic efficiency of aircrafts and propulsion systems to reducing noise emissions in populated areas near airports and wind farms. The research conducted on tomographic reconstruction by MTE and its assessment in turbulent shear flows, has been realized within the scopes of the FLOVIST project.

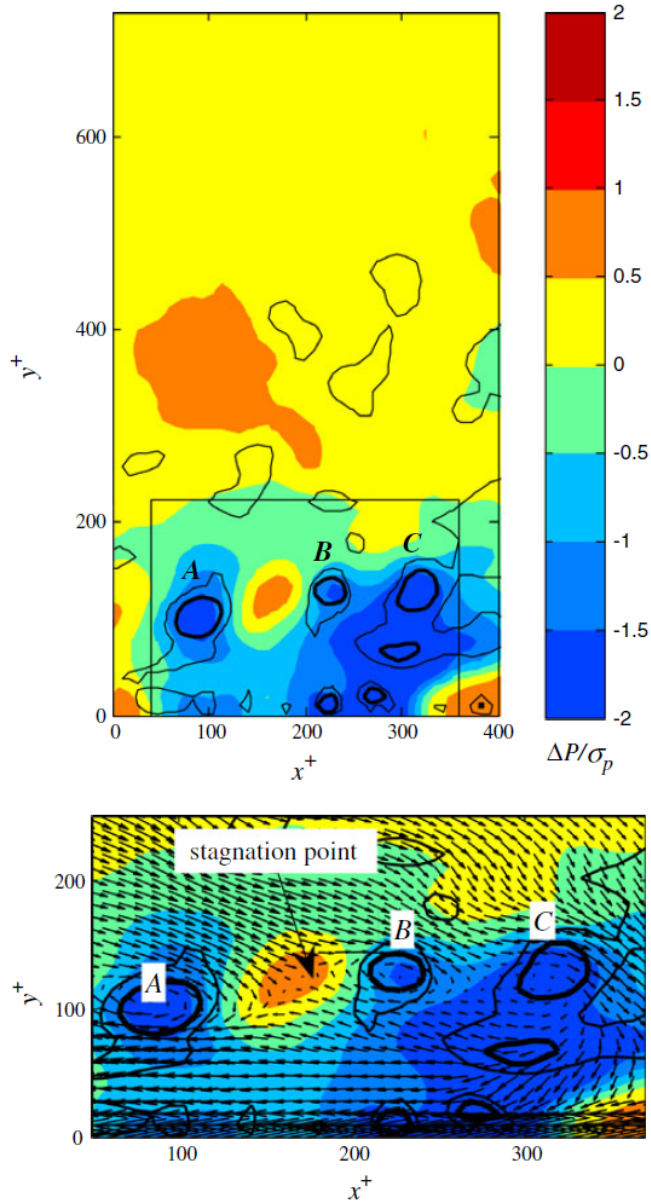


Figure 1.11 Top: pressure fluctuations in a turbulent boundary layer (pressure difference evaluated with respect to reference pressure). Bottom: magnified view of the region where vortex structures are identified (Ghaemi et al. 2012).

The relevance of tomographic PIV for industrial applications is confirmed by the attention devoted to its development within the AFDAR project ([www.afdar.eu](http://www.afdar.eu)). An international consortium encompasses ten international partners including a Russian research institute and

an Australian university and three industrial partners are involved either actively contributing to the research or providing access to facilities and dedicated instrumentation. The project is oriented to develop and assess image-based experimental technique for the analysis of aerodynamic and aerospace systems. Within the AFDAR project an entire work-package is dedicated to the tomographic PIV technique both from the aspect of advanced 3D reconstruction and interrogation algorithms. The research conducted on 3D adaptive interrogation and on Tomo-3D-PT has been conducted within the AFDAR work program.

## **1.6 Outline of the thesis**

The fundamental principles of the tomographic PIV technique are presented in Chapter 2; the working principle is discussed together with the main aspects involved in the experimental setup and in the data processing.

Methods to assess the performance of different processing approaches are given in Chapter 3; the attention is focused on establishing parameters to assess the accuracy of the result in real experimental conditions where the exact result is unknown.

In the last three chapters advanced techniques for tomographic reconstruction, motion analysis and acceleration and pressure estimation from Tomo-PIV data are presented, namely the Motion Tracking Enhancement technique (MTE, see Chapter 4), adaptive cross-correlation algorithm for 3D-PIV (see Chapter 5) and a Lagrangian method for acceleration estimate based on particle tracking (Tomo-3D-PT, see Chapter 6). The working principle of the above mentioned techniques is presented, followed by the performance assessment by means of both computer generated and real experimental data.

Finally the main results and conclusions of the thesis are summarized in Chapter 7 and future directions regarding the advanced techniques proposed in this work are discussed.

## Chapter 2

# Fundamentals of tomographic PIV

The entire thesis deals with tomographic PIV. In this chapter the fundamentals of the technique are sketched. Large amount of the presented material is taken from the available literature on the topic, in particular the work of Elsinga et al. (2006). The working principle of Tomo-PIV is described and several aspects regarding the experimental setup and its development are covered, such as the volumetric illumination, the choice of the particle tracers, the properties and the configuration of the imaging system and the calibration procedure. Subsequently, the processing phase of the tomographic PIV recordings is addressed. The treatment of the PIV images (image pre-processing), the tomographic reconstruction algorithm and the motion analysis performed by cross-correlation are discussed. The main limitations identified in the technique are highlighted, motivating the development work documented in the remainder of the thesis.

### 2.1 Working principle

The working principle of tomographic PIV is sketched in Figure 2.1-top. The experimental chain consists in three steps: images acquisition, tomographic reconstruction and motion analysis. A picture from an experimental setup from a Tomo-PIV experiment of a turbulent wake (Ghaemi and Scarano 2011) is shown in Figure 2.1-bottom.

The investigated domain, seeded with tracer particles, is illuminated by a laser light which is expanded in order to achieve the desired depth, approximately 30% of the size of the field of view along the height and width directions. Recordings are acquired by several digital cameras, typically 3 or 4, having different viewing directions with respect to the illuminated volume. Scheimpflug adapters are used in order to align the focal plane with the mid-plane of the 3D domain. In order to have particles in focus across the entire domain, the  $f$ -number ( $f_{\#}$ , obtained as the focal length of the lens  $f$  divided by the aperture diameter  $D$ ) needs to be increased to achieve the proper focal depth. Recordings are acquired at two subsequent time

instants separated by  $\Delta t$ ; in the case of time-resolved Tomo-PIV a sequence of recordings is acquired.

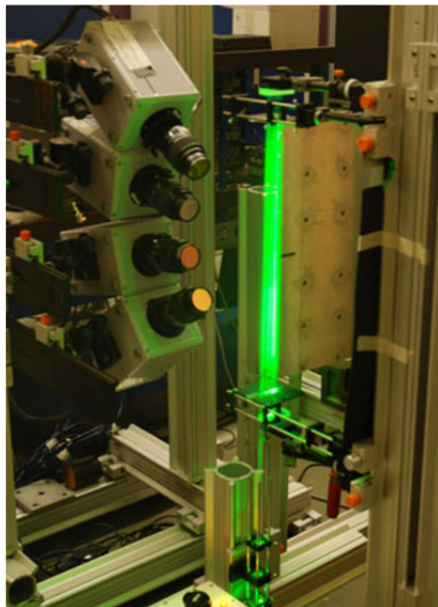
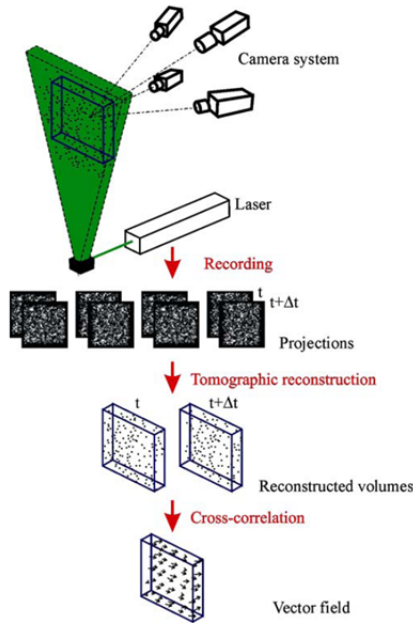


Figure 2.1 Top: working principle of Tomo-PIV (Elsinga et al. 2006). Bottom: example of tomographic PIV setup for the investigation of a turbulent wake (Ghaemi and Scarano 2011).

Two-dimensional images are reconstructed into three-dimensional light intensity distributions (reconstructed objects) by means of the multiplicative algebraic reconstruction technique (MART, Herman and Lent 1976). Since the method is based on the triangulation of the lines-of-sight of the single pixels in the camera sensors, the calibration of the imaging system needs to be very accurate (in the order of a fraction of a pixel).

The motion analysis is then performed by cross-correlation of the reconstructed objects in order to obtain the instantaneous vector fields. The correlation procedure is typically performed by 3D volume deformation iterative multigrid technique (VODIM, Scarano and Poelma 2009).

## **2.2 Experimental setup**

The present section illustrates the experimental setup of a tomographic PIV experiment. The aspects of illumination and seeding of the three-dimensional domain are covered as well as the calibration and configuration of the imaging system.

### **2.2.1 Volume illumination**

The illumination of the three-dimensional investigated domain is typically achieved through laser light, as for planar and stereo PIV experiments. Given the three-dimensionality of the domain, the constraints on the orientation of the illuminated region with respect to the imaging system are more relaxed than in planar PIV; in fact there is no need for a precise alignment of a thin light sheet to reduce out-of-plane motion, since particle tracers are imaged also when moving along the viewing direction.

Furthermore, the thickness of the illuminated area means a less complex optical arrangement since the laser beam diameter of most of lasers (e.g. Nd:Yag lasers) is large enough that a single cylindrical lens, or beam expander, can be sufficient to achieve the desired beam size.

Nevertheless, the need for a large laser beam also results in the need for stronger illumination. In fact, not only the light intensity decreases with the thickness of the beam, but, in order to image all the particles across the domain in focus, a large numerical aperture is required which further reduces the amount of light reaching the camera sensor. The situation is even more critical for time-resolved Tomo-PIV experiments (Schröder et al. 2008b), where more powerful illumination is needed to provide the proper light intensity within the pulse duration.

The type and dimensions of the particle tracers, therefore their light scattering properties, and the configuration of the imaging system (e.g. cameras in forward or backward scattering) also have an important effect on the choice of illumination configuration therefore on the final image quality, and will be discussed in the following sections.

In order to maximize the amount of light from a given laser source, methods such as the double-pass light amplification system (Scarano and Poelma 2009; Schröder et al. 2011) have been developed, Figure 2.2-top, where the laser light is back-reflected by a mirror placed on the opposite side of the light source; as a consequence the light intensity is amplified and also cameras placed in backward scattering can benefit from the reflected forward scattering.

A multi-pass light amplification system has been proposed by Schröder et al. (2008b) and Ghaemi and Scarano (2010), where the laser beam is directed with an angle towards a couple of high reflecting mirrors placed one in front of the other, Figure 2.2-bottom. The laser beam is therefore reflected back and forth within the mirrors multiple times increasing the light amplification effect up to 5 times when compared to the double-pass system (7 times if compared with the single-pass configuration).

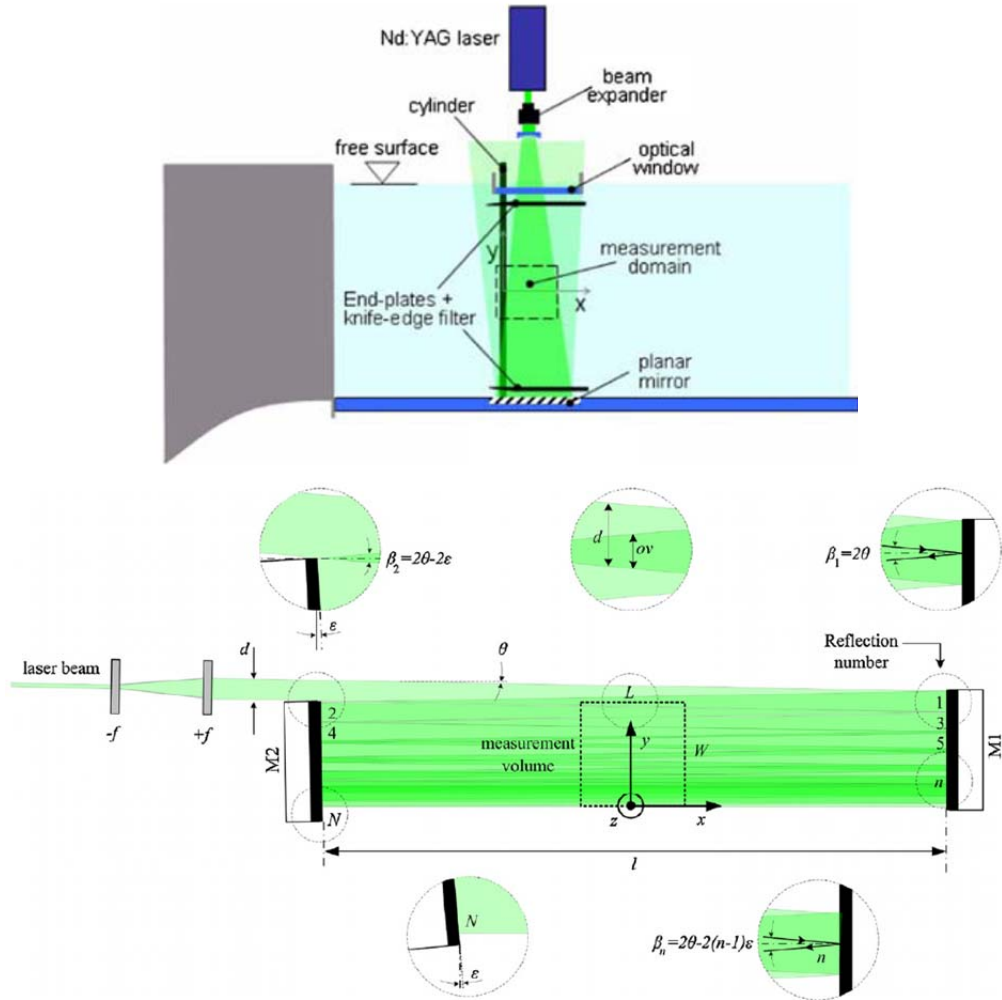


Figure 2.2 Top: double-pass illumination for Tomo-PIV experiment on cylinder wakes (Scarano and Poelma 2009). Bottom: multi-pass illumination schematic (Ghaemi and Scarano 2010).

Typical values for volume thickness and pulse energy employed in tomographic PIV experiments can be found in Scarano (2013); with the use of light amplification systems, illumination volumes of around 200 and 50 cm<sup>3</sup> can be achieved for water and air flows

respectively at a low repetition rate, while for high speed PIV, the illuminated volume is reduced approximately of a factor 1.5.

In particular conditions, typically for low speed water flow where the light requirements are lower, alternative illumination system to lasers can be used. For a study of the vortex generation mechanism of a flapping-wing model, Percin et al. (2011) used a normal Acer projector combined with a PowerPoint software to change color and position of the illuminated area, Figure 2.3-left. The amount of light was sufficient to successfully illuminate a  $100 \times 100 \times 40 \text{ mm}^3$  volume.

The use of light emitting diodes (LED) was proposed by Willert et al. (2010) in order to reduce costs and complexity of the light source setup, Figure 2.3-right. The feasibility of this technique for tomographic PIV has been discussed by Buchmann et al. (2011), where a turbulent flow in a water channel was investigated within a  $10 \times 20 \times 8 \text{ mm}^3$  volume.

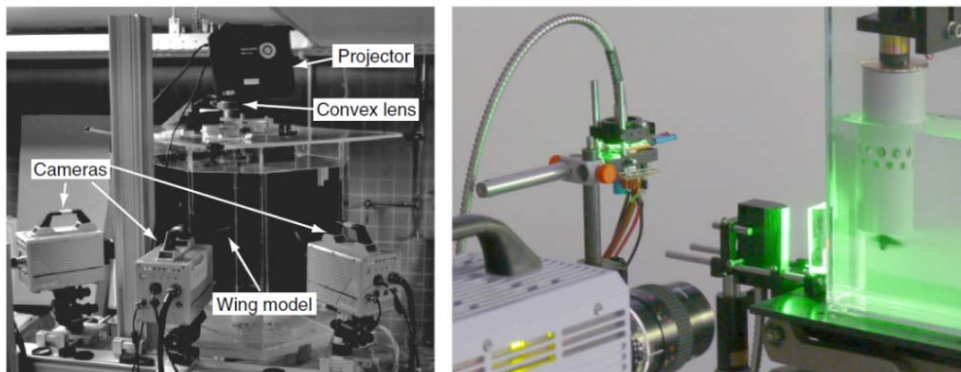


Figure 2.3 Left: experimental setup of a Tomo-PIV investigation of a flapping-wing in water; illumination provided by a normal projector (Percin et al. 2011). Right: LED illumination for tomographic PIV experiment of a small propeller in water (Willert et al. 2010).

### 2.2.2 Seeding particles

The choice of the seeding particles is a crucial aspect of every velocimetry technique based on particle imaging. In fact, the velocity of the flow is obtained indirectly from the measured displacement of the tracers. Moreover their concentration determines the spatial resolution.

#### *Fluid mechanical requirements*

The ideal particle tracers travel with the same velocity of the surrounding flow without affecting its behavior. Also, their light scattering property has to be good enough to be easily detectable on camera images.

Among the studies dedicated to the seeding particles to be used for PIV experiments, an overview of particle dynamic response is included in Enrich (1981) while criteria for the particles choice for different PIV application are proposed in Adrian and Yao (1985). Raffel et al (1998) used the Stokes flow interaction around a sphere to estimate the relative velocity between the particle tracer and the surrounding flow, based on the difference in the fluid and particle densities ( $\rho$  and  $\rho_p$  respectively) as:

$$\vec{V}_s = d_p^2 \frac{\rho_p - \rho}{18\mu} \vec{a} \quad 2.1$$

where  $d_p$  is the particle diameter,  $\mu$  the dynamic viscosity and  $\vec{a}$  the acceleration. Indicating with  $\vec{g}$  the gravitational forces acting on the particle,  $\vec{a}$  reads as:

$$\vec{a} = \frac{d\vec{V}}{dt} + \vec{g} \quad 2.2$$

As a consequence, the ideal particle tracer is the one that has the same density as the fluid in which it is immersed (neutral buoyancy condition); this situation can be easily achieved when dealing with liquid flows, but it is not simple to achieve for gaseous flows (e.g. air), where very small particles ( $d_p$  smaller than 10  $\mu\text{m}$ ) or hollow particles have to be adopted.

Based on the particle step response, a characteristic time  $\tau$  can be defines as:

$$\tau = d_p^2 \frac{\rho_p}{18\mu} \quad 2.3$$

indicating that smaller particles with a low density are preferable. On the other hand a smaller particle has weaker light scattering properties, Figure 2.4, which can undermine its detectability from the background noise in case of weak illumination.

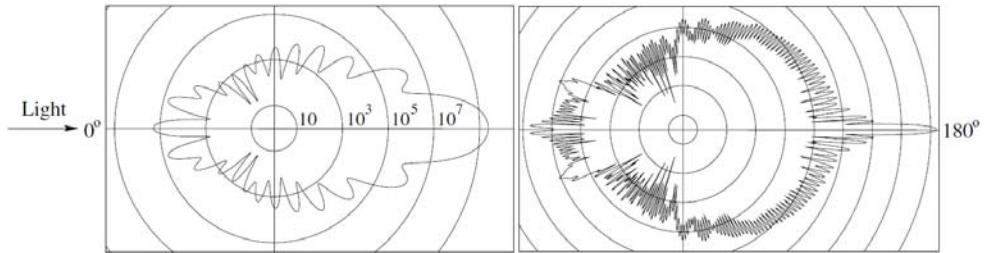


Figure 2.4 Light scattered by a 1  $\mu\text{m}$  (left) and by a 10  $\mu\text{m}$  (right) diameter oil particle in air (Raffel et al. 1998).

This consideration leads to the conclusion that performing a Tomo-PIV experiment is more challenging when an air flow is considered with respect to a water flow both from the point of view of the buoyancy condition to be satisfied and of the illumination of the particle tracers.

Another issue connected to the interaction between particle tracers and the flow medium is represented by multiple scattering effects, which limit the achievable seeding density. In fact, as discussed in Michaelis et al. (2010), increasing the seeding density also increases the opacity of the medium which results in diffuse illumination therefore poor contrast on the camera images. Since larger particles having stronger scattering properties are used in liquid flows, this effect is more critical in water than in air flows. The particle concentration  $C$  is limited to approximately 3 and 20 particles/ $\text{mm}^3$  for water and air respectively.

### Particle imaging

The particle image size on the camera sensor is determined by the combination of its geometrical diameter and the diffraction spot due to the optical response of the lens. Being  $d_p$  the particle diameter, the geometric image diameter  $d_g$  is obtained as  $M \cdot d_p$ , where  $M$  is the magnification factor. Since the lenses aperture is limited, the response of the lens can be defined by means of the Airy function, leading to a diameter of the diffraction spot as:

$$d_{diff} = 2.44 f_{\#} (M + 1) \lambda \quad 2.4$$

where  $f_{\#}$  indicates the  $f$ -number and  $\lambda$  is the wavelength of the reflected light (Goodman 2004). The final particle image diameter reads as:

$$d_{\tau} = \sqrt{d_{diff}^2 + d_g^2} \quad 2.5$$

or, in pixel units,  $d_{\tau}^* = d_{\tau} / \Delta_{pix}$ , where  $\Delta_{pix}$  is the pixel size (Adrian and Yao 1985).

This relation applies in the case of in-focus particles, when the depth of focus  $\delta Z$  is equal or larger than the size of the illuminated volume along the viewing direction  $\Delta Z$ . As indicated by Solf (1986), the depth of focus is given by:

$$\delta Z = 4.88 f_{\#}^2 \left( \frac{M + 1}{M} \right)^2 \lambda \quad 2.6$$

Tomographic PIV requires a large depth of focus depending on the thickness of the illuminated region. In order to increase  $\delta Z$ , the numerical aperture  $f_{\#}$  has to be increased, which results in a reduction of the amount of light collected by the sensor.

In combination with a large volume illumination and particularly for air experiments where smaller particles are used, following eqn. 2.6 can lead to insufficient light intensity on the image. In recent experiments, as observed from Scarano (2013), it has been shown that the condition on the  $\delta Z$  can be relaxed in order to have a limited out-of-focus effect (blur circle smaller than 2 pixels) which does not degrade the quality of the reconstruction. In the case of small magnification, the blur diameter  $d_B$  can be defined as:

$$d_B \approx \frac{\varepsilon_Z \cdot M^2}{f_{\#}} \quad 2.7$$

Where  $\varepsilon_Z$  is the distance between the particle and the focal plane, Figure 2.5.

In this situation, the particle image diameter definition at eqn. 2.5 is modified as:

$$d_{\tau} = \sqrt{d_{diff}^2 + d_g^2 + d_B^2} \quad 2.8$$

Moreover, recent developments in the calibration optical transfer function (OTF, Schanz et al. 2012) allow for an even larger out-of-focus effect which can be accounted for during the reconstruction process by means of an adaptive weighting function for the MART updates (see section 2.3.2).

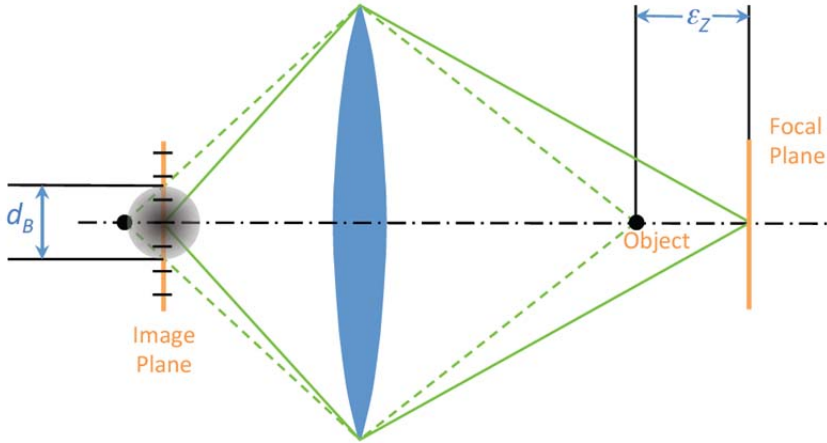


Figure 2.5 Blur circle of an out-of-focus particle (Scarano 2013).

### Seeding density

The number of particles within the investigated domain strongly affects the quality of the measurement. For planar PIV, a minimum number of approximately 10 particles inside the box have to contribute to the correlation map to obtain a robust correlation peak (Keane and Adrian 1992). Since the phenomenon of out-of-plane motion is not critical in Tomo-PIV, this number can be lowered down to 5-7 particles (Violato et al 2011).

On the other hand, the need for highly seeded flows, in order to increase the spatial resolution of the measurement, contrasts with the requirements in terms of tomographic reconstruction; as it will be illustrated in section 2.3.2, the quality of the reconstruction degrades with the seeding density. As a consequence, a compromise between accuracy and spatial resolution has to be achieved. This issue has been the main drive for the author to develop a method able to deal with higher seeding density without affecting the accuracy of the reconstruction (see Chapter 4).

When dealing with tomographic PIV images a common parameter to indicate the seeding concentration is the imaged seeding density or particles per pixel ( $ppp$ ). The particle per pixel has been used by Elsinga et al. (2006) to perform a parametric study of the reconstruction quality and it is therefore useful to identify proper working conditions when setting up an experiment. The value of  $ppp$  is obtained dividing the number of imaged particles by the number of pixels in the camera image; numerical simulation identified an optimum working condition for a 4 cameras imaging system of approximately 0.05  $ppp$ . Methods to evaluate the  $ppp$  value are presented in section 3.2 of this thesis.

Being the 3D domain discretized in voxels elements (cubic elements having typically the same linear size of a pixel), indicating with  $M$  the magnification factor and  $\Delta_{pix}$  the pixel pitch (in mm), the relation between the  $ppp$  and the number of particles per voxel ( $ppv$ ) is:

$$ppv = \frac{ppp}{\Delta Z \cdot M / \Delta_{pix}} \quad 2.9$$

where  $\Delta Z$  indicates the thickness of the illuminated region in mm. Equation 2.9 applies in case of rectangular illumination. When this condition is not verified (e.g. cylindrical illumination), the value of  $ppv$  can be evaluated as:

$$ppv = \frac{N_p}{V_d} \quad 2.10$$

Where  $V_d$  is the volume of the illuminated domain in voxels and  $N_p$  is the total number of particles in the domain computed as:

$$N_p = ppp \cdot DX \cdot DY \cdot \left( \frac{M}{\Delta_{pix}} \right)^2 \quad 2.11$$

Where  $DX$  and  $DY$  are the dimensions of the imaged illuminated domain in mm. The equation for  $V_d$  depends on the geometry of the illumination.

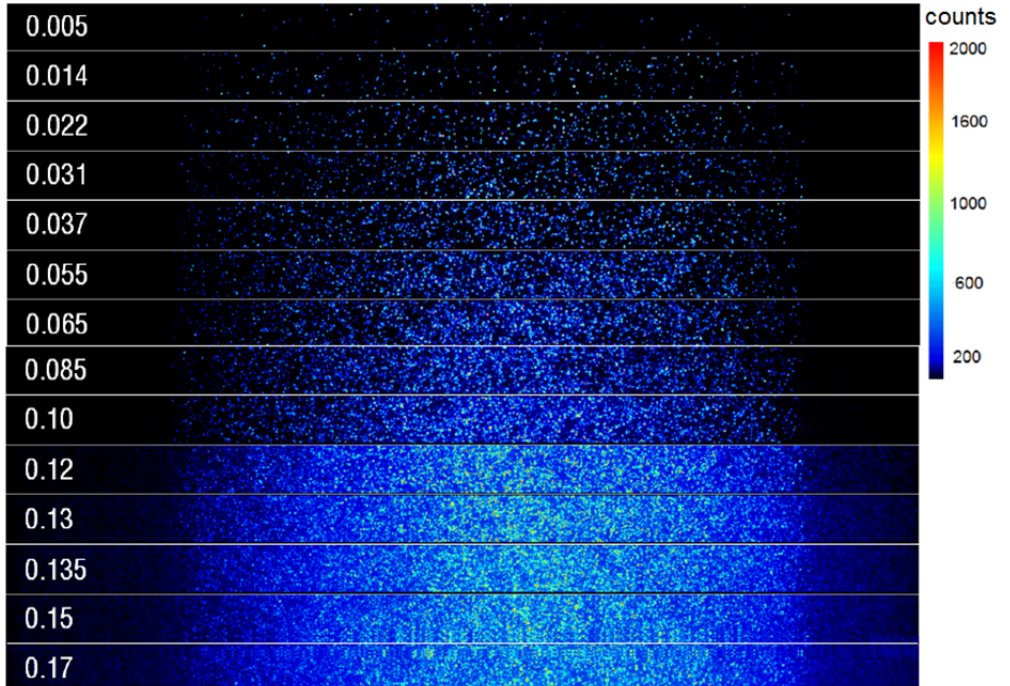


Figure 2.6 Examples of Tomo-PIV images at different seeding density from a water jet experiment (Michaelis et al. 2010).

From the  $ppv$ , the physical seeding concentration  $C$  (in particles/mm<sup>3</sup>) is obtained as:

$$C = ppv \left( \frac{M}{\Delta_{pix}} \right)^3 \quad 2.12$$

An alternative parameter to indicate the imaged seeding density is represented by the image source density  $N_s$  (Keane and Adrian 1992). The source density takes into account both the number of particles in the sensor and the imaged diameter  $d_\tau^*$  :

$$N_s = ppp \frac{\pi d_\tau^{*2}}{4} \quad 2.13$$

The source density can be estimated as the fraction of active pixels in the camera sensor and represents a more direct reference for the reconstruction quality; Novara et al. (2010) estimated that an accurate reconstruction can be achieved when  $N_s < 0.3$  for a 4 cameras tomographic system.

Examples of tomographic PIV images from a tomographic PIV experiment of a water jet are shown in Figure 2.6. The particle imaged diameter is approximately 2 pixels and the seeding density is varied between 0.005 *ppp* ( $N_s = 0.015$ ) and 0.17 *ppp* ( $N_s = 0.5$ ). The working range for an accurate reconstruction can be approximately identified between *ppp* 0.05 and 0.1 ( $0.15 < N_s < 0.3$ ).

### 2.2.3 Configuration of the imaging system

Unlike for planar PIV, the presence of multiple cameras in the tomographic imaging setup leads to further considerations about their arrangement and configuration. In fact, the angle between the cameras, therefore between the viewing directions, determines the angular aperture of the tomographic system.

The effect of the camera angle on the accuracy of the tomographic reconstruction has been studied by Elsinga et al. (2006) by means of numerical simulations. Being  $\theta$  the angle between adjacent cameras, they found an optimum angle of approximately  $30^\circ$ . Smaller angles cause a strong difference in the resolution along the depth with respect to the one attained in the other two directions; as a result reconstructed particles are elongated along the viewing direction causing a larger uncertainty during the correlation peak identification. On the other hand, wide angles cause the lines-of-sight to have a longer path within the reconstructed domain which results in a higher number of *ghost particles*.

Established that an optimum value for the solid angle subtended by the cameras maximizes the reconstruction accuracy, a further consideration is made by Scarano (2013). Here the parameter investigated by numerical simulation is not the angle between adjacent cameras, but the planar angle  $\beta$  formed considering the total solid angle of the tomographic system. Indicating with  $Q$  the reconstruction accuracy (quality factor, Elsinga et al. 2006), the angle  $\beta$  has been varied as well as the particle imaged diameter and two different camera configurations have been considered. In fact, given the three-dimensional arrangement of the setup, different arrangements of the imaging system are possible keeping the solid angle constant. A cross-like configuration is considered where 4 cameras are placed at the vertices of an horizontal-vertical cross, Figure 2.7-top-left. On the other hand a linear arrangement is considered where the 4 cameras are coplanar, separated by an angle equal to  $\beta/4$ , Figure 2.7-top-right.

As shown in Figure 2.7-bottom, the cross-like configuration provides a slightly more accurate reconstruction; this is due to the fact that the linear configuration produces more reconstructed spurious intensity along the viewing direction (particle elongation). Instead,

thanks to its 3D nature, the cross-like configuration is able to erode the elongated region by means of the lines-of-sight coming from the top, the bottom besides the ones from the sides of the particle; as a result less spurious intensity is produced by the reconstruction algorithm. Figure 2.7-bottom also shows the disadvantage of having an extremely small particle image diameter (1 pixel being the absolute minimum  $d_{\tau}^*$ ), which increases discretization errors.

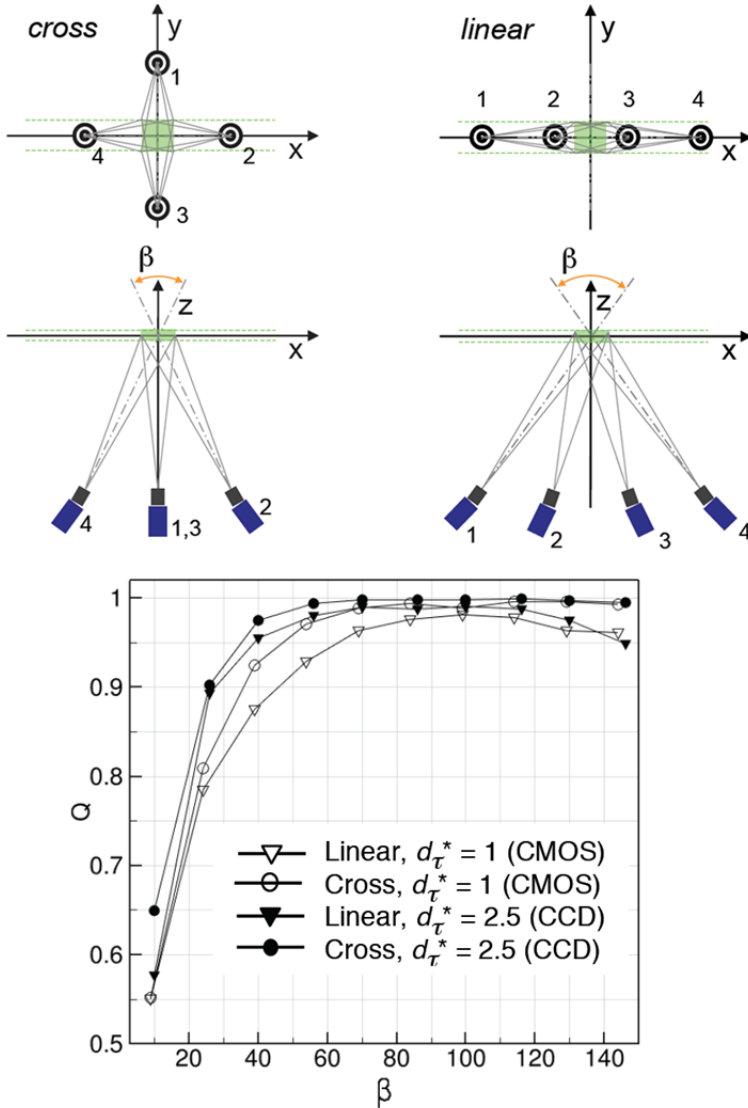


Figure 2.7 Top: two possible configurations of the tomographic imaging system. Bottom: reconstruction quality versus solid angle subtended by the camera system for cross-like and linear cameras configuration. Two different particle sizes are considered, (Scarano 2013).

## 2.2.4 Calibration

Since the tomographic reconstruction algorithm relies on the triangulation of lines-of-sight of individual pixels in the three-dimensional space, a calibration of the imaging system is required.

The calibration is carried out by means of a calibration target which is imaged at several positions (typically 3 to 5) along the depth of the illuminated volume, Figure 2.8-left. The markers on the target surface are identified by means of correlation of a template of the mark; based on the known positions of markers a relation can be found between the pixels coordinates  $(x, y)$  and their projection in the three-dimensional space  $(X, Y, Z)$ ; a third order polynomial in  $X$  and  $Y$  (Soloff et al. 1997) is used to obtain the mapping function which relates the physical and image coordinates within the whole investigated domain, Figure 2.8-right.

The mapping function is then linearly interpolated between the discrete  $Z$  positions at which the target is imaged or extrapolated to cover the complete measurement volume. The choice of the third order polynomial is usually preferred to the one of a pinhole camera model in situations where optical aberrations can be encountered (e.g. geometric distortions or blurring).

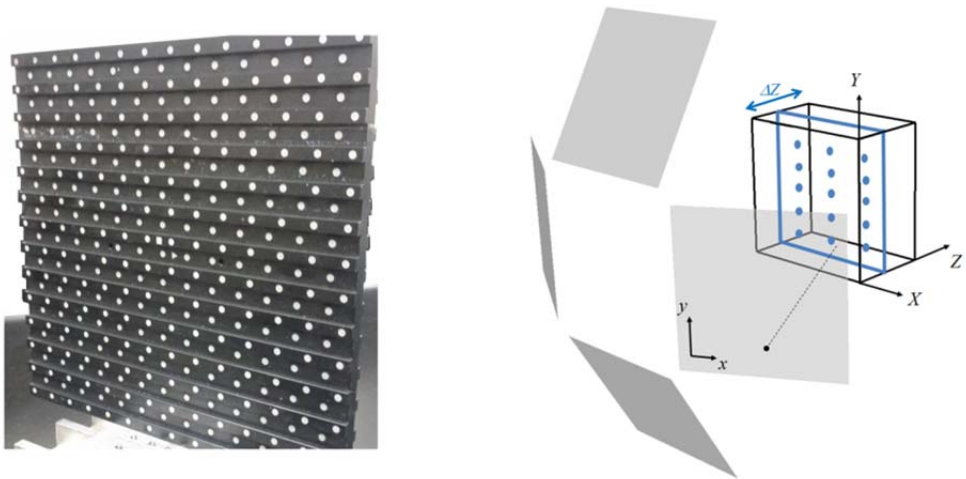


Figure 2.8 Left: example of a double-layered calibration target. Right: sketch of calibration procedure for Tomo-PIV.

The calibration procedure adopted in tomographic PIV is therefore close to the one used for Stereo-PIV, the main difference concerning the nature of the calibration errors.

While for stereoscopic PIV the main source of error is the misalignment between the calibration plate and the illuminated plane, for Tomo-PIV, the misalignment is not particularly critical since the mapping covers a full 3D volume instead of a single plane. Nevertheless, given the relatively large distance between the imaging system and the investigated domain, errors due to vibrations, thermal deformation within the camera optics and loose camera supports can result in a severe deviation of the mapped lines-of-sight. As a consequence, imaged intensity belonging to the same particle tracer do not triangulate in the

3D space, leading to cancellation of particles and therefore affecting the spatial resolution of the measurement.

As reported by Elsinga et al. 2006, during the first tomographic PIV experiments, the calibration error was tackled by means of a Gaussian smoothing applied to the camera images. As a result the particle image diameter was increased and so was the probability of intensity back-projected into the 3D space to intersect; the consequence was a lower rate of cancelled particle intensity.

Nevertheless this method carries an undesirable effect, which consists in the increase of the source density  $N_S$  as a consequence of the larger  $d_\tau^*$ , potentially leading to a poorer reconstruction in case of high seeding density.

A crucial step forward is represented by the introduction of the Volume Self-calibration method proposed by Wieneke (2008). The method is inspired by the planar self-calibration used in Stereo-PIV to correct misalignment between the laser sheet and the calibration plane (Coudert and Schon 2001; Wieneke 2005). The self-calibration technique is based on the minimization of the disparity between the images of the same particle onto the camera images. After individual particles are identified in the image plane, they are triangulated into a best-fit position  $(X, Y, Z)$  in the 3D domain; the disparity  $d_i$ , where  $i$  indicates the camera, is computed as the difference between the projected particle position  $(x'_i, y'_i)$  and the imaged particle position on the camera image as  $(x_i, y_i)$  and reads as:

$$d_i = (d_{ix}, d_{iy}) = (x'_i, y'_i) - (x_i, y_i) \quad 2.14$$

The value of the disparity is then used to correct the mapping function and therefore the lines-of-sight of the pixels. The disparity value is usually computed for groups of particles dividing the reconstructed domain in sub-volumes thus improving the robustness of the disparity measurement.

Since the technique relies on individual particles identification and matching (similar to the concept of 3D-PTV, Maas et al. 1993), recordings to be used for self-calibration purposes need to be taken at a lower seeding density than the one achievable in tomographic PIV, typically around 0.02 *ppp* (Figure 2.9).

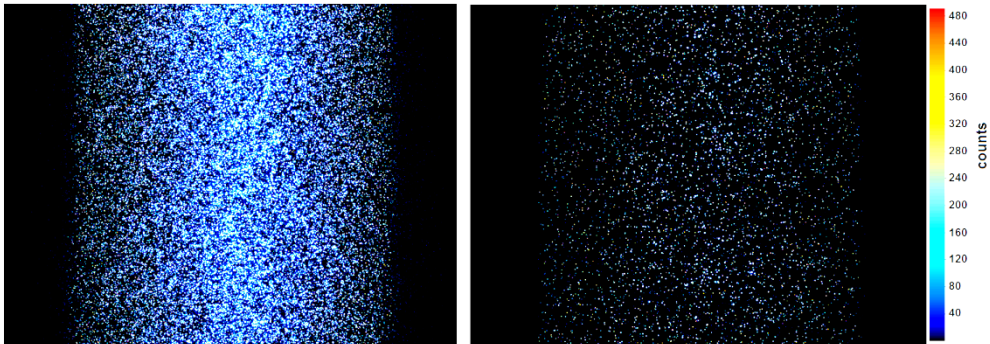


Figure 2.9 Left: typical imaged seeding density for tomographic PIV recording (*ppp*=0.05). Right: low seeding density image for self-calibration procedure (*ppp*=0.02).

In order to increase the number of particles over which the disparity map is evaluated, multiple recordings are analyzed to obtain a single disparity map, Figure 2.10. The procedure can be applied iteratively until the disparity value is reduced to an acceptable value; typically the calibration errors can be reduced from approximately 2-3 pixels to less than 0.1 pixels after the self-calibration procedure is applied.

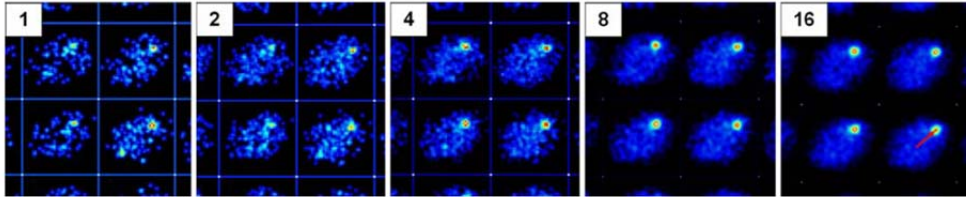


Figure 2.10 Example of disparity maps summed over a different number of recordings (from 1 to 16); as the number of evaluated particles increases a clearer peak is obtained (Wieneke 2008).

The application of the self-calibration technique has a dramatic effect on the reconstruction accuracy and, as a consequence, on the motion analysis. Figure 2.11 shows the increased robustness of velocity and vorticity field obtained with the self-calibration procedure. The corrected mapping function leads to lines-of-sight intersecting in the correct 3D location, therefore more actual particles are reconstructed which contribute to the formation of the cross-correlation peaks.

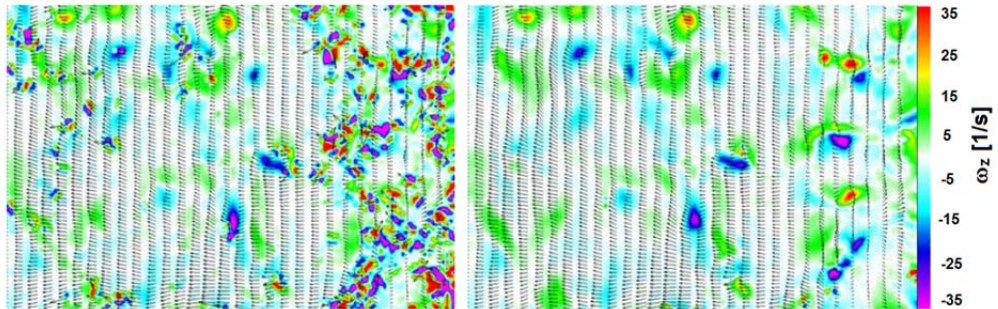


Figure 2.11 Velocity vectors and vorticity contours for a flow behind a cylinder investigated with Tomo-PIV without (left) and with (right) the use of the volume self-calibration technique (Wieneke 2008).

In a recent study from Michaelis and Wolf (2011) a method based on iterative disparity evaluation and a careful choice of the particle intensity peak threshold is investigated to obtain robust corrections even from the analysis of a single recording. This method proves useful when dealing with vibrations of the imaging system and low repetition rate; in such conditions calibration errors are unsteady and change from recording to recording.

## 2.3 Data processing

Concerning the accuracy of the Tomo-PIV measurement, the processing of the recorded images is as relevant as the experimental setup parameters. The pre-processing of the PIV signal, the 3D intensity field reconstruction and the motion analysis are discussed in this section.

### 2.3.1 Image pre-processing

The quality of the PIV images has a large impact on the reconstruction accuracy; spurious intensity such as background noise on the image is back-projected into the 3D domain by the MART algorithm (Elsinga et al. 2006). As a consequence images are processed before reconstruction is performed in order to reduce or cancel the background intensity.

As reported by Scarano (2013), an effective background removal technique is obtained combining the subtraction of a pixel-wise time-history minimum intensity and a minimum subtraction within a small spatial kernel around each pixel. Figure 2.12 shows an example of raw and pre-processed image after minimum intensity subtraction over a  $31 \times 31$  pixels kernel.

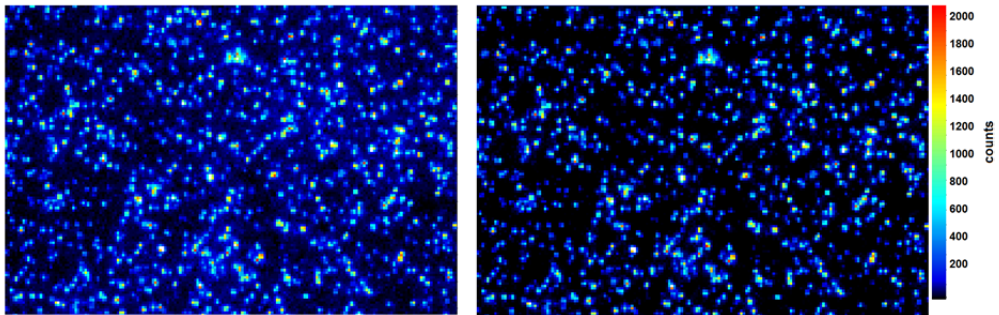


Figure 2.12 Example of tomographic PIV image before (left) and after pre-processing for background intensity removal.

Furthermore, the recorded light intensity can be different for the several cameras in the tomographic system due to different sensor sensitivity or to the different viewing direction (e.g. forward or backward scattering). In this case, in order to prevent the signal from one or more camera to be dominating with respect to the others, a normalization of the intensity is performed, taking one of the cameras as the reference frame.

As already mentioned in the previous section, a Gaussian filtering was often performed, before the introduction of the volume self-calibration procedure, in order to reduce calibration errors and to reduce image noise. Given the resulting increase in source density  $N_S$ , this filtering procedure is not recommended when the seeding density exceeds  $0.05 \text{ ppp}$  and a higher number of *ghost particles* would be generated.

In the presence of solid walls within the imaged domain (e.g. airfoil surfaces, jet nozzles), laser light reflections can affect or make the reconstruction of particle tracers in the proximity of the surface, which is most of times a region of interest, impossible. Dark paint applied to the surface or a different illumination angle can help solving the issue, but, in case

reflections are still important on the recorded images, something can be done at the image pre-processing stage. Scarano and Sciacchitano (2011) proposed a method to reduce light reflections from stationary or moving surfaces based on the availability of a time-resolved sequence of recording.

The method is based on the application of a high-pass filter on the frequency of the intensity recorded by each pixel; in such a way, the stationary or low frequency signal from the reflection can be filtered out from the recordings retaining only the high frequency signal from the particle tracers. The technique was found effective provided that the frequency of the reflection vibration is separated by the one proper of the tracers by at least a factor three.

### 2.3.2 Tomographic reconstruction

The Tomo-PIV technique is based on the concept of tomographic reconstruction. This step consists in the reconstruction of a three-dimensional object (3D particle field) from a set of its two dimensional projections (camera images). The reconstruction algorithm is described in this section. The reconstruction quality factor is introduced and an overview of advanced reconstruction techniques is offered.

#### *Reconstruction algorithm*

In tomographic PIV the object is represented by the 3D light distribution scattered by the particle tracers and its reconstruction is performed starting from the images taken by the camera system. Elsinga et al. (2006) assessed the suitability of several reconstruction algorithms and opted for algebraic reconstruction algorithms (Herman and Lent 1976), which were found to be the most adequate method for a signal such as the one from PIV images where peaks of light intensity emerge from a relatively low intensity background.

The reconstructed intensity,  $E(X, Y, Z)$ , is discretized in 3D cubic elements called voxels having approximately the same linear size as the pixels composing the camera images. The reconstruction technique makes use of the projection equation linking the intensity in the image space,  $I(x, y)$ , to the 3D object space as:

$$\sum_{j \in N_i} w_{i,j} E(X_j, Y_j, Z_j) = I(x_i, y_i) \quad 2.15$$

where  $i$  identifies the  $i^{\text{th}}$  pixel and  $N_i$  the number of voxels along the line-of-sight (LOS) of the pixel which contributes to its intensity. The value  $w$  defines the weight of the contribution of the  $j^{\text{th}}$  voxel to the  $i^{\text{th}}$  pixel's intensity and depends from the distance between the voxel and the line-of-sight.

A graphical representation of the imaging model is presented in Figure 2.13, where a top-view of the reconstructed domain is shown; as a consequence, camera sensors appear as linear arrays of pixels.

Assuming the pixel's projection as a prism having a cross-section coinciding with the pixel size and direction given by the calibration and self-calibration procedure and the voxel as a cube, the value of  $w$  can be computed as the fractional volume of their intersection. In order to simplify the calculation of the weights, the model is approximated with a cylinder intersecting a sphere which does not depend on the angle of the line-of-sight, but only from the pixel and voxels size and its distance from the LOS.

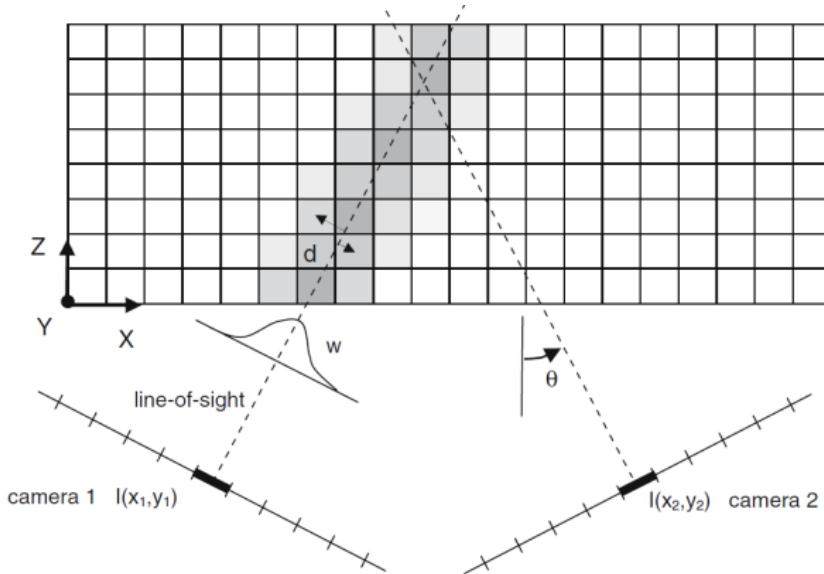


Figure 2.13 Two-dimensional sketch of the projection model for tomographic reconstruction; dashed lines indicate the pixels' lines-of-sight. Voxels are color-coded depending on the value of  $w$  and their distance from the LOS is indicated with  $d$  (Elsinga et al. 2006).

Moreover, given the computational burden of computing these values, the weights can be stored as a function of size and distance and read from a look-up table during the reconstruction iterations (Discetti and Astarita 2012a). The impact of different models for the computation of  $w$  is described in Thomas et al. (2010).

Among the available reconstruction algorithms, Elsinga et al. (2006) performed a numerical assessment of two of them, namely the ART (algebraic reconstruction technique, Gordon et al. 1970) and the MART (multiplicative algebraic reconstruction technique, Herman and Lent 1976) algorithms. Both algorithms make use of the projection equation (eqn. 2.15) to iteratively update an initial guess for the intensity distribution  $E(X, Y, Z)$ .

The difference between the two methods is in the update term; ART computes the update as the difference between the projected intensity and the recorded image intensity and adds this difference to the previous reconstructed intensity. On the other hand, MART multiplies the reconstructed intensity by the ratio between the image intensity and the projected one.

As discussed in Elsinga et al. (2006), the ART algorithm acts as an OR operator meaning that in order to have a non-zero-value of intensity in the reconstructed system it is sufficient a non-zero signal on the pixel of one single camera in the imaging system. As shown in Figure 2.14, the ART algorithm produces reconstructed intensity traces along the LOS of active pixels which remain even after some iterations.

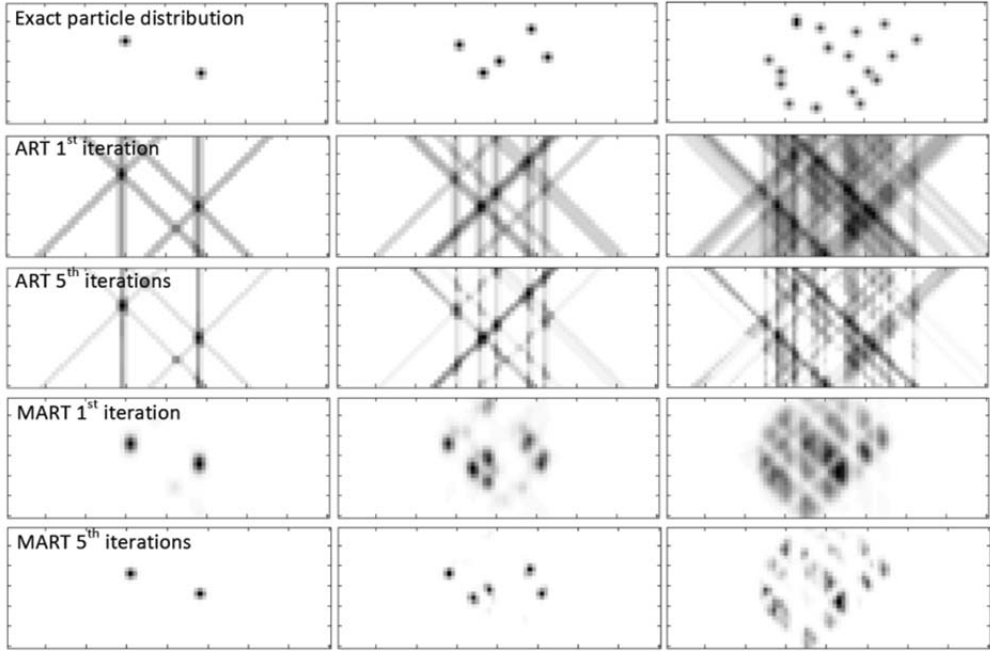


Figure 2.14 Computer simulated 2D tomographic reconstruction examples (3 cameras). Top: original particle distributions (seeding density increases from left to right). Middle: ART reconstruction at the 1st and 5th iterations. Bottom: MART reconstruction at the 1st and 5th iterations (Scarano 2013).

On the other hand, the MART algorithm behaves as an AND operator; therefore reconstructed intensity is retained only if the signal is present on every camera and traces from the LOS are reduced by successive iterations, Figure 2.14-bottom. As a consequence, the MART algorithm candidates as the most suitable technique for reconstruction the signal from Tomo-PIV images, where strong gradients are found due to single particles within a zero or low intensity background (Verhoeven 1993), and it was chosen by Elsinga et al. (2006) to perform reconstruction of tomographic PIV data.

The update equations for the MART algorithm is performed for each pixel in each camera  $i$  and for each voxel  $j$  along its LOS as:

$$E_{k+1}(X_j, Y_j, Z_j) = E_k(X_j, Y_j, Z_j) \cdot \left( \frac{I(x_i, y_i)}{\sum_{j \in N_i} w_{i,j} E_k(X_j, Y_j, Z_j)} \right)^{\mu w_{i,j}} \quad 2.16$$

where  $k$  indicates the iteration and  $\mu$  a relaxation parameter  $0 \leq \mu \leq 1$ , usually set to 1. The term  $\sum_{j \in N_i} w_{i,j} E_k(X_j, Y_j, Z_j)$  represents the projection of the intensity estimate at the iteration

$k$ . The weight  $w$  is used as an exponent for the update term of MART to ensure that only the voxels affected by the  $i^{\text{th}}$  pixel are updated. The initial guess  $E_0$  for the reconstruction algorithms is usually set to a uniform value while  $E$  and  $I$  are positive definite.

### Reconstruction quality

A parametric study was performed by Elsinga et al. (2006) making use of computer generated data, in order to assess the effect of several experimental and processing parameters on the accuracy of the reconstruction. The quality factor  $Q$  was used to quantify the reconstruction accuracy, where  $Q$  is the normalized cross-correlation coefficient computed between the actual particle field (known for numerical simulations) and the reconstructed one as:

$$Q = \frac{\sum E_{\text{actual}} \cdot E_{\text{rec}}}{\sqrt{\sum E_{\text{actual}}^2 \cdot \sum E_{\text{rec}}^2}} \quad 2.17$$

For iterative MART, the factor  $Q$  and the measured velocity field by cross-correlation analysis typically do not change appreciably after 5 iterations (Elsinga et al. 2006).

The reconstruction accuracy is affected by different types of error, which can be classified in three categories: discretization errors, shape errors and *ghost particles* (Maas et al. 1993). Discretization errors are due to the voxel representation of the intensity field and become important when the imaged particle diameter,  $d_\tau^*$ , is small (below 2 pixels). Shape errors are caused by the limited aperture of the tomographic system (solid angle subtended by the camera system); as a consequence, reconstructed particles are elongated along the viewing direction which reduces the accuracy of the velocity component along the depth.

Nevertheless, the main source of error is represented by the *ghost particles*. They arise from the non-uniqueness of solution to the under-determined algebraic problem defined by equation 2.15 and consist of spurious intensity peaks appearing in the reconstructed intensity field together with actual particles. Since they do not necessarily follow the flow motion, their presence can affect the motion analysis. Furthermore intensity contributing to the *ghosts* is subtracted from the actual field which leads to a less robust cross-correlation signal. A detailed description of the *ghost particles* behavior can be found in Elsinga et al. (2011).

In the hypothesis that the optical arrangement is such that the particle diameter on the image is sufficiently large and that the angle between cameras is within the optimal range (see section 2.2.3), the quality factor  $Q$  depends mostly upon the *ghost particles*.

Since the *ghost particles* form at the intersections of lines-of-sight correspondent to non-zero pixels their number strongly depends on the seeding density and the particle image diameter (therefore from the source density  $N_S$ ) and the number of cameras  $N_C$ .

Figure 2.15-top-left shows an example of the formation of *ghosts* from reconstruction of images of 2 particles from a 2 camera system; increasing the amount of information, number of cameras, leads to the cancellation of *ghost particles* (Figure 2.15-top-right). The situation becomes more complex when, as in real conditions, the number of imaged particles increases and distinct particle images cannot be distinguished on the camera sensor; multiple intersections from active LOS generate a higher number of *ghost particles*, Figure 2.15-bottom.

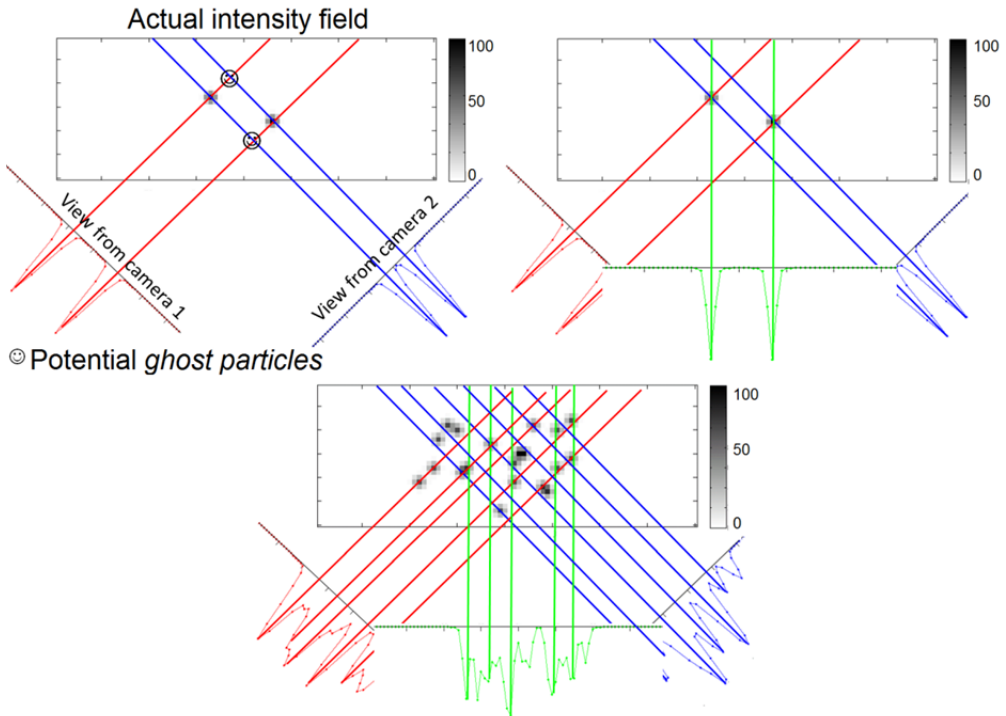


Figure 2.15 Top-left: example of *ghost particles* formation. Top-right: cancellation of *ghosts* due to the addition of one camera. Bottom: particle imaging in case of high seeding density (Scarano 2013).

The plots shown in Figure 2.16 summarize the effect of the above mentioned experimental parameters on the reconstruction accuracy. Elsinga et al. (2006) proposed a value of  $Q$  of 0.75 in order to achieve an acceptable accuracy for the velocity measurement; as a consequence, since most of Tomo-PIV experiments are performed with 3 or 4 cameras (Scarano 2013), the seeding density is limited to a value of  $N_s=0.3$  for a four camera system.

The limitation to the achievable seeding density represents a limit for the spatial resolution of the technique, a crucial aspect when dealing with transitional and turbulent where different scales are present. The limitation in spatial resolution has been the main drive for the development of a novel method to reduce the *ghost intensity* even for highly seeded flows, which is presented in Chapter 4.

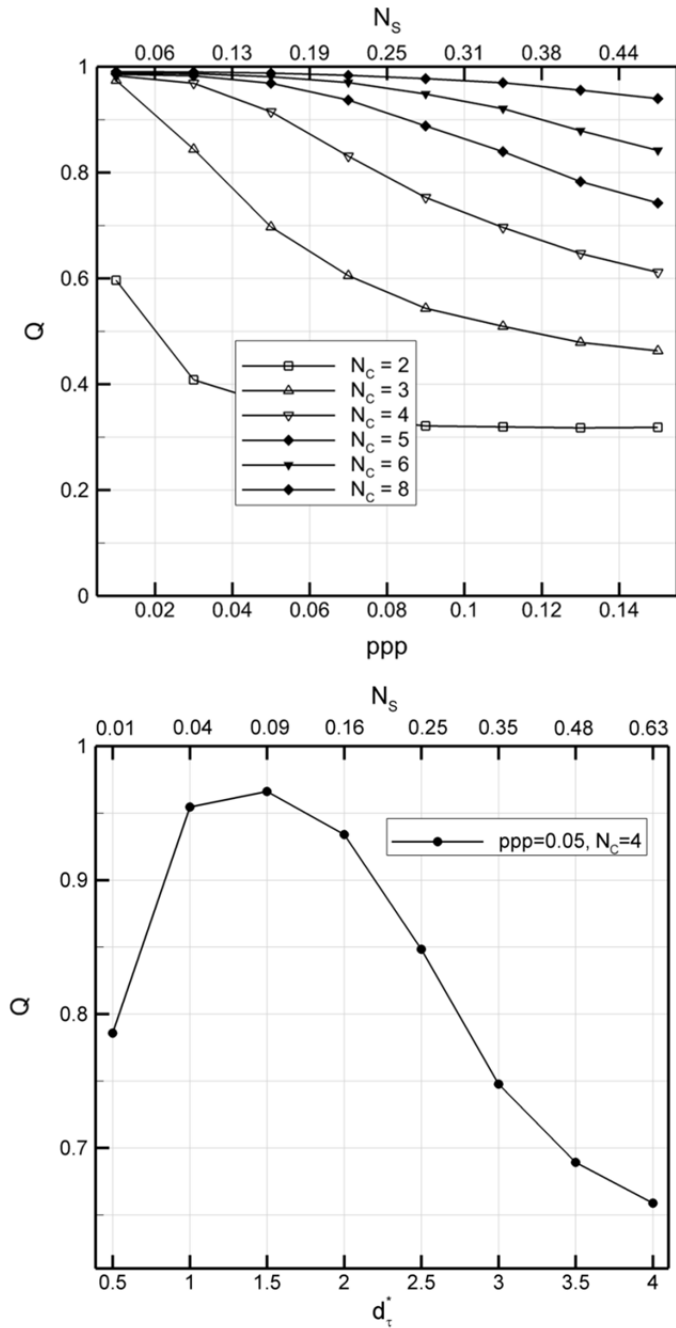


Figure 2.16 Reconstruction quality factor as a function of the seeding density, number of cameras, top, and particle imaged diameter, bottom, Scarano (2013).

### Advanced reconstruction techniques

Since the introduction of Tomo-PIV, several studies have been proposed focusing on the reconstruction step, a novel aspect with respect to the other PIV based techniques. Most of the studies aim to reduce the computational costs of the reconstruction procedure; the large amount of voxels, depending on the sensor size and illuminated volume depth, leads to intensive computation both from the point of view of memory and time required to go from the recorded images to the velocity fields. The long computational time represents a bottleneck not only in the data processing phase, but also during the experimental campaign, where a prompt feedback regarding the quality of the recorded data is necessary to apply the proper modifications to the experimental setup.

This motivated the first studies, such as the multiplicative first guess method (MFG, Worth and Nickels 2008) and the multiplicative line-of-sight technique (MLOS, Atkinson and Soria 2009) aimed to exploit the sparseness of the reconstructed domain. As indicated by eqn. 2.9, even at high levels of  $ppp$  on the camera image, the correspondent  $ppv$  is low and typically 90% of the total voxel space is empty.

The MFG and MLOS methods aims to identify the small portions of the volume where voxels are active (or potentially active) by means of the use of a simplified version of equation 2.15, where no weighting coefficient is used, which provides an important acceleration. After this step, an initial guess is obtained for further MART iterations where the update of the reconstructed intensity field is computed only for the previously identified non-zero voxels.

As shown in Figure 2.14 and discussed in Michaelis et al. (2010), the MART iterations applied to the sparse initial guess are necessary to reach a sufficient accuracy in the reconstructed field; nevertheless, MFG and MLOS can be used to obtain a fast reconstruction in case the seeding density is very low (below  $0.02 ppp$ ).

A multi-grid approach (MG) has been proposed by Discetti and Astarita (2012a) which reduces of approximately 5 times the computational time required for reconstruction (7 times if coupled with a MLOS approach) and reduces of around 40 times the memory load. The technique relies on an initial reconstruction performed at a lower spatial resolution, achieved by means of pixel binning on the images, which allows the identification of the active voxels which are then updated at the original resolution.

Alternative methods for the tomographic reconstruction have been proposed by Petra et al. (2009) and Gesemann et al. (2010), based on sparsity maximization algorithms which showed higher performances than MART in terms of reconstruction accuracy. Nevertheless, an experimental verification of these techniques is necessary in order to assess their robustness to real imaging effects and experimental errors. A different approach based on a hybrid algorithm between MART and 3D-PTV have been recently proposed by Wieneke (2011) which outperforms MART both for reconstruction accuracy and computational burden for relatively low seeding densities ( $ppp < 0.05$ ).

In conclusion, since the moment of its introduction, besides the improvement in computational efficiency, the reconstruction algorithm used to process real experimental data has not changed significantly and neither has its accuracy. To date, the MART algorithm has been used for experimental investigations performed with tomographic PIV.

This consideration led to the work presented in this thesis, in particular to the development of the Motion Tracking Enhancement technique (MTE, Novara et al. 2010), a method based on the use of multiple recording to enhance the reconstruction accuracy by means of *ghost particles* reduction, with the aim of overcoming the current limitations in seeding density, therefore spatial resolution, of the Tomo-PIV technique. The MTE-MART algorithm is described in detail in Chapter 4.

The MTE approach has then been combined with the MLOS technique by Atkinson et al. (2010) in order to increase its computational efficiency. Discetti et al. (2012) developed a low cost experimental setup for Tomo-PIV based on the use of two imaging systems made of low speed single frame cameras, where the application of the MTE technique can lead to a substantial improvement due to the incoherent behavior of the *ghost particle* system generated in the 2 subsequent recording.

Recently Schanz et al. (2012) proposed the application of a non-uniform optical transfer function (OTF) to compute the weighting coefficients used in eqn. 2.15. It has been proven to increase the accuracy of the MART reconstruction in presence of optical aberrations such as defocussing or astigmatism. A different model for the particle imaging is obtained during the self-calibration procedure which takes into account the different particle shape in different regions of the reconstructed 3D domain.

### 2.3.3 Motion analysis

Three dimensional velocity fields are obtained from the displacement of the particle tracers between two subsequent exposures, knowing the time separation and the magnification factor. The displacement is extracted by cross-correlation of the reconstructed intensity field from the two recordings as for planar PIV (Willert and Gharib 1991). The reconstructed volume is divided into sub-volumes, typically cubic, where the interrogation is performed by means of three-dimensional cross-correlation as:

$$R(m, n, l) = \frac{\sum_{i=1}^I \sum_{j=1}^J \sum_{k=1}^K E_a(i, j, k) \cdot E_b(i - m, j - n, k - l)}{\sigma_a \sigma_b} \quad 2.18$$

Where  $E_a$  and  $E_b$  are the reconstructed intensity (after mean intensity subtraction) within the interrogation volumes ( $IV$ ) at time  $t$  and  $t + \Delta t$  and  $\sigma_a$  and  $\sigma_b$  the standard deviations of the intensity distributions. The dimensions in voxels of the  $IV$  along  $X$ ,  $Y$  and  $Z$  is indicated by  $I$ ,  $J$  and  $K$  respectively, while  $m$ ,  $n$  and  $l$  represent the displacements in the 3D shifts space.

A common approach to speed up the calculation of the cross-correlation map is to perform the cross products in the Fourier space after FFT (fast Fourier transform) is applied; the correlation map  $R$  is then analyzed after inverse FFT is performed.

The location of the correlation map peak with respect to the center of the map indicates the most probable displacement of the particle tracers within the interrogation box. After the peak is located, a Gaussian peak fit is typically applied along the three spatial directions in order to achieve sub-pixel accuracy in the displacement estimate.

The choice of the interrogation volume size is determined by the seeding density; in fact a minimum number of particles contributing to the correlation map has to be included in the  $IV$ . For planar PIV it was suggested by Keane and Adrian 1992 that more than 10 particles

must be present in the correlation window for a statistically robust measurement. Since, for Tomo-PIV, the problem of out-of-plane motion is eliminated because of the three-dimensional illumination, this condition can be relaxed to a smaller number of particles in the  $IV$ , typically from 5 to 10.

The robustness of the cross-correlation analysis can be estimated by means of the signal-to-noise ratio ( $S/N$ ) which is computed as the ratio between the primary cross-correlation coefficient peak and the secondary peak value. The  $S/N$  is a number larger than 1 and gives an indication about the number of particles contributing to the formation of the correlation peak; a low signal-to-noise indicates a statistically poor measurement.

A crucial factor affecting the accuracy of the motion analysis by cross-correlation is the presence of velocity gradients within the interrogation box. In this situation, particles belonging to the same  $IV$  have a different displacement; as a consequence their contribution to the correlation map produces a broadened peak or a peak that splits in multiple local maxima.

Since this situation is commonly encountered in complex and turbulent flows, first Huang et al. (1993) Jambunathan et al. (1995) and then Scarano and Riethmuller (2000) proposed a multi-grid window deformation approach (WIDIM), an algorithm designed to compensate the presence of velocity gradients by means of deformation of the correlation region.

The method relies on the iterative application of the correlation procedure; typically a larger interrogation window is chosen at the beginning to increase robustness. The displacement field  $\vec{V}^k$  obtained at the iteration  $k$  is interpolated in order to obtain a dense pixel-wise displacement field  $\vec{V}_p^k$  which is used as a predictor to deform the intensity fields at  $t$  and  $t+\Delta t$  as:

$$\begin{aligned} E_a^{k+1}(X, Y) &= E_a^k\left(X - \frac{U_p^k}{2}, Y - \frac{V_p^k}{2}\right) \\ E_b^{k+1}(X, Y) &= E_b^k\left(X + \frac{U_p^k}{2}, Y + \frac{V_p^k}{2}\right) \end{aligned} \quad 2.19$$

where  $U$  and  $V$  indicate the displacement components along the directions  $X$  and  $Y$ . The result of the interrogation of the deformed fields produces a displacement field (corrector) which is added to the predictor. A filtering of the predictor field is necessary to ensure the stability of the interrogation algorithm (Nogueira et al. 1999; Astarita 2007; Schrijer and Scarano 2008). In the present study, a low-pass filter (2<sup>nd</sup> order least squares regression) applied on a kernel as large as the interrogation window is used to stabilize the cross-correlation analysis, following Schrijer and Scarano (2008).

The same approach can be followed when 3D reconstructed intensity fields from Tomo-PIV are dealt with; in this case the cross-correlation algorithm is referred to as VODIM (volume deformation iterative multigrid technique, Scarano and Poelma 2009). The interpolation scheme used to obtain the dense predictor field affects the accuracy of the displacement analysis; due to the computational costs involved in the three-dimensional case, typically a linear interpolation scheme is chosen even if the use of spline interpolation could reduce both bias and random errors (Astarita and Cardone 2005).

An example of the velocity field in the region close to the nozzle exit of a transitional jet is shown in Figure 2.17. A vortex-ring travelling along the jet axis is identified by means of the

vortex detection criterion  $Q$  proposed by Hunt et al. 1988. The application of multi-grid volume deformation technique largely solves the issue of discontinuous displacement obtained in the region of the highest velocity gradient (e.g. the shear layer at the nozzle exit); as a consequence also the description of the vortex ring is significantly improved, with the iso-surface of  $Q$  showing higher spatial coherence.



Figure 2.17 Three-dimensional velocity field measurement at the exit of a laminar jet. A vortex ring is formed at approximately one diameter downstream the nozzle exit. Iso-surface of vortex detection criterion  $Q$  (Hunt et al. 1988) in red. Cross-correlation performed without (top) and with (bottom) volume deformation.

After the velocity vector fields are obtained, a validation of the result is carried out to avoid the presence of spurious vectors. The universal outlier detection method proposed by Westerweel and Scarano (2005) is typically applied in order to detect erroneous vectors resulting from correlation of noise or artifacts instead of particle tracers. This method is based on setting a unique threshold value for the median test (Westerweel 1994) which is valid for a wide range of flows and Reynolds number. The detected vectors are then replaced with the result of a spatial regression performed among the neighboring values.

Computationally efficient algorithms

As for the tomographic reconstruction techniques, the computational challenges involved in the motion analysis of 3D objects led to several studies focused on the acceleration of the cross-correlation technique. As indicated by Scarano (2013), the three-dimensional domain accounts for four to five orders of magnitude more operations for each interrogation volume, when compared to planar PIV. Moreover, for the same size of camera sensors, and considering a typical depth of the reconstructed domain equal to one third of the other two dimensions, the number of non-overlapping interrogation volumes increases of one order of magnitude. Also the overload due to the overlap increases as a result of the third dimension.

Discetti and Astarita (2012a) suggested the use of voxel binning to reduce the number of voxels in the domain in the first stages of interrogation in order to speed up the cross-correlation procedure. The same authors recently proposed a number of solutions to accelerate 3D interrogation (Discetti and Astarita 2012b) based on multi-resolution and sparse approach to reduce redundant calculations of products between zero intensity values, which in fact constitute the great part of the total investigated volume. A similar approach, involving also the aspect of three-dimensional volume deformation, was followed by Atkinson and Soria (2009).

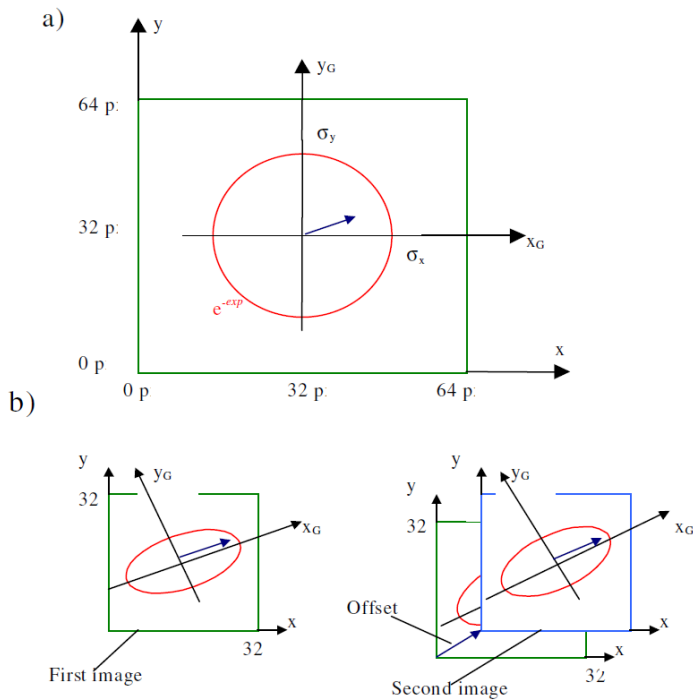


Figure 2.18 Example of adaptive weighting function applied to the cross- correlation window based on the local velocity vector (Di Florio et al. 2002). a) 64×64 pix isotropic correlation window. b) adapted cross-correlation weighting function at subsequent iteration, after grid refinement is applied (32×32 pixels).

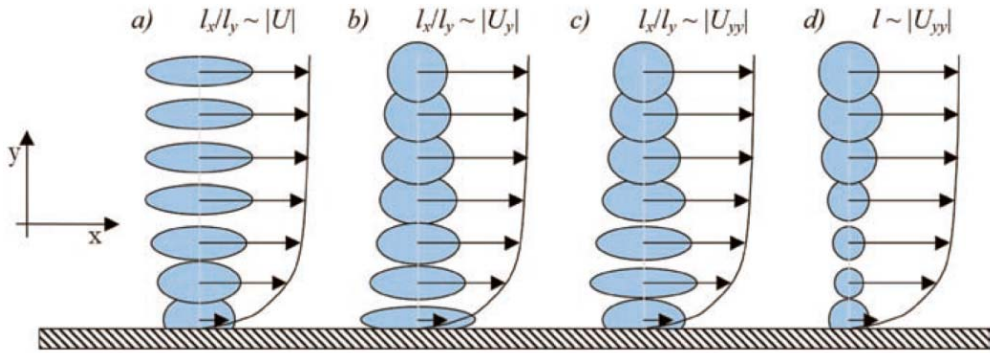


Figure 2.19 Sketch of adaptive correlation for a planar measurement of boundary layer flow. a) aspect ratio dependent on the velocity value. b) aspect ratio proportional to the velocity gradient. c) adaptivity based on the second derivative of the velocity. d) cross-correlation region diameter proportional to the curvature radius of the flow fluctuation (Scarano 2003).

### Advanced algorithms

When planar PIV is considered, a number of studies (Di Florio et al. 2002, see Figure 2.18; Theunissen et al. 2007; Astarita 2009 among others) focused on increasing the spatial resolution and reducing the velocity differences within the interrogation window by means of adaptation of the correlation regions to the local features of the flow. It is shown that a reduction of the window size along the direction of the velocity gradient leads to a visible improvement of the spatial resolution in highly sheared regions.

Although Scarano (2003) states that, since the velocity gradient is taken into account by window deformation, the interrogation regions should be adapted according to the curvature of the velocity field, the improvement shown by the above mentioned techniques can be due to a combination of two factors. On one hand, in regions of strong shear, the gradient is not completely compensated for by the deformation technique, therefore a reduction of the window size along that direction results in a more robust measurement. On the other hand, when a high value of the first derivative of the velocity also corresponds to high curvature, the adaptive approach implicitly takes care of the issue of the second derivative indicated by Scarano (2003), see Figure 2.19.

The lack of literature on 3D-PIV regarding adaptive correlation, and the even more critical need of improving the spatial resolution in 3D measurement of regions characterized by high vorticity (e.g. shear layers and vortices), motivated the development of an adaptive approach for 3D cross-correlation algorithms which is described in detail in Chapter 5.

Several methods have been proposed to increase the robustness of the correlation analysis when time resolved measurements are available. In this case the information from multiple exposures can be exploited to improve the accuracy of single recording. This procedure can be described as an attempt to transfer information from *time* (recording sequence) to *space* (single snapshot).

A first approach is the ensemble average correlation proposed by Meinhart et al. (2000), where correlation maps obtained along a sequence of recordings are averaged to obtain a

single map, where the random noise is reduced by the averaging and the peak is maintained, Figure 2.20. The latter condition is verified if the position of the peak is the same in the correlation map sequence, a situation encountered in stationary flows. As a result average velocity fields can be evaluated with increased resolution (smaller  $IV$ ) depending on the number of recordings in the sequence.

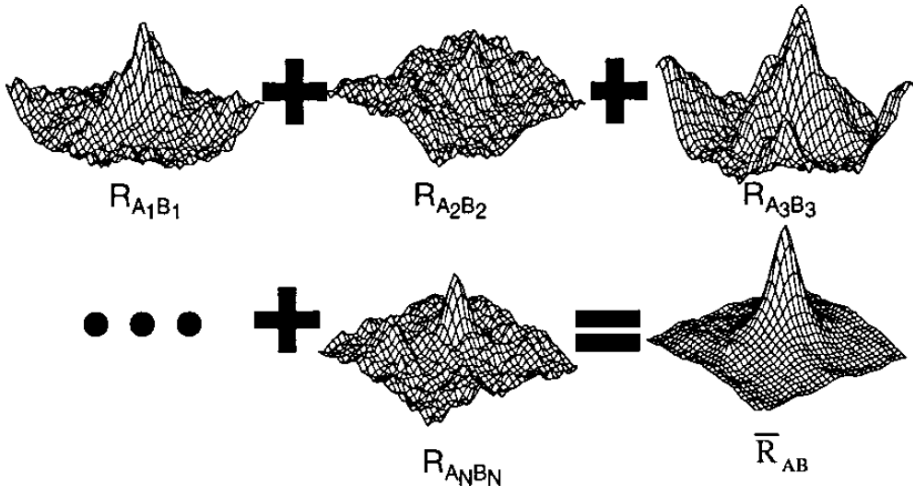


Figure 2.20 Instantaneous cross-correlation maps are averaged to obtain the average velocity vector; the average correlation function shows higher signal-to-noise ratio (Meinhart 2000).

A similar approach was followed by Scarano et al. (2010), where a sliding-average of correlation maps (SAC) is applied in the case of unsteady flows. The number of recordings defines the temporal kernel over which the correlation maps are averaged and needs to be chosen depending on the time-resolution of the acquisition. This method has been found to significantly reduce the precision errors in the velocity estimate, but the choice of the temporal kernel represent a parameter which needs to be tuned for each analysis. To overcome this limitation Sciacchitano et al. (2012) proposed the multi-frame pyramid correlation technique, which locally optimize the temporal kernel taking into account precision and acceleration errors. A reduction of random error is achieved without introducing significant modulation of the velocity signal, Figure 2.21.

A method based on the concept of particle tracking is proposed by Schröder et al. (2008), Figure 2.22. As reconstructed particles can be tracked along subsequent exposures, when time-resolved data are available, velocity and acceleration can be extracted with high accuracy from single particle trajectories. When compared to planar particle tracking, this approach benefits from the lower particle density in the 3D domain which simplifies the tracking procedure. In the present work, this method is expanded and its working principle described and assessed by means of computer generated and experimental data (Chapter 6).

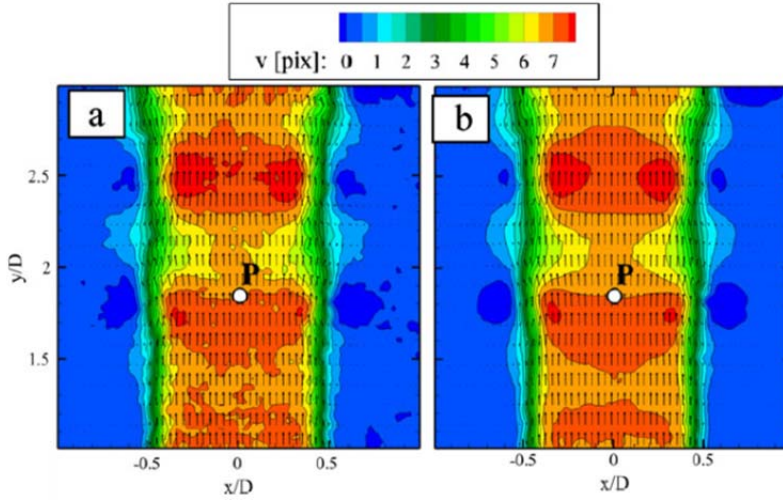


Figure 2.21 Contours of axial velocity in a transitional jet flow. Left: result from single-pair correlation. Right: result from pyramid correlation (Sciaccitano et al. 2012).

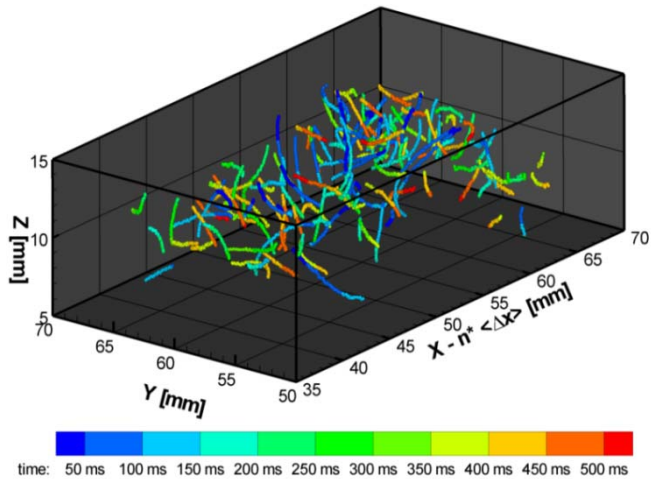


Figure 2.22 Reconstructed particles in a turbulent boundary layer tracked along 11 recordings; particles are color-coded with time. The X component of the displacement is shown after subtraction of the mean value ( $\langle \Delta X \rangle$ ) (Schröder et al. 2008a).



## Chapter 3

# Assessment methodology

The present chapter presents methods to assess the accuracy of tomographic PIV measurements in real experimental conditions. The estimate of the imaged seeding density is discussed. Subsequently, methods to infer the quality of the reconstruction and the accuracy of the velocity vector fields are presented.

### 3.1 Introduction

The choice of the system parameters for the setup of a tomographic PIV experiment is typically made relying on numerical analysis (such as proposed by Elsinga et al. 2006, Worth and Nickels 2008, Atkinson and Soria 2009, Thomas et al. 2010, Novara et al. 2010, among others) in order to optimize the experimental parameters (e.g. the number of cameras depending on the seeding density or the configuration of the imaging system).

When advanced techniques for the data processing are introduced, the analysis of computer generated data is a crucial step in order to assess the working principle of the novel method and to estimate the expected improvement in terms of accuracy of the reconstruction, displacement field, acceleration, vorticity and other quantities that can be extracted from the Tomo-PIV measurement.

Although important, this step cannot represent the ultimate test to determine the measurement performance of a novel method. In fact, when dealing with computer generated images, it is complicated to include all real imaging effects that are encountered in an experiment (e.g. optical aberrations, calibration errors, camera noise, reflections). The effect of erroneous models used to introduce errors in synthetic particle images has been studied by Westerweel (2000); it is concluded that a significant underestimation of the error can be made when overly simplified synthetic images are used to assess the accuracy of the processing technique.

On the other hand, when dealing with a real measurement, the exact result, both in terms of light intensity distribution and velocity vectors, is unknown; therefore it is not possible to evaluate the accuracy by means of the quality factor  $Q$  or the velocity error estimated as the distance between the measured and actual velocity.

One possible approach is to compare the results from Tomo-PIV with the ones obtained from other experimental techniques, depending on which quantities are of interest, such as hot wire anemometry (Atkinson et al. 2011) or planar (Novara et al. 2012) and stereoscopic PIV (Elsinga et al. 2006), having higher spatial resolution than the tomographic measurement.

In this chapter, methods to assess the performances of reconstruction and cross-correlation algorithms are proposed based on the observation and analysis of the results (reconstructed objects and vector fields) which do not make use of results from other experiments. Some of these methods are used to assess the performances of the advanced algorithms presented in Chapter 4, Chapter 5 and Chapter 6.

Moreover, the estimate of the imaged seeding density is discussed and two techniques are proposed to accurately evaluate the  $ppp$  from recorded images at high seeding density.

## 3.2 Imaged seeding density

The quality of a tomographic PIV image mainly depends on the signal-to-noise ratio and on the imaged seeding density.

The first aspect is typically evaluated by visual inspection during the setup of the tomographic system. The particle peak intensity is compared to the image background intensity; in order to clearly separate the signal from the imaged particles and the background noise and to obtain the reconstruction of single particles in the three-dimensional space, typically an order of magnitude higher particle peak signal with respect to the background noise is desirable (e.g. 10 counts for the background and 100 counts for the particles).

Regarding the second aspect, given the dependence of the number of *ghost particles* on the imaged seeding density, the estimate of the  $ppp$  achieved in the tomographic recording is of critical importance. The values of particles per pixel and source density  $N_S$  can be evaluated by means of a particle count performed on the images. The count is typically carried out through a local maxima search, where a threshold value is set for the particle peak intensity. The number of particles is then divided by the number of pixels in the sensor to obtain the value of  $ppp$ ; the source density  $N_S$  can be obtained from equation 2.13.

### 3.2.1 The TomoPIV Design Tool

The choice of the interrogation volume size, therefore the spatial resolution of the measurement, depends on the seeding concentration. In order to ease the analysis procedure, a Matlab (MathWorks, Inc.) application has been developed in the course of the present research. The TomoPIV Design Tool is a software application which allows to quickly estimate the  $ppp$  value of PIV images and to infer the minimum linear size of the interrogation regions based on the desired image density  $N_I$  (Adrian 1991). The tool is particularly useful during the design phase of a Tomo-PIV experiment, when data need to be analyzed rapidly to provide feedback to the experimentalist. This aspect is confirmed by the growing use of the TomoPIV Design Tool within the Aerodynamics group at TU Delft. The application includes four utilities dedicated to the imaged field of view (FOV), the illumination and imaging settings, the imaged seeding density and the particles concentration.

Part of the equations used in this section have been already presented in section 2.2.2 and are repeated here for convenience.

FOV	
Dpix [um]	20
Image size, x [pix]:	1024
Volume size, X [mm]:	50
M	pix/mm
0.41	20.48
GO	

Figure 3.1 The field of view utility of the TomoPIV Design Tool for the evaluation of the magnification factor  $M$ .

### Field of view

The magnification factor  $M$  is determined based on the pixel size ( $\Delta_{pix}$ ), the dimension of the sensor along the  $x$  direction in pixels and the size of the imaged field along  $X$  in millimeters, Figure 3.1. This parameters are input by the user and known from the hardware specifications and the calibration procedure respectively.

The magnification factor reads as:

$$M = \frac{x \cdot \Delta_{pix} \cdot 10^{-3}}{X} \quad 3.1$$

Where  $10^{-3}$  is used to convert  $\mu\text{m}$  to mm.

### Illumination and imaging

Based on the chosen  $f$ -number ( $f_{\#}$ ), the wavelength of the laser light ( $\lambda$ , in mm), the magnification factor  $M$ , the pixel size  $\Delta_{pix}$  and the physical diameter of the particle tracers ( $d_p$ , in  $\mu\text{m}$ ), the particle imaged diameter  $d_{\tau}^*$  is computed as (Figure 3.2):

$$d_{\tau}^* = \frac{\sqrt{d_g^2 + d_{diff}^2}}{\Delta_{pix}} \quad 3.2$$

where  $d_g$  is obtained as  $M \cdot d_p$  and  $d_{diff}$  as:

$$d_{diff} = 2.44 f_{\#} (M + 1) \lambda \quad 3.3$$

The depth of focus reads as:

$$\delta Z = 4.88 f_{\#} \left( \frac{M + 1}{M} \right)^2 \lambda \quad 3.4$$

### Imaged seeding density

With this utility the user can import a tomographic recording (tif or im7 format), split the image to choose a particular camera (in case of multi-frame image) and select a region which is then analyzed to evaluate the seeding density, Figure 3.3.

Particle peaks are identified within the selected region by means of a local maxima search based on the selected intensity peak threshold. The suitability of the chosen threshold value can be verified by visual inspection of the image, where identified peaks are highlighted by red circles.

The screenshot shows a window titled "Optics" with the following parameters and values:

Parameter	Value
lambda [mm]:	527e-6
M:	0.41
f#:	32
Dpix [um]:	20
dp [um]:	56
dt* [pix]:	3.12
dZ [mm]:	31.15

A "GO" button is located to the right of the dZ [mm] field.

Figure 3.2 The illumination and imaging utility; the imaged particle diameter  $d_{\tau}^*$  and the depth of focus ( $\delta Z$ ) are computed based on the optics parameters.

The particle per pixel is then estimated as:

$$ppp = \frac{n_p}{x^* \cdot y^*} \quad 3.5$$

where  $n_p$  indicates the number of detected particle peaks and  $x^*$  and  $y^*$  the size of the selected portion of image in pixels.

The source density  $N_s$  is computed from the  $ppp$  value and the particle imaged diameter as:

$$N_s = ppp \frac{\pi d_{\tau}^{*2}}{4} \quad 3.6$$

### Tracers concentration

The parameters regarding the illuminated region, namely the size ( $DX$ ,  $DY$  and  $DZ$ , in mm) and geometry, are input by the user. Based on the choice of the number of particles in the interrogation volume, the minimum linear size of the correlation box is computed, Figure 3.4.

Two choices are given for the illuminated volume geometry; rectangular and cylindrical, where the cylinder axis is assumed aligned with the  $Y$  direction of the reconstructed domain (being  $Z$  the depth and  $X$  the width directions).

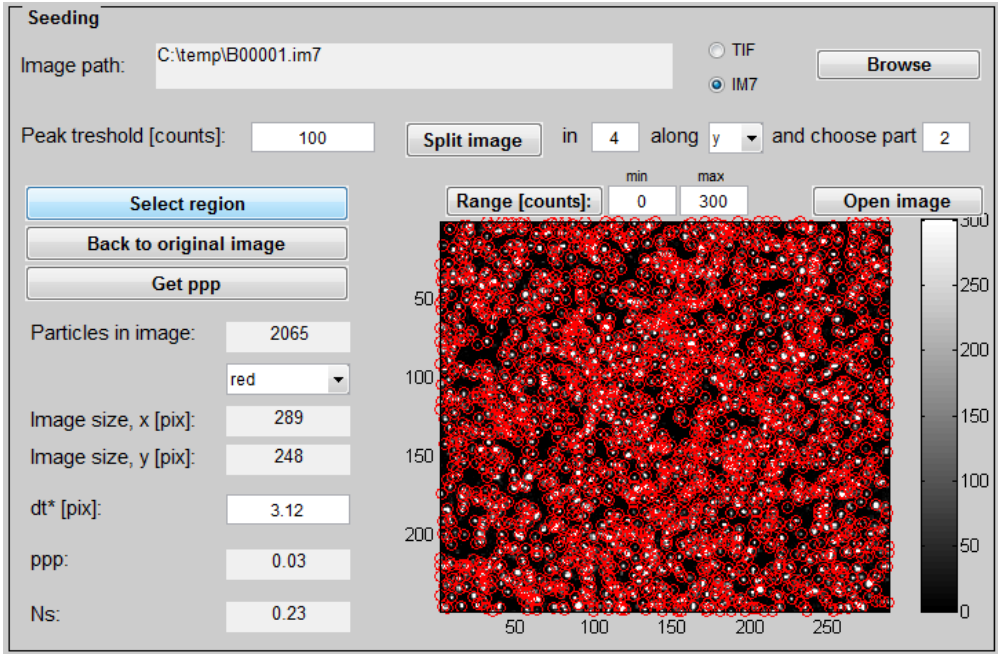


Figure 3.3 The imaged seeding density utility; the tomographic image is analyzed and the values of  $ppp$  and  $N_s$  estimated.

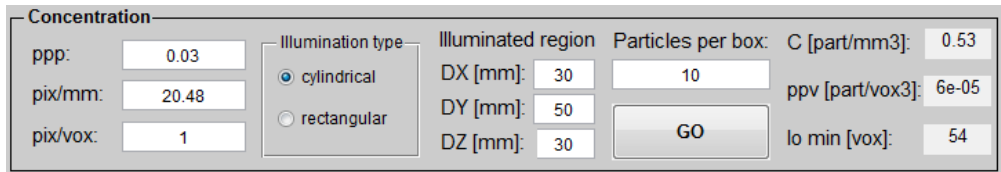


Figure 3.4 The particles concentration utility. The concentration  $C$  is defined and the minimum linear size of the interrogation box ( $l_0$ ) evaluated.

The volume of the illuminated region  $V_d$  ( $\text{mm}^3$ ) is defined, depending on the geometry as:

$$V_{d,rect} = DX \cdot DY \cdot DZ$$

$$V_{d,cyl} = \pi \left( \frac{DZ}{2} \right)^2 DY \quad 3.7$$

Where  $DZ$  and  $DX$  coincide for the cylinder case.

The total number of particles in the reconstructed volume,  $N_p$ , is obtained as:

$$N_p = ppp \cdot DX \cdot DY \cdot \left( \frac{M}{\Delta_{pix} \cdot 10^{-3}} \right)^2 \quad 3.8$$

The ratio between  $N_p$  and the illuminated volume  $V_d$  corresponds to the seeding particle concentration  $C$  (particles/mm<sup>3</sup>) as:

$$C = \frac{N_p}{V_d} \quad 3.9$$

The same ratio, after  $V_d$  conversion from millimeters to voxels, provides the particle per voxel value ( $ppv$ , particles/voxels).

Based on the chosen number of particles within the interrogation box ( $N_I$  typically larger than 5 for robust analysis, Violato et al. 2011), the minimum size of the interrogation volume is evaluated as:

$$l_{0,\min} = \sqrt[3]{\frac{N_I}{ppv}} \quad 3.10$$

The interrogation region is assumed as a cube having a volume of  $l_0^3$  voxels.

The estimate of the particles per pixel value based on counting the identified imaged particle peaks is affected by the seeding density itself. In fact, the accuracy of this method depends on the number of particles in the image and on their diameter ( $d_r^*$ ). When  $N_S$  increases, the probability of overlapping particles grows, which leads to less accurate identification of single particles, Figure 3.5-left. As a consequence, the number of imaged particles is systematically underestimated. Figure 3.5-right shows the detected  $ppp$  ( $ppp_{detected}$ ) versus the actual one ( $ppp_{actual}$ ) for computer generated images at different seeding concentrations; a 15% underestimate of the particles number is made at a seeding density of 0.06  $ppp$  (particle imaged diameter of 2 pixels).

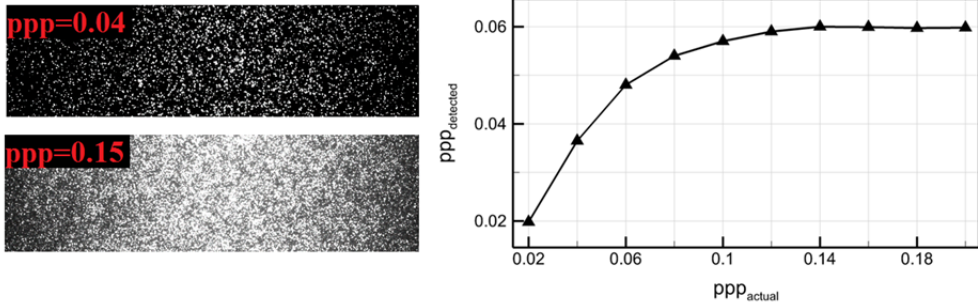


Figure 3.5 Left: detected  $ppp$  versus actual  $ppp$  ( $d_r^* = 2$ ). Results obtained from computer generated images. Right: example of Tomo-PIV recordings at a typical seeding density level (top) and in a highly seeded case (bottom).

For this reason, when the seeding density increases above approximately 0.04/0.05  $ppp$ , different solutions have to be found in order to accurately estimate the imaged seeding density. Two possible approaches are described in sections 3.2.2 and 3.2.3.

### 3.2.2 Thinning the illuminated domain

In order to obtain a more accurate estimate of the seeding density, the illuminated region depth  $\Delta Z$  can be reduced by means of a knife-edge filter to  $\Delta Z_{thin}$ . As a consequence, the imaged seeding density decreases and can be estimated by means of particles count ( $ppp_{thin}$ ). The  $ppp$  (and in turn  $N_S$ ) for full illumination is then computed multiplying the lower seeding density by the ratio of illuminated volumes as:

$$ppp = ppp_{thin} \cdot \frac{\Delta Z}{\Delta Z_{thin}} \quad 3.11$$

Figure 3.6-left shows the cylindrical illuminated volume for a transitional jet experiment and the corresponding PIV recording. When the thickness of the illuminated region is reduced from 30 mm to 5 mm, the number of particles on the image decreases significantly, Figure 3.6-right, and can be estimated by particle count, leading to a  $ppp_{thin}$  of approximately 0.077. In the present example the full volume is 6.5 times larger than that illuminated with the slit, which leads to an estimate of  $ppp=0.05$  for the full illumination case.

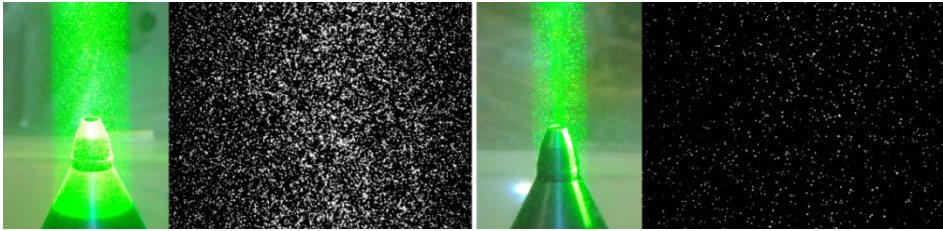


Figure 3.6 Left: detail of the illuminated region on the jet nozzle for circular illumination and recorded image on one camera ( $ppp=0.05$ ). Right: detail of the illuminated region on the jet nozzle for slit illumination and recorded image on one camera ( $ppp=0.0077$ ), Novara and Scarano 2012.

### 3.2.3 Average image intensity

A different approach for the  $ppp$  estimate in case of high seeding density is based on the average image intensity over a sequence of recordings.

In the same imaging conditions (laser power and cameras positions and settings) a sequence of images is recorded at a lower seeding density. The  $ppp$  is then evaluated by means of local maxima search ( $ppp_{low}$ ) and the average image intensity  $\bar{I}_{low}$  is computed, Figure 3.7-top. The seeding concentration can then be raised to working conditions ( $ppp$ ) and the same operation is carried out to obtain  $\bar{I}$ , Figure 3.7-bottom.

The  $ppp$  of the highly seeded images can be estimated multiplying the lower  $ppp_{low}$  value by the ratio between the average intensities as:

$$ppp = ppp_{low} \cdot \frac{\bar{I}}{\bar{I}_{low}} \quad 3.12$$

In this way, provided that the average intensity is homogeneous in the image portion where it is evaluated (i.e. a sufficient number of recordings is available to achieve convergence in the average computation), the  $ppp$  can be estimated at higher seeding concentrations without the

loss of accuracy of the particle count approach shown in Figure 3.5. The present method relies on the assumption that no multiple scattering occurs, a situation typical of water flows at high seeding density. In this condition, in fact, the background intensity level changes depending on the seeding density; since  $\bar{I}$  in eqn. 3.12 does not include the contribution given by the increased background level, the method will not provide an accurate estimate of the  $ppp$ .

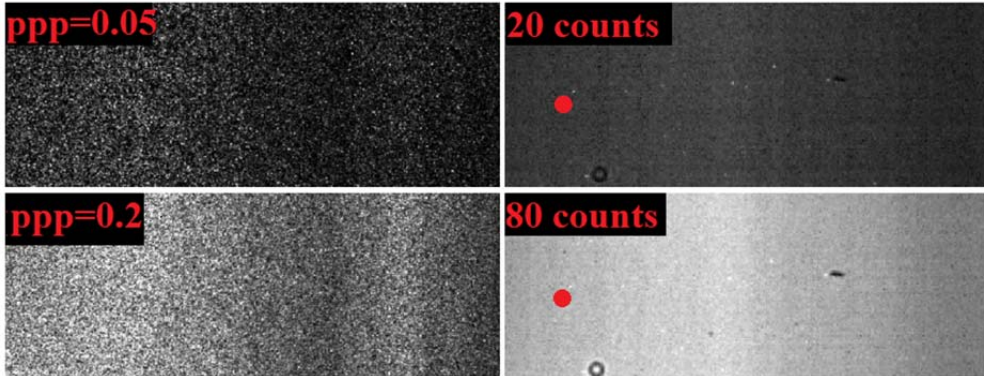


Figure 3.7 Top: image at  $ppp=0.05$  (left) and mean imaged intensity over 200 recordings (right). Bottom: image at  $ppp=0.2$  (left) and mean imaged intensity over 200 recordings (right). Average value measured at the location indicated by the red dot (Novara and Scarano 2012).

### 3.3 Tomographic reconstruction accuracy

The quality of the reconstruction can be predicted *a priori* by the analysis of the outputs of the calibration procedure. After the physical calibration (target calibration) is carried out, the residual of the curve fitting the mapping function gives an indication about the accuracy of the target analysis and of the transfer function that links the 2D image with the investigated volume. Scarano (2013) reports that a value of the residual should be lower than 0.5 pixel to achieve an accurate calibration.

A further verification of the quality of the imaging system is given by the disparity values obtained after the Volume self-calibration is performed (Wieneke 2008, see section 2.2.4). After the correction is applied, the disparity values should not exceed 0.1 pixels for an accurate reconstruction.

Regarding a posteriori methods to assess the reconstruction accuracy, four approaches are presented in the following, based on the analysis of the reconstructed intensity distribution.

#### 3.3.1 Reconstructed intensity profile

The reconstructed intensity profile along the viewing direction of the tomographic system can be used to evaluate the level of *ghost particles* generated by the MART algorithm. In fact, as discussed by Elsinga et al. (2006), the *ghost particles* are produced uniformly across the whole reconstructed volume; if a region thicker than the illuminated one is reconstructed, then, in the portion of the volume where there is no laser illumination, the only reconstructed

intensity would be the *ghost* one. It can be assumed that the same amount of spurious intensity is also present within the illuminated region.

Figure 3.8-top shows an example of a reconstructed intensity field aside and behind a cylinder. The intensity is averaged along the span of the cylinder to extract a reconstructed intensity profile along the depth direction ( $Z$ ), Figure 3.8-bottom. From the intensity profile is clearly identifiable the illuminated region, while the level of *ghost intensity* appears to be rather uniform in the outside regions. The level of intensity within the illuminated region can be considered as the sum of the actual signal and the *ghost* noise; Scarano (2013) suggests at least a ratio of 2 between the reconstructed intensity and the *ghost* one for reliable measurement.

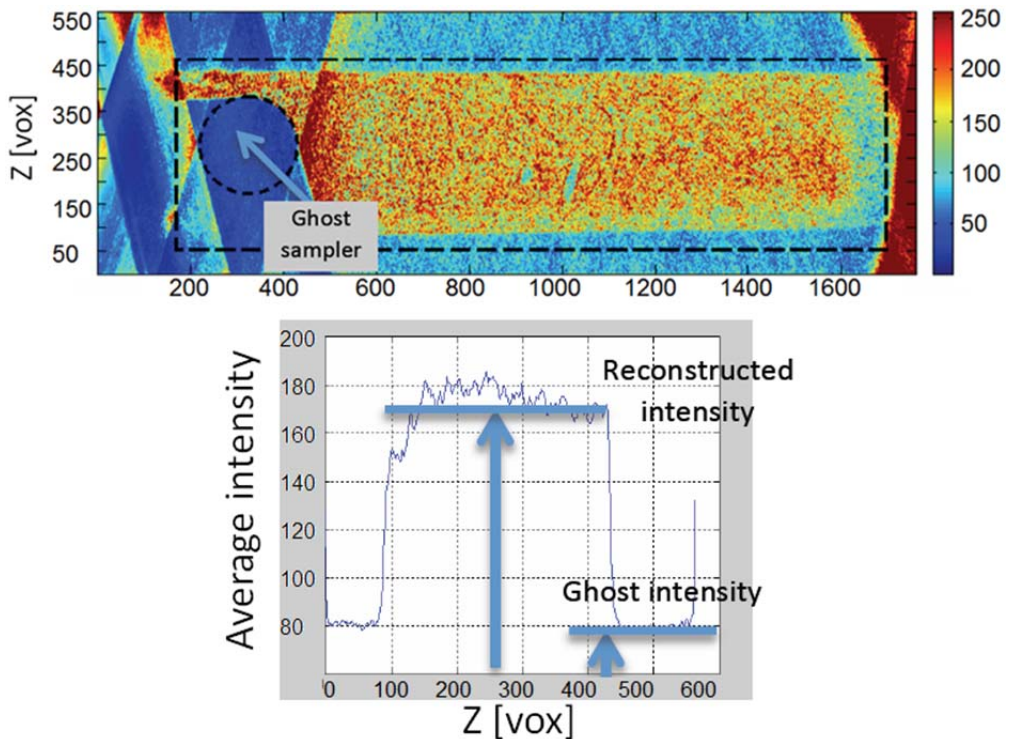


Figure 3.8 Top: reconstructed intensity distribution averaged along the span of a cylinder (Scarano and Poelma 2009). The section of the cylinder is indicated with the dash black line. Bottom: intensity profile along the viewing direction ( $Z$ ) extracted at location  $X=800$  vox, (Scarano 2013).

In order to use this criterion to assess the *ghost intensity* reconstruction, the illuminated region needs to be clearly separated by the outer region (e.g. using knife-edge filters to limit the illumination of the outer zone). Moreover multiple scattering and light reflection could contribute to undesired illumination of the outer region which would have a detrimental effect on the clarity of the reconstructed intensity profile.

In these conditions, the *ghost sampler* method has been proposed by Scarano (2013) where an opaque object is placed in a known position at the furthest edge of the reconstructed

domain. After the reconstruction is performed, the light intensity reconstructed within the object (i.e. *ghost sampler*) can be ascribed to *ghost intensity* and, based on the intensity outside the sampler, a signal-to-noise ratio can be estimated.

### 3.3.2 Relative quality factor

When the exact light distribution is unknown a reference intensity field ( $E_{ref}$ ) can be introduced and a relative quality factor ( $Q^*$ ) can be computed between the reconstructed field ( $E_{rec}$ ) and the reference one as:

$$Q^* = \frac{\sum E_{ref} \cdot E_{rec}}{\sqrt{\sum E_{ref}^2 \cdot \sum E_{rec}^2}} \quad 3.13$$

In the situation where a tomographic system composed by at least 4 cameras, the reference result can be produced making use of the full tomographic system while a subset of cameras (e.g. 3) is used to produce the reconstructed field  $E_{rec}$ . The relative quality factor ( $Q^*$ ) computed between the two fields indicates the loss of accuracy due to the reduced number of views.

This method can also be used when a novel reconstruction technique needs to be assessed. The relative quality factors achieved by the state-of-the-art (e.g. MART) and by the novel technique can be compared to assess the performance of the latter with respect to the well assessed method. This approach is followed in section 4.9 of this thesis to assess the performances of the Motion Tracking Enhancement technique (Novara and Scarano 2012).

### 3.3.3 Reconstructed intensity variance

A parameter which can be used to estimate the quality of the reconstruction without making use of a reference result is the intensity variance, which gives an indication about the “contrast” of the reconstructed intensity. Higher values of the intensity variance indicate the presence of stronger reconstructed particles emerging from a low level of background noise. Indicating with  $E_{rec}$  the reconstructed field, the normalized intensity variance  $\sigma_E^*$  reads as:

$$\sigma_E^* = \frac{\sqrt{(E_{rec} - \overline{E_{rec}})^2}}{\overline{E_{rec}}} \quad 3.14$$

The analysis of computer generated data shows that the behavior of the  $\sigma_E^*$  consistent with the one of the  $Q$  factor. Figure 3.9 shows that higher values of  $Q$  and  $\sigma_E^*$  are achieved when increasing the number of cameras in the tomographic system (or decreasing the seeding density).

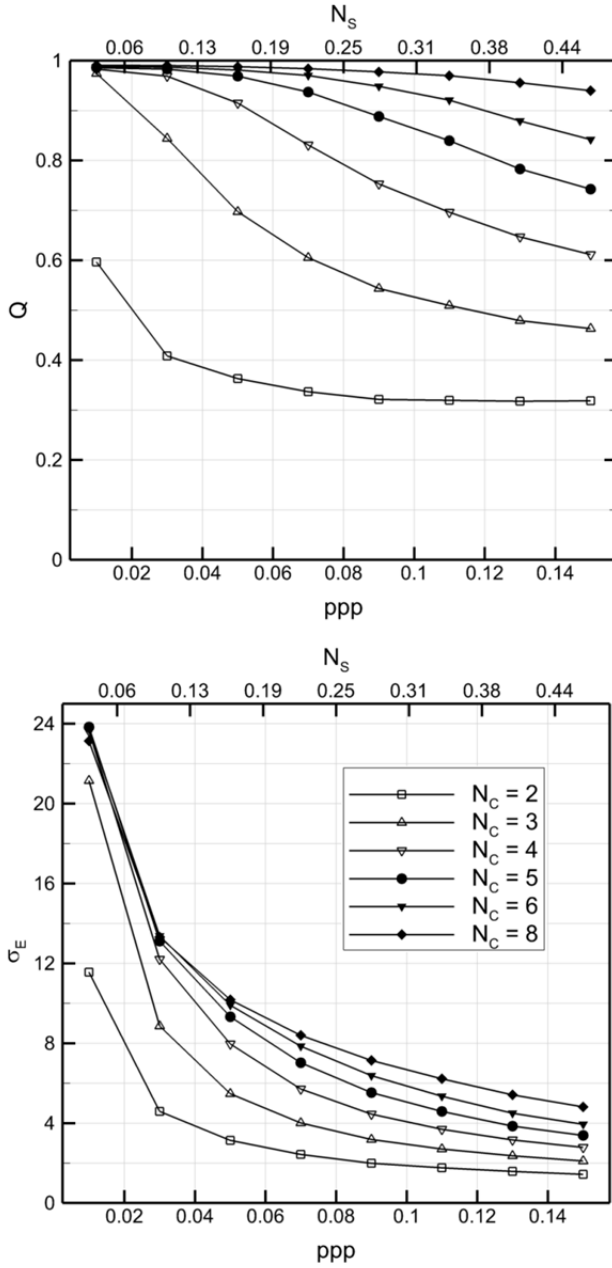


Figure 3.9 Reconstruction quality factor (top) and normalized intensity variance (bottom) as a function of the seeding density ( $ppp$  and  $N_s$ ) and the number of cameras  $N_C$ .

### 3.3.4 Consistency of particle trajectories

In case of time-resolved measurement, the concept of 3D particle-tracking can be used to estimate the number of *ghost particles* within the reconstructed volume.

Schroder et al. (2008) and more recently Novara and Scarano (2012) performed particle-tracking on a sequence of reconstructed objects from Tomo-PIV. As discussed in Chapter 6, if compared to standard 3D-PTV (Maas et al. 1993), the tracking algorithm in the 3D space is simplified since the distance between neighboring particles is larger than the one in the camera images. The lower probability of overlapping particles reduces the ambiguities in the particle identification along the sequence. Furthermore, displacement fields obtained by cross-correlation can be used as predictor to estimate the position of the particle in the subsequent recording. Therefore, particle trajectories can be accurately reconstructed over relatively long sequences (20/30 snapshots).

As indicated by Elsinga et al. (2006), *ghost particles* statistically have lower peak intensity compared to actual ones and they are typically not consistent with the flow pattern. Although *ghost particles* can produce *ghost pairs*, *ghosts* which are coherent with the displacement field when 2 recordings are considered (Elsinga et al. 2011), they usually exhibit an intermittent behavior when a longer observation time is considered.

This characteristic can be exploited to estimate their number. When particle-tracking is performed over a sequence of 10 or more recordings, indicating with  $N_{p0}$  the number of particle detected in the first object of the sequence and with  $N_{traj}$ , the number of complete trajectories, the number of *ghost particles* is estimated as:

$$N_g = N_{p0} - N_{traj} \quad 3.15$$

A threshold value for the particle peak intensity needs to be chosen, which depends on the illumination, camera sensitivity and image quality and it is chosen by visual inspection of the PIV recordings and camera images.

An example of particle-tracking over reconstructed objects from a tomographic experiment of a transitional jet (Violato and Scarano 2011) is shown in Figure 3.10-top. Short trajectories, 1 or 2 exposures long, suggest the presence of *ghost particles* exhibiting and intermittent behavior. The consistency of particles trajectory can also be used to compare performances between different reconstruction procedures. For example, increasing the number of camera results in the reconstruction of more regular trajectories, Figure 3.10-bottom-left and Figure 3.10-bottom-right.

The nature of the flow pattern has an influence on the accuracy of this method; in the extreme condition of uniform flow, the *ghost particles* are coherent with the actual tracers and will produce consistent trajectories, which results in  $N_g=0$ . Nevertheless, this situation is not likely to be encountered in Tomo-PIV experiment where the attention is focused mainly on 3D complex and turbulent flows.

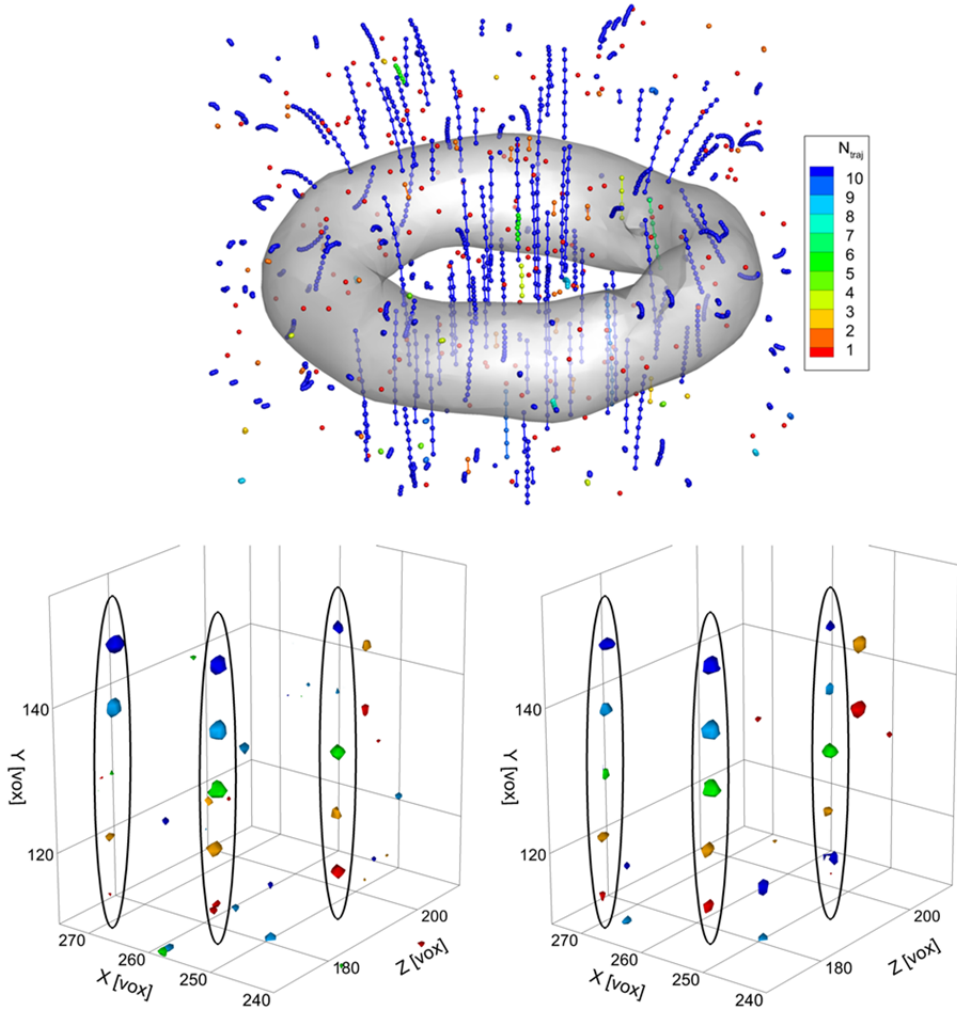


Figure 3.10 Top: samples of trajectories tracked along 10 recordings from a transitional jet experiment. Iso-surface of vortex identification criterion  $Q$  in gray. Trajectories are color-coded based on their length ( $N_{traj}$ ). Bottom-left: particle intensity reconstructed making use of 3 cameras (particles are color coded from red to blue based on the time instant of the recordings). Bottom-right: particle intensity reconstructed with 4 cameras (Novara and Scarano 2012).

### 3.4 Accuracy of the velocity measurement

The accuracy of velocity fields obtained by Tomo-PIV is typically assessed by comparison with results from different measurement techniques. Alternatively, a reference result can be introduced similarly to what proposed in section 3.3.2 for the reconstruction quality factor.

On the other hand a qualitative and quantitative *a posteriori* assessment can be performed based on several parameters which are discussed in the following. These methods aim in particularly to provide tools to assess the performances of innovative motion analysis techniques such as the ones presented later in this thesis.

### 3.4.1 Spatial and temporal coherence

The spatial coherence of the velocity fields can be used to provide a qualitative indication about the level of noise or the amount of modulation introduced by a certain motion analysis technique.

Michaelis et al. (2010) used contours of axial velocity component on a plane across a jet flow in order to assess the performances of different reconstruction techniques, Figure 3.11. This visualization clearly shows that the MLOS (Atkinson et al. 2010) and MinLOS (Maas et al. 2009) techniques (when no further MART iterations, as originally proposed by the respective authors, are applied) fail to capture the jet feature at high seeding density, while MART and MTE-MART (Novara et al. 2011) still provide the description of both the jet core and the shear layer region.

The availability of three-dimensional data allows the visualization of 3D iso-surfaces. In particular, the visualization of quantities such as vorticity or vortex identification criteria provides a clearer picture because of the sensitivity of these quantities to precision and truncation error.

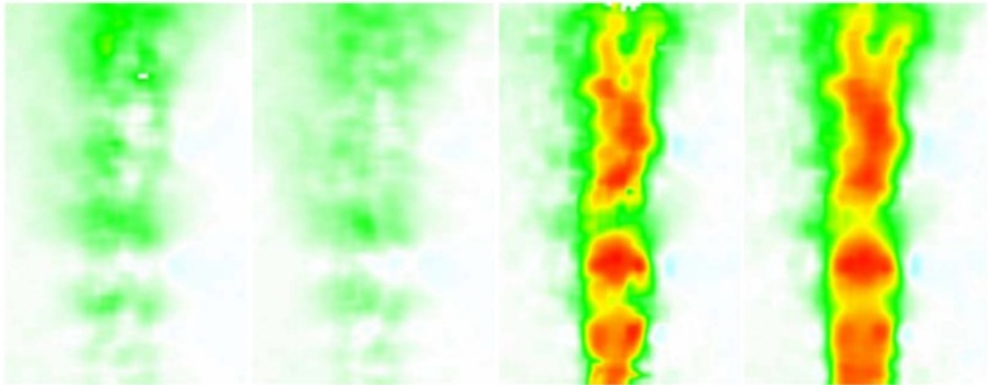


Figure 3.11 Contours of axial velocity in a plane across a transitional water jet (white color indicates zero velocity, red corresponds to approximately 0.4 m/s). Results from different tomographic reconstruction techniques are shown for a highly seeded experiment. From left to right: MLOS, MinLOS, MART and MTE-MART (Michaelis et al. 2011).

Figure 3.12-left shows iso-surfaces of vorticity magnitude in a transitional jet flow for isotropic and adaptive correlation (see Chapter 5); the modulation introduced by isotropic correlation is clear in the regions of the shear layer and the vortex-ring core, Figure 3.12-top-left.

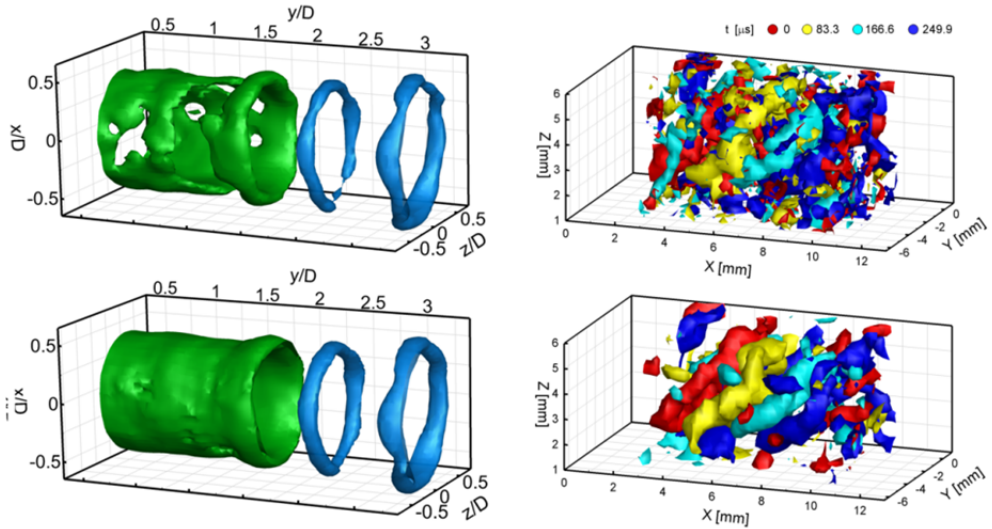


Figure 3.12 Left: iso-surfaces of vorticity magnitude in a transitional jet flow field ( $0.18$  and  $0.31 \text{ ms}^{-1}$  green and blue respectively) for isotropic (top) and adaptive (bottom) correlation (Novara et al. 2012). Right: visualization of an hairpin vortex travelling in a turbulent boundary layer by means of vortex identification criterion  $Q$ . Iso-surfaces color-coded based on the time instant. Result from MART (top) and MTE-MART (bottom) reconstruction (Novara and Scarano 2012).

The visualization of  $Q$  vortex identification criterion in a turbulent boundary layer for MART and MTE-MART reconstruction (see Chapter 4) shown in Figure 3.12 illustrates how the application of the motion tracking enhancement technique contributes to reduce the random noise level, providing smoother iso-surfaces and an easier identification of the vortical structure, Figure 3.12-bottom-right.

With the introduction of time-resolved Tomo-PIV also the temporal coherence of the above mentioned quantities provides valuable information on their accuracy. Figure 3.13 shows examples from PIV experiments performed in a wake of an airfoil and of a transitional jet where advanced algorithms for motion analysis are compared with single-pair cross-correlation. The inspection of the time-history of the signal shows that a reduction of random fluctuation without introducing modulation is achieved by the advanced interrogation methods.

### 3.4.2 Cross-correlation signal-to-noise

The cross-correlation signal-to-noise-ratio  $S/N$  gives an indication about the robustness of the measurement. It is computed as the ratio between the primary and secondary peak values in the cross-correlation map, Figure 3.14-top. As a consequence a higher  $S/N$  value means that the cross-correlation peak is stronger than the noise level and can be easily detected. Therefore, the  $S/N$  ratio depends on the number of particle within the correlation since a larger number of correlating particles leads to a stronger correlation peak, and on the cross-correlation algorithm (i.e. the application of window deformation increases robustness in gradient regions).

A value of  $S/N$  is obtained for each interrogation volume providing a local information on the robustness of the measurement. The probability density function of the  $S/N$  distribution is used by Sciacchitano et al. (2012) to compare the performances of different motion analysis algorithms, Figure 3.14-bottom.

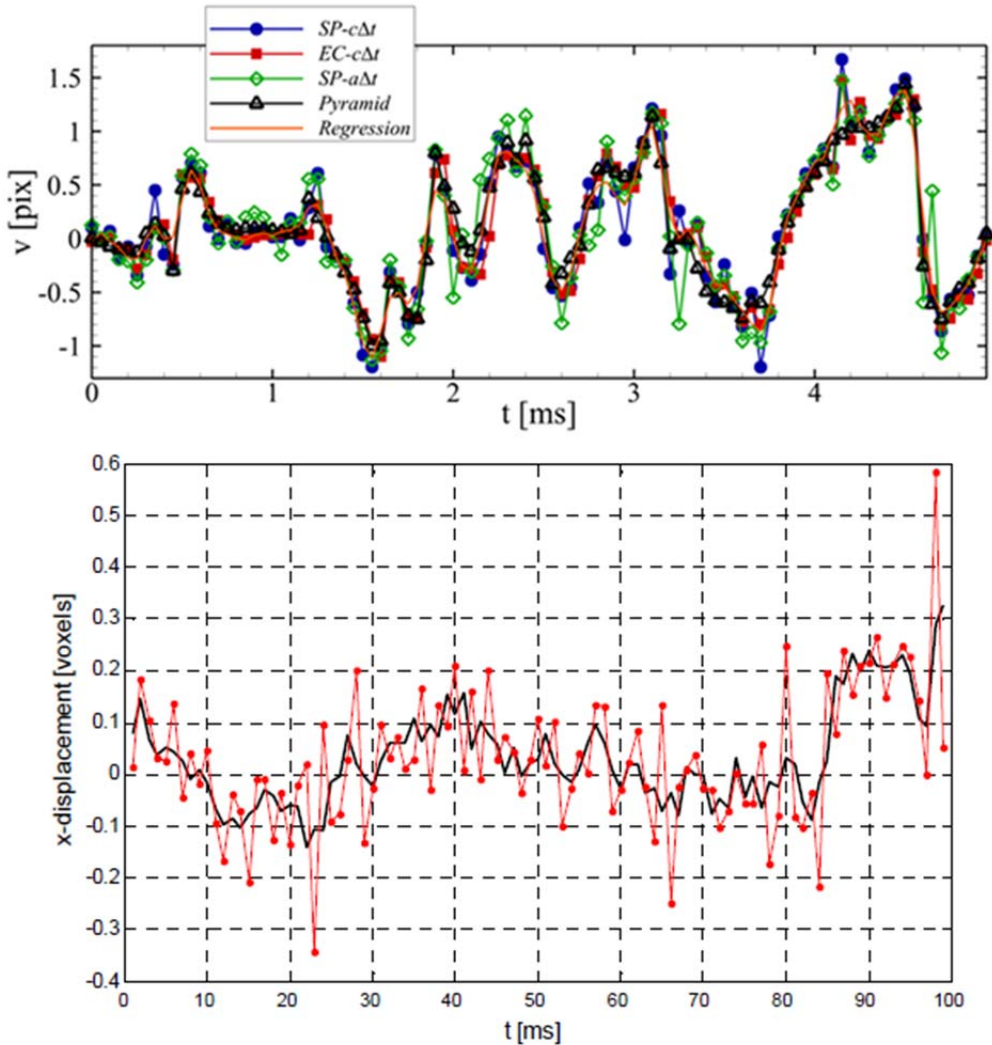


Figure 3.13 Examples of time-histories of velocity components for time-resolved PIV when different processing methods are used. Top: vertical velocity component in a wake behind an airfoil from planar PIV (Sciacchitano et al. 2012). Bottom: time-history of radial velocity component in transitional jet (Scarano 2013).

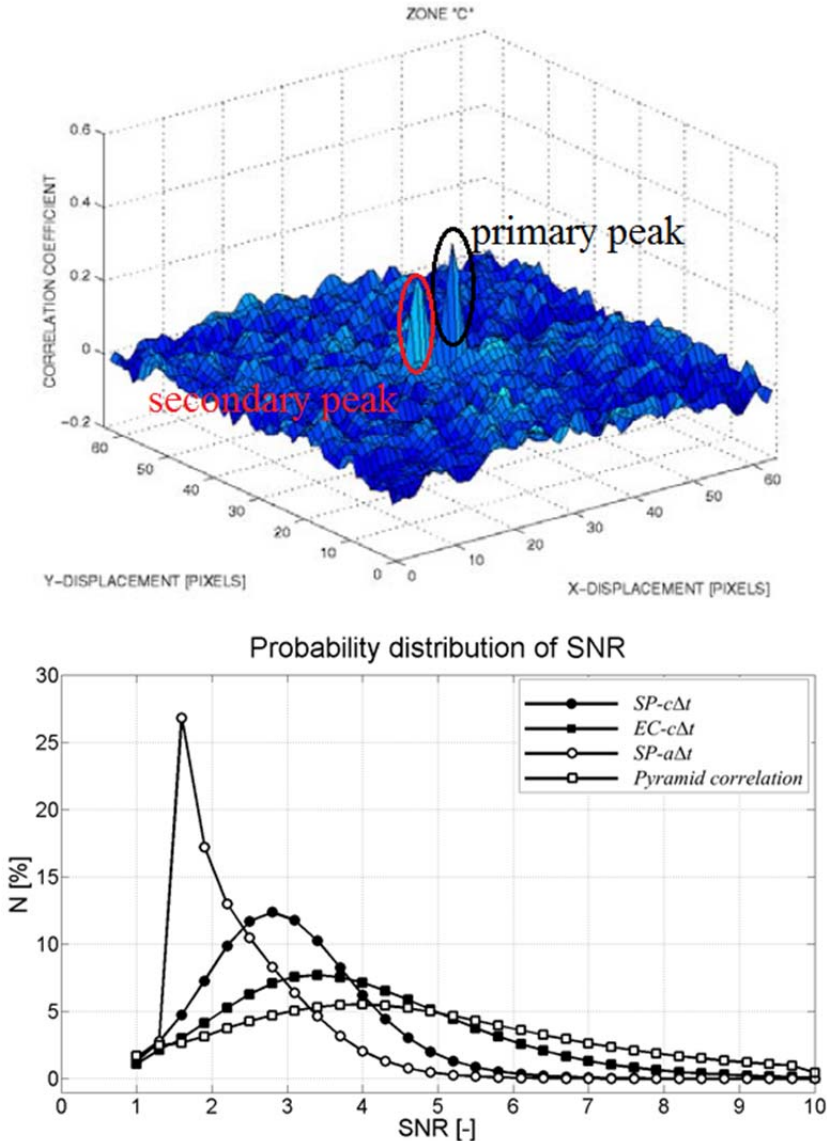


Figure 3.14 Top: example of cross-correlation map for planar PIV (Scarano 2001). Bottom: probability density function of cross-correlation signal-to-noise for single pair, ensemble average and pyramid correlation (Sciacchitano et al. 2012).

### 3.4.3 Compliance with physical laws

The compliance of the measured velocity field with physical properties of the investigated flow field can be used to assess its accuracy. The choice of the control quantities is necessarily flow-dependent. In this section a few possibilities are presented for incompressible flows, a common application for the tomographic PIV technique.

### Continuity and vorticity transport equation

The availability of instantaneous three-dimensional velocity fields as provided by Tomo-PIV, allows the evaluation of the divergence of the velocity  $\nabla \cdot \mathbf{V}$ . Therefore, the compliance with the continuity equation for incompressible flows

$$\nabla \cdot \mathbf{V} = 0 \quad 3.16$$

can be used to infer the accuracy of the measurement as lower levels of divergence characterize a more accurate result for the velocity vector field (Zhang et al. 1997, Scarano and Poelma 2009, Violato and Scarano 2011).

Figure 3.15 shows divergence iso-surfaces in a jet flow field where the tomographic reconstruction is performed with a different number of cameras. Increasing the number of views is proven to improve the accuracy of the measurement from Tomo-PIV; similarly the divergence magnitude decreases.

In case of time-resolved measurements of incompressible flows, the compliance with the vorticity transport equation, equation 3.17, can be an alternative to the divergence approach:

$$\frac{d\boldsymbol{\omega}}{dt} = \boldsymbol{\omega} \cdot \nabla \mathbf{V} + \nu \nabla^2 \boldsymbol{\omega} \quad 3.17$$

where  $\nu$  is the kinematic viscosity and  $\boldsymbol{\omega}$  indicates the vorticity vector.

### Spatio-temporal correlation

The spatio-temporal correlation between subsequent velocity vector fields can be used when time-resolved Tomo-PIV measurements are performed in an advected flow (Romano et al. 1999). After mean subtraction, the correlation map  $\Phi$  is computed for the streamwise component of the velocity field ( $U$  in this example) as:

$$\Phi_U(dx, dy, dz, \tau) = \frac{\sum_{i,j,k=1}^K U(i, j, k, t) \cdot U(i + dx, j + dy, k + dz, t + \tau)}{\sqrt{\sum_{i,j,k=1}^K (U(i, j, k, t))^2 \cdot \sum_{i,j,k=1}^K (U(i, j, k, t + \tau))^2}} \quad 3.18$$

where  $\tau$  indicates the time separation and  $K$  the size of the chosen portion of the velocity field used for space-time correlation. A correlation map is computed for each of the kernels in which the domain is partitioned and the correlation peak is identified ( $\Phi_{max}$ ).

When velocity fluctuation are mostly convected and when the acquisition frequency of the tomographic system is sufficiently high (e.g. one order of magnitude higher than the characteristic frequency of the flow fluctuations), the value of  $\Phi_{max}$  is supposed to be close to 1 as the velocity vectors are translated between the two exposures without significant variations.

The ones' complement of the peak value,  $\varepsilon = 1 - \Phi_{max}$ , can be regarded as an indication of the amount of uncorrelated component of the signal, which is ascribed to the measurement precision error. Figure 3.16 shows a graphical representation of the method when the value of  $\Phi_{max}$  is computed varying the time-separation  $\tau$ ; if the advection hypothesis is valid, within the characteristic time  $\Delta T$  of the velocity fluctuation, the value of  $\varepsilon$  is steady as the measurement random error is constant in each recording. This method is used in this thesis to

assess the performances of the MTE enhancement reconstruction technique (Novara and Scarano 2012).

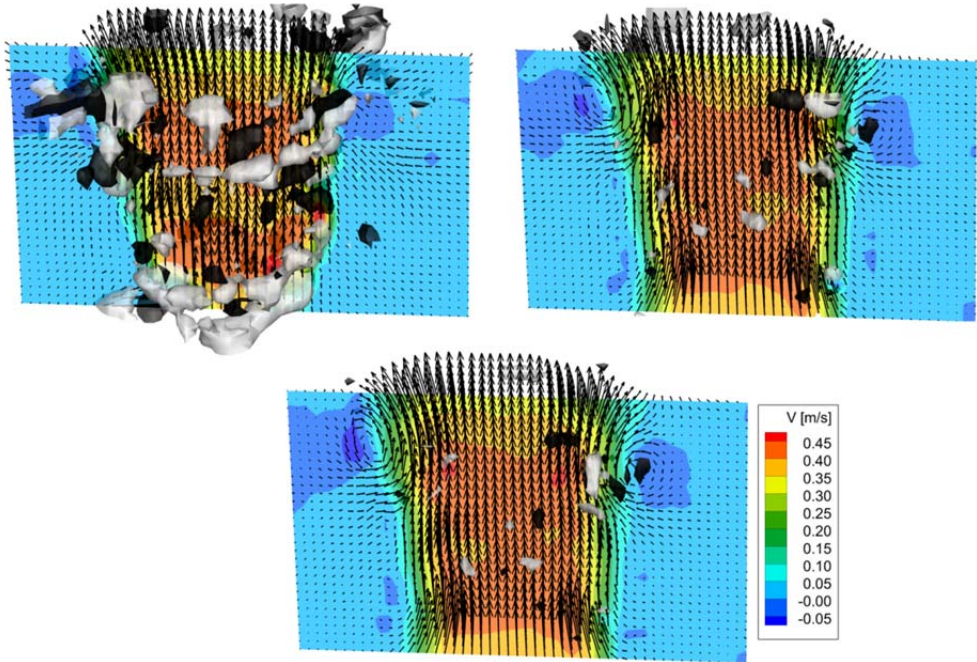


Figure 3.15 Iso-surfaces of divergence in a transitional jet flow field (0.1 1/s white and -0.1 1/s black). Contours of axial velocity in a plane across the jet core. Top-left: tomographic recordings reconstructed with 2 cameras. Top-right: reconstruction with 3 cameras. Bottom: reconstruction with 4 cameras.

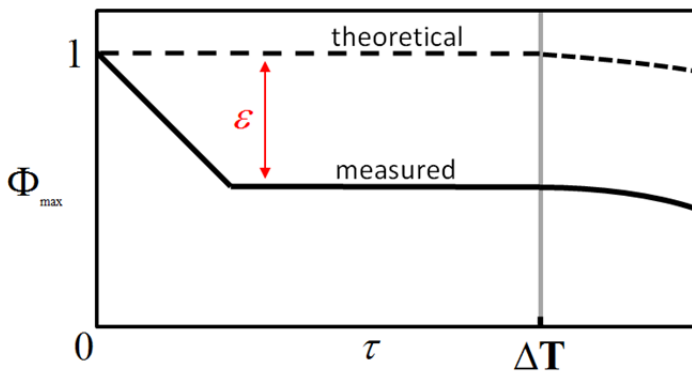


Figure 3.16 Space-time correlation peak value versus separation time for advected flows;  $\Delta T$  represents the characteristic time of the velocity fluctuations and  $\tau$  the time separation between recordings.  $\epsilon$  provides an indication of the measurement precision error.



## Chapter 4

# Motion tracking enhancement

Novara M, Batenburg KJ and Scarano F (2010) Motion tracking-enhanced MART for tomographic PIV, *Meas. Sci. Technol.*, 21:035401.

Novara M and Scarano F (2012) Performances of motion tracking enhanced Tomo-PIV on turbulent shear flows, *Exp. Fluids*, 52:1027-1041.

The present chapter presents a novel technique to increase the accuracy of the reconstruction of Tomo-PIV recordings. The basic idea behind the method is presented and the problem of *ghost particles* is depicted. Subsequently, a theoretical model for the Motion Tracking Enhancement technique (MTE) is presented and its working principle is described. The implementation of the MTE algorithm is then discussed and its performances are assessed by means of computer generated and experimental data.

### 4.1 Background

The reliability and accuracy of Tomographic PIV strongly depends upon the density of imaged particles on the source (source density  $N_S$ ). Experiments performed in the past years showed that a seeding density such that approximately 30% of the sensor is occupied by particle images ( $N_S \sim 0.3$ ) can be accurately reconstructed and their motion faithfully tracked by spatial cross-correlation. It is also well known that an excessive particle image density ( $N_S \sim 1$ ) compromises the reconstruction and returns a low quality factor  $Q$ , which results in largely inaccurate velocity vector fields. As a consequence, the current best practice suggests that the image seeding density should typically not exceed 50,000 particles/Mpixel ( $ppp < 0.05$ ).

As already mentioned in Chapter 2, the main source of error in the tomographic reconstruction process is represented by the formation of *ghost particles*. Spurious intensity is reconstructed at the intersection of lines-of-sight crossing actual particles. Such *ghost particles* also degrade the intensity field of the actual particles since the projection of the overall intensity must match the intensity on the images. A consequence of the *ghost particles* is that they may affect the cross-correlation signal, introducing random and bias errors in the velocity field, as demonstrated in the recent study from Elsinga et al. (2011). The number of *ghost particles* in a reconstructed intensity field depends upon several

experimental parameters, mostly the number of simultaneous views and the seeding particles concentration (Elsinga et al. 2011). Therefore, the phenomenon of *ghost particles* formation currently represents one of the largest obstacles to increasing the spatial resolution of Tomo-PIV measurements and as such it has received considerable attention.

Increasing the number of simultaneous views of the tomographic system may be regarded as a possible solution, provided that the system complexity and costs remain affordable.

The main difference between regular tomography and Tomo-PIV is that the latter is always based upon two or more subsequent recordings of the object (particles field). Although the particles position changes in between the exposures, one may reasonably assume that the same set of particles is illuminated at the two time instants. This leads to the concept of *fluid tomography*; subsequent recordings of the same *fluid object* (the particle field subjected to the flow motion) can be regarded as projections of the same solid object recorded from an imaging system which has moved, Figure 4.1. In this analogy subsequent recordings can be exploited as additional independent views of the object, virtually increasing the number of cameras.

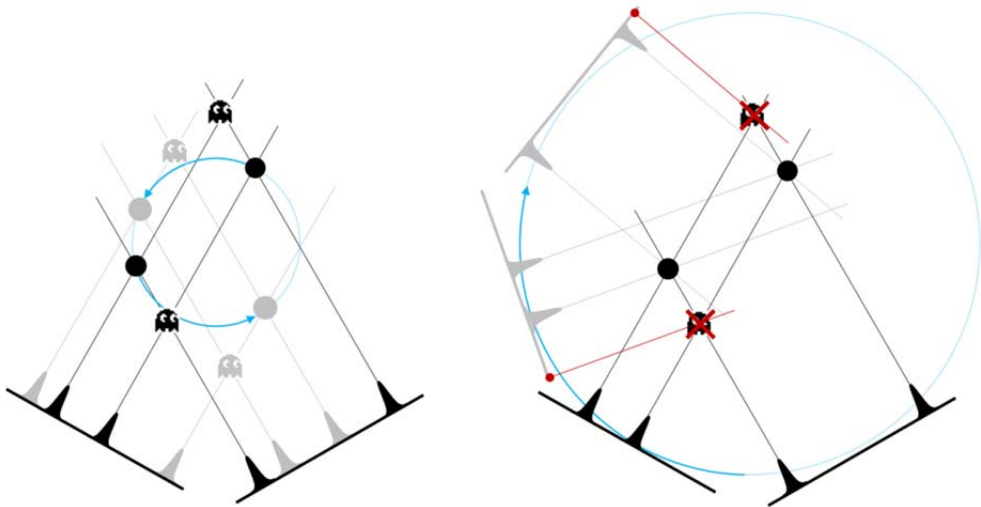


Figure 4.1 Working principle of *fluid tomography*. Left: two subsequent exposures (black and gray respectively) from a two-cameras tomographic system are reconstructed and produce two sets of *ghost particles* (actual particles indicated by circles). Particles are subjected to solid-body rotation (blue arrows). Right: images from the second recording are rotated following the flow pattern (in the opposite direction) to virtually create two additional views (in gray); the reconstruction of the first exposure is then carried out making use of 4 views leading to the cancellation of the *ghost particles* (red lines indicate lines-of-sight corresponding to zero-intensity pixels).

This concept is exploited by the Motion Tracking Enhancement technique, where reconstructed intensity fields from two or more subsequent recordings are combined to enhance the reconstruction accuracy of single snapshots.

The method relies on the dependence of the iterative MART reconstruction algorithm from the initial guess and on the formation mechanism of the *ghost particles* which is discussed in the following section.

## 4.2 The ghost particles

The *ghost particles* arise from the non-uniqueness of the solution to the under-determined algebraic problem defined by the projection equation used by the MART algorithm (equation 2.15). The number of *ghost particles* produced by MART can be comparable and often larger than the number of actual particles and it depends mainly on three experimental parameters, namely the number of simultaneous views, the seeding density and the thickness of the illuminated volume (Maas et al. 1993).

Following Discetti and Astarita (personal communication), the number of *ghost particles* can be modeled as a function of the above mentioned parameters. Considering an illuminated volume of size  $\Delta X$ ,  $\Delta Y$  and  $\Delta Z$  (in voxels) and a particle image on the first camera, a ghost particle can be located anywhere along the portion of line-of-sight crossing the reconstructed volume, which length is approximated with  $\Delta Z$  (the effect of the viewing angle is not taken into account). The projection of the line-of-sight onto the sensor of the second camera defines a region where possible candidates for matching the single particle in camera one can be located. In case of a pixel-to-voxel ratio of 1, this area can be estimated as the length of the line-of-sight  $\Delta Z$  multiplied by the particle imaged diameter  $d_\tau^*$ . The number of candidates for matching each particles of the first image is obtained multiplying this area by the particle image density  $ppp$ . Based on the number of actual particles  $N_p$ , the number of *ghost particles* relative to the 2 cameras system reads as:

$$N_g^{N_c=2} = N_p \cdot ppp \cdot d_\tau^* \cdot \Delta Z \quad 4.1$$

where  $N_c$  represents the number of cameras. Equation 4.1 indicates the number of potential *ghosts*. The projection of the location of a potential *ghost particle* onto the sensor of the third camera defines a circular region which area is approximately that of a particle image  $A_p = \frac{\pi d_\tau^{*2}}{4}$ . The number of *ghost particles* is obtained multiplying this area by the imaged seeding density  $ppp$  and by the number of ghost candidates  $N_g^{N_c=2}$ . Considering  $N_c$  cameras in the tomographic system, the number of ghosts  $N_g$  can be generalized as:

$$N_g = N_g^{N_c=2} \cdot (ppp \cdot A_p)^{N_c-2} \quad 4.2$$

The ratio of actual to *ghost* particles, which represents a possible indicator of signal-to-noise ratio, can be modeled as follows:

$$\frac{N_p}{N_g} = \frac{1}{ppp^{N_c-1} \cdot A_p^{N_c-2} \cdot d_\tau^* \cdot \Delta Z} \quad 4.3$$

It is also useful to introduce the source density  $N_s$ , which takes into account both the number of particle images per unit sensor area and the diameter of individual particle images. Since

$N_s = ppp \cdot \frac{\pi d_\tau^{*2}}{4}$ , the ratio between the number of actual particles and that of the produced *ghosts* reads as follows:

$$\frac{N_p}{N_g} = \frac{\pi \cdot d_\tau^*}{4 \cdot N_s^{N_c-1} \cdot \Delta Z} \quad 4.4$$

In this form, the dependence upon the number of simultaneous views is only present on the exponent of the source density. Instead the effect of the particle image diameter and reconstruction depth is independent of  $N_c$ .

To illustrate the dependence of the reconstruction accuracy upon the source density, Figure 4.2 shows the results of a two 2D simulation using 4 viewing directions, with a total aperture angle of  $60^\circ$  at values of the seeding density corresponding to that commonly adopted in experiments ( $ppp=0.05$ ,  $N_s=0.15$ ) and far beyond it ( $ppp=0.3$ ,  $N_s=0.9$ ). The particles images diameter is 3 pixels and the results are shown for 5 MART iterations. The present results can be transposed to the 3D case adopting the same value of  $N_s$  or dividing the  $ppp$  by the particle image diameter. As a result the equivalent particle image density for the 3D case would be 0.0167 and 0.1  $ppp$  for the low and high concentration case respectively. The effect of seeding density is clearly visible, whereby the reconstruction at low particle concentration does not show any significant artifact because the probability of particles interaction along the same line of sight is rather low.

Instead at high  $N_s$  a significant degradation of the actual particles occurs with intensity transferred from the latter to the *ghost particles* field. The value of the quality factor evaluated for the two reconstructed fields is  $Q=0.95$  and  $Q=0.5$  respectively. The second case corresponds to a situation where no reliable Tomo-PIV experiment can be performed. Much attention is therefore devoted to the proper selection of the seeding concentration such to optimize tomographic PIV experiments and reach the maximum allowed seeding density in order to increase the spatial resolution without compromising the reconstruction accuracy.

The technique proposed in the present study aims at enhancing the reconstruction accuracy at levels of the seeding concentration that are beyond (typically from two to three times) the current limits of Tomo-PIV experiments.

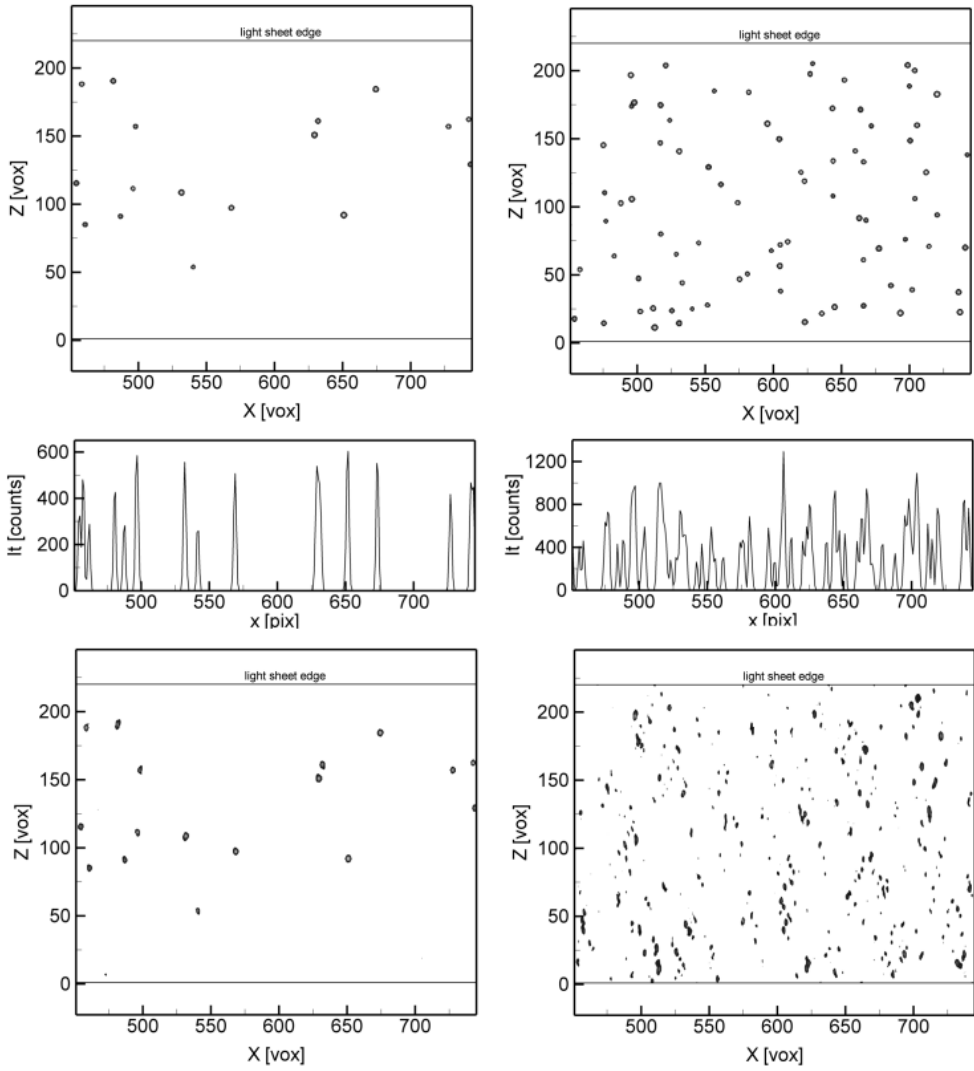


Figure 4.2 Numerically simulated 2D intensity field (top) and reconstructed field by MART (bottom).  $N_S=0.15$  (left) and  $N_S = 0.9$  (right). Intensity distribution on the 1D camera sensor at  $0^\circ$  (middle).

### 4.3 Theoretical model for MTE

The mathematical problem of tomographic reconstruction by algebraic methods from a small number of views is under-determined and several solutions exist in principle for a given set of images. It has been shown, however, that for PIV recordings at relatively low density, the MART technique returns a reliable and accurate estimate of the actual intensity field ( $Q > 0.9$ ).

Moreover it was shown recently by Elsinga et al. (2011) that many *ghost particles* do not produce a coherent pattern in the correlation map, which makes the cross-correlation analysis of tomograms significantly less affected by *ghost particles* than methods based on individual particle detection and tracking.

On, the other hand, when the seeding concentration increases, the solution of the MART reconstruction becomes less accurate, as shown in Figure 4.2 and also cross-correlation analysis may fail in determining the actual particle motion.

A crucial point that is not covered in the existing literature, which is dealt with in the present study, is the dependence of the MART solution upon the initial guess. This is associated to the undetermined nature of the solution of the algebraic problem posed by the reconstruction.

#### 4.3.1 Geometrical analogy for MART solution representation

Iterative projection methods convergence does lead to a solution which minimizes the distance from the initial guess in the space of the solutions. Therefore, different initial intensity fields can result in different reconstructed objects. This behavior becomes clear when the exact intensity field is considered as initial guess; in this case the iterative reconstruction algorithm returns the exact solution after the first iteration, without altering the initial guess. The main reason why probably this aspect has not been dealt with is that it is difficult to build a-priori information on the particles random distribution. The most common approach to the problem is to deny any initial information and assume a uniform (non-zero) intensity distribution to start the reconstruction algorithm.

The problem requires a representation in a hyperspace, however, for sake of clarity the case of an object composed of only two voxels and with a single projection equation is illustrated in Figure 4.3. The solution is represented as a point in 2D space. The single equation admits solutions belonging to a straight line  $r_I$ . If the initial condition is chosen as a point in the neighborhood of the origin  $E_{G0}$  (as commonly done for MART object initialization), the application of the MART update equation will project the result onto  $r_I$ , returning a solution  $E_I$  at a distance  $|E_I E_0|$  from the exact solution.

For usual problems, the latter distance is known to depend mostly upon the number of simultaneous views  $N_C$  and the particle images density  $N_S$ . Therefore, for a given value of the latter parameters, any MART reconstruction yields a solution that may lay on a circle centered in  $E_0$ .

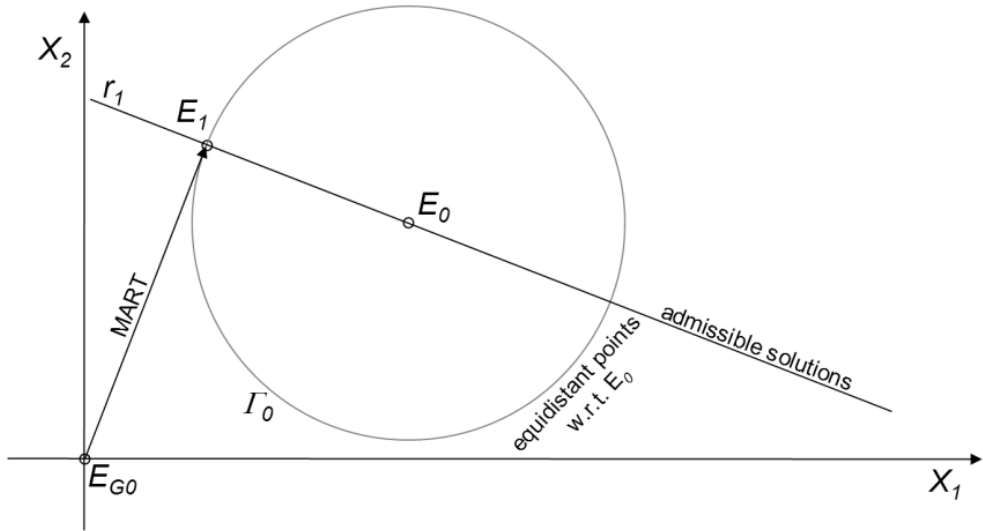


Figure 4.3 Geometrical interpretation of the space of solutions for a two-voxels/one-equation system. Initial value for MART is close to the origin. The circle indicates all solutions that are equidistant from the exact solution.

The problem generalization to Tomo-PIV operating conditions requires an  $N$ -dimensional space to represent all the possible solutions ( $N$  independent voxels). Projection equations available for the  $M$  pixels (with  $M \ll N$ ) are provided by the imaging system. Each equation defines a hyper-plane and the combination of the  $M$  hyper-planes defines a sub-space where the admissible solutions exist.

The mentioned sub-space depends upon the given initial condition. In case that the initial condition coincides with the exact solution, the sub-space only contains one point, the exact solution. Because the problem is strongly under-determined, the option of introducing a few more additional projection equations will not yield a unique solution (it may be wrongly suggested by the graphical representation in Figure 4.3 based on a 2D space: adding a second non-parallel line to  $r_i$ , their intersection appears uniquely determined). This is because the number of additional projections must be orders of magnitude beyond that of the available projections. Instead, the current discussion focuses on the fact that if a better initial condition would be available, for instance if the point  $E_{G0}$  is slightly moved to the right, then the distance between the MART solution and the exact value will decrease.

### 4.3.2 Iterative first guess evaluation

Consider now that a hypothetical second solution of the same problem is available, for instance obtained from a second view of the same set of particles at a subsequent time instant. We denote this solution as  $E_2$ , to indicate that it follows  $E_1$  in time, Figure 4.4.



## 4.4 MTE algorithm

The 3D particle pattern undergoes a transformation between the two (or more) exposures, which requires the particle motion field to be known or estimated by some means in order to deform the object intensity to a single time instant. Because a-priori information on the motion field is not available, the method can only be implemented with an iterative algorithm.

The main objective of the MTE is that of iteratively building a first guess for the 3D intensity field  $E_G$  to be used as input for the MART algorithm. This guess is obtained combining the information from the first and second, or a multiple set of, exposures as previously illustrated in Figure 4.4 making use of the MART reconstruction, cross-correlation analysis and object deformation technique similarly to that used in the interrogation of the objects.

The MTE method can be schematically described by 5 main steps:

1. MART reconstruction of individual recordings, returning  $E(\mathbf{R}, t)$  and  $E(\mathbf{R}, t + \Delta t)$ , shortly  $E_n$  and  $E_{n+1}$
2. cross-correlation analysis of the pair of objects  $E_n$  and  $E_{n+1}$ , which yields the particles velocity  $\mathbf{V}(\mathbf{R}, t + \frac{\Delta t}{2})$ , shortly  $V_n$
3. evaluation of the pseudo simultaneous object (*PSO*) by deforming one particle field according to the estimated motion field. Two *PSOs* are obtained:  $E_{n+1}'(\mathbf{R} - \mathbf{V} \cdot \Delta t, t + \Delta t)$  and  $E_n'(\mathbf{R} + \mathbf{V} \cdot \Delta t, t)$
4. linear combination of the two objects to obtain  $E_{Gn} = \frac{1}{2}(E_n + E_{n+1}')$  and  $E_{Gn+1} = \frac{1}{2}(E_{n+1} + E_n')$
5. input the result as first guesses for further MART iterations:  $E_n^0 = E_{Gn}$  and  $E_{n+1}^0 = E_{Gn+1}$

In the above points the vector  $\mathbf{R}=(X, Y, Z)$  indicates the coordinates in the object space. After step 5, the sequence from 1 to 4 can be repeated several times until the result exhibits convergence.

The first 2 steps are straightforward and do not require specific discussion. The deformation of one object (e.g. from the exposure at time  $t + \Delta t$ ) to obtain the intensity field that would be expected at time  $t$  is made by the deformation technique used for the 3D iterative interrogation (see section 2.3.3).

The following sections discuss the way how the information from different exposures is combined, the initialization of the MART iterative calculation and the overall iterative structure of the MTE algorithm.

### 4.4.1 Suppression of incoherent ghost intensity

The operating principle of the MTE technique is visually explained by showing how the structure of the *ghost intensity* field evolves at subsequent time instants. A *ghost particle* is returned by the MART reconstruction at the intersection points of different lines-of-sight

corresponding to pixels characterized by non-zero intensity. Thus the *ghost particle* position depends on the relative position of the actual particles and the lines-of-sight of the imaging system.

This means that, while the actual tracers move from one exposure to another according to the flow motion, the *ghosts* generally disappear or move along different directions since the relative position of the actual particles and the viewing cameras can change, which depends on the particle tracers displacement field. This aspect is discussed in more details in Elsinga et al. (2011).

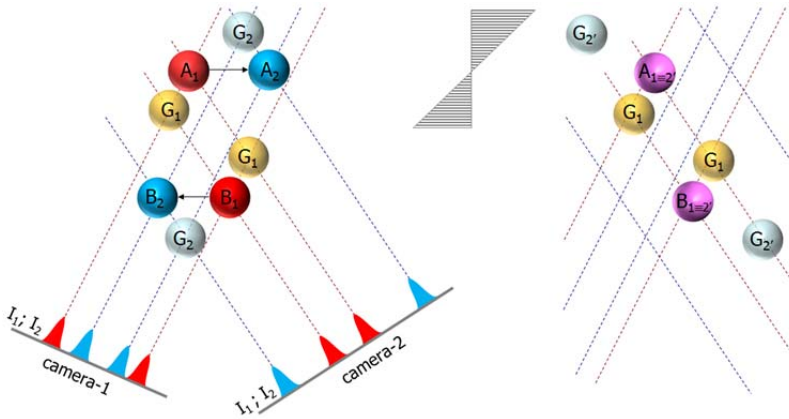


Figure 4.5 Left: two particles  $A$  and  $B$  imaged from two directions exposed twice (first exposure field “1” in red and second exposure “2” in blue). Particles motion according to a hypothetical displacement field (gray pattern on the left). The *ghost particles* produced by MART represented in lighter colors. Right: superimposed actual particles (purple) and ghost field after that the second exposure field is tracked back to the first exposure time considering the displacement field known.

Figure 4.5-left illustrates the case of two particles  $A$  and  $B$  forming two pairs of *ghosts*  $G_1$  and  $G_2$  at the first and second exposure respectively. For the given displacement field, the two sets of *ghost particles* do not occur at the same location. The necessary condition for this to occur is that the difference between the displacements of the particle tracers from which the *ghosts* are produced is larger than the diameter of the reconstructed particle. If an estimate of the displacement field is available, the intensity field reconstructed at the second time instant can be deformed according to the displacement field into that at the first time instant returning the *PSO*. The positions of the particles  $A'_2$  and  $B'_2$  will in this case coincide to those of  $A_1$  and  $B_1$ , whereas  $G_1$  and  $G_2$  do not necessarily interfere.

If the fields 1 and 2' are considered, two independent observations and reconstruction of the same particle field undergoing a transformation due to the particles motion is used to enhance the reconstructed particle field at any of the two time instants. For instance, multiplying the intensity will retain the (coherent) intensity associated to the actual particles and suppress most of the (incoherent) intensity associated to the *ghost particles*. However, any error in the estimate of the displacement field will also introduce a cancellation of the coherent intensity field. Instead, averaging the two intensity fields will not eliminate coherent intensity even in case of local erroneous velocity information. As a drawback, the

incoherent intensity is not suppressed as rapidly as in the case of multiplication, but only halved after every iteration.

The reconstructed intensity field can be decomposed into the coherent  $E_C$  and incoherent  $E_I$  part respectively:

$$E_{MART} = E_C + E_I \quad 4.5$$

The term  $E_C$ , although associated to the actual particles, does not correspond exactly to the actual intensity field  $E_0$  (accounting for all the energy in the reconstructed volume) because part of such energy is captured by the *ghost particles*.

The above decomposition is valid at each of the time instants when a reconstruction is made. If the second exposure is deformed towards the first time instant by knowledge of the displacement field (2'), one obtains that  $E_C$  mostly coincides from the two time instants, instead  $E_I$  will not correspond. The deformed particle field is called the pseudo simultaneous object (PSO), as introduced at step 3 of the MTE sequence. More in details:

$$E_2'(X, Y, Z) \equiv PSO_1 = E_2(X + U_{pred} \cdot \Delta t, Y + V_{pred} \cdot \Delta t, Z + W_{pred} \cdot \Delta t) \quad 4.6$$

Here, the subscript *pred* indicates a velocity predictor from cross-correlation. In the hypothesis that velocity predictor is accurate within a particle image diameter, the average between the two fields can be written as:

$$E_G \approx E_C + \frac{1}{2}(E_{I,1} + E_{I,2'}) \quad 4.7$$

which indicates that the above procedure would keep unaltered the coherent part of the signal (actual particles) and decrease the peak intensity of the *ghost particles* that do not travel according to the actual particles velocity. An initial estimate of the particle motion is to be produced by cross-correlation analysis between the two reconstructed objects. As a consequence the MTE method will effectively reduce the *ghost intensity* field only if the estimate of the particle motion is at least reliable. A first approach could be to consider as tomographic experiment design rule that proposed by Elsinga et al. (2006) in a less conservative way and at a lowered spatial resolution (e.g. increased interrogation block size).

#### 4.4.2 MART first guess and iterative evaluation

The use of the intensity field  $E_G$  to initialize the MART computation is demonstrated to further improve the accuracy of the reconstructed object as graphically described in Figure 4.4, because the *ghost intensity* field  $G_2'$  is rapidly eliminated by the MART algorithm where these particles do not fall at positions where actual intensity is present on the images.

Recalling Figure 4.5, the light blue particles do not correspond to the intensity field recorded from both cameras. The MART iteration is therefore evaluated using  $E_G$  instead of a uniform intensity field. The evaluation may be iterated until convergence is attained to a good degree. This procedure is performed for the reconstructed objects from both exposures, yielding an enhanced intensity field at both time instants  $E_1^{MTE-1}$  and  $E_2^{MTE-1}$ , where the subscript indicates the order in the exposure and the superscript the number of times that MTE is repeated.

One MTE iteration step consists of the operations listed above from point 1 to 5: the MART reconstruction of two tomographic recordings  $E_n$  and  $E_{n+1}$ , the cross-correlation between the

reconstructed objects, the deformation of the objects to obtain the pseudo-simultaneous-fields ( $POS_n$  and  $POS_{n+1}$ ) and the evaluation of the intensity field to be used as first guess  $E_{Gn}$  for the subsequent application of the MART algorithm. The enhanced intensity fields are again interrogated by cross-correlation analysis yielding an updated displacement field, which can be used in turn to further enhance the two reconstructed and enhanced objects.

Successive iterations of the method are expected to progressively improve the results because the initial guess for the velocity field may be inaccurate as a result of the large amount of *ghost particles*. Therefore, at following iterations, the *ghost intensity* is progressively reduced increasing the accuracy of the displacement field either for a final output or for a successive enhancement. The number of times that MTE is repeated or enhancement steps, referred to as  $N_E$ , is therefore a crucial parameter expected to affect the result of the MTE technique. Other important factors are the structure of the velocity field, the diameter of the tracer particle images and the viewing angles of the imaging system. Moreover, the MTE-MART technique can be applied also in multiple-frames tomographic experiments.

A synthetic description of the algorithm is given in form of flow-chart (Figure 4.6) for the double-frame operating mode. In the case of continuous PIV recordings, as typically obtained by high-repetition rate PIV systems, the availability of time-resolved data allows to build the pseudo-simultaneous-object for the  $n^{th}$  recording using one or more exposures acquired before and after the considered time instant. The number of recordings used to create the PSO will be denoted by  $N_O$ : for the double-frame mode  $N_O$  is equal to 2.

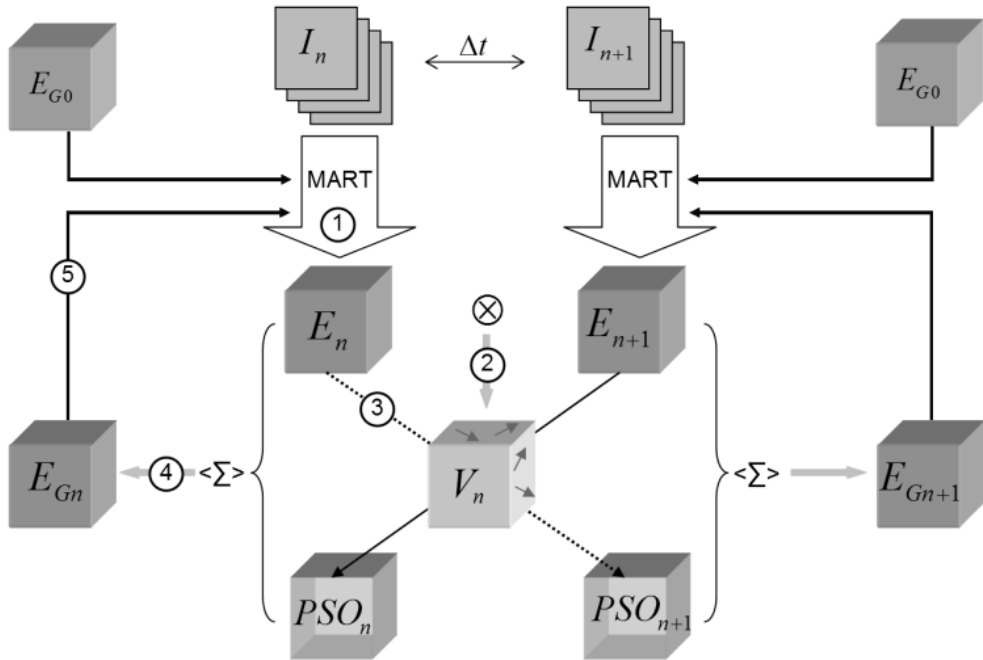


Figure 4.6 Flow chart of the MTE-MART technique for double-frame recordings. 1) MART reconstruction of individual recordings; 2) cross-correlation analysis of the objects pair; 3) evaluation of  $PSO$  by deformation of the objects according to the motion field; 4) averaging

the reconstructed and pseudo-simultaneous objects; 5) input result as first guess of the next MART reconstruction.

#### 4.4.3 Numerical evaluation

The effect of the MTE method on the reconstruction is simulated with a 2D numerical model and the results are shown in Figure 4.7. The displacement field between the exposures was chosen as a shear along the depth of the domain, similarly to what shown in Figure 4.5; the maximum displacement between the exposures is 5 voxels.

The tomographic recordings are characterized by a high seeding density ( $N_S=0.9$ ,  $ppp=0.3$ ), and the imaging system is composed by 4 cameras. For sake of clarity the results are shown in a small region of the complete reconstruction volume ( $1000 \times 200$  voxels). The actual particle field distribution is indicated by circles at locations where particles are placed. The MART reconstruction in these conditions reproduces most of the particles but at a reduced intensity and with distorted shape. The corresponding quality factor  $Q$  is 0.55; a value well below the criterion proposed by Elsinga et al. (2006) for a reliable correlation ( $Q > 0.75$ ). Moreover a significant amount of *ghost particles* with intensity comparable to that of the actual particles is returned.

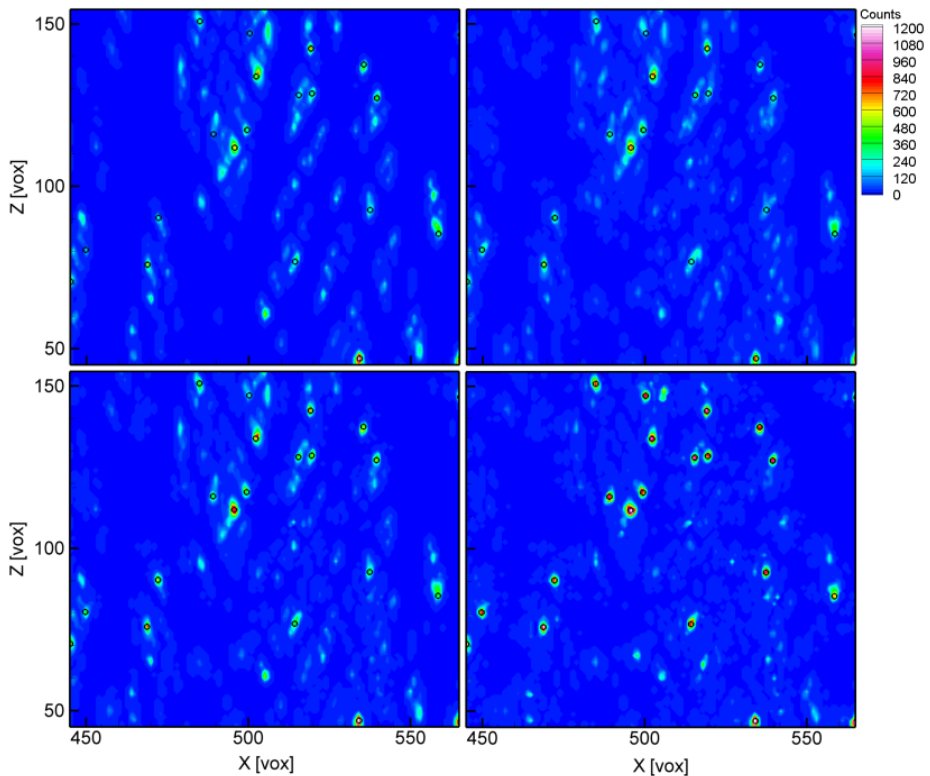


Figure 4.7 Top-left: MART reconstructed intensity field for one exposure. Top-right: intensity field used as initial guess for the first MTE step. Bottom-left: reconstructed field after one MART iteration of the first enhancement step. Bottom-right: reconstructed fields

after 10 MTE-MART steps. The position of the actual particles is indicated by solid black circles.

Averaging the reconstructed object and its *PSO* from a pair of exposures (Figure 4.7-top-right) returns some *ghost intensity* reduction and improves the precision on the position of the actual particles ( $Q=0.6$ ). Performing a MART computation that takes as initial guess the result on the top-right yields a result shown in the bottom-left picture. An improvement comparable to the previous step is observed ( $Q=0.65$ ). The iterative application of MTE approaches an asymptote after approximately 25 steps; here the result after 10 steps is shown ( $Q\approx 0.85$ ), a value above the criterion for accurate cross-correlation analysis.

In conclusion, the improvement obtained with the MTE technique can be seen as the result of two contributions:

- the *ghost particles* intensity is progressively reduced
- consequently, the intensity is redistributed among the actual particles, which are reconstructed more accurately

Regarding the cross-correlation procedure, the second aspect is particularly significant: since the MTE method gives the best results when the *ghost intensity* displacement is poorly correlated to the flow motion (Elsinga et al. 2011), one can expect that this contribution will not affect the cross-correlation signal significantly, but only reduce the effect of the *ghost intensity* field. As it will be shown in the following section, also the velocity field resulting from correlation of enhanced objects is more accurate.

## 4.5 Numerical performance assessment

The detailed effect of the main MTE parameters variation on the measurement accuracy is investigated by computer-simulated tomographic images of a known flow field. A two-dimensional object is projected onto one-dimensional virtual sensors, similarly to the approach followed by other studies (Elsinga et al. 2006; Atkinson et al. 2008; Worth and Nickels 2008).

Particle images are generated within objects of  $1000\times 200$  voxels at random locations by Monte Carlo technique. The diameter of the particle images expressed in pixel units is set to 3, a representative value for Tomo-PIV experiments reported in literature. The particle tracers concentration in the object is varied such to obtain a particle image density  $ppp$  on the imager ranging between 0.05 and 0.3 ( $N_S \in [0.15, 0.9]$ ). The particle displacement field is a sinusoidal shearing motion of 200 voxels wavelength and 3 voxels amplitude, representative of shear layers flows measured with the velocity gradient aligned with the depth direction. The object is imaged by one-dimensional array sensors of 1000 pixels size, with uniform angular displacement ( $\mathcal{A} = \{-30, -10, +10, +30\}$  degrees).

The particle image density and the number of cameras are reported to be the most important parameters governing the tomographic reconstruction process. The number of viewing cameras  $N_C$  is varied from 4 to 8. To date, most Tomo-PIV experiment are performed with values of  $ppp \in [0.02, 0.1]$  and  $d_r^* = 2-4$ . The range investigated in the present simulation may initially appear unrealistic because it extends far beyond the currently practiced values.

However it will be discussed in the reminder that the measurement range extension, making use of MTE, justifies the present choice of the simulation range.

The parameters governing the MTE method are the number of iterative enhancement steps  $N_E$  and the number objects involved in the MART enhancement  $N_O$ . The discussion initially considers the case  $N_O=2$  (double-frame images). Subsequently the simulation is performed for the case of more than 2 reconstructed objects (time-resolved imaging) obtained from subsequent exposures, which correspond to the case of time-resolved measurements performed in continuous single-frame mode ( $N_O=\{3,5,7\}$ ). Two evaluation criteria are used: the reconstruction quality factor  $Q$  and the standard deviation of the velocity measurement error  $\sigma$ .

#### 4.5.1 Double-frame recordings

The quantitative evaluation of the effects shown in Figure 4.7 is given by the occurrence histogram of the particles peak intensity  $I_p$  illustrated in Figure 4.8. Distinction is made between the peak intensity of actual particles (blue) and that of *ghost particles* (red).

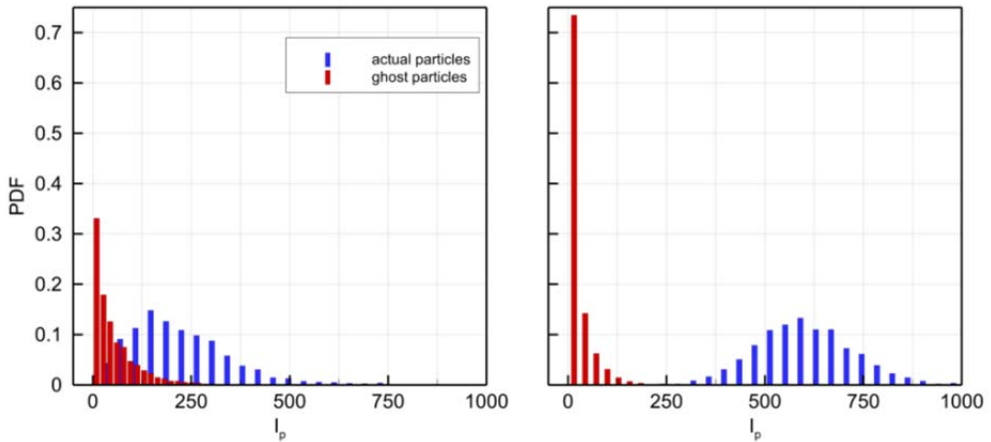


Figure 4.8 Probability density function of particle peak intensity for actual and *ghost particles* in the reconstructed object. Left: MART reconstruction ( $N_S=0.3$ ,  $N_C=4$ ). Right: MTE-MART after 10 enhancement steps.

From the MART reconstruction, the reconstructed actual particles peak intensity occurrence attains a maximum at 100 counts and extends till about 500 counts. Considering that the exact value of the generated particles peak intensity is centered on 1000 counts, the MART reconstruction in these conditions does not retrieve more than 10% of it. The distribution of the *ghost particles* exhibits lower values in agreement with previous findings from Elsinga et al. (2006).

However, under these conditions, the distribution of actual and *ghost particles* intensity, overlap to a large extent, which decreases the signal-to-noise ratio of the reconstructed object. The application of MTE by 10 iterative steps, Figure 4.8-right, strongly alters the situation. First, the peak intensity distribution of the actual particles reconstruction is raised

with a factor six with a maximum occurrence attaining 600 counts. Secondly, the *ghost intensity* is slightly reduced with a significantly higher number of low-intensity *ghost particles*. In this case, MTE allows to completely separate the histograms of actual particles and *ghosts*.

Also the precision of the individual particles reconstruction and their peak location appears to be improved. The precision error of the reconstructed particle (Gaussian) centroid location is represented with a 2D dispersion plot, Figure 4.9-left, where  $\varepsilon_Z = Z_R - Z_0$  is the difference between the measured position of the reconstructed particle  $Z_R$  with respect to the exact position  $Z_0$ ; the same applies for the position along  $X$ .

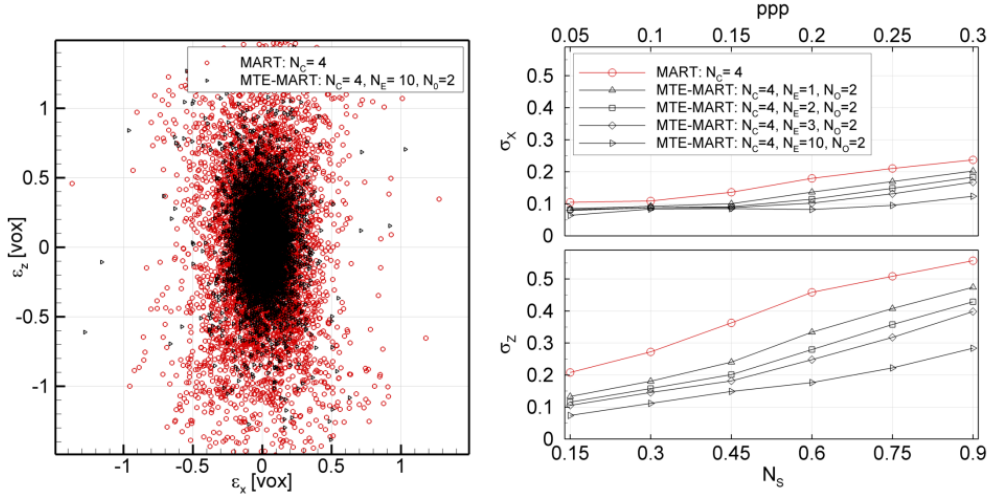


Figure 4.9 Left: 2D error dispersion plot of the difference between the actual and the reconstructed particles peak position ( $N_S=0.9$ ). Right: standard deviation of the error on the peak position as a function of  $N_S$  (ppp) varying the number of enhancement steps  $N_E$ .

It can be observed that the precision error on the location of the particle centroid is considerably reduced when the MTE technique is applied, which also follows from the observations made in Figure 4.7. Not surprisingly, the error along the  $Z$ -coordinate direction has a higher dispersion than that along the  $X$ -direction (in-plane). The dependence of the particle centroid position error  $\varepsilon$  upon the source density  $N_S$  is shown by the ensemble standard deviation  $\sigma$ , Figure 4.9-right.

The diagrams indicate that  $\sigma_x=0.1-0.2$  voxels and about twice as much for  $\sigma_z$  when MART alone is applied. Adopting MTE reduces these errors of a factor 2 to 3 depending on the value of  $N_S$ . This also indicates that MTE-MART could be a well suited technique to improve the measurement precision for experiments that require individual particle tracking (PTV) in 3D (e.g. Schröder et al. 2008a, Novara and Scarano 2012).

The reconstruction accuracy is quantified by the quality factor  $Q$  and depends mostly upon the number of viewing cameras  $N_C$  and the source density  $N_S$  (Elsinga et al. 2006).

The comparison of the accuracy returned by MART and that obtained by MTE in the present study is also shown for different values of the number of enhancement steps  $N_E$ , Figure 4.10-left. The dependence of  $Q$  upon the seeding density for MART is in agreement with previous

studies. The criterion stated by Elsinga ( $Q > 0.75$ ) may be taken as an upper limit for the seeding density in Tomo-PIV experiments, which is currently around  $N_S = 0.5$  for a system with four cameras.

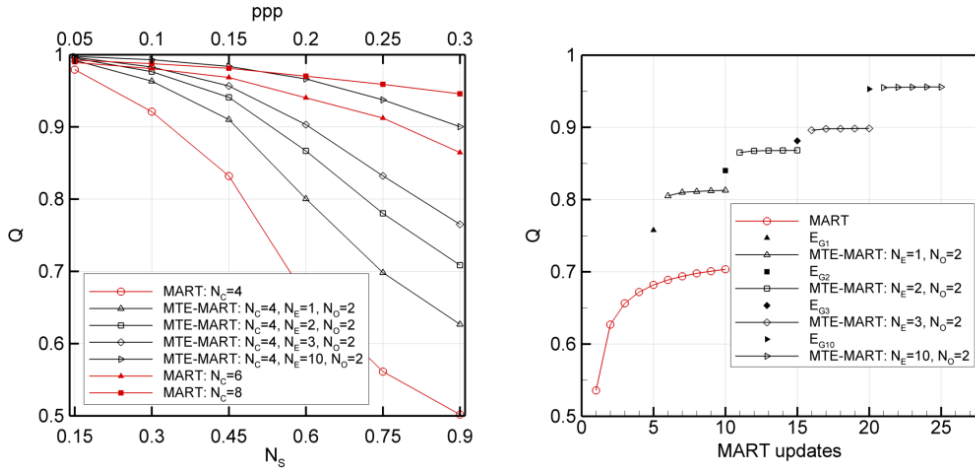


Figure 4.10 Left: reconstruction quality factor obtained by MART and MTE-MART (double-frame recordings) as a function of particle image density  $N_S$  ( $ppp$ ). Curves are given for varying number of enhancement steps. Right: effect of iterative MART analysis and initial guess enhancement ( $N_S=0.6$ ,  $N_C=4$ ).

Results from MTE-MART show that it is possible to increase the accuracy of the reconstruction and in turn extend the limit for the maximum seeding density:  $Q$  approaches 0.9 even for a seeding density corresponding to approximately  $N_S=1$  if 10 MTE steps are applied. Moreover, the effect of the enhancement technique is comparable to the one of increasing the number of cameras; the asymptotic behavior of the MTE-MART reconstruction compares well to the MART reconstruction doubling the number of simultaneous views.

The relative importance of the MART iterations and the guess intensity field to the reconstruction quality is shown in Figure 4.10-right. Except for the first MART reconstruction process, where several iterations are needed to reach a reconstruction quality that enables a reliable analysis by cross-correlation, the most prominent improvement is made when  $E_G$  is evaluated after the results from the two exposures are combined. An additional improvement, comparable to the latter is obtained after the first MART iteration of the enhanced guess field. This may also suggest that the MTE technique can be implemented in a relatively efficient way, limiting the number of time-consuming MART iterations to a single one or two at most, when the first enhanced objects have already been obtained.

The velocity field between reconstructed 3D objects is obtained with the Volume Deformation Iterative Multigrid technique (VODIM, Scarano and Poelma, 2009). In the present case the problem has been reduced to 2D objects, which are therefore analyzed with WIDIM (Scarano and Riethmuller 2000) using interrogation windows elongated in the  $X$  direction.

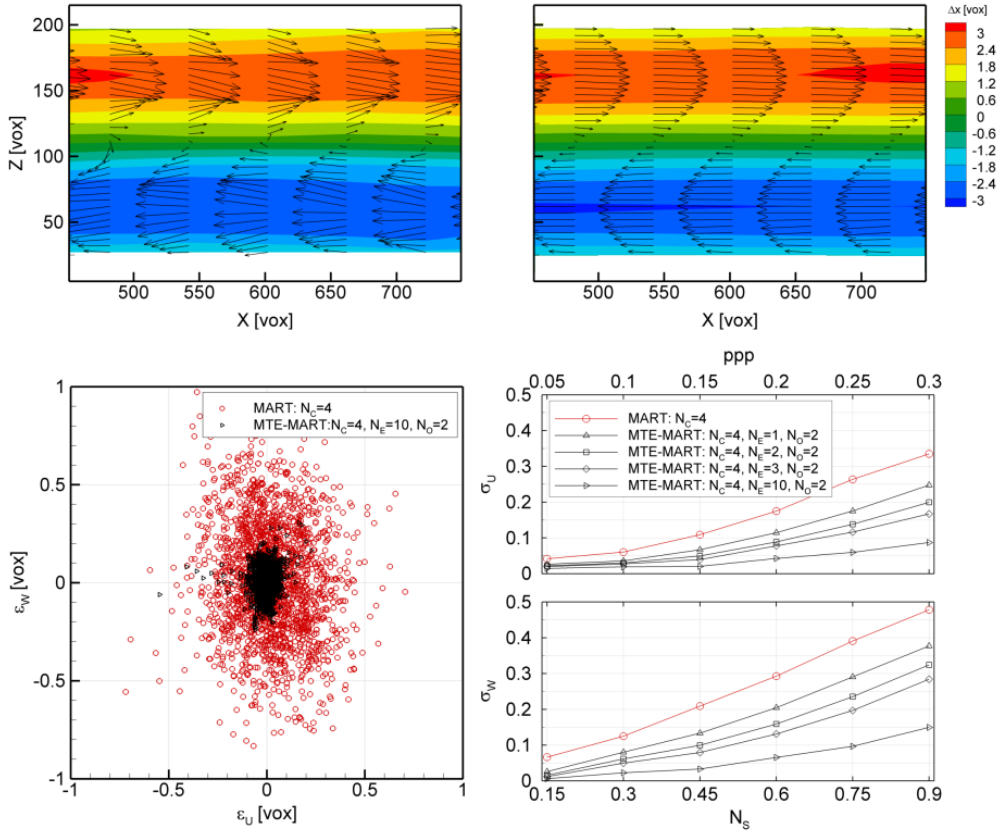


Figure 4.11 Top-left: displacement field obtained by cross-correlation between two objects reconstructed by MART ( $N_S=0.6$ ). Top-right: displacement field obtained by cross-correlation between the objects reconstructed using 10 steps of MTE-MART. Bottom-left: scatter plot of the difference between the actual and the computed displacement for the two components  $U$  and  $W$ , relative to the displacement field presented in the top row. Bottom-right: standard deviation of the error on the displacement components as a function of  $N_S$  ( $ppp$ ) and  $N_E$ .

The window size is chosen such to obtain, on average, 5 particles in the interrogation area also at the lower values of  $N_S$  considered in the simulation. A detail of the velocity field obtained from the objects pair reconstructed with MART is shown in Figure 4.11-top-left and compared with that resulting from MTE with 10 enhancement steps, Figure 4.11-top-right. Although the overall velocity pattern is well represented already for the MART reconstruction, a significant reduction of random errors is obtained with the MTE method.

A detail of the cross-correlation map in a  $21 \times 21$  voxels neighborhood of the origin is shown in Figure 4.12. The comparison between the correlation coefficient obtained from MART reconstructed objects and that from enhanced objects shows the extent of the signal-to-noise improvement obtained by the MTE technique. The position of the peak indicates a

displacement of 3 voxels along the  $X$  direction; the signal to noise ratio is three times higher after 10 MTE steps.

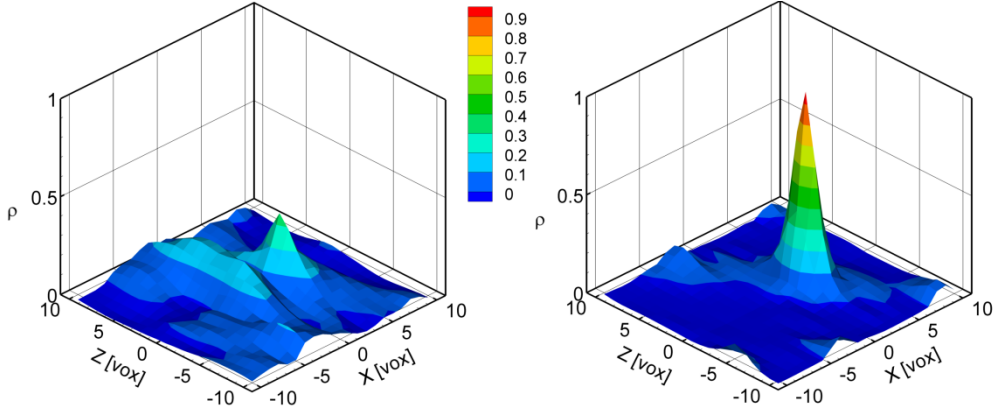


Figure 4.12 Detail of cross-correlation map obtained by 2 reconstructed subsequent exposures at  $N_S=0.6$ . Left: objects reconstructed with MART. Right: enhanced reconstructed objects after 10 MTE steps.

The dispersion plot of the precision error of velocity measurement is shown in Figure 4.11-bottom-left, where  $\varepsilon_w=w_R-w_0$  is the difference between the displacement along the depth direction obtained from cross-correlation of the reconstructed objects ( $W_R$ ) and the one obtained from correlation of the original intensity fields ( $W_0$ ); the same applies for the  $U$ -component.

The standard deviation of the two components of the error, Figure 4.11-bottom-right, increases with the seeding density; values comparable with those obtained applying MART only are reached after 10 MTE steps for approximately three times higher seeding density. Conversely, for high values of the seeding density, the measurement precision error is reduced by a factor three with the MTE technique. More iterations appear to be required for the  $W$ -component to obtain the same improvement.

#### 4.5.2 Time-resolved recordings

When the particle motion is measured by a continuous sequence of single exposures in time-resolved mode, recordings are available that allow to include more than two exposures in the MTE technique for each single object. In this case, equation 4.7 needs to be rewritten in a more general form as:

$$E_G \approx E_C + \frac{1}{N_O} \left( \sum_{n=1}^{N_O} E_{I,n} \right) \quad 4.8$$

where  $N_O$  is the number of exposures taken into account to form the guess. When  $N_O > 2$  important advantages are found:

- the rate at which the incoherent (*ghost*) intensity decays is directly proportional to  $N_O$

- the asymptotic behavior of the MTE method is expected to be that of a tomographic system with a number of cameras multiplied by  $N_O$

The present analysis is carried out for  $N_O=\{3,5,7\}$  and values beyond 7 are considered unrealistic for real applications. The displacement predictor between the  $m^{th}$  and  $n^{th}$  exposure is given in this case by the sum of the individual displacement fields obtained between subsequent exposures.

Figure 4.13 summarizes the effect of the number of objects  $N_O$  and that of enhancement steps  $N_E$  upon the reconstruction accuracy  $Q$ . The increase in  $Q$  with the number of exposures is visible but somehow less pronounced than that obtained with subsequent enhancement steps. For  $N_E=10$  and  $N_O>5$ , the reconstruction quality becomes almost independent of  $N_S$  and is always above 0.95, which confirms the potential of the MTE approach to analyze tomographic PIV recording from highly seeded images.

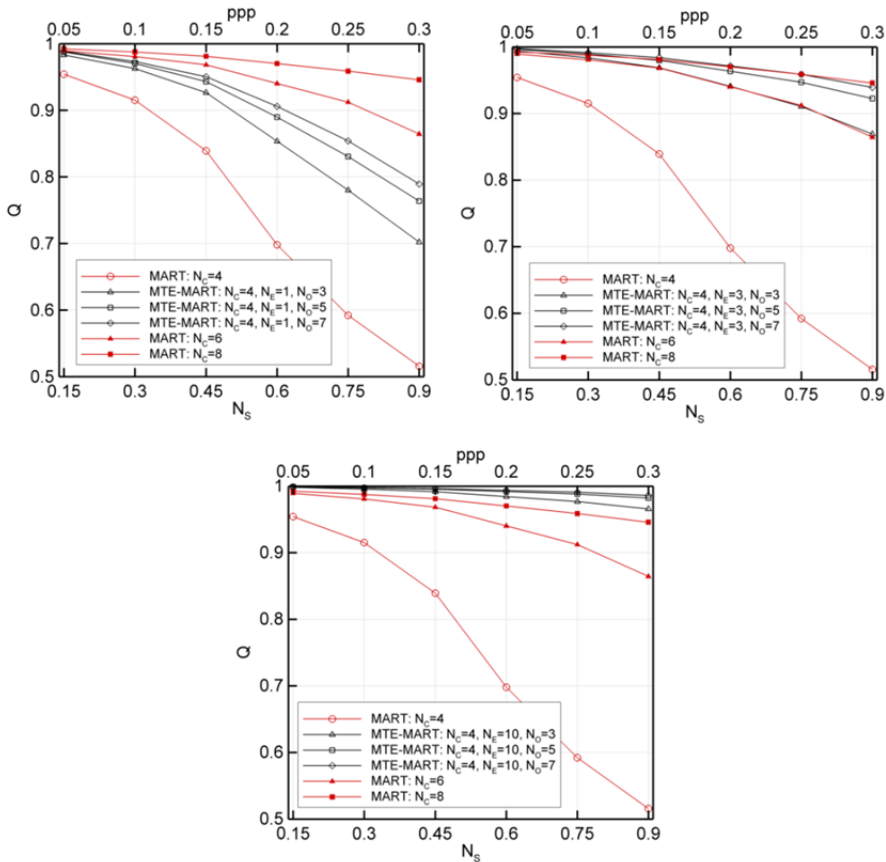


Figure 4.13 Effect of number of objects  $N_O$  and enhancement steps  $N_E$  to the accuracy of reconstruction by MTE-MART. Top-left:  $N_E=1$ . Top-right:  $N_E=3$ . Bottom:  $N_E=10$ .

The corresponding velocity field is significantly more regular than that obtained for a single MART analysis and the error standard deviation reduces to approximately 0.05 voxels with a

difference in the convergence rate between  $W$  and  $U$  that is similar to the case of two exposures, Figure 4.14.

For low values of the seeding density ( $N_S < 0.3$ ), the reduction of precision error is larger than that expected solely for the *ghost particles* attenuation. This may be ascribed to a slight reduction of discretization errors in that the particles are reconstructed at a different sub-voxel locations in each pseudo simultaneous object.

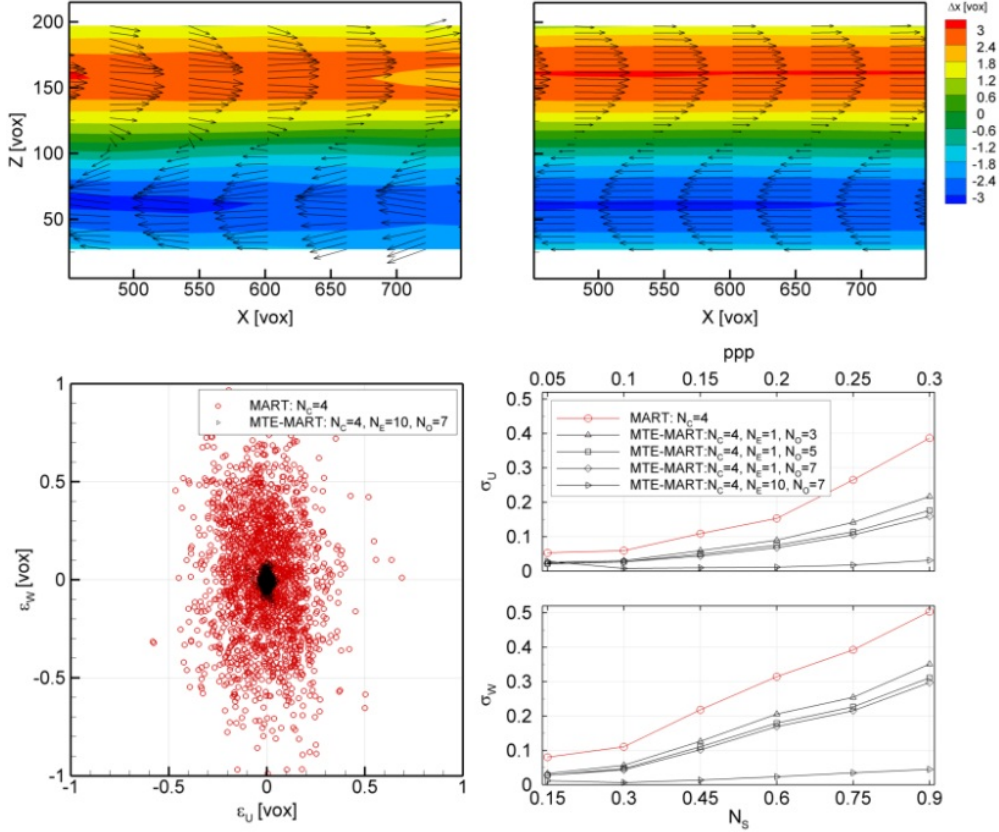


Figure 4.14 Top: displacement field obtained by cross-correlation between two objects reconstructed by MART (left) and MTE-MART (right) with  $N_E=10$  and  $N_O=7$  ( $N_S=0.6$ ). Bottom-left: 2D scatter plot of the displacement error. Bottom-right: standard deviation of the error on the displacement components as a function of  $N_S$  (ppp) varying the value of  $N_E$  and  $N_O$ .

## 4.6 Multiplicative variant of the MTE algorithm

The MTE technique so far discussed is implemented with an average between the reconstructed object and the *PSOs* to form the initial guess. The incoherent intensity field due to *ghost particles* is expected to be reduced in relation to the number of exposures  $N_O$  used to build the new guess. When double-frame recordings are available, the *ghost intensity*

can be halved during this procedure. An alternative to the averaging operation is to multiply the reconstructed field and its *PSO* and raise them to the power  $1/N_O$ .

This approach can lead to a faster suppression of the incoherent intensity improving the convergence rate of the MTE-MART method. In the following the MTE method based on the averaging approach (indicated with the symbol  $\Sigma$ ) and that based on multiplication (symbol  $\Pi$ ) are compared in terms of quality factor  $Q$  as a function of the seeding density  $N_S$ , Figure 4.15.

The accuracy of the reconstruction, performed with 4 cameras, is shown at different enhancement steps ( $N_E=1$  and  $N_E=10$ ) for both  $MTE_{\Sigma}$  and  $MTE_{\Pi}$ .

Two different test cases are analyzed: in the first case (solid lines) the velocity field between the exposures is computed by means of cross-correlation; instead, in the second one (dotted lines) the velocity field is arbitrarily set to zero. The latter is intended to verify the robustness of the method with respect to errors (e.g. spurious vectors) in the displacement predictor field. For an accurate displacement field, the first step of  $MTE_{\Pi}$  largely improves the result and is comparable to 2 steps of  $MTE_{\Sigma}$ .

The iterative use of  $MTE_{\Pi}$  does not maintain the same trend: after 10 steps, actually, the  $MTE_{\Sigma}$  appears to provide a more accurate reconstruction. Both methods, however, attain more accurate object reconstruction compared to MART.

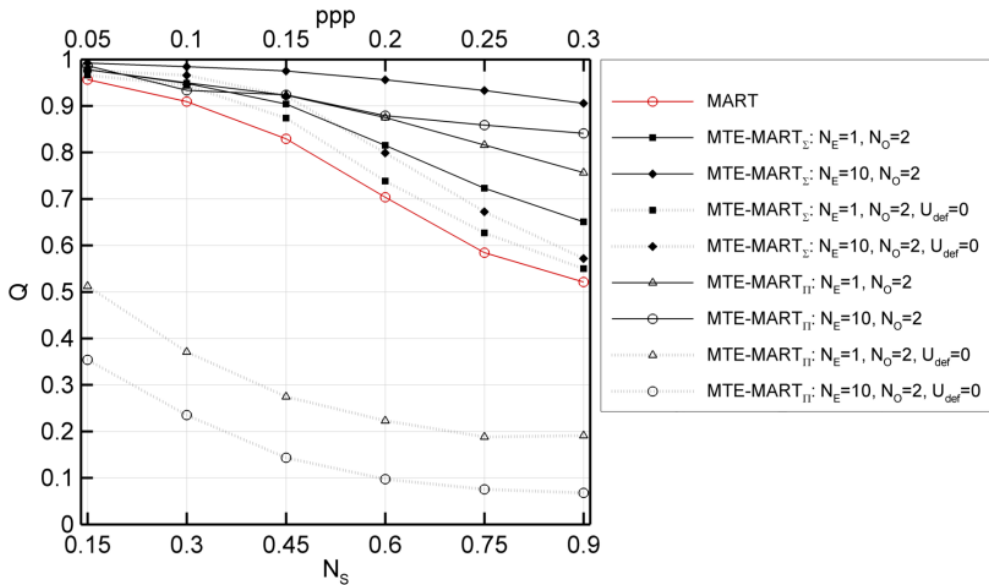


Figure 4.15 Comparison between the averaging ( $\Pi$ ) and multiplicative ( $\Sigma$ ) approach for MTE-MART. Reconstruction quality factor  $Q$  as a function of  $N_S$  (*ppp*). Results from computed motion field from cross-correlation (black lines) and from an erroneous motion field (dotted lines).

Instead, when the velocity field used in the deformation procedure ( $V_{pred}$ ) is set to zero,  $MTE_{\Pi}$  becomes very inaccurate with a reconstruction accuracy more than halved compared to MART. Instead, for the same condition ( $V_{pred}=0$ )  $MTE_{\Sigma}$  basically maintains the same

accuracy as MART. The undesired behavior of  $MTE_{\Pi}$  can be explained recalling the discussion in section 0: the multiplication approach leads to cancellation of the coherent part of the reconstruction (actual particles) if they are not simultaneously present at the same location in the reconstructed object and the *PSO*.

Instead, the averaging approach maintains at least the part of the coherent intensity coming from reconstructed object. In conclusion, it can be stated that the  $MTE_{\Sigma}$  algorithm, or briefly  $MTE$ -MART, candidates best for an accurate and reliable reconstruction and the multiplicative approach may only be considered useful if the displacement field is known with a high level of reliability.

## 4.7 Computational cost of MTE

Considering that the data processing associated to the Tomo-PIV technique is already computationally intensive, the MTE method requires even higher computational resources. The combination of MTE with the acceleration techniques proposed by Atkinson and Soria (2009) resulted in an advanced method recently presented by Atkinson et al. (2010). In the present section the essential computational aspects are discussed for the MTE technique.

The tomographic reconstruction of two exposures and one three-dimensional cross-correlation between the intensity fields are needed to obtain a single velocity field. During reconstruction, the MART algorithm is usually repeated over 5 iterations. The 3D particle motion is evaluated by the volume deformation iterative multigrid technique (VODIM, Scarano and Poelma 2009) with typically three iterations of the cross-correlation analysis.

Indicating with  $t_{MART}$  the computation time needed for a single MART iteration and with  $t_{CC}$  the time needed for one cross-correlation iteration, the time required for the Tomo-PIV analysis of  $N_O$  exposures reads as follows:

$$t_{TOMO} = N_O \cdot t_{MART} \cdot N_{MART} + (N_O - 1) \cdot t_{CC} \cdot N_{CC} \quad 4.9$$

where  $N_{MART}$  indicates the number of MART iterations and  $N_{CC}$  the number of cross-correlation iterations. When the Motion Tracking technique is applied, the computational cost increases depending on the number of MTE iterations ( $N_E$ ); in order to analyze the same number of exposures, if 10 enhancement steps are used, the total computational time needed is 10 times larger than the one needed by typical Tomo-PIV.

Nevertheless, since the reconstruction process is repeated for each MTE iteration, it has been observed that the MART iteration needed for each MTE step can be reduced from 5 to 2-3 iterations without affecting the reconstruction accuracy of the final enhanced objects. Furthermore, as will be shown in section 4.9.1, 5 MTE iteration are sufficient to achieve the maximum improvement expected from MTE.

A possible reduction in the computational cost of cross-correlation analysis can be achieved if the multigrid procedure (interrogation box size refinement) is stopped at an earlier stage during the first MTE steps and extended to the full range only at the end.

It is estimated that the total computational time increases by approximately a factor 3 when the Motion Tracking Enhancement technique is applied. At present, the computation time required for the analysis of a double frame recording obtained with 4 Mpixel cameras is in the order of 12 min for the MART analysis and 45 min when MTE is applied. The above

figures are based on the use of LaVision DaVis software, using a 8-core XEON PC with 2.66 GHz.

A further reduction of the computational time can be achieved making use of sparse reconstruction techniques where only the non-zero voxels identified within the enhanced guess are updated in subsequent MART iterations (Atkinson and Soria 2009).

## 4.8 Effective volume for MTE

The efficiency of the MTE procedure in reducing the *ghost intensity* depends upon the particle motion field. It can be easily verified, for instance, that the ghost-particles field produced by particles at rest cannot be reduced by the MTE approach, because the *ghost particles* move coherently with the actual particles. The same applies for particles traveling with exactly the same velocity. As discussed in section 4.4.1, only the incoherent intensity can be reduced in the process of evaluating the enhanced guess.

A *ghost pair* occurs when the relative displacement between the particles producing the *ghost*, varies by less than a particle image diameter  $d_r^*$  in the direction normal to the viewing one. A model to estimate the number of recurring *ghost particles* (e.g. *ghost pairs*) in subsequent exposures,  $N_g^*$ , was formulated by Elsinga et al. (2011); the ratio between  $N_g^*$  and the total number of *ghosts* is found to be proportional to  $\Delta Z^*/\Delta Z$ , where  $\Delta Z$  is the reconstructed volume thickness and  $\Delta Z^*$  is the fraction of depth along which the particles displacement varies less than  $d_r^*$ .

Here the approach is generalized for the purpose of defining a theoretical efficiency for the MTE technique. The volume  $V^*$  is the portion of the total volume  $V$  producing coherent *ghost intensity*. The complementary volume will be that effective for MTE,  $V_{eff}=V-V^*$ . The ratio  $V_{eff}/V$  provides an estimate of the MTE efficiency  $\eta_{MTE}$ . The numerical simulation shown in section 4.5 may be regarded as a case with  $\eta_{MTE}\sim 1$  because the planar shear divides the measurement volume into slices of negligible thickness with respect to the that of the overall volume.

As a result, the application of MTE in the above conditions corresponds to a virtual multiplication of the number of viewing cameras  $N_C$  by the number of considered exposures  $N_O$  and yielding a system with  $N_O \cdot N_C$  virtual views.

For experiments conducted at values of  $\eta_{MTE}$  below 1, the favorable effect of MTE is reduced. A theoretical estimate is given for the quality factor achievable with MTE, that takes into account the effective volume. For a given number of exposures  $N_O$ , the reconstruction quality obtained with  $N_C$  cameras  $Q_{MART}^{N_C}$  can be enhanced with MTE to  $Q_{MTE}^{N_C}$  according to the expected efficiency as follows:

$$Q_{MTE}^{N_C} = Q_{MART}^{N_C} + \eta_{MTE} \cdot (Q_{MART}^{N_O \cdot N_C} - Q_{MART}^{N_C}) \quad 4.10$$

One may easily verify from equation 4.10 that, when  $\eta_{MTE} \rightarrow 1$  then  $Q_{MTE}^{N_C} \rightarrow Q_{MART}^{N_O \cdot N_C}$ , yielding the previously mentioned virtual camera multiplication effect. For the experimental conditions produced in section 4.9, when MTE is applied with 2 or more exposures, the

value of  $Q_{MART}^{N_o \cdot N_c}$  is very close to 1, which simplifies the evaluation of the relative reconstruction quality in the remainder.

The above discussion is conducted under the simplifying hypothesis that the efficiency is a constant parameter only depending upon the flow field. In principle, the efficiency will also depend upon the number of exposures  $N_o$ , whereby the integral effect of the particles motion causes the ghost pairs to lose coherence, which should further increase the value of the efficiency.

## 4.9 Experimental assessment of MTE

Two time-resolved experiments are conducted on turbulent shear flows in water and air flows. The PIV apparatus is based on a Quantronix Darwin-Duo Nd:YLF laser ( $2 \times 25 \text{ mJ/pulse@1 kHz}$ ) and four Photron Fastcam SA1 CMOS cameras ( $1024 \times 1024 \text{ pixels}$ ,  $5,400 \text{ fps}$ ) equipped with Nikon objectives ( $f=105 \text{ mm}$ ). Details on the jet experiments are reported by Violato and Scarano (2011) whereas the trailing edge boundary layer experiment is described in Ghaemi and Scarano (2012). In both cases the system is operated in single-frame continuous mode to record time-resolved series. The synchronization, acquisition and tomographic data analysis is performed by LaVision DaVis 7.2 software on a PC equipped with INTEL dual quad-core 2.66 GHz CPU and 3GB RAM memory.

### 4.9.1 Time-resolved measurements of a transitional jet

The flow is seeded with  $56 \mu\text{m}$  polyamide particles at a concentration of approximately  $0.7 \text{ particles/mm}^3$ . The jet exit diameter is 10 mm and the exit velocity is 0.45 m/s. A cylindrical volume of 30 mm diameter is illuminated from above the jet exit, Figure 4.16-left.

The cameras objectives are set at  $f_{\#}=32$  to obtain focused particle images along the entire depth of the illuminated volume. An optical magnification  $M=0.4$  yields a field of view of approximately  $50 \times 50 \text{ mm}^2$  and a digital resolution of 20 pixels/mm. The measurement domain extends from the jet exit up to 5 diameters downstream. The system records sequences at 1,000 Hz. The raw images (Figure 4.16-top-right) are processed subtracting the background intensity (estimated with local minimum over a spatial kernel of  $31 \times 31$  pixels) and then the peak intensity is normalized taking the local maximum over  $5 \times 5$  pixels regions. As a result a background-free image is produced with rather uniform peak intensity for the particle images, Figure 4.16-bottom-right.

The performance of the reconstruction algorithm, and therefore of the MTE technique, strongly depends on the image source density  $N_s$ . The latter can be obtained evaluating the number of particles per pixel ( $ppp$ ) and estimating the area covered by each particle image.

The particles image density is estimated by means of the slit-illumination method (see section 3.2.2) as  $ppp=0.05$ ; given the particle imaged diameter  $d_r^*=3$  pixels, the resulting source density  $N_s$  is approximately 0.3.

Time-resolved measurement by four-cameras shows that the displacement measured in potential flow regions yields a noise level of approximately 0.15 voxels (2% of the displacement at the jet exit), Violato and Scarano (2011). The jet flow undergoes first a Kelvin-Helmholtz like instability with the formation of vortex rings, which subsequently pair (leap-frogging). Further away from the exit ( $Y/D > 4$ ), the transition to the 3D regime is

observed first with azimuthal wiggles in the vortex rings and then with the formation of vortex filaments inclined with respect to the jet axis.

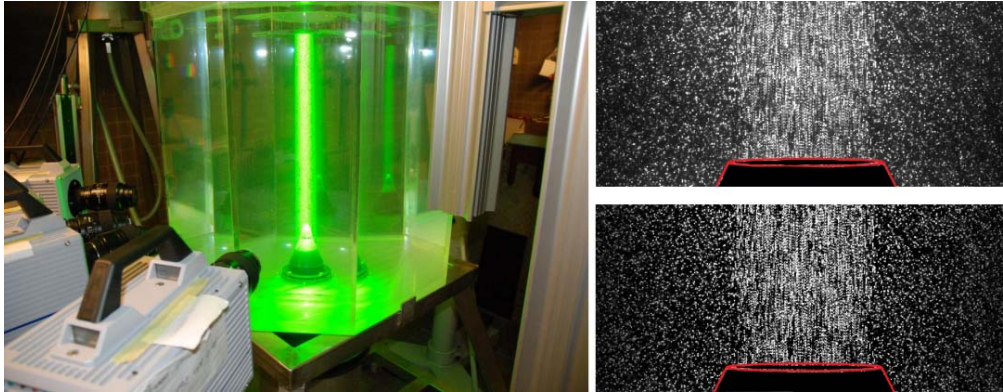


Figure 4.16 Left: Jet tomography facility. Right: 5-exposure image of tomographic recordings above the jet exit (in red); (top: raw image, bottom: pre-processed).

The red box in Figure 4.17-left shows the region of flow considered for the present analysis; the reconstructed region extends over  $501 \times 301 \times 392$  voxels. A large region of stagnant flow surrounds the jet core (Figure 4.17-right); as a result, the *ghost particles* produced by the quiescent particles in the region  $V^* = 0.6 \cdot V$  will not be eliminated by MTE. The resulting MTE efficiency is estimated as  $\eta_{MTE} = 0.4$ .

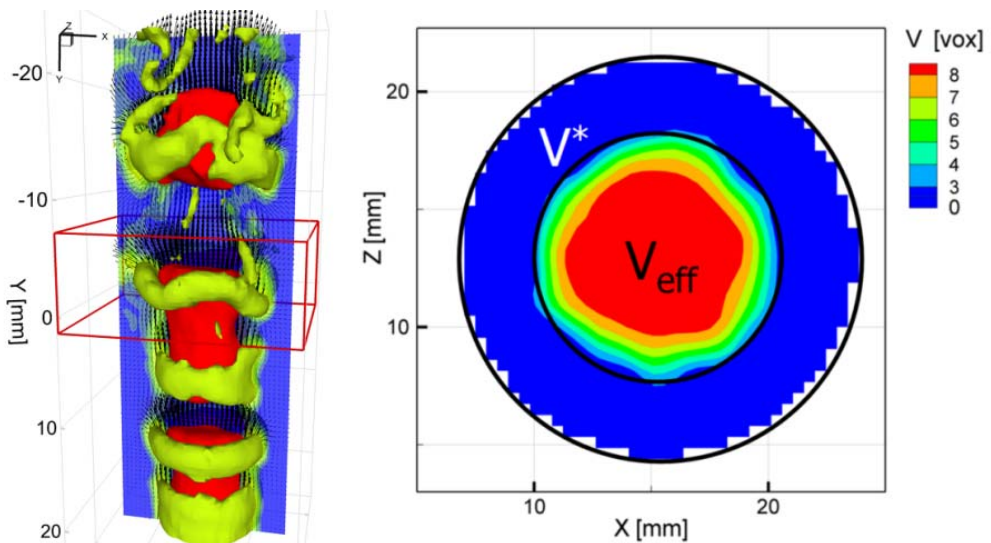


Figure 4.17 Left: jet flow, instantaneous vorticity magnitude (0.2 1/s, green) and vertical velocity (0.35 m/s, red) iso-surfaces. Velocity vectors and vorticity magnitude contours on axial data slice. Right: iso-contours of axial velocity and indication of ghost pairs-producing volume  $V^*$  (top view).

### Quality of tomographic reconstruction

For the present source density, given the absence of important optical aberrations, the good image contrast and the application of Volume Self-calibration (Wieneke 2008), the tomographic reconstruction by MART using 4 cameras provides an accurate estimate of the intensity fields, with an expected quality factor indicated by numerical simulations as beyond 0.9. If the number of cameras is reduced to three, numerical simulations indicate that the tomographic system should reach nearly the same performances of the 4-cameras system when MTE is applied.

Therefore, the result obtained with 4 cameras is taken as reference ( $E_{ref}$ ) for comparison with that produced by the 3-cameras ( $E_{rec}$ ) system with and without MTE. For such purpose a relative quality factor  $Q^*$  (see section 3.3.2) is introduced in this study as follows:

$$Q^* = \frac{\sum E_{ref} \cdot E_{rec}}{\sqrt{\sum E_{ref}^2 \cdot \sum E_{rec}^2}} \quad 4.11$$

Figure 4.18-left presents the evolution of the relative quality factor with the MART updates; double-frame and multi-frame modes have been considered here. Five MART iterations are used at the beginning of the reconstruction process; then, for each MTE step, a single MART update is applied.

The improvement is more pronounced when more than 2 frames are considered. The result from  $N_O=3$  clearly departs from the two frames case and increasing the number of frames to 5 yields a marginal improvement, indicating that an asymptotic condition for  $N_O$  may have been reached. The results reach the value  $Q^* \approx 0.83$ , which indicates the maximum theoretical value to be expected on the basis of the estimated MTE efficiency, equation 4.10. A 5% uncertainty on the maximum expected value of  $Q^*$  has been included, taking into account the uncertainty in the estimate of the effective volume for MTE.

The improvement of the reconstruction quality can also be estimated without knowledge of a reference distribution, making use of the normalized intensity variance  $\sigma_E^* = \sqrt{E'^2} / \bar{E}$  (see section 3.3.3). The result is shown for MART and MTE-MART in Figure 4.18-right;  $\sigma_E^*$  follows the same qualitative behavior of  $Q^*$  along the updates, indicating the overall improvement of the reconstructed field. Higher values of  $\sigma_E^*$  indicate that the reconstructed particle intensity field will be more sparse and intensity peaks of higher amplitude emerge from the background intensity.

The numerical simulations showed that the main reason for the improved quality of reconstruction is the transfer of intensity from the *ghosts* to actual particles. This occurs because a *ghost particle* forms at the intersection of lines of sight which correspond to non-zero pixels. Therefore, the pixel intensity, which is the result of the projected actual particle intensity, is distributed among the actual and the *ghost particle* during the back-projection operation which is at the base of the MART algorithm. If the *ghost intensity* is diminished by MTE, the energy is redistributed towards the actual particle positions.

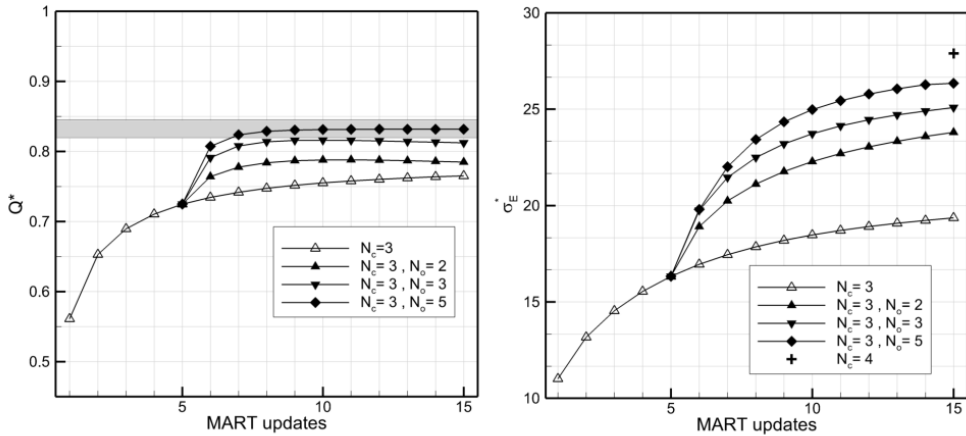


Figure 4.18 Left: relative quality factor with 3 cameras for MART and MTE-MART ( $N_o=\{2,3,5\}$ ). Grey region indicating maximum  $Q^*$  expected by MTE for the given efficiency. Right: normalized intensity variance of the reconstructed field for MART and MTE-MART.

This behavior is qualitatively verified in the experiments observing the reconstructed field in time, which produces particle dots distributed along physical trajectories. A portion inside the jet core is considered, with particles moving uniformly along straight lines and being detected at regular spatial intervals.

Figure 4.19 shows the intensity field reconstructed using MART and 4 cameras with 5 exposures color coded by time; several sequences are easily recognized (red to blue). Eliminating one camera some particles disappear between subsequent exposures and then appear again.

This behavior is ascribed to the more frequent occurrence (with respect to the 4-camera system) of *ghost particles* which subtract intensity from those actual particles lying along the same line of sight. The reconstruction with the MTE technique exhibits a more regular distribution of the particle intensity along the sequence. This specific improvement suggests the possible use of MTE also to improve the reliability of particle motion analysis by PTV techniques (e.g. Schröder et al. 2008a).

### Cross-correlation analysis

Results from three-dimensional cross-correlation are presented in Figure 4.20; velocity vectors and contours of axial velocity are showed together with iso-surfaces of  $Q$ -criterion (Hunt et al. 1988). Cross-correlation analysis is performed by Volume Deformation Iterative Multigrid Technique (VODIM) with a final interrogation volume of  $40 \times 40 \times 40$  voxels with 75% overlap, which gives a vector pitch of 0.5 mm. The same correlation settings have been used for each MTE iteration, including the first estimate of the velocity field. Vector validation based on the universal median test (Westerweel and Scarano 2005) is applied after each interrogation with an outlier detection rate of approximately 1.5%. The reference velocity field is obtained by sliding average of multiple correlation maps (SAC, see section 2.3.3).

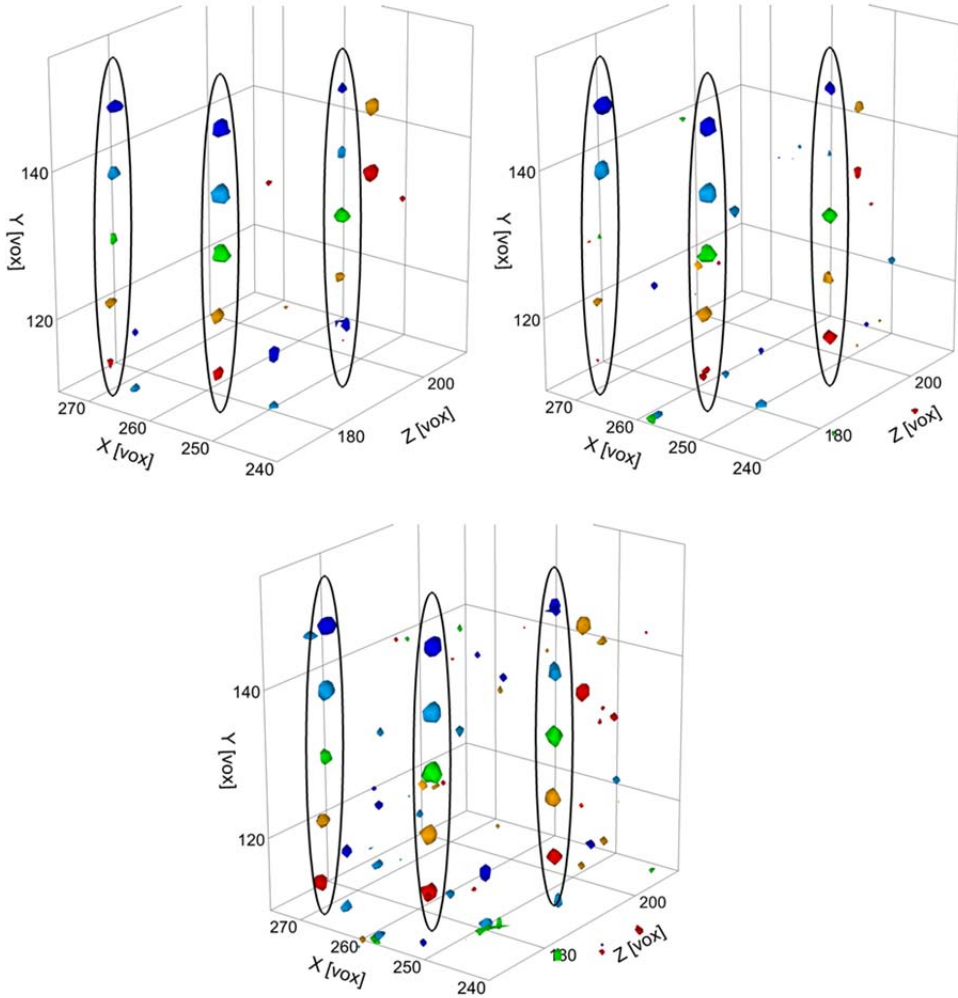


Figure 4.19 Iso-surface of reconstructed intensity field (70 counts) in the center of the reconstructed region (jet core). Result from 5 MART updates with 4 cameras (top-left), 3 cameras (top-right) and 3 cameras with 10 steps of MTE  $N_O=2$  (bottom). Particles color relative to time instant ( $t_1$  red,  $t_5$  blue, time separation of 1 ms).

The method makes use of four subsequent objects (three object-pairs) and produces averaged cross-correlation signals that significantly reduce random correlation errors. The flow time scale of the present experiment is approximately 30 ms and no amplitude modulation due to temporal filtering is expected with a kernel spanning 3 ms. When MART is applied with 3 cameras, the flow pattern closely resembles that obtained at  $N_C=4$ . Nevertheless, the vortex visualized by the iso-surface of  $Q$ -criterion reveals a slightly higher noise level. The application of MTE appears less affected by irregularities indicating some degree of noise reduction.

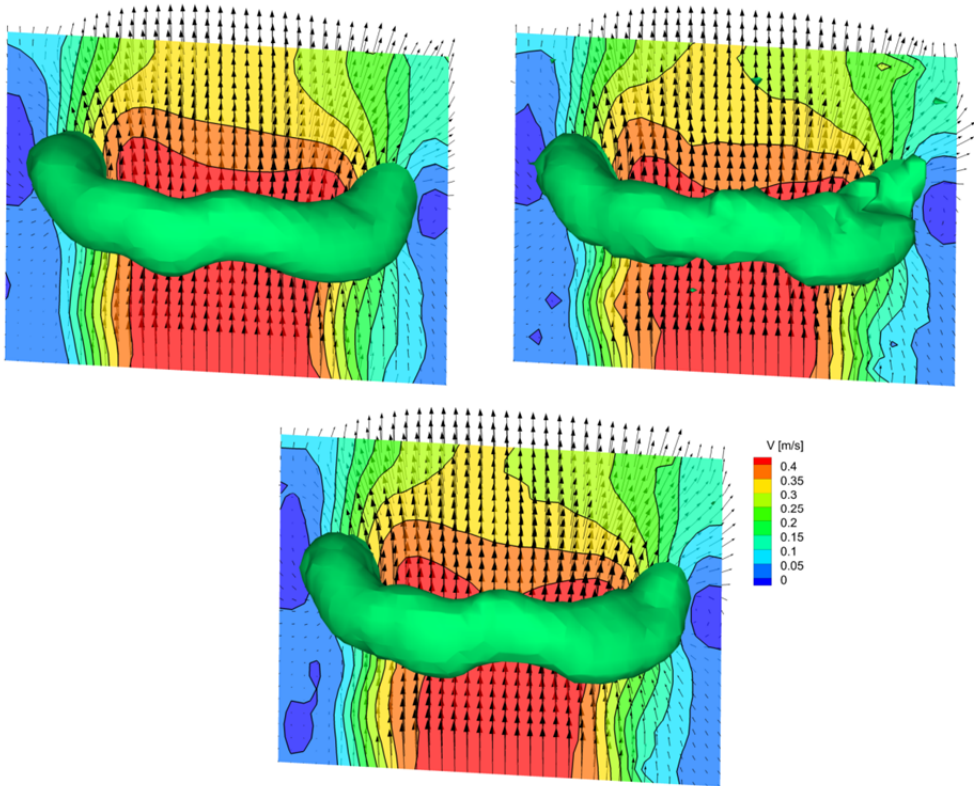


Figure 4.20 Detail of the jet flow in proximity of a vortex ring. Iso-surface of  $Q$ , velocity vectors and vertical velocity magnitude contours in data slice on the symmetry axis. Top-left: reference velocity field. Top-right:  $N_c=3, N_e=0$ . Bottom:  $N_c=3, N_e=5, N_o=3$ .

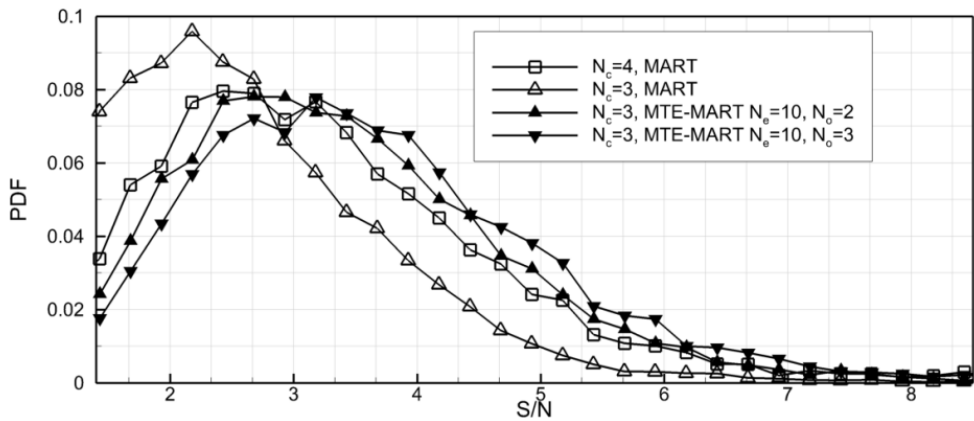


Figure 4.21 Cross-correlation signal-to-noise probability density function for MART and MTE-MART.

	$(U - U_{ref})_{RMS}$ [vox]	$(V - V_{ref})_{RMS}$ [vox]	$(W - W_{ref})_{RMS}$ [vox]
MART $N_C=4$	0.17	0.2	0.18
MART $N_C=3$	0.22	0.27	0.23
MTE-MART $N_C=3, N_O=2$	0.19	0.23	0.19
MTE-MART $N_C=3, N_O=3$	0.18	0.22	0.18

Table 4.1 Root mean square of the relative velocity error to the reference (SAC) for MART with 3 and 4 cameras and MTE-MART ( $N_E = 5$ ) with 3 cameras.

A more marked difference is visible in terms of correlation signal-to-noise ratio, Figure 4.21. The introduction of MTE yields a generally higher value of correlation signal-to-noise ratio, indicating a more robust estimate of the reconstructed particles velocity. Moving from 4 cameras to three introduces a general drop of  $S/N$  with the maximum shifting from 2.5 towards 2. A three-camera system appears to yield already  $S/N$  of 2.5 with two objects, which is equivalent to four cameras. Using a triplet objects outperforms the four cameras system, with  $S/N$  above 3.

The velocity precision error is estimated by the root mean square of the relative difference to the reference data (SAC analysis); results are summarized in Table 4.1.

The error is reduced by about 15% when 5 steps of MTE are applied in double-frame mode; the reduction is slightly larger (approximately 20%) when 3 exposures are considered. Results are confirmed by the visual inspection of the time-history of the velocity components in a single point in the jet shear-layer, where the discrepancy between the reference case and the 3 cameras case is reduced by the application of MTE, Figure 4.22.

It should be kept in mind that the error in this case is also due to finite number of particle in the interrogation volume and does not only depend upon the spurious reconstruction. Moreover, the low value of  $V^*$  limits the MTE efficiency for the jet flow configuration, therefore marginal improvements are expected. The reconstruction from the 3-camera system is already rather close to that with 4 cameras for the present seeding density. As a consequence, the velocity measurement error becomes dominated by the cross-correlation analysis rather than by artifacts introduced in the reconstruction. Nevertheless, it is proven that the trend is consistent with that of the numerical simulations and in this case MTE does bring some measurable increase of measurement accuracy.

In order to further investigate the effect of MTE on the jet velocity field, the technique is applied to a reconstruction making use of only 2 cameras which significantly affects the accuracy of the measurement. The divergence field is chosen as a quality indicator for the velocity vectors and it is shown in Figure 4.23 for the MART and MTE-MART reconstruction ( $N_C=2$ ).

If compared to the results presented above, a 2 camera system proves to be insufficient to accurately describe the flow field even after MTE is applied. Nevertheless a clear indication about the improvement in the velocity field accuracy is given by the reduction of the divergence value, particularly in the region of the vortex-ring.

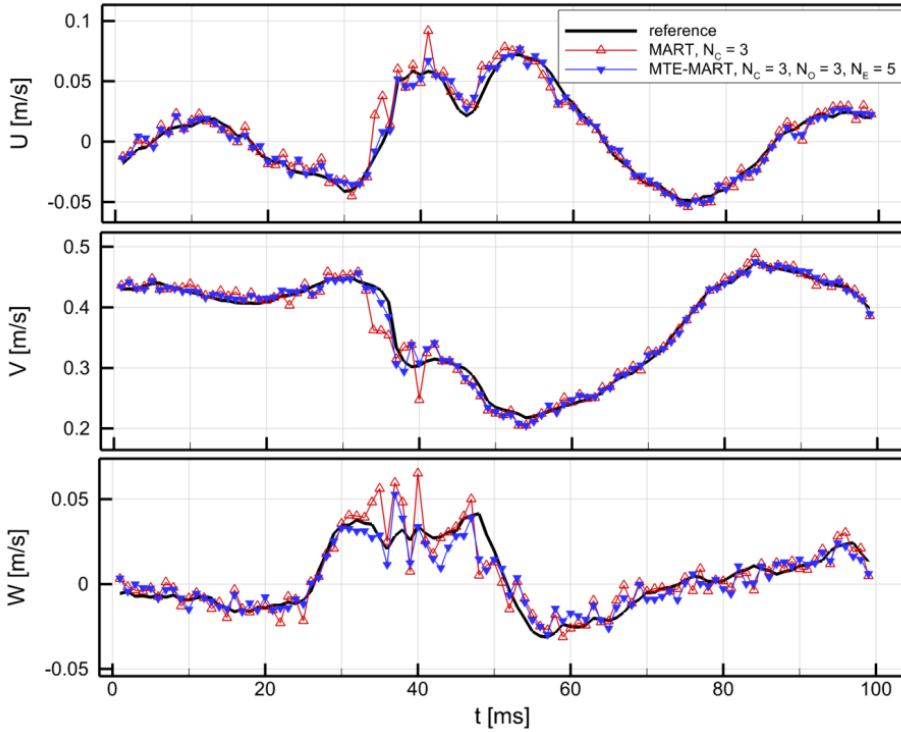


Figure 4.22 Time-history of the velocity components along 100 exposures in one point in the jet shear layer.

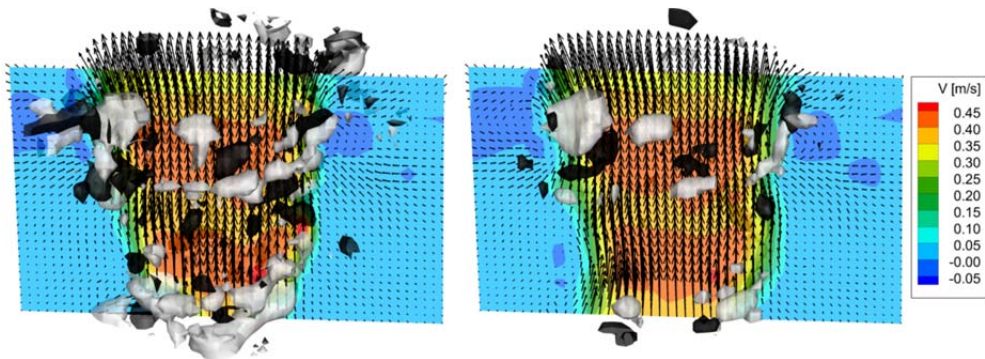


Figure 4.23 Iso-surfaces of divergence in proximity of a vortex-ring (0.1 1/s white and -0.1 1/s black). Contours of axial velocity in a plane across the jet core. Left: reconstruction by MART with 2 cameras. Right: result from MTE-MART with 2 cameras ( $N_E=5, N_O=2$ ).

#### 4.9.2 Turbulent boundary layer

The experiment is performed in a low-speed wind tunnel where a NACA-0012 airfoil of 40 cm chord is installed at zero angle of attack. The free-stream velocity is 14 m/s and the  $Re_c$  is

370,000 (being  $c$  the chord of the airfoil). Light amplification is provided by the use of mirrors reflecting the beam multiple times forming an extended illuminated domain, Figure 4.24-left (Ghaemi and Scarano 2011). The depth of the illuminated volume is 8 mm. The imaging system is set with numerical aperture  $f_{\#}=22$ . In the chosen reference system  $Z$  indicates the direction normal to the airfoil surface ( $Z=0$  mm),  $X$  and  $Y$  are aligned with the streamwise and spanwise directions respectively. The field of view is approximately  $40\times 25$  mm<sup>2</sup> in the streamwise and spanwise direction respectively and it is located at the trailing edge of the airfoil. The digital resolution is 20 pixels/mm and the acquisition frequency is 12 kHz.

A fog generator produces droplets of 1  $\mu\text{m}$  diameter; given the present imaging conditions, the observed particle image diameter  $d_r^*$  is 2 pixels. Two experiments are conducted at different seeding density; the first one with approximately 3 particles/mm<sup>3</sup>, corresponding to a  $ppp$  of 0.05 (example of recorded image in Figure 4.24-middle-top) while the second is well beyond this value, Figure 4.24-middle-bottom.

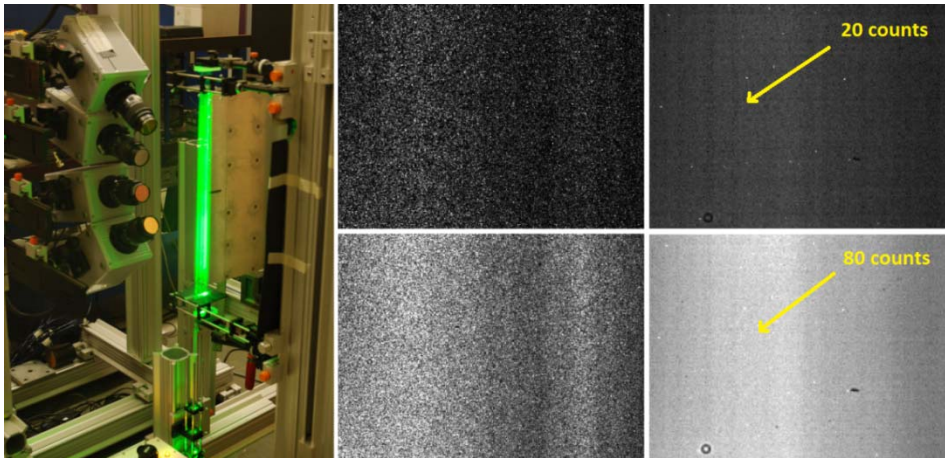


Figure 4.24 Left: Tomographic PIV setup. Top-middle: detail of Tomo-PIV image for the boundary layer experiment at  $ppp=0.05$ . Bottom-middle: image at  $ppp=0.2$ . Top-right: mean imaged intensity over 200 images at  $ppp=0.05$ . Bottom-right: mean imaged intensity over 200 images at  $ppp=0.2$ .

Due to the high particles overlap probability for the highly seeded case, the seeding density can be obtained by detection of imaged particles for the first experiment. For the latter case, the  $ppp$  is estimated by means of the method based on the average image intensity presented in section 3.2.3. The average intensity of the latter experiment, computed over 200 recordings, is approximately 4 times higher than the first one (80 and 20 counts respectively), which leads to a  $ppp$  of 0.2 (12 particles/mm<sup>3</sup>), Figure 4.24-right.

The source density  $N_S$  is 0.15 and 0.6 for the low and high density case respectively. As previously discussed, the latter condition is recognized as beyond optimum for a tomographic system with 4 cameras.

Figure 4.24-middle shows pre-processed images at  $ppp=0.05$  and raw images at 0.2, where pre-processing is not performed because the background intensity cannot be separated from the signal produced by the actual particles.

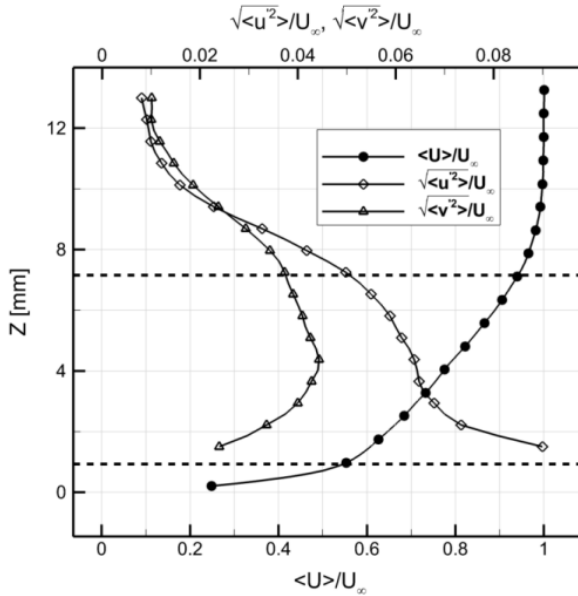


Figure 4.25 boundary layer mean streamwise velocity component and fluctuating velocity profiles. Data obtained from two-components PIV (Ghaemi and Scarano 2011); dotted lines indicate the measurement domain for the Tomo-PIV experiment.

The domain is discretized into  $890 \times 550 \times 200$  voxels and reconstructed using 5 MART iterations for both the seeding densities; motion tracking enhancement is applied making use of 10 steps and 2 MART iterations are used for each enhancement step. The effective volume  $V_{eff}$  is estimated to be above 90% of the total ( $\eta_{MTE} > 0.9$ ); as shown in

Figure 4.25, the investigated domain is in fact completely within the turbulent boundary layer ( $\delta_{99} = 9.5$  mm). The cross-correlation analysis applies multi-grid with final interrogation volume of  $24 \times 24 \times 24$  voxels ( $1.2 \times 1.2 \times 1.2$  mm<sup>3</sup>). With 75% overlap factor the vector pitch is 0.27 mm. For the given block size and particle concentration, the analysis counts on average 4 and 15 particles within the interrogation box for the low and high seeding respectively. The same correlation settings and validation by universal median test (Westerweel and Scarano 2005) used for the final interrogation analysis have been used for the velocity field estimate at each intermediate MTE iterations.

The instantaneous velocity field (raw velocity vectors) is shown in Figure 4.26-left on a data slice 2.6 mm above the airfoil surface. A uniform velocity (80% of the free-stream) is subtracted to highlight the pattern of local fluctuations. Contours of the wall-normal component of vorticity are displayed in the background. The flow pattern returned by the low density experiment reveals alternating low and high speed regions; counter-rotating swirling patterns identified in the velocity vector field suggest the presence of hairpin vortices, Figure 4.26-top-left.

The number of particle tracers present in each interrogation volume appears to be sometimes insufficient for the given seeding concentration, which is revealed by a blocky pattern with rather constant velocity due to the combined effect of signal loss and the overlap factor between neighboring volumes (oversampling). The distribution of cross-correlation signal-to-noise ratio below 1.5 by more than 50% of the measurement domain, confirms indirectly the above observation, Figure 4.26-top-right.

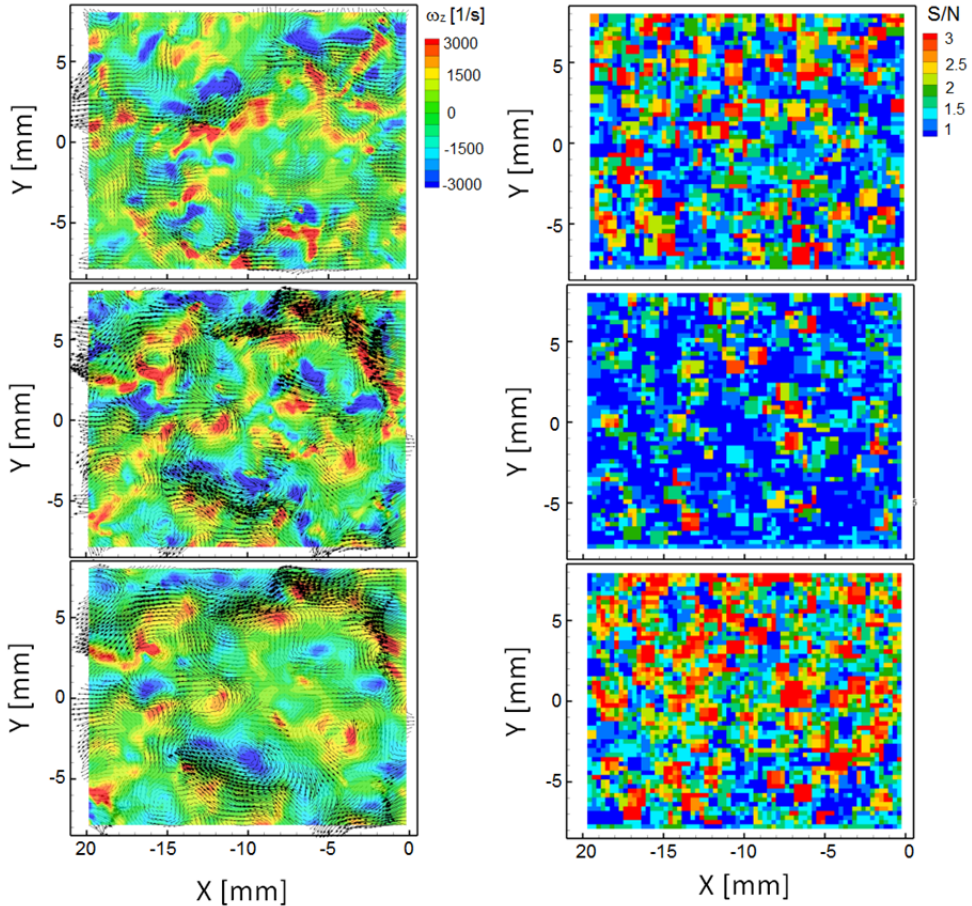


Figure 4.26 Detail of turbulent boundary layer at  $Z=2.6$  mm. Left: relative velocity vectors and  $z$ -vorticity contours. Right:  $S/N$ . Top:  $ppp=0.05$ , MART. Middle:  $ppp=0.2$ , MART. Bottom:  $ppp=0.2$ , MTE-MART,  $N_E=10$ ,  $N_O=2$ .

When the experiment is performed at higher seeding density, the results based on MART reconstruction, Figure 4.26-middle, yield a similar flow arrangement but a higher level of spurious fluctuations is evident from the vorticity peaks and from groups of vectors clearly out-of-pattern. The signal-to-noise drops further and is close to 1 nearly everywhere, indicating that the correlation signal is largely affected by reconstruction noise. These conditions would typically be avoided for a Tomo-PIV experiment designed upon the MART reconstruction technique.

The Motion Tracking Enhancement is applied to the same recordings making use of 2 exposures by 10 steps resulting in the velocity field and correlation  $S/N$  are shown in Figure 4.26-bottom. A significant increase of the correlation signal (typically a factor 2 with respect to the MART analysis) indicates that *ghosts* are largely reduced ( $S/N > 1.5$  in more than 60% of the measurement volume) resulting in a more robust estimate of the particles motion. Also the measurement accuracy appears increased, with a more coherent velocity and vorticity fields.

A quantitative assessment of the measurement accuracy is made invoking the physical principle that velocity fluctuations are convected by the flow and their typical evolution time is significantly longer than the measurement inter-framing time ( $\Delta T = 83.3 \mu s$ ). Assuming Taylor's hypothesis of frozen turbulence to be valid within such inter-framing time we can obtain an indication of the measurement precision error from the analysis of the spatio-temporal correlation function peak height (see section 3.4.3). Cenedese and Romano (1991) investigated the validity of this assumption in a highly turbulent flow with the general conclusion that the hypothesis holds valid for large flow structures and small time separation. Following Tennekes (1975), the Lagrangian de-correlation time scale of turbulent fluctuations for isotropic turbulence is estimated around 10 ms for the present case, which is two orders of magnitude longer than  $\Delta T$ . As a consequence, no significant loss of correlation is expected between subsequent velocity fields along a time series for more than 10 exposures.

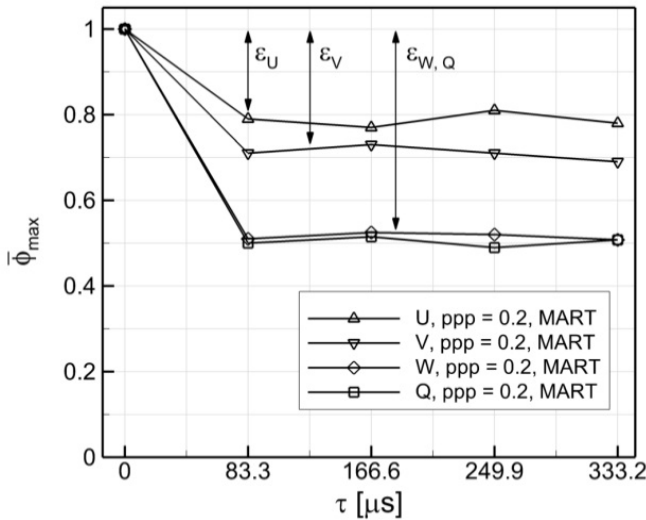


Figure 4.27 Mean correlation peak height ( $\bar{\Phi}_{max}$ ) and mean indicator ( $\bar{\epsilon}$ ) of the precision error as a function of the time delay between exposures (for the velocity components and the  $Q$  criterion).

The space-time correlation function  $\Phi$  is evaluated for each of the velocity components, equation 3.18. The displacement of the turbulent structures between two subsequent realizations is also accounted for applying a relative shift between interrogation boxes in the streamwise direction based on the estimated convective velocity (11.2 m/s). The height of the

correlation peak, indicated by  $\Phi_{max}$ , is obtained as the maximum of the correlation function. Under these hypotheses the height of the correlation peak is expected to maintain unit value, except for the uncorrelated component of the signal  $\varepsilon \propto (1 - \overline{\Phi_{max}})$ , which is then ascribed to the measurement precision error, where  $\overline{\Phi_{max}}$  is the average value of the correlation map peak.

The mean value of the correlation peak height  $\overline{\Phi_{max}}$  is evaluated for several values of the time delay between measurements  $\tau$  (equation 3.18), also to verify the validity of frozen turbulence, Figure 4.27. After dropping from unit value (by definition in the origin) to the value of the first sample at  $\tau=83.3 \mu s$ , the correlation height remains practically constant up to separations beyond 1 ms. This confirms that the loss of coherence is dominated by uncorrelated noise affecting the velocity field measurement rather than by the evolution of the flow. Therefore the difference between results obtained at low and high seeding density are only ascribed to measurement precision errors.

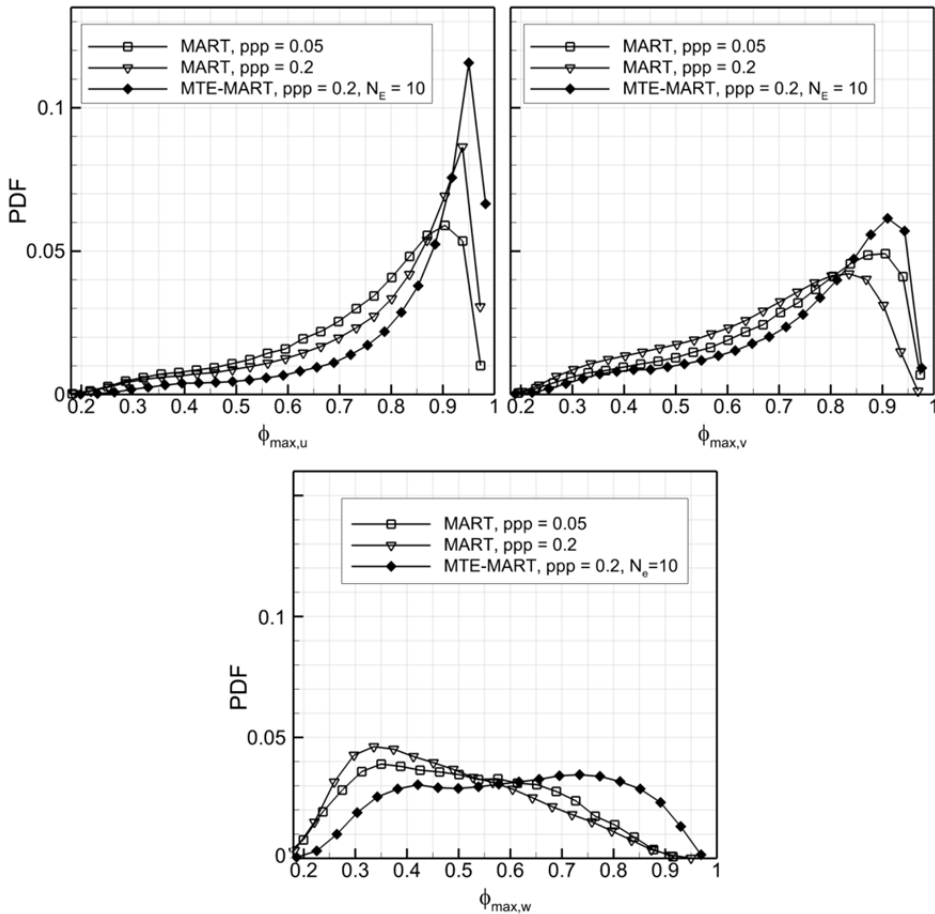


Figure 4.28 Probability density function of the peak value of the space-time correlation map between two subsequent velocity fields.

The probability density function (PDF) of the correlation peak height reveals that the measurements performed at low seeding density are weaker than that at high-density when analyzed with MTE-MART, Figure 4.28. By coincidence the PDF of the low density case appears to be similar to that at  $ppp=0.2$  when only MART is applied, which is ascribed to a combination of effects. In the low seeding case, too few particles are included in the interrogation boxes and the error is dominated by the cross-correlation noise. In the high-seeding case, the information density is higher; but the ghost component affects the result more widely. The streamwise velocity component fluctuations exhibit the highest correlation, Figure 4.28-top-left.

In contrast, the spanwise component shows a less pronounced peak at 0.95 for the MTE analysis and below 0.9 and 0.8 or the MART analysis of the high and low seeded case respectively. The most critical component is  $W$ , showing a flat distribution, because of the combined effect of its relatively small range of fluctuations (approximately 2 voxels) and the larger absolute uncertainty resulting from the geometry of the tomographic system.

$\overline{\phi}_{\max}$	$ppp=0.2$		$ppp=0.05$		
	MART $IV=24^3$ vox	MTE-MART $IV=24^3$ vox	MART $IV=24^3$ vox	MTE-MART $IV=24^3$ vox	MART $IV=32^3$ vox
$U$	0.79	0.87	0.74	0.76	0.85
$V$	0.71	0.76	0.66	0.67	0.77
$W$	0.51	0.62	0.55	0.55	0.62
$\omega_x$	0.53	0.61	0.55	0.56	0.67
$\omega_y$	0.53	0.61	0.5	0.5	0.64
$\omega_z$	0.72	0.78	0.7	0.72	0.84
$Q$	0.5	0.57	0.47	0.48	0.6

Table 4.2 Spatial mean of the cross-correlation function peak value ( $\overline{\phi}_{\max}$ ) for MART and MTE-MART ( $N_E=10$ ,  $N_O=2$ ) at  $ppp=0.05$  and  $0.2$  for velocity components, vorticity components and  $Q$  criterion.

In conclusion, the MTE analysis of the high-seeding case appears to offer a significant increase of the space-time correlation peak height. The estimated reduction of the precision error is approximately 40% for the streamwise component and somewhat less for  $V$  and  $W$ . Instead, at  $ppp=0.05$  only a marginal improvement is obtained, which is consistent with the above discussion. To make a fair comparison between the low and high seeding density cases, the interrogation volume is increased by more than a factor two (interrogation box of  $32^3$  voxels), which brings the average number of particles per interrogation box up to 9. This condition guarantees a more robust correlation analysis at the cost of a lowered spatial resolution. In this case, the analysis performed with MART yields results that approaches that of MTE-MART obtained with an interrogation of  $24^3$  voxels. Results regarding the mean value of the correlation peak are summarized in Table 4.2.

Time resolved Tomo-PIV is often used to visualize the temporal evolution of turbulent structures in the boundary layer (Schröder et al. 2008b; Elsinga et al. 2008). In the present

case a low-speed region and a single hairpin vortex are selected and tracked in time. A qualitative inspection of the time series at high seeding density is shown in Figure 4.29.

The evolution of a low speed streak, detected by means of iso-surface of streamwise velocity ( $U=10$  m/s), along 4 subsequent exposures is presented together with iso-surfaces of  $w$  component which indicate the ejection events distributed above the streak. As indicated by the spatio-temporal correlation analysis, the result obtained by MTE, Figure 4.29-right, shows a reduction in measurement noise and an increased temporal coherence.

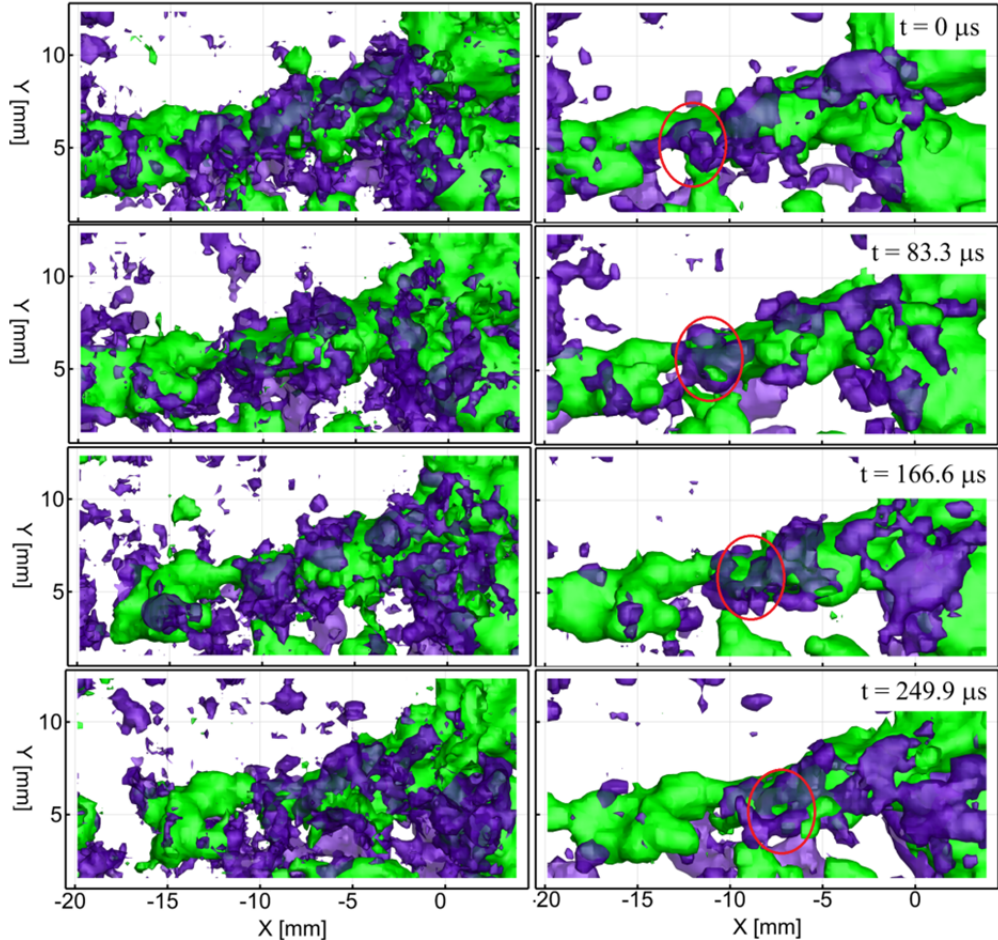


Figure 4.29 Evolution of a low-speed streak along 4 subsequent time-instants for MART (left) and MTE-MART (right). Iso-surface of streamwise velocity ( $U=10$  m/s) in green and of wall-normal component ( $W=1$  m/s) in blue. Red circle indicates the position of the same ejection event in the 4 realizations.

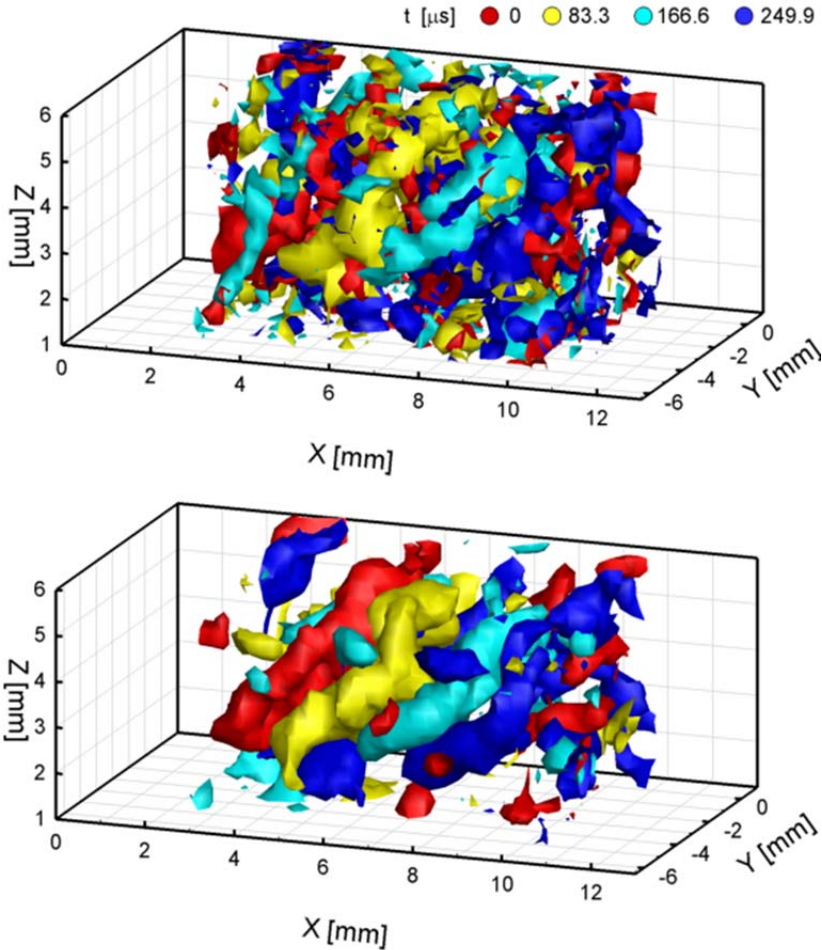


Figure 4.30 A hairpin vortex convected along four exposures (red, yellow, light blue and blue). Iso- $Q$  surfaces for MART (top) and MTE-MART (bottom). Iso-surface of streamwise velocity ( $U=10$  m/s) in green.

The same applies for the vortical structures, Figure 4.30; a detail of the boundary layer is extracted where a hairpin vortex is convected during four snapshots (total observation time 3.3 ms). The result is presented as a sequence of snapshots color-coded in time (red to blue) for clarity. As detection criterion the  $Q$ -criterion iso-surface is chosen. The result obtained with the MART reconstruction shows the hairpin structure, however embedded in a dense noisy pattern hiding several details of the vortex topology. The MTE-MART analysis removes the noisy fluctuations to a large extent and details such as hairpin legs with two different inclination angles become more clear, resulting also in an overall higher temporal coherence. The latter effect is not ascribed to a different spatial resolution of the MTE-MART since the same size of interrogation box is used for the comparison.

## 4.10 Conclusions

A novel technique for the enhancement of the MART reconstruction in Tomo-PIV has been introduced. The theoretical background and working principle of the motion tracking enhancement (MTE) have been discussed and its performances have been assessed by means of two-dimensional simulations of the reconstruction of both double-frame and time-resolved recordings. The accuracy of the reconstruction, evaluated through the quality factor  $Q$ , returned the most significant increase for seeding density approximately three times larger than those reported in literature for double-frame recordings. When time-resolved data are available, the accuracy of the reconstruction appears to further increase in relation to the number of exposures employed. The displacement fields obtained by spatial cross-correlation of reconstructed objects after enhancement have been analyzed showing a decrease of the precision error of approximately three times for double-frame and almost ten times for multiple recordings. The robustness of the MTE algorithm with respect to large errors in the measurement has been verified, with the conclusion that the present approach returns in the worst case a result comparable to simple MART. Instead the potentially faster approach by multiplication of object and pseudo simultaneous objects is extremely sensitive to errors and rapidly degrades the result.

The overall effect of the MTE-MART method is comparable to that of increasing the number of viewing cameras: the asymptotic behavior provides comparable reconstruction accuracy of the one obtained by doubling the number of cameras with MART. According to the current analysis, the MTE technique could enable Tomo-PIV experiments with seeding particles concentration two to three times higher than that currently practiced (50,000 particles/Mpixel) possibly leading to experiments with more than 100,000 particles/Mpixel.

The Motion Tracking Enhancement technique was applied to Tomographic-PIV experiments in turbulent shear flows. For the transitional jet in water the analysis with a 3-camera system is compared to reference results obtained with an additional camera. The application of MTE increases the relative quality of reconstruction as a function of the number of exposures used in the enhancement process. The concept of MTE efficiency has been also introduced along with a model to predict the reconstruction performance increase from MTE. The experimental verification yields an increase nearly reaching the theoretical prediction and the precision error is decreased of about 20%.

In the air flow experiment of turbulent boundary layer a seeding density of approximately 4 times higher than currently practiced ( $ppp=0.2$ ) is obtained. Results show that MTE largely improves the robustness of the measurement increasing the cross-correlation signal-to-noise from below 1.5 to 3. The height of the spatio-temporal correlation function between subsequent time instants has been taken as an indicator of the accuracy of the measurement. Significant improvements are observed in this case, with 40% reduction of the precision error for the streamwise velocity component and approximately 20% for the other components. Also for derived quantities such as vorticity and vortex detection based on the  $Q$ -criterion, the MTE technique yields more clear description of the topology of coherent structures and their temporal evolution.

Given its iterative structure the MTE technique is computationally more intensive than the data processing currently practiced for Tomo-PIV. Atkinson et al. (2010) presented a method, inspired to the Motion Tracking Enhancement, combined with the Multiplicative

Line of Sight (MLOS, Atkinson and Soria 2009) which allows for a reduction of the computational time required by the enhanced reconstruction of approximately 5 times.

Recently, Discetti et al. (2012) proposed the use of low speed single frame cameras arranged in two separate imaging system to record the first and second Tomo-PIV recordings separately. The aim of the study is to lower the cost of the tomographic PIV setup avoiding the use of expensive high repetition camera. A further advantage of using two imaging system is the fact that, since the *ghost intensity* distribution depends on the relative position between object and cameras, the reconstruction of the two recordings will produce uncorrelated *ghost particles*, independently from the nature of the flow field. In this situation the efficiency of MTE is expected to be close to 1 and its application in principle provides a much higher improvement than for the standard configuration analyzed in the present thesis.

## Chapter 5

# Adaptive 3D correlation

Novara M, Ianiro A and Scarano F (to appear) Adaptive interrogation for 3D-PIV, *Meas. Sci. Technol.*

In this chapter an adaptive correlation approach is proposed for the motion analysis performed by means of cross-correlation of three-dimensional objects reconstructed from Tomo-PIV images. The main steps towards adaptive correlation for planar PIV are presented. Then the unique features of the three-dimensional measurement from Tomo-PIV are discussed and the working principle of the adaptive interrogation method is introduced. The adaptivity criterion is presented and the implementation of the adaptive cross-correlation is discussed. The adaptive interrogation is then applied to numerical generated data and to real experimental data of a transitional jet in water and a turbulent boundary layer in order to assess its performances.

### 5.1 Adaptivity in planar PIV

The spatial resolution of particle image velocimetry has been the subject of many studies since its introduction up to the recent times (Elsinga and Westerweel 2011; Kähler et al. 2012). Particular efforts have been devoted in the last decade to improve the spatial resolution of cross-correlation based interrogation techniques with specific attention to the treatment of regions with large velocity gradients, a situation commonly encountered when dealing with turbulent shear flows. In such regions, the velocity differences between particles belonging to the same interrogation window have a detrimental effect on the correlation peak formation resulting in a drop of the correlation signal-to-noise ratio. The window deformation technique (Huang et al. 1993; Scarano and Riethmuller 2000, Figure 5.1) largely compensates for the effect of the in-plane velocity gradient. However, regions where the scale of fluctuations is comparable to that of the interrogation window still challenge the robustness and the spatial resolution of the velocity measurement.

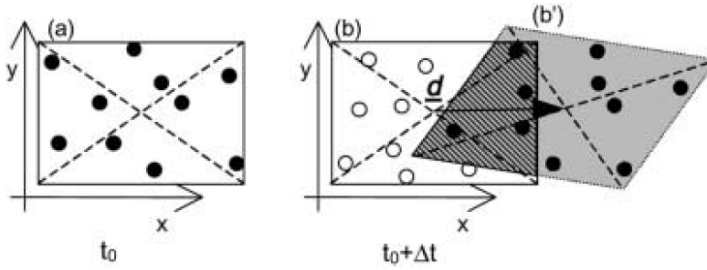


Figure 5.1 Schematic of window deformation for planar PIV; particles follow the mean displacement and the local gradient of displacement (Scarano and Riethmuller 2000).

As a result of early studies, the cross-correlation analysis requires a minimum number of particle image pairs to yield a reliable estimate of the group velocity. Any attempt to reduce this number much below 10 results in a significant loss of correlation signal-to-noise ratio. Working around this limit can be done considering a local adaptation of the window shape, yet maintaining it with a constant area.

The study of Di Florio et al. (2002) proposed elliptical windows elongated along the local direction of the velocity. Although theoretically the windows should be elongated and rotated according to the local curvature of the velocity field to reduce the effect of spatial modulation (Scarano 2003), in the study of Di Florio an improvement could be observed because the velocity difference across the window was minimized.

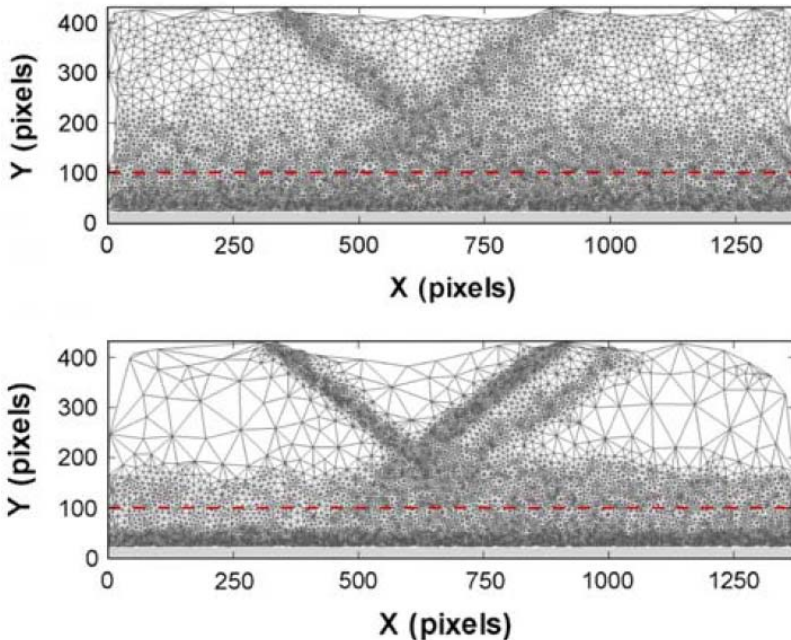


Figure 5.2 Sampling grid of adaptive interrogation based on the flow curvature in a turbulent boundary layer flow investigated by planar PIV. Top: sampling location obtained based on instantaneous adaptivity. Bottom: result from ensemble adaptivity (Theunissen et al. 2010).

Theunissen et al. (2007) initially proposed a more extensive application of window adaptivity to the presence of seeding tracers and to the local flow velocity fluctuations. The conclusion was that adaptation is possible in principle but very few practical examples could demonstrate its advantage in comparison to uniform window size and shape. Instead, the application of window shape adaptivity turned out to be very effective if the adaptivity criterion is based on the mean flow properties (Theunissen et al. 2010), Figure 5.2.

Similarly, Astarita (2009), Figure 5.3, made use of the local signal content and displacement field variations to adapt the shape of the window used in the filtering step of the interrogation algorithm therefore retaining the evaluation of the displacement on a structured grid unlike in the approach followed by Theunissen et al. (2007) where the reduction to structured grid was performed as a post-processing step. The technique was proven to enable higher spatial resolution in the regions of highest velocity gradient. Recently a similar approach was followed by Wieneke and Pfeiffer (2010); the adaptivity criterion was based on the local correlation value and velocity gradient to shape and rotate the correlation windows with the purpose of minimizing the differences of the displacements inside.

It may be concluded with some generality from the above studies that it is possible to achieve a visible improvement of spatial resolution across highly sheared regions. In contrast, when the velocity gradient has no preferred direction such as in case of an axisymmetric vortex, decreasing the size of the interrogation window has the undesired side effect of a lowered robustness due to the reduction of particle image pairs.

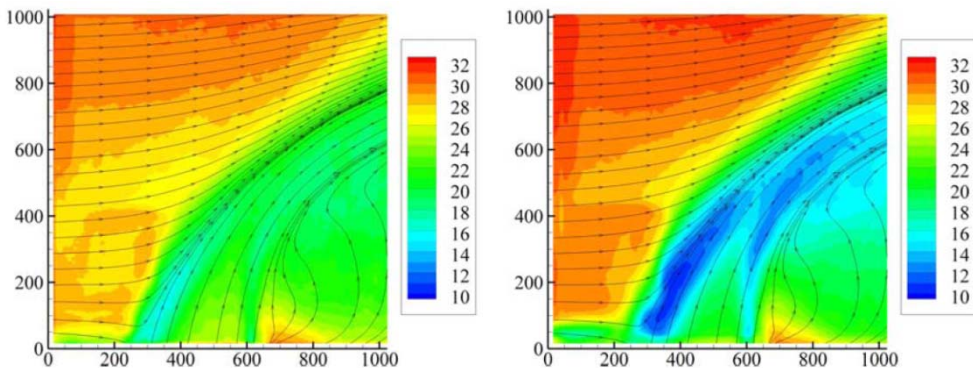


Figure 5.3 Mean streamlines of a jet in cross flow. Contours indicate the mean linear dimension of the region used in the filtering step based on the local seeding density and velocity gradient. Left: interrogation region linear size is 32 pix. Right: cross-correlation window is  $64 \times 64$  pixels (Astarita 2009).

No study is available on this subject that deals with the analysis of three-dimensional (3D) data from techniques such as digital holographic PIV (Coëtmelec et al. 2001), scanning PIV (Brücker 1995) and tomographic PIV (Elsinga et al. 2006). To date, the interrogation technique is commonly based on cross-correlation, making use of volume deformation technique, where the interrogation volumes are typically cubic arrays of voxels. In 3D measurements, the velocity gradient tensor assumes 9 components and three Hessian tensors are introduced to characterize first and second spatial derivatives, with a clear increase of complexity for the choice of window shape and orientation.

The present work examines the potential of applying spatial adaptivity in 3D PIV cross-correlation analysis. The chosen approach is based on a 3D extension of previous concepts for 2D analysis where the square interrogation window was replaced by an elliptical one characterized by two different semi-axes and one orientation angle. For the 3D analysis the interrogation volume becomes an ellipsoid, therefore three semi-axes and three orientation angles need to be determined. The main objective of the adaptation is that of increasing the spatial resolution of 3D PIV interrogation, which is tackled minimizing the particle velocity differences within the interrogation volume. Therefore, the criterion guiding the adaptation is based on the components of the local velocity gradient carried out by means of the singular value decomposition (SVD, Eckart and Young 1939).

## 5.2 Working principle

The behavior of the iterative cross-correlation operator has been often approximated with that of iterative linear filters. Under the hypothesis that particle tracers are homogeneously dispersed in the measurement domain and with sufficiently high concentration such that the particle tracers signal can be considered as continuous in the interrogation box, the spatial resolution does not depend upon the particle concentration, but only on the physical size of the interrogation region. For a single-step analysis, the spatial response of the cross-correlation operator is well approximated by a low-pass filter applied to the displacement field (Willert and Gharib 1991). When the window-deformation technique is applied, the spatial response corresponds to that of an iterative moving average filter with significantly lower spatial modulation effects (Astarita 2007; Schrijer and Scarano 2008), which however requires stabilization to avoid the growth of unstable waves (Nogueira et al. 1999).

A reduction of the window size reduces the modulation of the velocity fluctuation. However, the interrogation region must contain a statistically significant number of pairing particles ( $N_i$ , Adrian 1991), which poses a lower limit for reducing it.

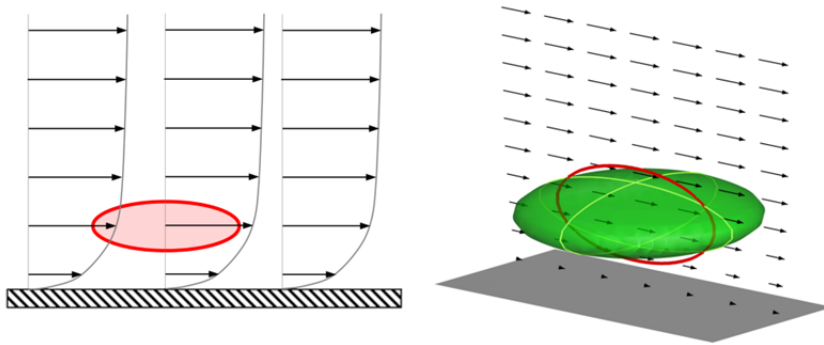


Figure 5.4 Gradient-based adaptation of the interrogation window in a planar shear layer (e.g. laminar boundary layer). Possible adaptation of the interrogation region for a 2D (left) and a 3D PIV measurement (right). The red line in the right figure indicates the adaptive interrogation region in the planar PIV case. A smaller axis of the interrogation volume can be obtained along the wall-normal direction provided that the volume is stretched both in the streamwise and spanwise directions.

The general idea behind local adaptation of the interrogation windows, as discussed by Theunissen et al. (2007), is that, for a given flow topology, directions of minimum and maximum velocity variation exist which can be determined by linearized analysis (velocity gradient tensor). The interrogation region can be shaped in order to take advantage of the non-isotropy of velocity fluctuations. A possible adaptive approach consists in reducing the size of the correlation window along the direction of the largest flow fluctuation, increasing the size in the other directions in order to keep the interrogation volume and the average number of particles constant.

A simple case is that of a planar shear layer such as the boundary layer flow. In a planar PIV measurement the error associated to the large in-plane velocity variation along the wall-normal direction is reduced when the correlation window is stretched along the tangential direction and contracted in the wall-normal direction, Figure 5.4-left. Compared to planar measurements, three-dimensional data offer a larger margin of adaptation because the window can be stretched along two coordinate directions and thinned even further along the wall-normal direction featuring a coin-like shape and maintaining the same volume, Figure 5.4-right.

Transitional and turbulent flows are populated by large variety of vortices interacting with each other. Usually their small size challenges the measurement capabilities and for planar measurements, when a vortex cross-section is investigated, the gradient-based analysis does not yield any preferential direction because of the axial symmetry. As a result, no specific adaptation can be chosen to better resolve the radial velocity fluctuation. Except for specific cases, such as in 2D turbulence, vortex filaments occur with a characteristic axial dimension that is much longer than their radius. This is consistent with the hypothesis of small influence of viscosity, where the first and second Helmholtz's theorems state that the vortex strength is constant along its axis and the filament either extends unlimited in 3D space or forms a closed path, like a vortex ring.

Therefore, when a 3D measurement of vortices is taken, the vortex axis can be chosen as the preferred direction along which the interrogation volume can be elongated; the correlation volume is then contracted in the radial direction to preserve the volume and will feature a cigar-like shape, Figure 5.5-right. For planar PIV, when the measurement plane is perpendicular to the vortex axis, the only option to increase spatial resolution is that of reducing the interrogation area at the cost of lower signal-to-noise ratio of the cross-correlation, Figure 5.5-left.

In the present discussion, the interrogation region is considered with ellipsoidal shape. This is obtained weighting a cubic correlation kernel with a 3D Gaussian function. The choice of a continuous weighting function versus top-hat weighting has been proven beneficial in terms of robustness and cross-correlation noise (Nogueira et al. 2005). When no preferential direction is found, the interrogation volume features a sphere.

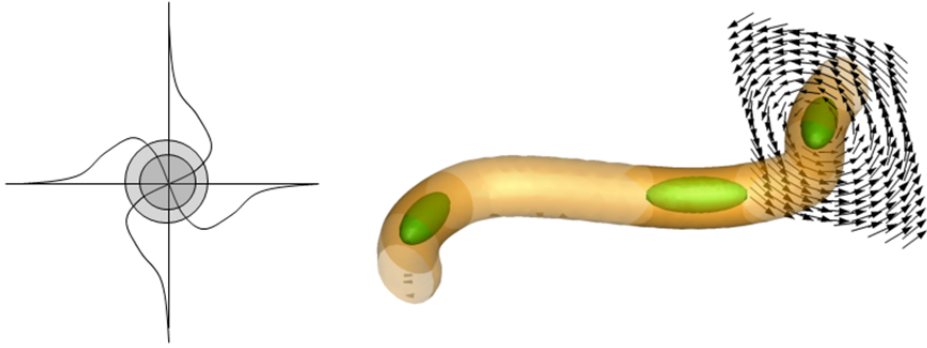


Figure 5.5 Examples of interrogation area in a vortex measured with planar PIV along its cross-section (left); spatial resolution can be increased only reducing the interrogation area size. A 3D vortex filament measured from 3D PIV (right); the cigar-like measurement volume can be arranged with major axis along the vortex axis without compromising the interrogation volume.

Schrijer and Scarano (2008) reported the spatial response of the cross-correlation analysis for one-dimensional as well as two-dimensional signals. The normalized response depends on the non-dimensional ratio  $l^*$  between the interrogation window size  $l_0$  and the wavelength of the velocity fluctuation in the flow field  $\lambda$ . Increasing  $l^*$  beyond 0.7 leads to appreciable modulation (higher than 20%) for 1D velocity fluctuations. For 2D fluctuations, this occurs earlier at approximately  $l^*=0.5$ . The reduction of the correlation region along the direction of the fluctuation will result directly in a reduction of  $l^*$  improving the spatial response of the correlation analysis.

The condition of constant volume  $V_0$  of the ellipsoidal interrogation region is ensured by the following condition, where  $l_1$ ,  $l_2$  and  $l_3$  are the dimensions of the ellipsoid principal axes (with  $l_3 \geq l_2 \geq l_1$ ):

$$V_0 \propto l_1 \cdot l_2 \cdot l_3 = l_0^3 \quad 5.1$$

The maximum aspect ratio is indicated with  $AR=l_3/l_1$ . To prevent the formation of extremely elongated ellipsoids, a criterion limiting  $AR$  to a maximum of 4 may be necessary (Wieneke and Pfeiffer 2010).

The ratio between  $l_1$  and  $l_0$  indicates the achievable reduction of  $l^*$ . In the case of planar measurements and a one-dimensional flow fluctuation (e.g. planar shear layer), the interrogation window can be shaped such that  $AR=4$ .

Being  $l_2=AR \cdot l_1$ , the condition of constant interrogation area leads to:

$$l_{\min} \cdot AR \cdot l_{\min} = l_0^2 \quad \rightarrow \quad \frac{l_{\min}}{l_0} = AR^{-\frac{1}{2}} \quad 5.2$$

In case of a 2D velocity fluctuation (e.g. cross section of a vortex) no reduction is possible due to the isotropy in the measurement plane, Figure 5.5-left.

The scenario changes for 3D measurements. In the above considered case of the shear layer the interrogation volume is elongated in two directions (coin-like shape) and the constant interrogation volume constrain becomes:

$$\underbrace{AR \cdot l_{\min}}_{l_1} \cdot \underbrace{AR \cdot l_{\min}}_{l_2} \cdot \underbrace{l_{\min}}_{l_3} = l_0^3 \quad \rightarrow \quad \frac{l_{\min}}{l_0} = AR^{-\frac{2}{3}} \quad 5.3$$

For  $AR=4$  the maximum reduction of  $l^*$  is approximately 60% as shown in Table 5.1. For a vortex filament the volume is elongated along the vortex axis and reduced along the radial direction (cigar-like shape) and equation 5.1 reads as:

$$\underbrace{AR \cdot l_{\min}}_{l_1} \cdot \underbrace{l_{\min}}_{l_2} \cdot \underbrace{l_{\min}}_{l_3} = l_0^3 \quad \rightarrow \quad \frac{l_{\min}}{l_0} = AR^{-\frac{1}{3}} \quad 5.4$$

yielding a maximum reduction of around 40%.

It is convenient to introduce the exponent  $\gamma$  generalizing the relation between  $l_1$ ,  $l_0$  and  $AR$ :

$$\frac{l_{\min}}{l_0} = AR^\gamma \quad 5.5$$

The dimensions of the measurement domain  $N_{D,meas}$  and the number of non-uniform directions of the flow fluctuation  $N_{D,flow}$  (e.g.  $N_{D,flow} = 1$  for a planar shear layer and 2 for a vortex tube) determine the coefficient  $\gamma$  according to the simple relation:

$$\gamma = \frac{N_{D,flow} - N_{D,meas}}{N_{D,meas}} \quad 5.6$$

Table 5.1 summarizes the values of the ratio  $l_1/l_0$  for the cases so far discussed. It should not surprise that in case of a hypothetical 3D velocity fluctuation no increase in spatial resolution is possible by the present approach.

$N_{D,flow} \backslash N_{D,meas}$	2 (planar meas.)	3 (Tomo-meas.)
1 (e.g. shear layer)	$AR^{-1/2}$ (0.5)	$AR^{-2/3}$ (0.4)
2 (e.g. vortex)	$AR^0$ (1)	$AR^{-1/3}$ (0.63)
3	-	$AR^0$ (1)

Table 5.1 The ratio  $l_1/l_0$  as a function of the aspect ratio for different planar and 3D PIV (values in brackets are for  $AR=4$ ).

### 5.2.1 Adaptive criterion

Once clarified what is the theoretical improvement that can be achieved in case of shape adaptation (Table 5.1), a criterion must be found that consistently detects the direction of the ellipsoid principal axes and their ratios. The adaptive criterion is based on the analysis of the local velocity gradient tensor  $\nabla \mathbf{V}$ . The method relies on a prior estimate of the velocity field

as obtained from a previous analysis of the particle tracers motion. In the present study, the image and 3D interrogation follows the iterative multi-grid approach with volume deformation. The shape adaptation is applied in the last 2-3 correlation steps, at a constant final interrogation volume size.

The local velocity gradient tensor is analyzed by means of the singular value decomposition (SVD, for the numerical algorithm see Golub and Van Loan 1996) in order to identify the direction of maximum and minimum velocity variation. The SVD consists in the factorization of a matrix  $M$  as:

$$M = USW^* \quad 5.7$$

where  $U$  and  $W$  are matrices containing the eigenvectors of  $MM^*$  and  $M^*M$  respectively, being  $M^*$  the adjoint of  $M$ , and they represent a set of orthonormal vector basis of  $M$ . The diagonal matrix  $S$  contains the singular values of  $M$ , which are the square roots of the eigenvalues of  $MM^*$  and  $M^*M$ .

In the present case, the matrix  $M$  corresponds to the velocity gradient tensor  $\nabla V$  and the singular values  $s_1$ ,  $s_2$  and  $s_3$  refer to the magnitude of the velocity variations along the principal directions  $l_1$ ,  $l_2$  and  $l_3$  (columns of the matrix  $W$ ). The singular values are sorted in descending order ( $s_1 > s_2 > s_3$ );  $\vec{l}_1$  represents the direction of maximum velocity variation,  $\vec{l}_2$  and  $\vec{l}_3$  lie in the plane perpendicular to  $\vec{l}_1$  with  $\vec{l}_2$  being the direction of the maximum velocity variation in that plane. As a result  $\vec{l}_3$  is aligned along the direction of minimum velocity variation.

The non-isotropic interrogation volume is arranged as an ellipsoid with axes aligned along the singular directions and length inversely proportional to the singular values. The ellipsoidal shape is approximated making use of a three-dimensional Gaussian weighting function that defines the weight ( $w$ ) of the voxels within the cubic kernel:

$$w(x, y, z) = e^{-\sum_{i=1}^3 \frac{d_i^2(x, y, z)}{2\sigma_i^2}} \quad 5.8$$

where  $d_i$  represents the distance of each voxel from the center of the interrogation volume along the directions  $\vec{l}_1$ ,  $\vec{l}_2$  and  $\vec{l}_3$  respectively.

The distances  $d_1$ ,  $d_2$  and  $d_3$  along the principal directions are obtained from the distances of each voxel along the  $X$ ,  $Y$  and  $Z$  axis ( $dx$ ,  $dy$  and  $dz$ ) by applying the rotation matrix  $W$ , as obtained from the singular value decomposition, equation 5.7, as:

$$[d_1 \ d_2 \ d_3] = [d_x \ d_y \ d_z] \cdot W = [d_x \ d_y \ d_z] \cdot [\vec{l}_1 \ \vec{l}_2 \ \vec{l}_3] \quad 5.9$$

The Gaussian half-width along each singular direction is indicated with  $\sigma_i$ .

The function  $w$ , equation 5.8, approximates the ellipsoidal region of space which is effective for cross-correlation: the ratio between  $s_3$  and  $s_1$  defines the aspect ratio  $AR_{31}$  of the ellipsoid in the plane identified by  $\vec{l}_1$  and  $\vec{l}_3$  as:

$$AR_{31} = (AR_{\max} - 1 + \varepsilon) \cdot \left(1 - \frac{s_3}{s_1}\right) + 1 \quad 5.10$$

where a maximum aspect ratio,  $AR_{max}$ , of 4 is chosen ( $AR_{31} \leq AR_{max}$ ). The term  $\varepsilon$  is positive and smaller than 1. This term is introduced in order to ensure that the maximum aspect ratio is achieved when the ratio  $s_3/s_1$  becomes very small. A value of 0.3 corresponds to the maximum aspect ratio for any value of  $s_3/s_1$  below 0.1. The above equation applies also for  $AR_{21}$ . Figure 5.6 shows the aspect ratio as a function of the ratio between the singular values relative to the minimum and maximum eigenvalues obtained from the SVD analysis (singular directions 3 and 1).

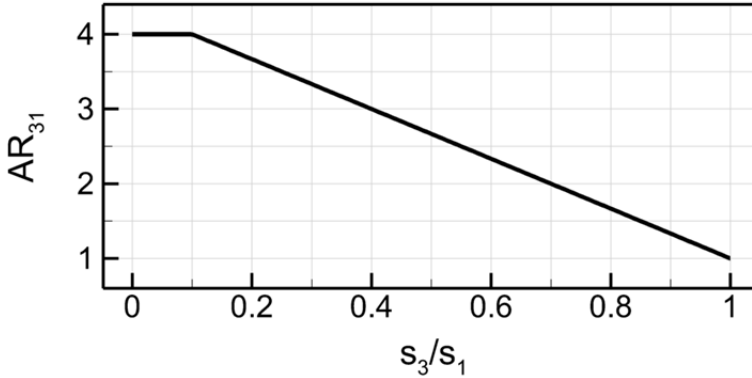


Figure 5.6 Aspect ratio in the plane defined by singular directions 1 and 3 as a function of the ratio between the minimum ( $s_3$ ) and maximum ( $s_1$ ) singular values.

Moreover, a lower threshold  $s_{min}$  is set for the value of the maximum singular value  $s_1$ ; when  $s_1 < s_{min}$  there is no need for an ellipsoidal interrogation volume and a spherical Gaussian weight is applied. The value of  $s_{min}$  is chosen considering that  $s_1$  represents the magnitude of the velocity gradient; therefore, the value of  $s_1 \cdot l_0$  is representative of the deformation (in voxels) within the correlation window. For the results presented in the following sections a minimum deformation of 0.1 voxels is set to activate the adaptive interrogation leading to  $s_{min} = 0.1/l_0$ .

Being  $\sigma_0$  the spherical Gaussian half-width used for isotropic analysis, imposing the constant-volume property, the values of  $\sigma_i$  are then obtained as:

$$\begin{aligned} \sigma_1 &= \frac{\sigma_0}{\sqrt[3]{AR_{31} \cdot AR_{21}}} \\ \sigma_2 &= \sigma_1 \cdot AR_{21} \\ \sigma_3 &= \sigma_1 \cdot AR_{31} \end{aligned} \quad 5.11$$

The Gaussian weight is applied to an interrogation volume which is double the size of the interrogation cubic region in each direction; the choice of  $\sigma_0$  is made such as the value of the weighting function equals  $1/e$  at the edge of the cubic interrogation region.

An example of the adaptive interrogation volumes for the Tomo-PIV data of the transitional jet flow in water is shown in Figure 5.7. The shape of interrogation volumes selected in the jet core, in the shear layer at the jet exit and in a vortex ring is shown. The ellipsoids appear with a clear contraction of the principal axis in the direction of largest velocity variation. The

resulting interrogation volume acts as an optimized filter for the vorticity magnitude field. The direction of the two largest axes for the region of the shear layer (yellow coin-like ellipsoid) becomes inessential. Similarly, in the core of the ring vortex the interrogation volume (blue cigar-like ellipsoid) has the major axis aligned with the vortex axis. The direction of the other axes (almost identical in length) in the plane perpendicular to the vortex axis does not alter the shape of the ellipsoid.

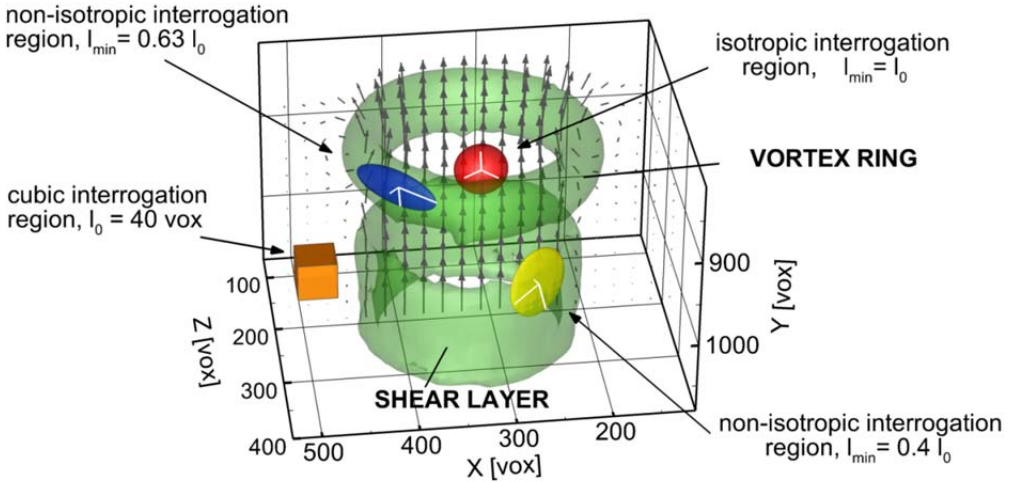


Figure 5.7 Detail of interrogation regions in the jet flow; iso-surface of vorticity magnitude in green (0.2 1/ms).

### 5.2.2 Numerical implementation of shaped cross-correlation

The adaptive criterion relies on a previous estimate of the velocity field. Therefore, the adaptive Gaussian weight is applied only in the last 2-3 iterations of the iterative cross-correlation process. The computational burden, is reduced by using symmetric direct correlation (Nogueira et al. 2002) with a small search radius (2 or 3 voxels).

Because this is applied at a later stage of the iterative cross-correlation analysis, the displacement correction is mostly confined in the range of 1 voxel. Under these conditions direct correlation becomes more efficient than FFT cross-correlation in particular when one considers that most voxels have a value of zero and they may not need to be accounted for (Scarano 2013).

The direct correlation approach is significantly accelerated when partitioning the interrogation area into sub-portions of size corresponding to the required vector distance. The correlation maps in the sub-portions only need to be computed once even when interrogation areas are overlapping (Roth and Katz 2001). The size of these correlation blocks depends on the overlap factor  $OF$  between adjacent interrogation volumes and corresponds to  $w_{s0}(1-OF)$  where  $w_{s0}$  is the linear size of the nominal interrogation region.

The correlation blocks belonging to a single interrogation region are summed up to yield its correlation signal. Typically a 75% overlap is used in Tomo-PIV data processing, which leads to a partition of the cubic interrogation volume into 64 (4×4×4) correlation blocks.

When a Gaussian weighting is used in a direct cross-correlation step, the weight is applied to the correlation blocks rather than to the single voxels, which largely reduces the amount of calculations. The Gaussian weighting is applied to a kernel twice as large to allow the elongation of the interrogation region along preferential directions. As a result, the correlation region is partitioned into 512 ( $8 \times 8 \times 8$ ) correlation blocks. Each block is weighted according to the Gaussian function in equation 5.8, Figure 5.8-top-left, before performing the summation into a single 3D correlation map.

The discretization effect of the Gaussian weight becomes important especially when the shaped interrogation volume is thinned along a specific direction (i.e. *coin-like*) as the function is evaluated on a rather coarse grid of typically  $8 \times 8 \times 8$  points instead of the voxels grid. Along the direction of stronger velocity gradient the Gaussian function is narrowed and discretized over even fewer points yielding a poor description of the weighting function, as shown in Figure 5.8-top-right.

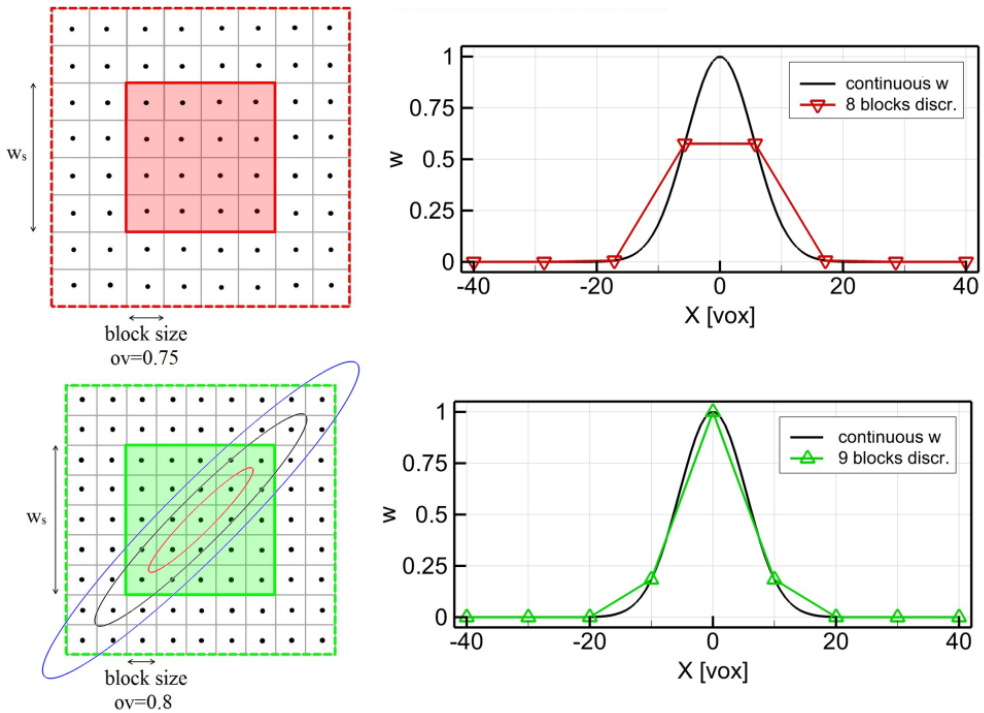


Figure 5.8 Left: two-dimensional description of the interrogation volume partitioned into sub-portions for symmetric direct correlation; 75% overlap (top) and 80% overlap (bottom). Filled areas indicates the original top-hat interrogation window; the wider areas included within the dashed-squares represent the double-sized correlation windows over which the Gaussian weight is computed. Gaussian weight  $w$  iso-contours, in case a 60% reduction of the interrogation region is achieved along one direction, are superimposed to the interrogation volume for the case of 0.8 overlap (blue line:  $w=0.1$ , black line:  $w=0.4$ , red line:  $w=0.8$ ), bottom-left. Right: continuous and discretized Gaussian weight for an interrogation volume equivalent to  $40 \times 40 \times 40$  voxels in the case of a 60% reduction of the correlation volume as a result of the adaptive technique; 75% overlap (top) and 80% overlap (bottom).

The discretization effect is significantly reduced when the interrogation region is partitioned with an odd number of sub-regions along each coordinate direction. For instance, an overlap factor of 0.8 leads to  $5 \times 5 \times 5$  correlation blocks per volume ( $9 \times 9 \times 9$  in the larger volume for Gaussian weighting). As illustrated in Figure 5.8-bottom-left the weight distribution is improved by the presence of one block at the interrogation volume center that captures the Gaussian peak even when the window size has been reduced by 60% (the maximum reduction expected for a 1D flow fluctuation), Figure 5.8-bottom-right.

When an adaptive approach is applied, the computational time increases by approximately 30% if compared to an isotropic Gaussian weighting correlation step since the adaptive Gaussian weight needs to be evaluated for each interrogation volume. For the reasons given above, the correlation in the Fourier domain is very unpractical because of the high computational burden when analyzing objects at high overlap factor. In practice, the very first analysis is computed by FFT at low or zero overlap followed by direct correlation at subsequent iterations. The application of the fast Fourier transform (FFT) approach with Gaussian weighting results in orders of magnitude increase of the computational time and is not considered further in the present study.

### 5.3 Numerical assessment

Computer-generated three-dimensional objects are obtained with parameters similar to those encountered in the tomographic PIV experiments of Violato and Scarano (2011). Results obtained with the adaptive technique are compared with the case of isotropic correlation making use of a spherical Gaussian weighting function. Particles having a reconstructed diameter of 3 voxels are generated within objects of  $300 \times 300 \times 700$  voxels at random locations by Monte Carlo technique. Subsequent exposures are obtained imposing a known displacement field; a one-dimensional and a two dimensional velocity fluctuations are investigated. A planar shear layer ( $N_{D,flow}=1$ ) along  $Y$  is imposed according to the expression:

$$V_x = 7 \cdot \sin^2(\pi \cdot Y / \lambda) \quad 5.12$$

The parameter  $\lambda$  is the length scale of the fluctuation and, after normalization by the equivalent cubic interrogation window size ( $w_{s0}=40$  vox), it is varied in this analysis between 0.0625 and 1.0.

The 2D case ( $N_{D,flow}=2$ ) is a vortex tube aligned with the  $Z$  axis. When expressed in polar coordinates, the only non-zero velocity component is the azimuthal  $V_g$ , which varies only along the radial distance from the vortex center according to the following expression:

$$V_g = 32 \cdot R / \lambda \cdot e^{-4 \cdot R / \lambda} \quad 5.13$$

where  $R$  is the distance from the vortex. The wavelength of the fluctuations ( $\lambda$ ) is varied in order to investigate the relevant range of the non-dimensional parameter  $l^*$  (0.1,1). In this analysis the  $l^*$  is computed using the interrogation nominal linear size  $w_{s0}$  to normalize  $\lambda$ .

The cross-correlation analysis is performed by a Volume Deformation Iterative Multi-grid algorithm (VODIM) with 6 iterations both for isotropic and non-isotropic analysis; in the case of adaptive interrogation the ellipsoidal Gaussian weight is applied in the last 3 iterations. The tracers concentration is  $1 \cdot 10^{-4}$  ppv (particles per voxel); the final interrogation volume is chosen to be equivalent to  $40 \times 40 \times 40$  voxels which leads to an average of

approximately 6 particles per interrogation volume. The vector grid spacing  $h$  is 8 voxels given the chosen overlap factor of 0.8. The vector spacing is made non-dimensional dividing it by the fluctuation length scale  $\lambda$  that yield  $h^*$ . The latter parameter indicates the importance of spatial discretization effects on the measurement of the velocity field and of its gradient.

Results from isotropic and adaptive motion analysis are compared in terms of vorticity magnitude ( $\omega = |\vec{\omega}|$ ) attained in the center of the shear layer and along the centerline of the vortex filament. The vorticity is evaluated by finite central differences. The peak vorticity ( $\hat{\omega}$ ) is normalized making use of the theoretical exact value ( $\hat{\omega}_{th}$ ) obtained from the imposed displacement field. The difference between the measured and theoretical value is due both to the modulation error (spatial response of the correlation related to  $l^*$ ) and the discretization error, due to the finite distance between measured vectors; the latter would tend to zero increasing sampling frequency of the signal (i.e. overlap factor). Nevertheless, this option is highly unpractical because of the constraints on computational efficiency.

Figure 5.9 shows results relative to the 2D shear layer (left) and the 3D vortex (right); the maximum aspect ratio of the interrogation region ( $AR=4$ ) is attained in proximity of the vorticity peak in both cases. The solid black line shows the normalized vorticity peak as obtained from the theoretical velocity field sampled using the same vector pitch as the correlation analysis ( $\hat{\omega}_{th}^{disc}$ ); it represents the vorticity peak achievable making use of adaptive interrogation regions having an infinite aspect ratio ( $l_{min} \rightarrow 0$ ). It emerges clearly that the error due to discretization is rather important, particularly for the case of two-dimensional flow fluctuation where a 40% error is attained at  $h^*=0.1$ . This suggests that the minimization of the error requires not only the non-isotropic interrogation window, but also a reduction of discretization effects. A possible approach is the local refinement of the measurement grid. This, however, goes beyond the scope of the present study.

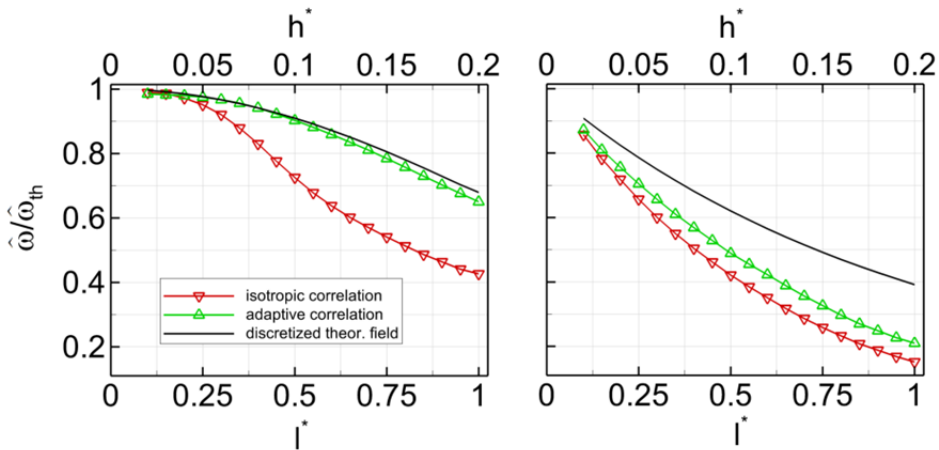


Figure 5.9 Peak vorticity normalized with the theoretical values versus  $l^*$  and  $h^*$  for one-dimensional (left) and two-dimensional (right) flow fluctuations.

For the shear layer case, at small values of  $l^*$  ( $l^* < 0.2$ ) the vorticity peak can be accurately calculated even without the use of a shaped interrogation volume. Beyond this value the curves depart from each other and the adaptive correlation follows closely the exact solution, which however suffers from the discretization effect on the derivative. The modulation due to the finite differences is approximately 10% at  $l^* = 0.5$  ( $h^* = 0.1$ ) and becomes 30% at  $l^* = 1$  ( $h^* = 0.2$ ). In comparison, the isotropic interrogation yields less than 50% of the peak vorticity in the latter conditions.

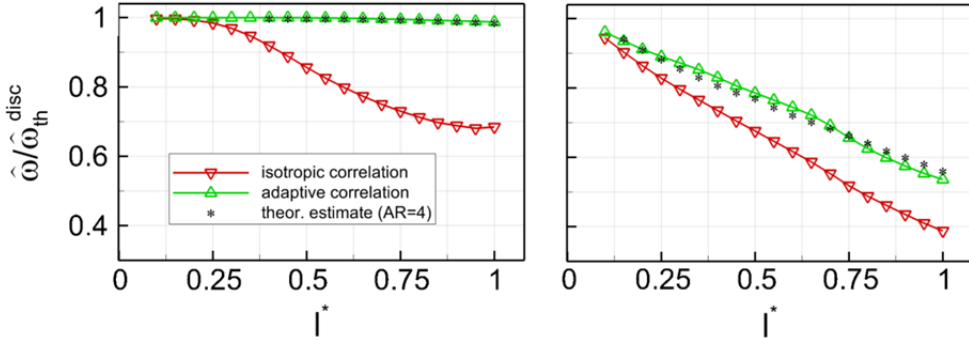


Figure 5.10 Peak vorticity normalized with the one obtained by the theoretical discretized velocity field versus  $l^*$  for one-dimensional (left) and two-dimensional (right) flow fluctuations.

The case of the vortex is more critical as also theoretically predicted because in that case the interrogation volume can be elongated only along one direction. As a result, both discretization errors as well as spatial filtering effects are important already at small values of  $l^*$ . At  $l^* = 0.5$  the theoretical drop of vorticity solely due to the finite difference operation is 40%. The normalized vorticity peak obtained by cross-correlation is 0.4 for the spherical interrogation volume and 0.5 for the adapted cigar-like interrogation volume.

In order to focus the attention on the component of the error due to the averaging effect associated to the interrogation volume, the results are also shown when the peak vorticity is normalized with that obtained from the discretized theoretical velocity field, Figure 5.10.

This way, only the modulation error due to the correlation spatial response is considered and the vorticity peak achievable by adaptive analysis when  $l_{min} \rightarrow 0$  corresponds to  $\hat{\omega} / \hat{\omega}_{th}^{disc} = 1$ . A significant reduction in the modulation error is observed, with approximately 80% and 45% for the shear layer, Figure 5.10-left, and the vortex case, Figure 5.10-right, respectively at  $l^* = 0.5$  when non-isotropic correlation is performed.

The theoretical estimate shown in Figure 5.10 with black asterisks considers that the adaptive correlation performs as the isotropic one when the latter applies to smaller  $l^*$ . The estimated value for adaptive analysis at a given  $l^*$  is given by the value attained by the isotropic analysis at  $l^* \cdot AR^l$ . Considering that the maximum aspect ratio of 4 is attained by the adaptive criterion,  $AR^l$  is 0.4 and 0.63 for the shear and vortex case respectively. Results from adaptive correlation appear to be in good agreement with this estimate.

In contrast with the widespread analysis of the spatial response by using sinusoidal functions (Willert and Gharib, 1991; Nogueira et al. 1999; Scarano and Riethmuller 2000; Schrijer and Scarano 2008; Astarita 2006) some recent studies highlighted the importance of the correlation point-spread-function (Elsinga and Westerweel 2011; Kähler et al. 2012).

A discontinuous velocity distribution is adopted (step function) to investigate the spatial response of cross-correlation techniques and infer about the actual spatial resolution. It is shown that the iterative deformation technique causes a modulation in the velocity gradient and the point spread function (PSF), computed as the velocity gradient across the step, exhibits positive and negative lobes (overshoot wiggles) at both sides of the step location. This behavior indicates a loss of precision due to the region with displacement in phase opposition with respect to the central point, in agreement with the previous findings of Nogueira et al. 1999.

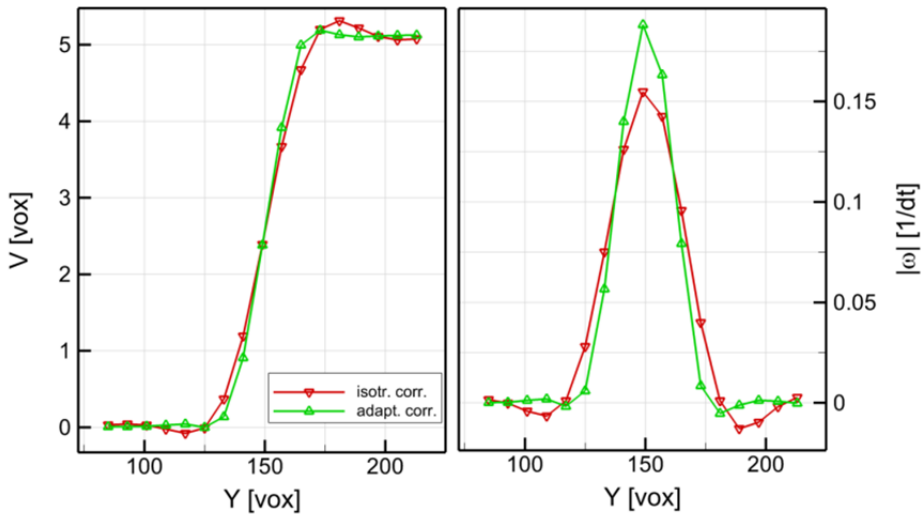


Figure 5.11 Velocity (left) and vorticity magnitude (right) profiles across the simulated shear layer at  $l^*=0.5$ .

Figure 5.11 shows the displacement and vorticity profiles across a shear layer at  $l^*=0.5$  for the isotropic and adaptive interrogation. In the present context it is relevant to consider both the peak vorticity as well as the relative amplitude of the side lobes due to the above-mentioned effects as shown in Figure 5.10, where an increase of spatial resolution is achieved when the interrogation volume is shaped adaptively.

The cross-correlation signal-to-noise ratio ( $S/N$ ) is analyzed to understand the implications of the adaptive interrogations in terms of measurement robustness. The full-correlation map is needed to evaluate the  $S/N$ , which is not obtained by direct correlation. Therefore for the present analysis FFT cross-correlation is performed at the last iterations. The probability density function (PDF) of the signal-to-noise ratio is shown in for the case of  $l^*=0.5$ ; the data ensemble includes only correlation regions with a value of aspect ratio larger than 3. In both cases the level of  $S/N$  is not critical, however, for the shear layer, thinning the interrogation region moves the peak of the distribution towards a higher value.

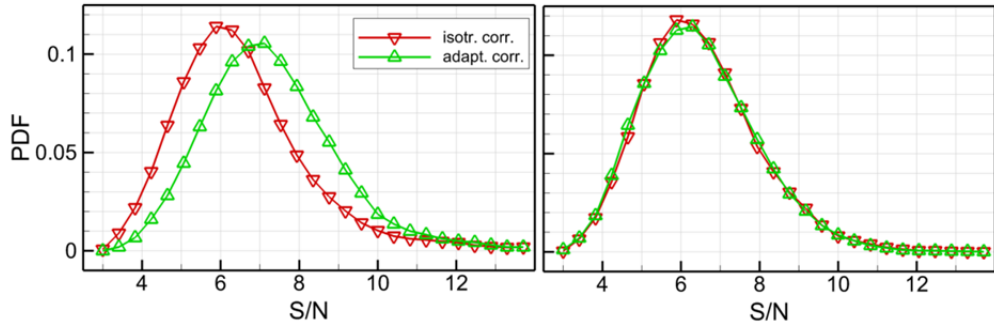


Figure 5.12 Probability density function of cross-correlation signal-to-noise ratio for the isotropic and adaptive approaches for the shear layer (left) and vortex filament case (right) at  $l^*=0.5$ .

As already shown in Figure 5.9 and Figure 5.10, the effect of the adaptive technique when a 2D fluctuation is considered is significantly lower due to the limited reduction achievable in the interrogation volume size. This behavior can be also observed concerning the correlation signal-to-noise ratio for the vortex case, Figure 5.12-right, where only a slight improvement in the PDF peak position (from 6 to approximately 6.5) is achieved after the adaptive interrogation is applied.

## 5.4 Transitional jet experiment

The availability of a large data set obtained from time-resolved Tomo-PIV experiments to investigate a transitional round jet at  $Re$  5,000 in water (Violato and Scarano 2011) enables a detailed analysis of the proposed method for experimental data. A detailed description of the experimental setup and flow conditions is given in section 4.9 of this thesis.

Reconstructed objects of  $563 \times 964 \times 563$  voxels are analyzed with interrogation regions equivalent to a  $40 \times 40 \times 40$  voxels, given the particle tracers density contain approximately 6 particles. The jet flow is characterized by a laminar shear layer at the jet exit; at a distance of approximately  $Y/D=1.5$  from the jet exit (where  $Y$  is the axial coordinate and  $D$  is the nozzle diameter) the onset of the Kelvin-Helmholtz instability causes the formation of vortex rings, which subsequently pair ( $Y/D \approx 3$ ).

The value of  $l^*$  calculated with the size of the spherical interrogation region is approximately 0.6 and 0.3 for the shear layer and the vortex ring case respectively. Cross-correlation is performed by VODIM, making use of 6 iterations with adapted ellipsoidal shape in the last 3. As for the simulated objects analysis, when the adaptive correlation is performed, the aspect ratio of the interrogation regions within the shear layer and in the vortex core is limited to a maximum value of 4.

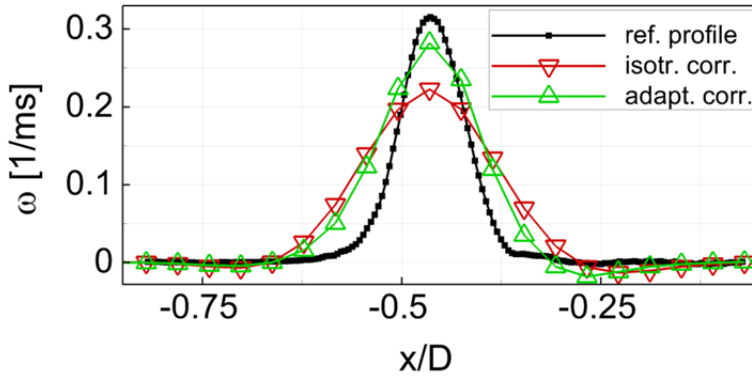


Figure 5.13 Vorticity magnitude profiles along the shear layer of the jet at  $Y/D=0.8$  for isotropic and adaptive correlation. Reference from 2D-PIV data.

The laminar shear layer at the jet exit is stationary; the mean vorticity profile is shown in Figure 5.13 for the isotropic and adaptive analysis. The reference vorticity profile (black line) has been obtained from planar PIV data at higher spatial resolution. The peak vorticity increases of approximately 25% when the adaptive correlation is applied; this result also agrees with the numerical simulation for the one-dimensional fluctuation at  $l^*=1$ , Figure 5.9-left, where an increase of approximately 30% was predicted.

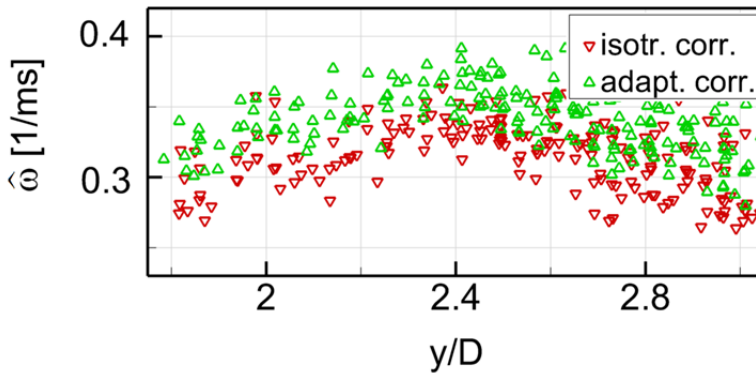


Figure 5.14 Peak vorticity of axisymmetric vortices as they travel along the axial coordinate for isotropic (red gradient symbol) and adaptive (green delta symbol) interrogation.

The peak vorticity of vortex rings shed by the shear layer is followed while the vortex travels along the jet axis between  $Y/D=1.8$  and  $Y/D=3$ , Figure 5.14. The distribution of peak vorticity for adapted windows is above that obtained with spherical interrogation volumes in the same order as found in the numerical simulation (around 5% increase in vorticity peak).

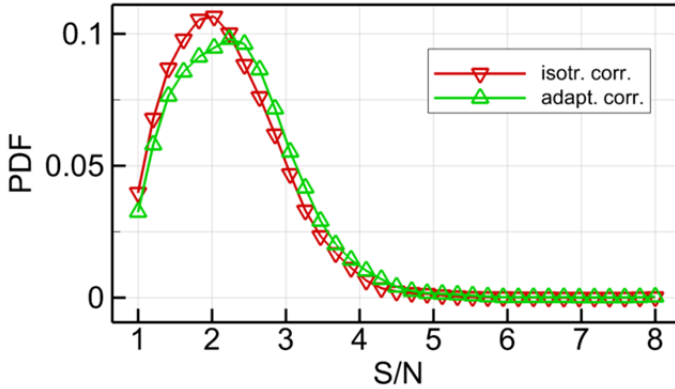


Figure 5.15 Probability density function of cross-correlation signal-to-noise ratio for the isotropic and adaptive approaches for the transitional jet flow.

The distribution of the  $S/N$  for this experiment ( $AR > 3$ ) yields a PDF with some increase of measurement robustness. The peak of the distribution is shifted from a value of 1.8 to 2.3 approximately, Figure 5.15. The measurement accuracy is inspected qualitatively by observing the 3D vorticity field distribution. In Figure 5.16 the iso-surfaces of vorticity magnitude in the shear layer and vortex rings are somehow wiggled and exhibit variations leading to holes or interruptions when using the spherical interrogation volume, Figure 5.16-left. This effect is even more pronounced when using the cubic shape due to its anisotropy. The interrogation by adapted shape yields a more regular surface and generally higher peak values when compared to the isotropic interrogation volume, Figure 5.16-right.

## 5.5 Turbulent boundary layer experiment

Data from a Tomo-PIV experiment of a turbulent boundary layer in air (Ghaemi et al. 2012) are analyzed with the isotropic and adaptive technique to assess the adaptive technique performances in the near wall region. The boundary layer is generated over a 2 m long flat plate placed at zero angle-of-attack in an open test-section vertical wind tunnel operating at a free stream velocity of 9.3 m/s ( $U_\infty$ ); the Reynolds number based on the displacement thickness is 2420. The transition from laminar to turbulent flow is forced at a location 150 mm downstream of the leading edge; the measurement region is located 1.5 m downstream of the leading edge. The measurement equipment is mentioned in the previous section. The field of view is 58.7 mm and 53.9 mm in the streamwise ( $X$ ) and wall-normal ( $Y$ ) directions respectively; the depth direction of the illuminated volume ( $Z$ ) is aligned with the spanwise direction and the laser thickness is 3.5 mm. Given a magnification factor of 4.3, the digital resolution is 21.5 vox/mm. The acquisition frequency is 20 Hz and the time separation between the image pairs is 80  $\mu$ s; average quantities are computed over 200 snapshots. The flow is seeded with 1  $\mu$ m diameter droplets at a concentration of 0.08 *ppp*, approximately 10 particles/mm<sup>3</sup>. A detailed description of the flow conditions and experimental setup can be found in Ghaemi et al. 2012.

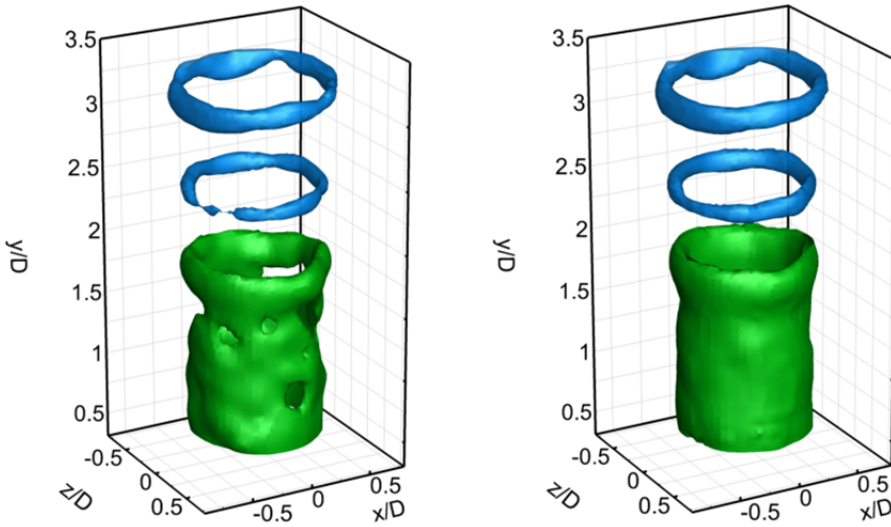


Figure 5.16 Iso-surfaces of vorticity magnitude (green 0.18 1/ms, blue 0.31 1/ms) for isotropic (left) and adaptive (right) interrogation.

Reconstructed objects of  $1003 \times 548 \times 65$  voxels are interrogated with interrogation regions equivalent to a  $30 \times 30 \times 30$  voxels. The mean vorticity magnitude profile along the wall-normal direction is shown in Figure 5.17;  $Y=0$  mm corresponds to the position of the wall. The abrupt increase in vorticity in the near-wall region causes a step-like profile. Some “ringing” at  $Y=2.5$  mm is observed as a result of the unstable behavior of the window deformation towards unresolved scales. The “ringing” is clearly reduced when a coin-like correlation volume is utilized; a reduction of approximately 45% in the amplitude of the spurious oscillation is achieved. The increase of peak vorticity towards the wall is marginal.

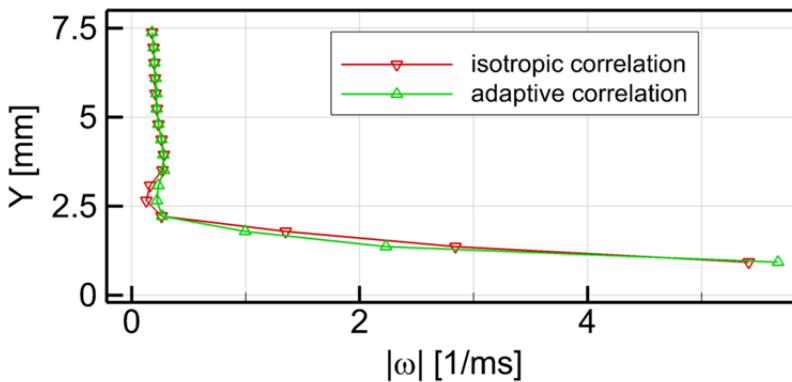


Figure 5.17 Mean vorticity magnitude profile along the wall-normal direction ( $Y$ ) for isotropic and adaptive interrogation approaches.

The ability to measure the turbulent fluctuations in the boundary layer is briefly examined hereafter. Figure 5.18 shows the  $\overline{u'u'}$  profile for the two techniques and the reference profile obtained by planar PIV with ensemble correlation (interrogation windows of  $4 \times 4$  px<sup>2</sup>). The spatial resolution of tomographic experiments is typically lower than that attainable with planar experiments. The distribution of streamwise velocity fluctuations exhibits a peak in the inner layer, which is difficult to capture with limited spatial resolution due to the large value of the velocity gradient at wall proximity. Comparing the adapted with the isotropic interrogation volume one observes that the increase of streamwise fluctuations is captured two grid nodes closer to the wall. As a result the measured fluctuations amplitude is increased and in good agreement with the high-resolution data. The analysis of the fluctuations from the other two components does not exhibit significant differences, which can be partly explained with the fact that the tomographic results are already very closely following the reference data.

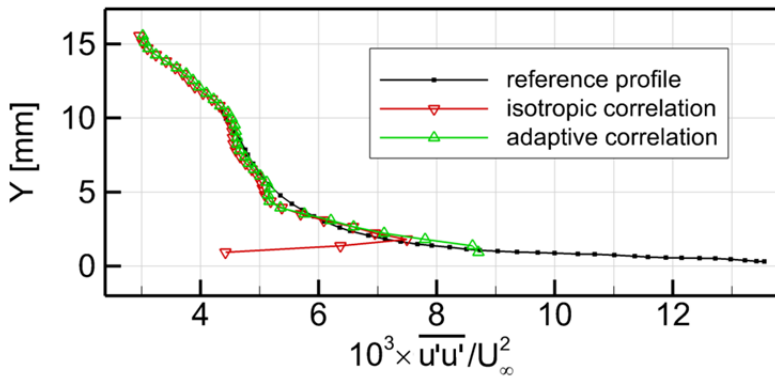


Figure 5.18 Profile of  $\overline{u'u'}$  along the wall-normal direction for the isotropic and adaptive approaches. Black line indicates the reference profile obtained by planar PIV.

## 5.6 Conclusions

The principle of spatial adaption of the interrogation region is introduced for 3D-PIV. The adaptive criterion is based on the analysis of the local velocity gradient tensor and allows stretching and orienting the interrogation volume along the direction of the minimum velocity magnitude variation. The technique aims to increase the spatial resolution in regions of the flow where strong gradients and vortical structures are present, such as shear layers and vortices.

The performances have been assessed by means of computer simulated 3D objects and its applicability is verified with the application to Tomo-PIV experiments of a transitional jet in water and a turbulent boundary layer in air. The discussion shows that the spatial resolution of tomographic PIV can be enhanced more in case of one-dimensional velocity fluctuations where a coin-like interrogation volume is featured with minimum ellipsoid diameter reduced by 2.5 times. In case of vortices, the adaptive method features a cigar-like shape and the reduction of radial dimension is somewhat smaller (1.5 times). These effects only depend upon the maximum aspect ratio and the dimensions ratio  $\gamma$ .

From the discussion it emerges that any further increase of spatial resolution for the determination of the velocity gradient will require a reduction of the distance between neighboring vectors. The application to the experiments illustrates that this approach can be used to improve the vorticity field measurement to a significant extent in the jet shear layer, where the value of the vorticity peak increases of around 25% as a consequence of the strong reduction in the interrogation volume size in the direction of the fluctuation, therefore of the modulation of the signal. A limited effect is seen for the vortex peak vorticity which increases of about 5%. Results show a good agreement with the predicted values obtained from numerical simulations; 30% and 8% increase of vorticity peak for the shear layer and the vortex filament respectively. In the turbulent boundary layer, the application of the adaptive technique leads to a significant improvement in the description of the mean and fluctuating properties of the streamwise component in the near-wall region. Moreover, the amplitude of the “ringing” artifact in the vorticity profile is reduced by approximately 45% for the adaptive interrogation.



## **Chapter 6**

# **A particle-tracking approach for accurate acceleration measurements**

Novara M and Scarano F (submitted) A particle-tracking approach for accurate material derivative measurements with tomographic PIV, *Exp. Fluids*.

In this chapter a particle-tracking based approach is presented which aims to improve the accuracy of the acceleration measurement from time-resolved tomographic PIV, in turn providing a more accurate estimate of the 3D pressure field. The relevance of the acceleration measurement is discussed and the theoretical background of the pressure evaluation from tomographic PIV snapshots is described. The tomographic approach based on particle tracking (Tomo-3D-PT) is then introduced; the aspects of trajectory identification and fitting are discussed as well as the interpolation of sparse information to a regular grid, a necessary step when spatial gradients are object of interest. A comparison with the trajectory reconstruction and acceleration estimate approach from tomographic PIV data is carried out by means of synthetic data of an advecting vortex ring. The technique is then applied to data from a Tomo-PIV experiment of a transitional jet in water to assess its performances.

### **6.1 Acceleration and pressure from PIV**

The measurement of the instantaneous pressure field is of high interest for many aerodynamic applications ranging from air transport systems to wind energy. In the last years techniques based on particle image velocimetry have been successfully employed to determine aerodynamic loads (Lin and Rockwell 1996; van Oudheusden et al. 2007, see Figure 6.1) and to perform aeroacoustic predictions (Haigermoser 2009, see Figure 6.2; Koschatzky et al. 2010; Lorenzoni et al. 2009). The evaluation of the three-dimensional

instantaneous pressure field has been attempted with time-resolved tomographic PIV (Tomo-PIV, Elsinga et al. 2006) in more recent studies (Ghaemi et al. 2012; Probsting et al. 2012).

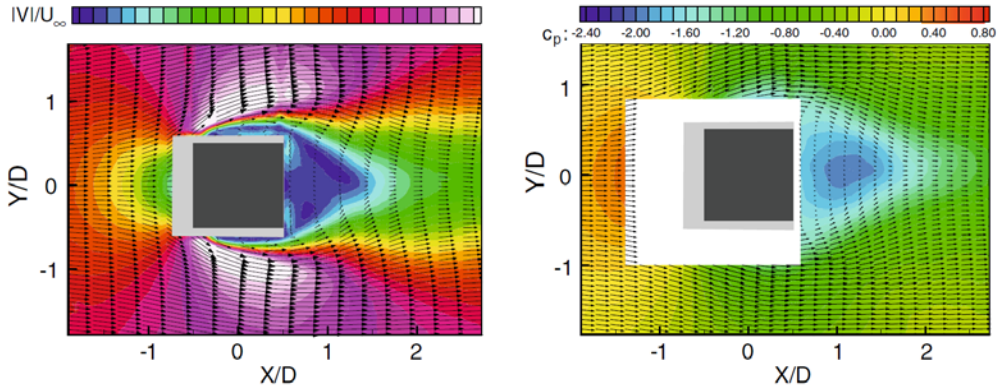


Figure 6.1 Mean velocity magnitude (left) and pressure coefficient (right) fields around a square section cylinder from 2-component PIV (van Oudheusden et al. 2007).

The instantaneous fluid flow pressure is not directly measured with PIV and it has to be inferred from the analysis of the flow kinematics. The pressure gradient is first obtained by means of the Navier-Stokes equations and then integrated across the measurement domain; the integration can be carried out by means of multiple integration path approaches (Baur and Kongeter 1999; Liu and Katz 2006) or by the solution of the Poisson equation for pressure (Gurka et al. 1999).

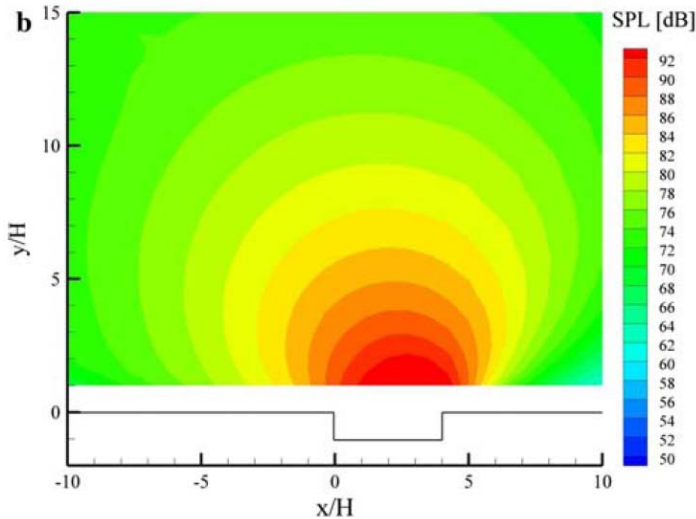


Figure 6.2 Sound pressure level inferred from a PIV investigation of a rectangular cavity flow (Haigermoser 2009).

The evaluation of the material derivative is at the basis of this method; this step represents a challenge for the technique since it requires the computation of both spatial and temporal

derivatives, which strongly rely upon the precision of each instantaneous velocity measurement in the sequence. To date, concerning PIV based techniques, the material derivatives have been computed by means of Eulerian approach (Baur and Kongeter 1999; de Kat and van Oudheusden, 2010) or by Lagrangian approach estimating the fluid parcel trajectory from a short time sequence of velocity fields (Liu and Katz 2006; Violato et al. 2011). For further details the reader is referred to an extensive review of the state-of-the-art of PIV based pressure evaluation and aerodynamic forces given by van Oudheusden (2013).

Lagrangian motion analysis has been performed much earlier by 3D particle tracking velocimetry (3D-PTV, Maas et al. 1993). Several studies demonstrated that accurate Lagrangian statistics can be constructed following particles over long trajectories (Voth et al. 1998; La Porta et al. 2000, Figure 6.3). However, the drawback of the PTV approach for pressure evaluation is the low spatial density of information. Since particles are identified onto the camera images and then triangulated into the 3D domain, the robustness of the algorithm is strongly affected by overlapping particles or crossing trajectories. As a result the seeding concentration is typically limited to one order of magnitude less than that practiced in Tomo-PIV experiments.

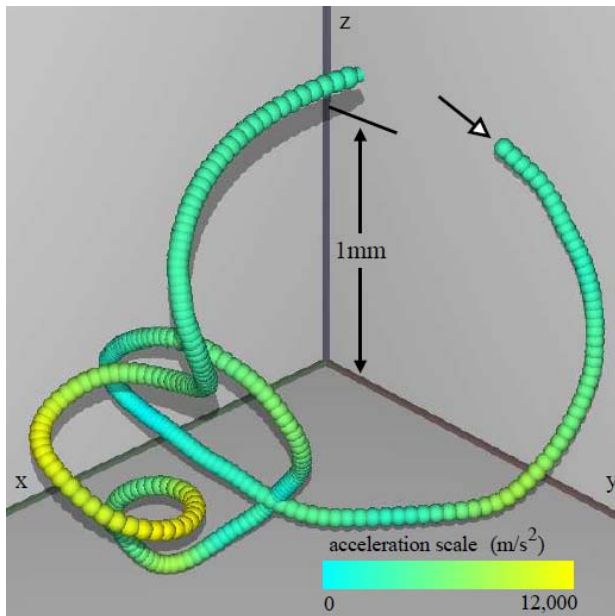


Figure 6.3 Particle trajectory tracked in a turbulent water flow; spherical marker indicates the particle position and it is color-coded based on the local acceleration (La Porta et al. 2000).

An early attempt to benefit from the higher seeding density offered by Tomo-PIV and from the accuracy in the description of Lagrangian trajectories of PTV has been carried out by Schröder et al. 2008a, where reconstructed particles from Tomo-PIV were tracked along a relatively long sequence to infer the material derivative. However, the data was presented in terms of Lagrangian statistics and no further step was reported to estimate the material derivative field and the instantaneous pressure field. More recently, Wieneke (2011) has proposed a hybrid algorithm for 3D particle fields reconstruction for Tomo-PIV where the

concept of 3D-PTV is exploited to reduce the error on the reconstructed particle peak location. This method has not been employed yet to determine the flow material derivative.

The present study extends the prior effort by Schröder et al. 2008a. Particle tracking is performed on reconstructed 3D intensity fields from tomography (Tomo-3D-PT). In this case the typical distance between reconstructed particles is rather large if compared to that projected on the camera images. The availability of a-priori information on the velocity field from cross-correlation analysis makes it possible to evaluate individual particle trajectories with high reliability. Following the particle path over a long observation time is expected to reduce the precision error of the material derivative estimate. Compared to a trajectory integration and velocity finite differences as reported by Violato et al. (2011), the current method based on Tomo-3D-PT approach is also expected to significantly reduce the truncation error.

## 6.2 Theoretical background

The instantaneous 3D pressure field can be inferred from velocity measurements from Tomo-PIV recalling the Navier-Stokes equations. For an incompressible, isothermal flow the instantaneous pressure gradient reads as:

$$\nabla p = -\rho \left( \frac{D\mathbf{V}}{Dt} + \nu \nabla^2 \mathbf{V} \right) \quad 6.1$$

where  $\mathbf{V}$  is the velocity vector,  $\rho$  the fluid density and  $\nu$  the fluid kinematic viscosity.

The pressure field can be obtained by integration of the pressure gradient. Different techniques have been proposed; Liu and Katz (2006) used an omni-directional virtual boundary integration scheme, while the average value from different integration paths from neighbouring grid points have been used by Baur and Kongeter (1999) in order to minimize the random errors in the acceleration. Gurka et al. (1999) proposed further differentiation in order to solve the Poisson equation for pressure:

$$\nabla^2 p = -\rho \nabla \cdot \left( \frac{D\mathbf{V}}{Dt} + \nu \nabla^2 \mathbf{V} \right) \quad 6.2$$

If compared with integration path based techniques, this approach reduces the non-isotropic propagation of local errors. The pressure evaluation relies on the accuracy of the material derivative of velocity, i.e. the time rate of change of the velocity evaluated along a moving fluid element. The relation between the material derivative and the Eulerian time rate of change, involves the velocity gradient and reads as:

$$\frac{D\mathbf{V}}{Dt} = \frac{\partial \mathbf{V}}{\partial t} + (\mathbf{V} \cdot \nabla) \mathbf{V} \quad 6.3$$

To date the material derivative has been evaluated from velocity fields obtained by PIV either with an Eulerian or Lagrangian approach. In a comparison between the two methods by Violato et al. (2011) and Ghaemi et al. (2012) it is shown that the Lagrangian method offers the advantage of being less sensitive to truncation errors when the time separation is made longer. The difference is particularly pronounced in flows dominated by convection (e.g. boundary layers and wakes). The Lagrangian approach from tomographic PIV over a

thin volume has been applied by Ghaemi et al. (2012) to investigate pressure fluctuations in a fully developed turbulent boundary layer. Therefore the Lagrangian approach for PIV is chosen as the reference method and its results are taken as term of comparison for the performance assessment of the Tomo-3D-PT technique (section 6.4 and 6.5).

### 6.2.1 Fluid parcel trajectory reconstruction from PIV data

The technique is based on the reconstruction of a fluid particle trajectory over a number of PIV recordings. At a time instant  $t_0$  and spatial location  $\mathbf{x}_{t_0}$  the trajectory is assumed to be tangent to the velocity vector obtained by cross-correlation analysis (Figure 6.4-top). The position of the particle along the trajectory at the previous and subsequent instant is estimated as:

$$\begin{aligned}\mathbf{x}_{t_0-\delta t} &= \mathbf{x}_{t_0} - \mathbf{V}_{t_0} \cdot \delta t \\ \mathbf{x}_{t_0+\delta t} &= \mathbf{x}_{t_0} + \mathbf{V}_{t_0} \cdot \delta t\end{aligned}\tag{6.4}$$

where  $\delta t$  is the time separation between the recordings.

The velocity of the fluid particle at time instants  $t_0-\delta t$  and  $t_0+\delta t$  can be evaluated by spatial interpolation from the correspondent velocity fields from PIV at  $\mathbf{x}_{t_0-\delta t}$  and  $\mathbf{x}_{t_0+\delta t}$  respectively. With the same principle the trajectory can be extended over a longer sequence; Figure 6.4-top shows an example of trajectory reconstruction over 5 exposures. As a result, a truncation error  $\varepsilon_t$  is introduced due to the linear approximation of the trajectory between subsequent recordings; this error increases with the length of the reconstructed sequence.

The Lagrangian derivative is then computed by finite difference of the velocity as:

$$\frac{D\mathbf{V}}{Dt}(\mathbf{x}_{t_0}, t_0) \approx \frac{\mathbf{V}(\mathbf{x}_{t_0+\Delta T}, t_0 + \Delta T) - \mathbf{V}(\mathbf{x}_{t_0-\Delta T}, t_0 - \Delta T)}{\Delta T}\tag{6.5}$$

where

$$\Delta T = (n - 1) \cdot \delta t\tag{6.6}$$

indicates the time separation between the beginning and the end of the reconstructed trajectory ( $n$  being the number of exposures). Increasing the time separation  $\Delta T$  lowers the precision (random) error of the material derivative estimate; instead a short time separation, the velocity difference in equation 6.5 can be in the same range as the precision error for the velocity leading to a material derivative affected by large random error.

On the other hand the truncation error  $\varepsilon_d$  increases with  $\Delta T$ ; Figure 6.4-bottom shows the truncation error for different choices of  $\Delta T$  in the hypothesis of a perfectly reconstructed trajectory. In a real case, the error due to the finite difference ( $\varepsilon_d$ ) would add to the one due to the trajectory reconstruction ( $\varepsilon_t$ ). In conclusion, the optimal choice of time separation is obtained as a well-known trade-off between random and bias errors. A similar discussion has been applied to the optimization of pulse separation by Boillot and Prasad (1996). A more specific discussion of this aspect applied to time-resolved tomographic PIV data is given in Violato et al. (2011).

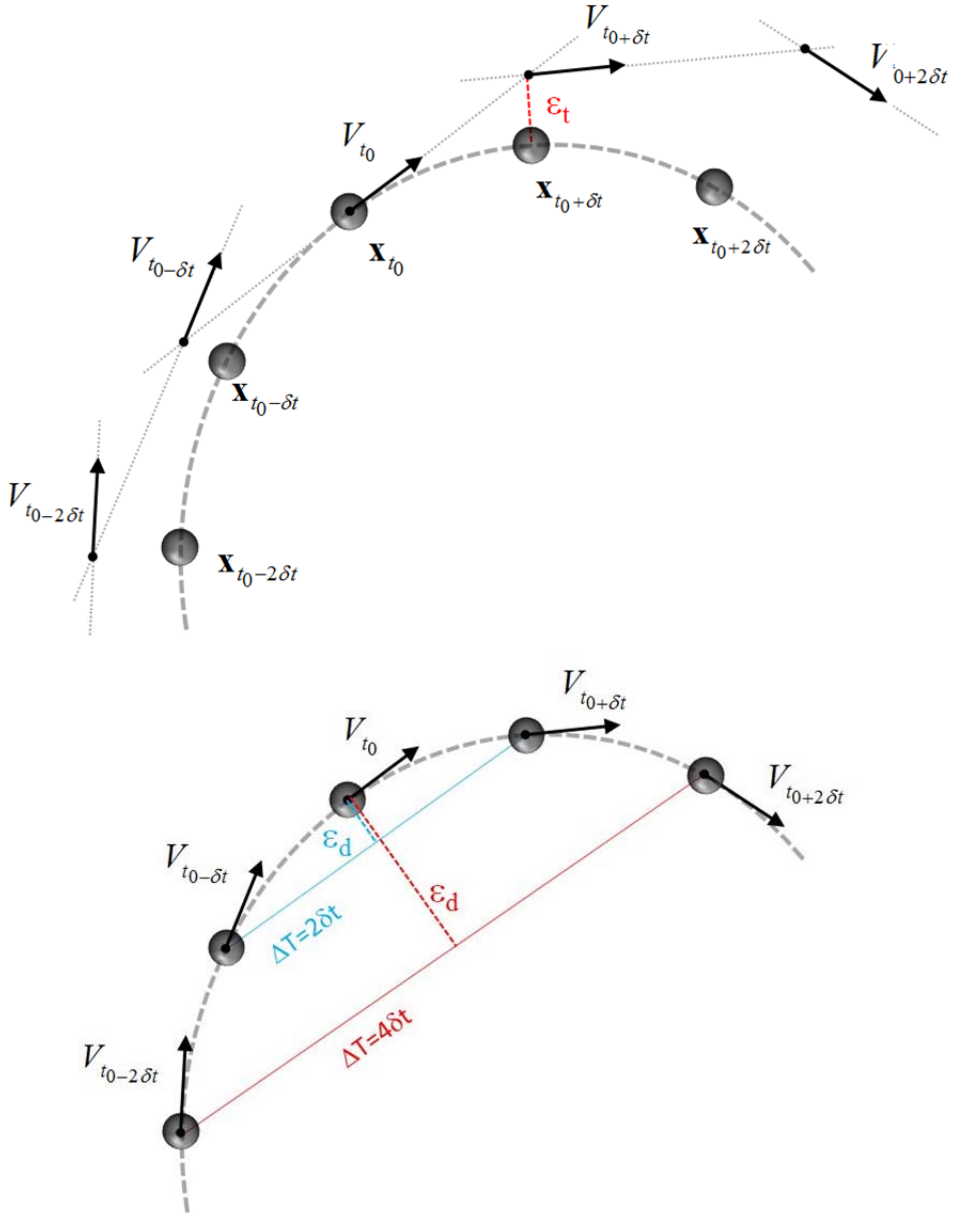


Figure 6.4 Top: truncation error ( $\epsilon_t$ ) in the trajectory reconstruction from PIV data along 5 time instants separated by  $\delta t$  (grey spheres indicate the real particle positions). Bottom: truncation error in the material derivative evaluation from finite differences ( $\epsilon_d$ ) for small and large time separation for a perfectly reconstructed trajectory.

### 6.3 The Tomo-3D-PT approach

Three dimensional particle tracking velocimetry (Maas et al. 1993) is a technique based on reconstruction of single particle trajectories over long sequences and it allows an accurate evaluation of the Lagrangian properties (Voth et al. 1998; La Porta et al. 2000). If compared with the PIV based trajectory reconstruction technique, the PTV approach avoids the propagation of the error when reconstructing the particle trajectory. Moreover, when the location of the particle is known as a function of time, a high-order fitting function can be used to reduce the random error in the particle location and the velocity and acceleration can be computed analytically from the fitting function, thus reducing the truncation error introduced by finite differences  $\varepsilon_d$  (Figure 6.4-bottom).

The major drawback of the 3D-PTV technique consists in the limitation on the achievable seeding density within the measurement domain. Since particles are identified and matched on the camera images, ambiguities and errors in their triangulation in 3D space strongly affect the result when the average distance between particles decreases, with the probability of overlapping particles becoming higher. The typical imaged seeding density reported in 3D-PTV experiments is 0.005 *ppp* (particles per pixel). As a consequence, the information provided by particle tracking is highly sparse and not suitable for the pressure field evaluation, where dense information on a regular grid is needed for spatial gradients to be computed, equation 6.1. On the other hand, tomographic PIV (Elsinga et al. 2006) is performed at a seeding density of 0.05 *ppp* or even higher (Novara and Scarano 2012).

The aim of the Tomo-3D-PT approach is to combine the advantages of the two techniques; on the one hand the reconstruction of trajectories from PTV enables the computation of the material derivative with a high accuracy. On the other hand, the higher spatial information density provided by the tomographic reconstruction leads to results with a higher spatial resolution, which can be interpolated and spatially differentiated.

Unlike for standard 3D-PTV techniques, tracking particle tracers in 3D space is significantly less prone to ambiguities. Indicating with *ppv* (particles per voxel) the seeding tracers concentration in the measurement domain, the imaged seeding density is obtained as:

$$ppp = ppv \cdot \Delta Z \quad 6.7$$

where  $\Delta Z$  is the size of the reconstructed volume along the viewing direction (in voxels). Following Adrian (1991), the average distance between neighboring particles can be estimated, in the 2D image and in the 3D volume respectively, as follows:

$$\begin{aligned} \bar{r}_{2D} &= 0.5 \cdot ppp^{-1/2} \\ \bar{r}_{3D} &= 0.55 \cdot ppv^{-1/3} \end{aligned} \quad 6.8$$

For instance, let us consider a tomographic PIV experiment conducted with one Mpixel cameras on a measurement domain with a width-to-depth ratio of 10:3 ( $\Delta Z=300$  voxels). If the particle image density is *ppp*=0.04, the average distance between particles in the 3D reconstructed object would be of 10 voxels against 2.5 pixels in the camera images. Moreover, the robustness of the tracking algorithm benefits from the relatively small displacement of the tracers between the recordings and from the availability of predictor fields from PIV analysis of the reconstructed objects.

### 6.3.1 Trajectory reconstruction

Trajectories are reconstructed following the particle position over  $n$  recordings, which defines the observation time  $\Delta T$  (equation 6.6). Reconstructed particles are identified in the 3D object at time  $t_0$  by means of a local maxima search. A threshold value, based on the particle intensity on the camera image, is set for the particle peak intensity in order to discard spurious intensity peaks (*ghost particles*) present in the tomographic reconstruction. Sub-voxel precision in the particle peak location is achieved using a Gaussian fit in the three spatial dimensions, analogous to that used for the sub-pixel analysis of the correlation peak position in PIV (Willert and Gharib 1991). A velocity field predictor obtained from cross-correlation of reconstructed objects at time  $t_0$  and  $t_0 + \delta t$  (blue vector in Figure 6.5-left) is used to guess the particles locations in the subsequent object ( $\mathbf{x}_{t_0 + \delta t}^g$ ). Cross-correlation is performed using 3D iterative window deformation technique (VODIM, Scarano and Poelma 2009).

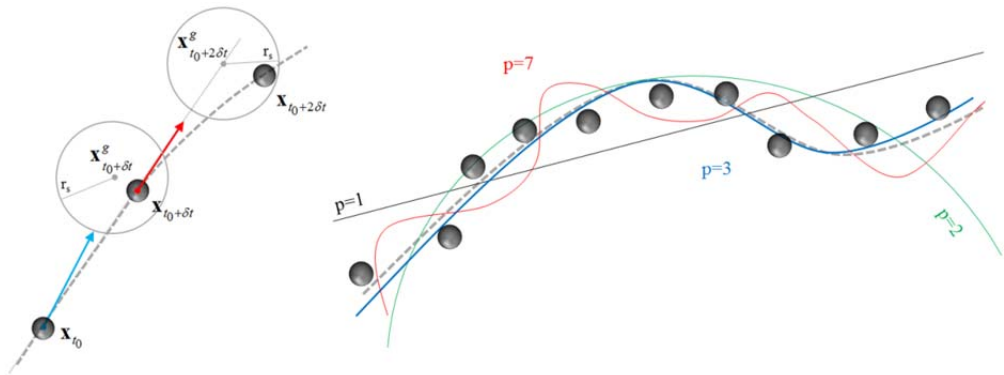


Figure 6.5 Left: particle tracking algorithm along the first three recordings in the sequence; predictor from cross-correlation in blue, predictor from tracked particle displacement in red. Search region for particle peak location identified by  $r_s$ . Right: trajectory polynomial fit in case of random error on reconstructed particle location;  $p$  is the order of the polynomial (grey dashed line represents the actual trajectory).

A search region with radius  $r_s$  (typically 2 to 3 voxels) is considered to search for the particle at the subsequent recording; for a large average distance between particles any ambiguous pairing is avoided. Once the particle at  $t_0 + \delta t$  is found, the difference  $\mathbf{x}_{t_0 + \delta t} - \mathbf{x}_{t_0}$  is used to obtain the displacement predictor (red vector in Figure 6.5-left) to estimate the particle location in the subsequent recording ( $\mathbf{x}_{t_0 + 2\delta t}^g$ ). Alternatively, a predictor field can be computed between each couple of recordings by means of cross-correlation analysis, which increases the accuracy of the peak location estimate in regions exhibiting strong gradients at the cost of higher computational time. For the cases presented in this study, both synthetic and experimental, no substantial difference in the tracked particles was found between the two predictors.

Particles identified along the whole sequence compose a trajectory. *Ghost particles* do not interfere with the process since their temporal coherence is relatively short and they do not

result in consistent trajectories over a long observation time (Elsinga et al. 2011; Novara and Scarano 2012). On the other hand, actual particles might also be discarded when exhibiting strong temporal fluctuations of the peak intensity. This situation can derive from poor stability of illumination, noisy imaging or excessive seeding density. Methods that deal with intermittent trajectories can be devised, however, they have not been investigated in the present study. After a particle has been tracked over the sequence, a polynomial fit is applied to the trajectory as follows:

$$\begin{aligned} x(t) &= a_p t^p + a_{p-1} t^{p-1} + \dots a_1 t + a_0 \\ y(t) &= b_p t^p + b_{p-1} t^{p-1} + \dots b_1 t + b_0 \\ z(t) &= c_p t^p + c_{p-1} t^{p-1} + \dots c_1 t + c_0 \end{aligned} \quad 6.9$$

where  $a_i$ ,  $b_i$  and  $c_i$  are the coefficient of the polynomial representation of the position with order  $p$ . This approach is expected to largely reduce random errors (especially when  $n \gg p$ ) introduced in the particle location by the reconstruction process (e.g. real imaging effects, limited aperture of the tomographic system, discretization effects), Figure 6.5-right.

The material derivative is then analytically evaluated at the centre of the trajectory. The spatially scattered data is interpolated on a regular grid to allow the further evaluation of spatial derivatives (see sections 6.4.2 and 6.4.3).

## 6.4 Numerical assessment

In order to assess the tracking procedure and to quantify the effect of the trajectory fit, a procedure based on simulated tomographic PIV data is followed. Particles with a diameter of 2 voxels are generated by Monte-Carlo technique in a volume of  $500 \times 420 \times 500$  voxels (along  $X$ ,  $Y$  and  $Z$  direction respectively). Trajectories are generated integrating a known displacement field, therefore the particle position, velocity and acceleration are known at each time instant.

A Gaussian vortex ring superimposed with a uniform motion along  $Y$ , yielding an advecting vortex, Figure 6.6-top. The diameter of the vortex ring is 180 voxels and the advection displacement is 6 voxels. The tangential velocity induced by the Gaussian vortex reads as:

$$V_g = \frac{\Gamma}{2\pi r} \left( 1 - e^{-\frac{r^2}{c_g}} \right) \quad 6.10$$

where  $r$  is the distance from the point to the vortex axis in the plane normal to the vortex axis. The circulation  $\Gamma$  and  $c_g$  are computed as:

$$\Gamma = \frac{2\pi r_c^2}{v_r} \quad c_g = \frac{r_c^2}{\gamma} \quad 6.11$$

where  $r_c$  is the vortex radius (50 vox) and the tangential displacement at the vortex radius (6 vox);  $\gamma$  is a constant equal to approximately 1.26. The particles seeding concentration is approximately  $1.5 \cdot 10^{-4}$  particles/voxels ( $ppv=0.00015$ ) a realistic value for Tomo-PIV experiments; a subset of particle trajectories is shown in Figure 6.6-bottom. The position of

the particles is purposely corrupted with random noise ( $\varepsilon_r$ ) that simulates a typical registration error of 0.2 voxels.

### 6.4.1 Particle tracking

The error on the particle peak position along the  $X$  direction is computed as:

$$\varepsilon_{rX} = X_{p,meas} - X_{p,actual} \quad 6.12$$

where  $X_{p,meas}$  indicates the measured peak position and  $X_{p,actual}$  the exact one. Only the  $X$  component of the location error is analyzed in the following; the same considerations apply for the other two components.

The standard deviation of the particle peak position error is presented in Figure 6.7-left. An optimal length for the trajectory ( $n$ ) can be identified for different order of the polynomial fit ( $p$ ). A third order polynomial appears to minimize the error when 15 exposures are considered; when the sequence is longer, a higher order ( $p=5$ ) better suits the trajectory curvature. When  $p$  is larger than 5 oscillations are generated which affect the accuracy of the trajectory fit.

At relatively low order of the polynomial ( $p=3$ ) and for an observation encompassing 23 recordings, the error is increased, which is justified by truncation errors. The representation of the error dispersion through the PDF shows that for long trajectories with low polynomial order, a high error probability is also found for large values of the error (around 0.6 vox), blue line in Figure 6.7-right. On the other hand, the Gaussian dispersion of the error becomes broader when  $n/p$  approaches unity. For instance, when particles are tracked over only 5 recordings, the reduction of the random error, indicated by the width of the PDF distribution, is minimal, (red line in Figure 6.7-right). In the most favourable condition ( $p=5$  and  $n=21$ ,  $n/p=4$ ) the standard deviation of the error is reduced from 0.22 vox to 0.14 vox.

### 6.4.2 Evaluation of Lagrangian acceleration

The three components of the material derivative ( $DU/Dt$ ,  $DV/Dt$ ,  $DW/Dt$ ) are obtained in each point of the trajectory by analytically computing the second time derivative of the fitting polynomials in equation 6.9. An example of the fluid particle acceleration along the particle trajectory is shown in Figure 6.6-bottom. The error on the axial component of the acceleration ( $\varepsilon_{aY}$ ) is computed as the difference between the measured value and the actual one:

$$\varepsilon_{aY} = \frac{DV}{Dt}_{meas} - \frac{DV}{Dt}_{actual} \quad 6.13$$

The same applies for the components along  $X$  and  $Z$ . For the error analysis, the values of material derivative in the central point of the trajectory are considered since a lower accuracy is attained by the polynomial fit at the extremes of the sequence. The acceleration is obtained at particle locations scattered in the 3D domain and compared with the exact values.

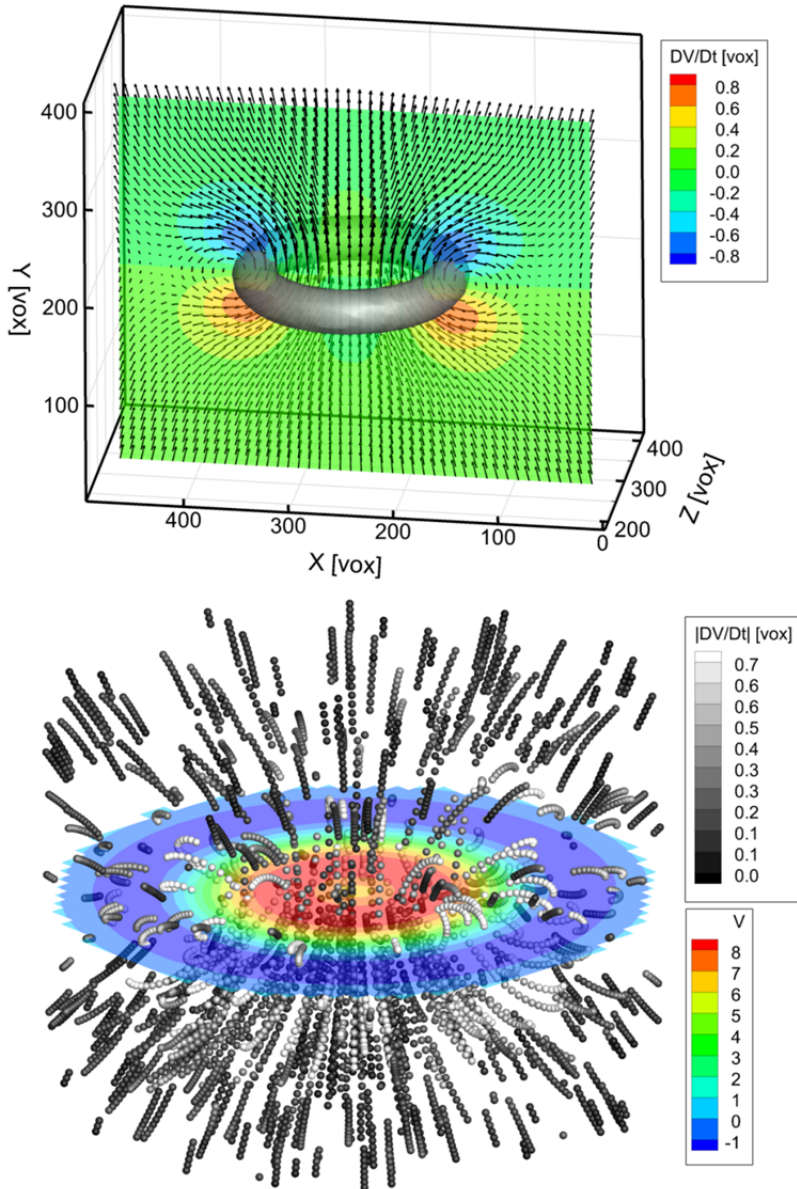


Figure 6.6 Top: instantaneous vorticity magnitude iso-surface (0.3 vox/vox). Velocity vectors and Lagrangian derivative axial component ( $DV/Dt$ ) contours on axial data slice. Bottom: instantaneous axial displacement contours on cross-sectional data slice and sample of tracked particles trajectories along 11 exposures (markers are color-coded by the magnitude of material acceleration).

Results from the Tomo-3D-PT approach are compared with the trajectory reconstruction from velocity field by Tomo-PIV varying the sequence length  $n$ . For the PT technique the optimal trajectory fit  $p$ , is chosen based on Figure 6.7, depending on the trajectory length.

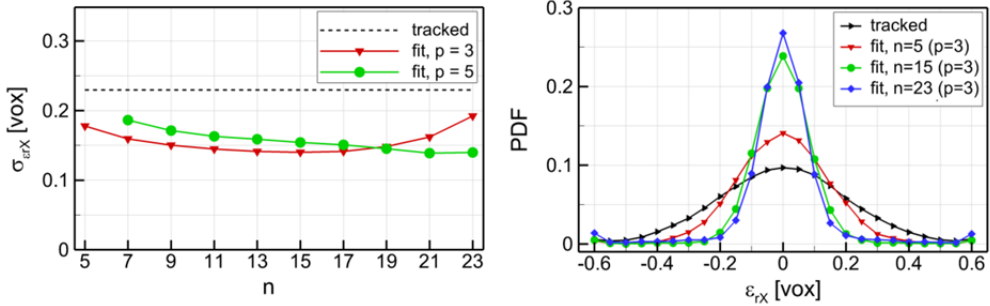


Figure 6.7 Left: standard deviation of the particle peak location error as a function of the trajectory length  $n$ ; results from different polynomial fit order ( $p$ ) compared with result from particle tracking alone. Right: probability density function of the position error for tracked and fitted trajectories ( $p=3$ ) varying the observation time.

Figure 6.8 shows the error on the acceleration as a vector field where the vector components are  $\epsilon_{aX}$ ,  $\epsilon_{aY}$  and  $\epsilon_{aZ}$  respectively. Vectors are color-coded based on the magnitude of the error compute as:

$$|\epsilon_a| = \sqrt{\epsilon_{aX}^2 + \epsilon_{aY}^2 + \epsilon_{aZ}^2} \quad 6.14$$

Vectors are located in the scattered points corresponding to the centre of the trajectories, where the acceleration is evaluated. The distribution of the error shows that, when the PIV based technique is applied making use of 3 exposures, the error is dominated by its random component. Conversely, when a long sequence is considered, the truncation error becomes particularly evident in the region of the vortex core. Both error components are significantly reduced with the PT approach applied with a sequence of 21 exposures. These results are quantified and summarized in Figure 6.9 where the error on the  $Y$  component of acceleration is plotted versus the actual value of the acceleration.

The diagram is made with intervals of 0.2 voxels (unit time separation is assumed) bin width and spans the range from -0.8 to 0.8 voxels. Data-points belonging to each interval are identified within the exact field and the error on the material derivative is computed as in equation 6.12. The mean value of the error is computed for each bin to obtain the curves presented in Figure 6.9; the values of  $DV/Dt$  on the abscissa indicate the centre value of each bin. Error bars represent twice the value of the standard deviation of the error. The slope of the curves is representative of the truncation error while the half-length of the error bars represents the random error.

Trajectories reconstructed by means of Tomo-PIV data over a long sequence ( $n=21$ ) exhibit large truncation error as a result of under-estimation of the trajectory curvature (Figure 6.4-top) and of the large  $\Delta T$  used for the finite difference evaluation of equation 6.5 (Figure 6.4-bottom), blue curve in Figure 6.9. The result obtained from a short sequence ( $n=3$ ) is affected by random error (red curve in Figure 6.9). A compromise in terms of trajectory length must be considered. For the present case, the best result is obtained for  $n=15$ . For the Tomo-3D-

PT approach the result obtained with  $p=5$  is virtually unaffected by bias errors with a very limited amplitude of random error (0.01 vox). A value of 0.025 is attained for the PIV based method when 15 time instants are considered (green curve in Figure 6.9). Although the error on particle location, Figure 6.7-left, is approximately the same for  $p$  equal to 3 and 5 ( $n=15$  and 21 respectively), a larger error in the material derivative is observed when the third order polynomial is used.

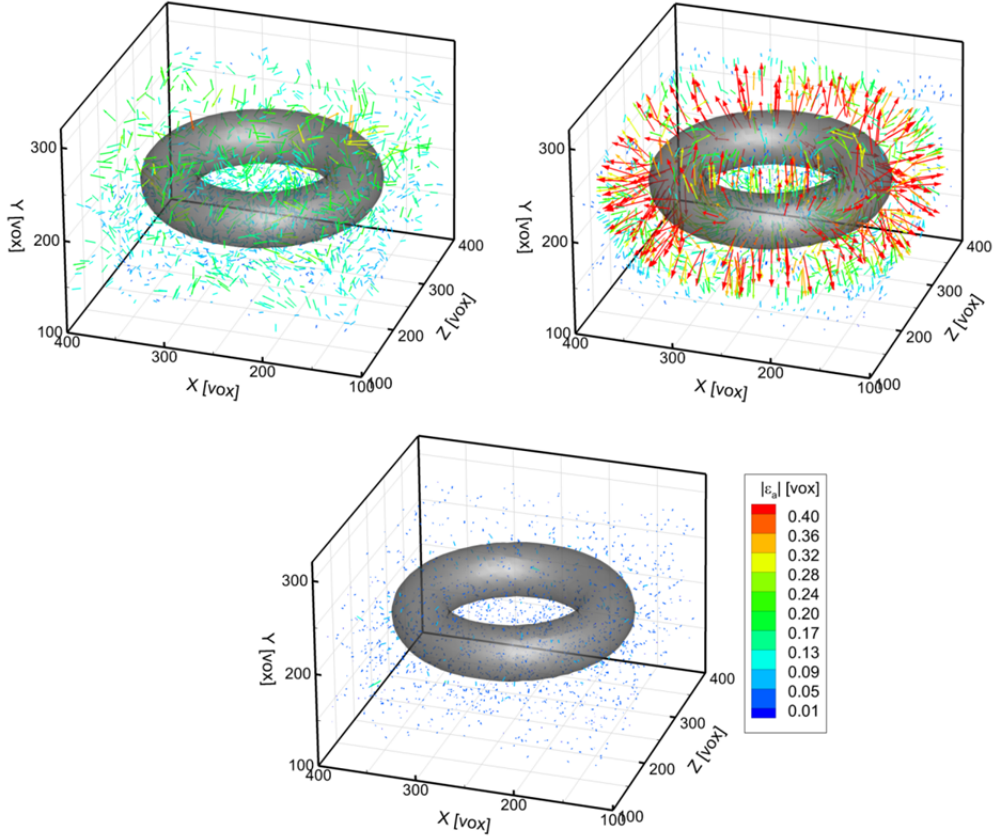


Figure 6.8 Error on the acceleration visualized by means of a vector field; vector components computed as the error on the 3 components of acceleration. Top-left: Tomo-PIV based method with  $n=3$ . Top-right: Tomo-PIV based method with  $n=21$ . Bottom: Tomo-3D-PT with  $n=21$  and  $p=5$ .

### 6.4.3 Evaluation of dense information onto regular grid

The data reduction technique to evaluate the pressure field is based on the solution of the Poisson equation, equation 6.2. This can be obtained if the divergence operator is applied to the pressure gradient, which requires data distributed on a regular grid. The material derivative information from the Tomo-3D-PT approach is obtained in scattered locations corresponding to the particle tracers position within the investigated domain. In this section,

the effect introduced by the process of redistributing the scattered data onto a regular grid is considered.

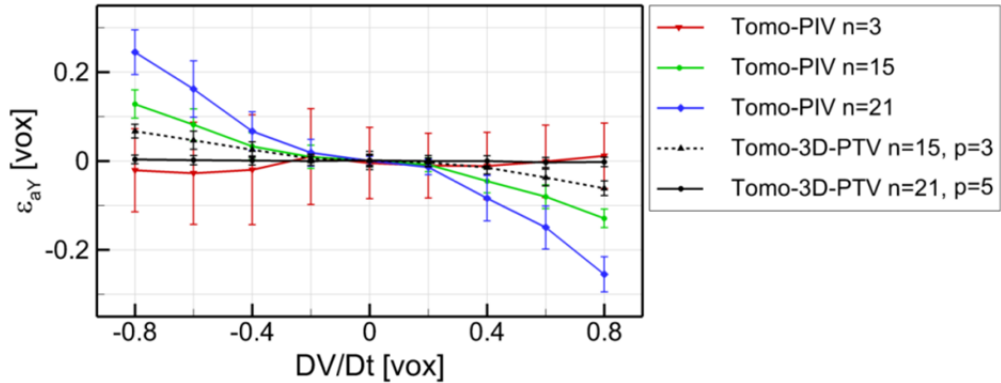


Figure 6.9 Error on the axial component of material derivative as a function of the acceleration value. Trajectory reconstruction technique by tomographic PIV and particle tracking based approach applied for different trajectory length  $n$ . Markers indicate the mean value of the error in the range of acceleration specified by the width of the bin (0.2 vox) while error bars represent twice the value of its standard deviation.

When a linear interpolation based on Delaunay triangulation of the scattered data location is applied, a significant truncation error is introduced (red curve in Figure 6.10); also the random error at large values of  $DV/Dt$  is increased. As a result, the use of a linear interpolation nullifies the improvement achieved by the particle tracking based approach as the error resembles the one achieved by the Tomo-PIV based method when 15 exposures are used (green line in Figure 6.9).

When a second order least squares regression in space is used, green curve in Figure 6.10, a moderate increase in both the truncation and precision errors is observed. For each grid-point, a second order polynomial in  $X$ ,  $Y$ , and  $Z$  is used to fit the data from a neighbourhood of scattered data points. The selection of the neighbourhood is based on the distance between the scattered and the grid point; for this study a region having a volume comparable to the one of the cross-correlation interrogation box for Tomo-PIV has been chosen to obtain the same spatial resolution with the two methods.

The comparison between the PIV based method and the Tomo-3D approach, Figure 6.11, confirms the potential of the technique in reducing both the precision error, introduced when a short sequence is exploited by the Tomo-PIV method (Figure 6.11-top-left), and the truncation error, attained when the observation time increases (Figure 6.11-top-right). For the synthetic vortex data, the highest accuracy is achieved when particles are tracked over a long sequence (21 recordings) and a fifth order polynomial is used to fit the tracked trajectories (Figure 6.11-bottom).

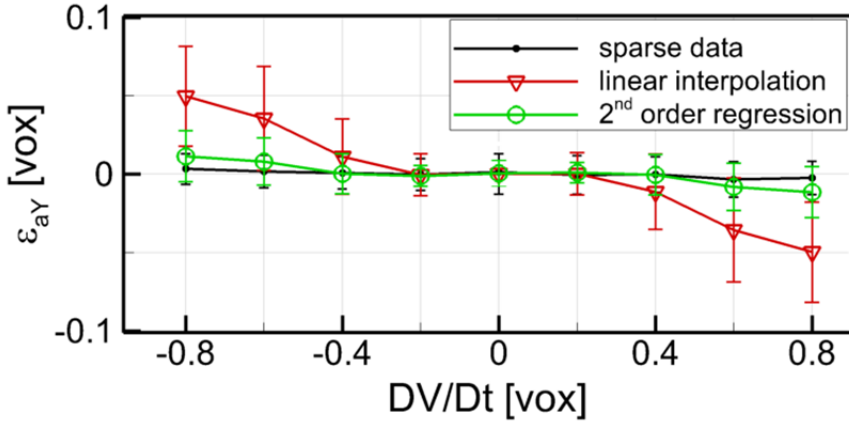


Figure 6.10 Error on the axial component of material derivative as a function of the acceleration value for the sparse data from Tomo-3D-PT and for the dense data on regular grid obtained by linear interpolation and second order spatial regression ( $n=21$ ,  $p=5$ ).

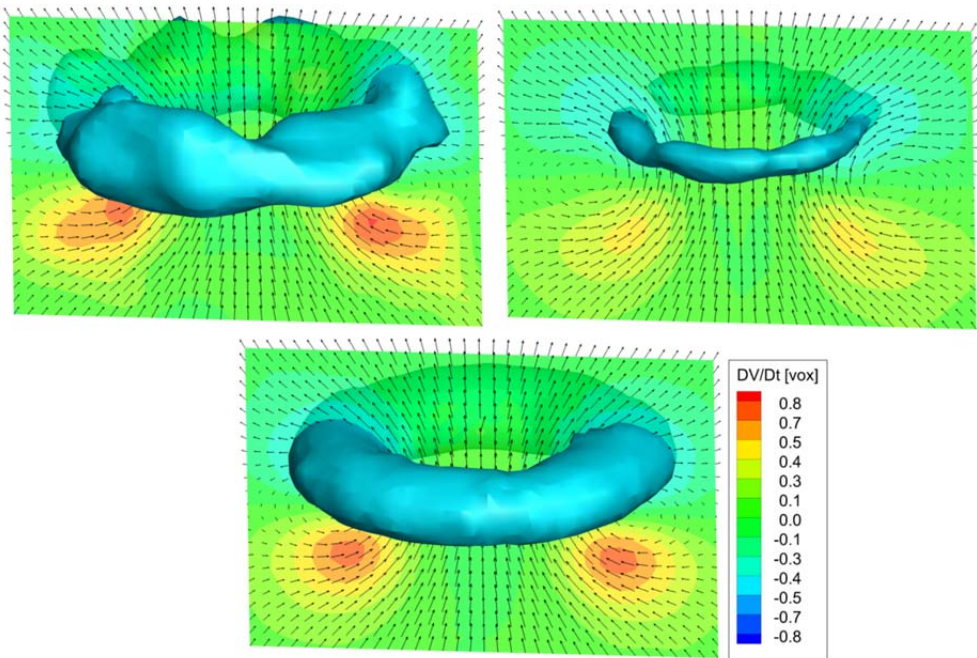


Figure 6.11 Iso-surface of instantaneous axial component of the Lagrangian acceleration ( $-0.5$  vox). Velocity vectors and Lagrangian derivative axial component contours on axial data slice. Top-left: Tomo-PIV based method with  $n=3$ . Top-right: Tomo-PIV based method with  $n=21$ . Bottom: Tomo-3D-PT with  $n=21$  and  $p=5$ .

The density of the sparse information affects the random error introduced by the data fitting on regular grid. When the particle seeding density is 10 times lower, a typical value for the 3D-PTV technique, an increase of a factor 5 in the precision error is observed after the spatial regression is applied.

## **6.5 Experimental results**

The particle tracking based technique is applied to data from a Tomo-PIV experiment of a jet flow in water. A transitional jet at  $Re_D=5,000$  (where  $D=10$  mm is the nozzle diameter) is issued in a  $60\times 80$  cm octagonal Perspex tank. The illumination is provided by a Quantronix Darwin-Duo Nd:YLF laser ( $2\times 22.5$  mJ/pulse at 1kHz) and the imaging system is formed by four Photron Fastcam SA1 cameras with a CMOS sensor of  $1024\times 1024$  pixels (pixel size is 20  $\mu\text{m}$ ); Nikon objectives of 105 focal length have been used. The acquisition frequency is 1,000 Hz. A 30 mm diameter cylindrical laser beam aligned with the jet axis is obtained by means of a Linos expander; the field of view is approximately  $50\times 50$  mm yielding to a resolution of 20 pixels/mm. The measurement domain extends from the jet exit to five diameters downstream. Polyamide particles are used as seeding at a concentration of 0.7 particles/mm<sup>3</sup>. A more detailed description of the facility and experimental conditions can be found in Violato and Scarano 2011 and in section 4.9.1 of this thesis.

Reconstructed objects of  $669\times 1060\times 523$  voxels are analyzed with cross-correlation making use of a  $40\times 40\times 40$  voxels interrogation region. The same volume is chosen to select the neighborhood of scattered data-points when fitting the results from Tomo-3D-PT onto the regular grid by means of second order spatial regression. The jet flow is characterized by a laminar shear layer at the jet exit; approximately 1.5 diameters downstream Kelvin-Helmholtz instabilities lead to the formation of vortex rings which later pair.

### **6.5.1 Lagrangian derivative evaluation**

The flow field around a vortex ring approximately two diameters downstream the nozzle is shown in Figure 6.12; the result from the PIV based trajectory reconstruction technique making use of 3 and 11 exposures is compared with the one from the tracking method.

The same considerations made for the synthetic data apply for the experimental case; when a short sequence is used to reconstruct the trajectories with the PIV based method the precision error is dominant, Figure 6.12-top-left. Instead, a long observation time  $\Delta T$  results in a reduction of random error in favour of the truncation error. The loss of peak intensity visible in Figure 6.12-top-right is recovered when the particle tracking technique is applied, Figure 6.12-bottom; in this case the shape and the intensity of the iso-surface of material acceleration suggest a reduction of both the random and the truncation error.

The time history of the axial component of the material derivative at a position crossed by vortices shed in the shear layer shows an improvement in the temporal coherence for the Tomo-3D-PT result; the spurious oscillations visible for the Tomo-PIV technique when 3 or 5 exposures are used are visibly reduced. On the other hand, the magnitude of the physical fluctuation does not appear to be damped or low-pass filtered, by the use of longer trajectories as it occurs for the PIV based method (Figure 6.13).

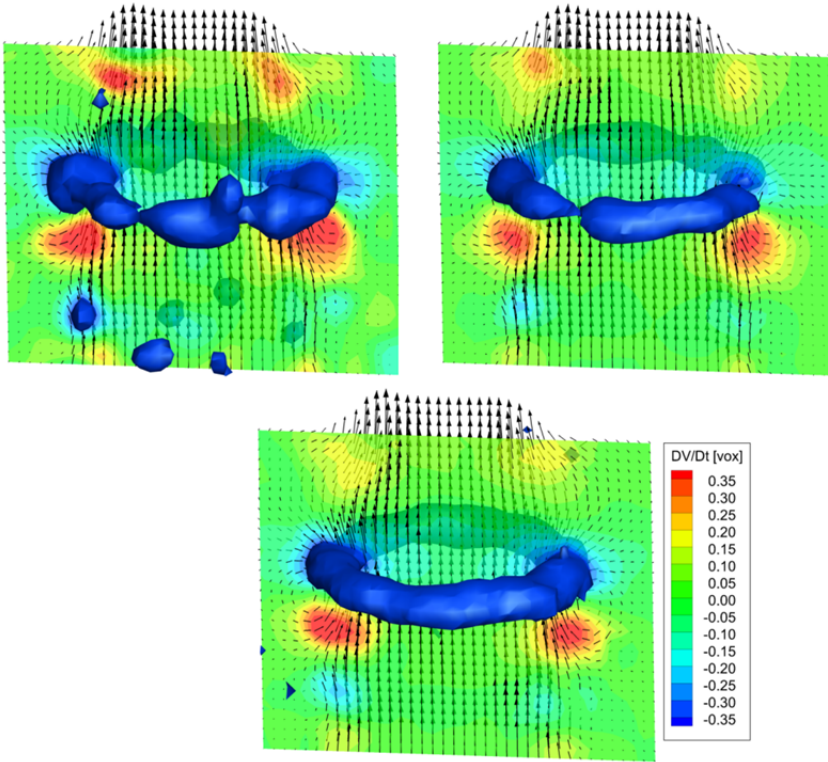


Figure 6.12 Detail of a vortex ring in the jet flow at around 2 diameters downstream the nozzle exit. Iso-surface of axial component of Lagrangian acceleration ( $DV/Dt=-0.3$  vox); velocity vectors and contours of  $DV/Dt$  on axial data slice. Top-left: Tomo-PIV based method with  $n=3$ . Top-right: Tomo-PIV based method with  $n=11$ . Bottom: Tomo-3D-PT with  $n=11$  and  $p=3$ .

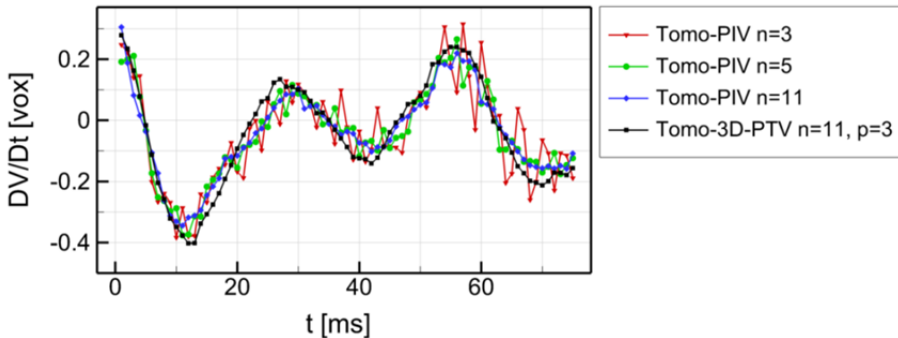


Figure 6.13 Time history of axial component of the material acceleration in a point located approximately 2.5 diameter downstream the nozzle exit, along the path of the vortex ring core region. The method based on trajectory reconstruction from Tomo-PIV data is compared with the Tomo-3D-PT technique.

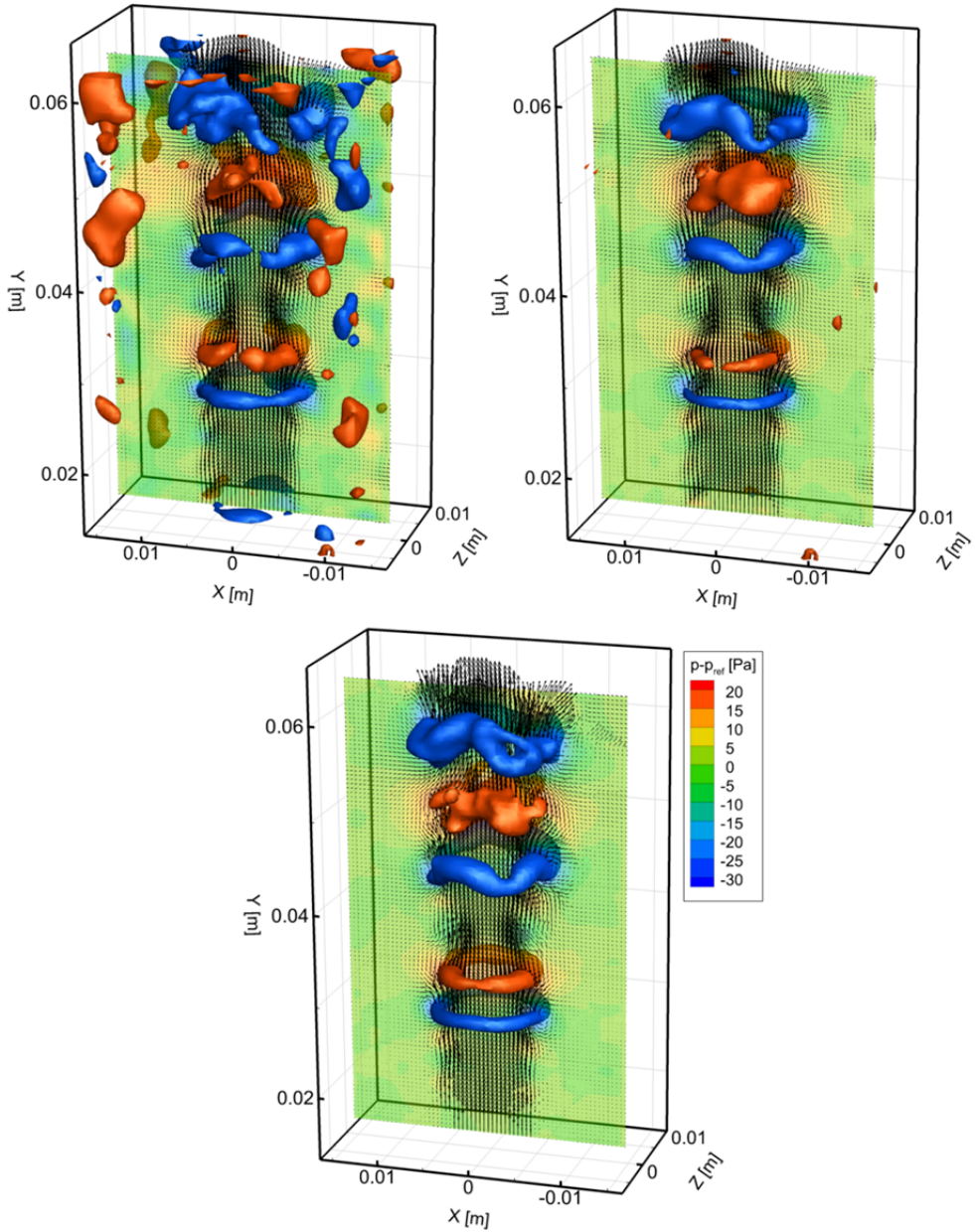


Figure 6.14 Iso-surfaces of pressure in the jet flow (blue  $p - p_{ref} = -23$  Pa, red  $p - p_{ref} = 15$  Pa). Top-left: Tomo-PIV based method with  $n=3$ . Top-right: Tomo-PIV based method with  $n=11$ . Bottom: Tomo-3D-PT with  $n=11$  and  $p=3$ .

## 6.5.2 Pressure field evaluation

The three-dimensional pressure field is obtained from the accelerations field solving the Poisson equation (equation 6.2). Neumann boundary conditions are applied on the sides of the domain normal to the jet axis ( $XZ$  planes) as:

$$\nabla p = -\rho \frac{D\mathbf{V}}{Dt} \quad 6.15$$

while Dirichlet conditions are imposed on the lateral surfaces of the domain ( $XY$  and  $ZY$  planes). Since these edges are far from the jet region in the centre of the domain, the assumption of steady and irrotational flow is made and the value of the pressure is obtained invoking Bernoulli's equation as:

$$p - p_{ref} = \frac{1}{2} \rho (|\mathbf{V}_{ref}^2| - |\mathbf{V}^2|) \quad 6.16$$

Iso-surfaces of pressure are shown in Figure 6.14; the pressure field is obtained from the material derivative computed with the PIV based and PT based methods. The same considerations made with regard to the acceleration field can be made, where the result from PIV suffers from random and truncation error depending on the length of the sequence (3 and 11 recordings respectively), Figure 6.14-top-left and Figure 6.14-top-right. The result from Tomo-3D-PT combines a lower level of precision error with a recovery of the positive and negative peak of pressure, where the latter is found in correspondence with the location of the vortex-cores, Figure 6.14-bottom.

Also the time-history of the pressure confirms the observations made for the single snapshot, where the signal from the particle-tracking approach, black line in Figure 6.15, exhibits higher time-coherence when compared to the result from the PIV approach with  $n$  equal to 3 and 5 (red and green lines in Figure 6.15). At the same time the pressure signal does not suffer from the modulation observed for the PIV-based method with  $n=11$ , blue line in Figure 6.15.

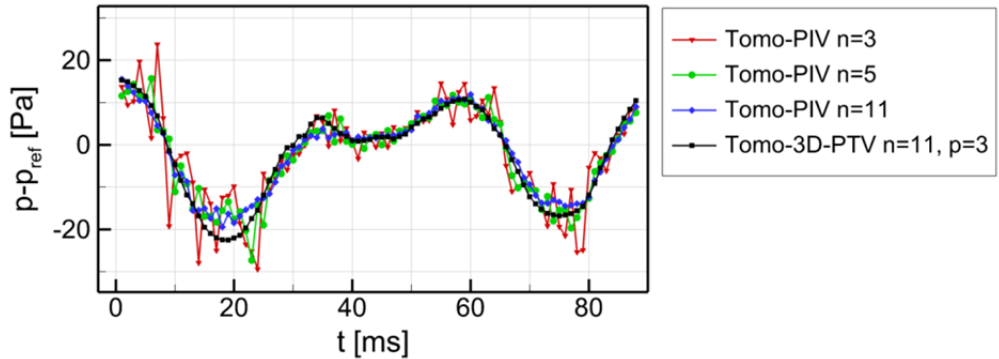


Figure 6.15 Time-history of pressure in a point located approximately 2.5 diameter downstream the nozzle exit, along the path of the vortex ring core region for the PIV (3, 5 and 11 recordings) and for the particle-tracking (11 recordings and 3<sup>rd</sup> order polynomial for the trajectory fit) approaches.

## **6.6 Conclusions**

A particle tracking based technique to increase the accuracy of the material derivative evaluation from time-resolved tomographic PIV data (Tomo-3D-PT) has been investigated. The tracking algorithm is performed on three-dimensional reconstructed objects from Tomo-PIV and benefits from the relatively large distance between particle tracers in the physical space as opposed to the higher particle density on the image projections. Results from the analysis of synthetic generated data of an advecting vortex ring show the suitability of the technique in reconstructing particle trajectories over long sequences; the accuracy of the particle peak location in case of reconstruction errors is enhanced by the polynomial fit of the trajectories. The material derivative is evaluated analytically as the second temporal derivative of the function fitting the particle position.

When compared to results from the PIV-based technique, a reduction of the precision error on the material derivative up to a factor 2.5 is attained due to the longer observation time. On the other hand the truncation error introduced by the Tomo-PIV method is almost completely eliminated when Tomo-3D-PT is applied, due to the accurate trajectory reconstruction and to the analytical evaluation of the acceleration that avoids the error caused by the finite differences. Scattered data obtained at random particle locations within the 3D domain are fitted to a regular grid, which is required for the evaluation of the pressure gradient. The precision and truncation errors introduced by a linear interpolation are significant. Instead, data reduction on a regular grid can be obtained without degrading the information when a second order spatial regression is applied.

The potential of the method in increasing the overall accuracy of the material derivative is confirmed when the technique is applied to data from a Tomo-PIV experiment of a transitional jet. A significant reduction of both precision and truncation error is indicated by visual inspection of the 3D material derivative and the time history at selected locations.

The three-dimensional pressure field is evaluated by means of the solution of the Poisson equation. The results confirm the overall effectiveness of the present approach in reducing random and truncation errors exhibited by the results obtained following the PIV based approach.

# Chapter 7

## Conclusions

In this chapter the main results and conclusions of this thesis are summarized and put into perspective regarding the development of tomographic PIV.

### 7.1 Motion Tracking Enhancement

A novel technique to improve the accuracy of the MART reconstruction of tomographic PIV recordings has been presented. The working principle and the theoretical background have been described and the performances of the MTE-MART reconstruction method assessed by means of two-dimensional simulations of both double-frame and time-resolved data.

Results show that the effect of the MTE technique is comparable to that of increasing the number of cameras in the imaging system, largely reducing the number and intensity of the *ghost particles*. As a result the seeding density can be increased by a factor 3 for double-frame data. The use of more recordings in case of time-resolved data appears to further improve the reconstruction quality. The effect on the accuracy of the displacement field follows the one of the reconstruction accuracy as a reduction up to a factor 3 and 10 in the precision error on velocity is obtained after MTE is applied for double-frame and time-resolved data respectively. The robustness of the MTE algorithm with respect to large errors in the measurement has been verified; it is concluded that, in the worst case scenario, the Motion Tracking Enhancement approach returns a result comparable to the one from MART reconstruction. Based on the analysis of synthetic data, the MTE technique could enable increasing up to a factor 3 the seeding particle concentration possibly leading to experiments with more than 100,000 particles/Mpixel.

The technique is applied to data from a tomographic experiment of a transitional jet in water at  $Re_D=5,000$  ( $D$  is the nozzle diameter). The performances of MTE with a 3-camera tomographic system are assessed by means of comparison with results obtained with an additional camera. The analysis of the relative quality factor confirms the results obtained in the simulations. A model to predict the reconstruction quality improvement is introduced together with the concept of MTE efficiency; results appear to be in good agreement with the

theoretical prediction. A 20% reduction in the relative precision error on velocity is achieved after the application of MTE.

The application of MTE on data from an experiment of a turbulent boundary layer over an airfoil in air ( $Re_c=370,000$ ,  $c$  being the airfoil chord) allows a seeding density of approximately 4 times higher than currently practiced ( $ppp=0.2$ ). The measurement accuracy is estimated by means of the cross-correlation signal-to-noise ratio (up to a factor 3 increase after MTE is applied) and by the height of the spatio-temporal correlation function between subsequent time instants (under the hypothesis of *frozen turbulence*). Based on this assessment method, a 40% and 20% reduction of the precision error are attained for the streamwise and the other components respectively when MTE is performed.

## 7.2 Adaptive cross-correlation

An adaptive cross-correlation technique for 3D-PIV has been proposed. Interrogation volumes are stretched and oriented along the direction of minimum velocity variation in order to minimize the presence of velocity differences between particles belonging to the same interrogation region. The adaptive criterion is based on the singular value decomposition analysis (SVD) of the local velocity gradient tensor.

The working principle is verified by means of numerical simulated data of a planar shear-layer (1-D fluctuation) and of a vortex tube (2-D fluctuation). The achievable reduction of the interrogation region size along the directions of velocity variations is estimated taking into account the maximum aspect ratio and the spatial dimensions of the flow fluctuation. For the one-dimensional case the minimum interrogation ellipsoid size is reduced by 2.5 times with respect to the spherical isotropic case. In the vortex case the reduction is limited to a factor 1.5. Any further increase of spatial resolution for the determination of the velocity gradient will require a reduction of the distance between neighboring vectors.

The application to the experimental data confirms a significant improvement of the vorticity field in the jet shear layer; the vorticity peak increases of around 25% as a result of the lower signal modulation. A limited effect is seen for the vortex peak vorticity which increases of about 5%, in line with the estimated moderate reduction in terms of interrogation region size.

For the turbulent boundary layer case, a significant improvement in the description of the mean and fluctuating properties of the streamwise component in the near-wall region is observed and the amplitude of ringing artifacts in the vorticity profile is reduced by approximately 45% when the adaptive correlation is applied.

## 7.3 Acceleration evaluation by Tomo-3D-PT

A technique to evaluate the material derivative of velocity from time-resolved Tomo-PIV data has been introduced. The method exploits the concept of particle tracking in order to accurately reconstruct particle trajectories over a long sequence of recordings. The tracking algorithm is simplified by the relatively large distance between neighbouring particle tracers in the 3D domain if compared to the 2D image.

Results from Tomo-3D-PT have been compared to those obtained reconstructing fluid parcel trajectories making use of velocity vector fields from 3D cross-correlation. The analysis of computer generated data of an advected vortex ring shows that the use of a polynomial fit

reduces the error in the tracked particle peak location. The use of long trajectory and the analytical evaluation of the material derivative produces nearly a complete cancellation of the truncation error and a reduction of the precision error on the acceleration components of a factor 2.5. Scattered data obtained at random particle locations within the 3D domain are fitted to a regular grid without a significant loss accuracy in the measured acceleration.

The visual inspection of acceleration iso-surfaces for the transitional jet experimental case confirms a strong reduction of both the truncation and random errors. Results are confirmed by the time-history of material derivative which shows higher coherence than the PIV based technique, without compromising the signal fluctuations amplitude. The same considerations apply for the 3D pressure field evaluated from the acceleration field making use of the Poisson equation.

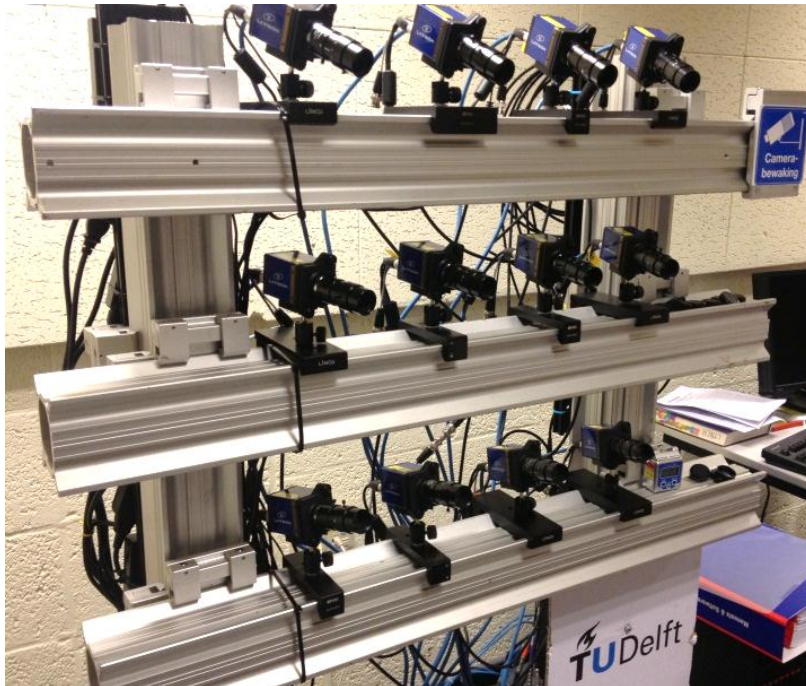


Figure 7.1 Imaging system for the 4-pulses Tomo-PIV experiment for the investigation of high-speed separated flows performed at TU Delft (courtesy of Kyle Lynch).

## 7.4 Perspectives

The development of an efficient algorithm based on the Motion Tracking Enhancement technique by Atkinson et al. (2010) can play an important role in the diffusion of the method among research groups, as the computational time needed for the enhanced processing is reduced by a factor 5.

The impact of MTE is confirmed by the study from Discetti et al. (2012) where the use of two distinct tomographic systems based on low speed single-frame cameras is proposed for the acquisition of the two PIV exposures. This solution, on one hand allows the reduction of

the experimental setup costs and, on the other hand, maximizes the MTE efficiency as the *ghost particles* belonging to the two objects are generated by independent imaging systems, theoretically suppressing the chance of coherent *ghosts*.

Based on this concept, the application of the Motion Tracking Enhancement reconstruction will be of particular interest concerning an ongoing state-of-the art Tomo-PIV experiment which is being performed at the Aerodynamics Department of Delft University of Technology. Three 4-camera tomographic systems are employed to perform 4-pulses PIV for the investigation of high-speed separated flows, Figure 7.1. This configuration can certainly take advantage from the approach suggested by Discetti et al. (2012). Furthermore, the possibility to combine the 12 cameras into a single imaging system offers the possibility to create an accurate reference result for the performance assessment of novel processing techniques.

The overall development of tomographic PIV processing technique will benefit from the upcoming *PIV Challenge*, whose activity will be initially coordinated in the framework of the AFDAR project. In this context, the assessment methodologies for experimental results proposed in this thesis assume particular relevance.

# Bibliography

## References

- Adrian RJ (1991) Particle-imaging techniques for experimental fluid mechanics. *Ann Rev Fluid Mech*, **23**:261-304.
- Adrian RJ (1997) Dynamic ranges of velocity and spatial resolution of particle image velocimetry, *Meas. Sci. Technol.*, **8**:1393-1398.
- Adrian RJ (2007) Hairpin vortex organization in wall turbulence, *Phys. of Fluids*, **19**:041301.
- Adrian RJ and Yao CS (1985) Pulsed laser technique application to liquid and gaseous flows and the scattering power of seeds materials, *Applied Optics*, **24**, 44:52.
- Adrian RJ, Meinhart CD and Tomkins CD (2000) Vortex organization in the outer region of the turbulent boundary layer, *J Fluid Mech*, **422**:1-54.
- Arroyo MP and Greated CA (1991), Stereoscopic particle image velocimetry, *Meas. Sci. Technol.*, **2**:1181-1186.
- Arroyo MP and Hinsch KD (2008) Recent Developments of PIV towards 3D Measurements, *Topics in Applied Physics*, **112**:127-154.
- Astarita T (2006) Analysis of interpolation schemes for image deformation methods in PIV: effect of noise on the accuracy and spatial resolution, *Exp. Fluids*, **40**:977-987.
- Astarita T (2007) Analysis of weighting windows for image deformation methods in PIV, *Exp. Fluids*, **43**:859-872.
- Astarita T (2009) Adaptive space resolution for PIV, *Exp. Fluids*, **46**:115-123.
- Astarita T and Cardone G (2005) Analysis of interpolation schemes for image deformation methods in PIV, *Exp. Fluids*, **38**:233-243.
- Atkinson CH and Soria J (2009), An efficient simultaneous reconstruction technique for tomographic particle image velocimetry, *Exp. Fluids*, **47**:553-568.
- Atkinson CH, Buchmann N, Stanislas M and Soria J (2010), Adaptive MLOS-SMART improved accuracy tomographic PIV (2010), *15th Int. Symp. Appl. Laser Tech. Fluid Mech.*, Lisbon, Portugal.
- Atkinson CH, Couderc S, Foucaut JM, Stanislas M and Soria J (2011) The accuracy of tomographic particle image velocimetry for measurements of a turbulent boundary layer, *Exp. Fluids*, **50**:1031-1056.
- Atkinson CH, Dillon-Gibbons CJ, Herpin S and Soria J (2008), Reconstruction techniques for Tomographic PIV of a turbulent boundary layer, *14th Int. Symp. Appl. Laser Tech. Fluid Mech.*, Lisbon, Portugal.
- Baur X and Kongeter J (1999) PIV with high temporal resolution for the determination of local pressure reductions from coherent turbulent phenomena, *PIV'99*, Santa Barbara, California.

- Boillot A and Prasad AK (1996) Optimization procedure for pulse separation in cross-correlation PIV, *Exp. In Fluids*, **21**:87-93.
- Brücker C (1995) Digital-particle-image-velocimetry (DPIV) in a scanning light sheet: 3D starting flow around a short cylinder, *Exp. Fluids*, **19**:255-263.
- Buchmann NA, Willert C and Soria J (2011) Tomographic particle image velocimetry using pulsed, high power LED volume illumination, *9th Int. Symp. PIV*, Kobe, Japan.
- Cenedese A, Romano GP and Di Felice F (1991) Experimental testing of Taylor's hypothesis by L.D.A. in highly turbulent flow, *Exp. Fluids*, **9**:351-358.
- Coëtmelec S, Buraga-Lefebvre C, Lebrun D and Özkul C (2001) Application of in-line digital holography to multiple plane velocimetry, *Meas. Sci. Technol.*, **12**:1392-1397.
- Coudert SJM and Schon JP (2001) Back-projection algorithm with misalignment corrections for 2D3C stereoscopic PIV, *Meas. Sci. Technol.*, **12**:1371 doi:10.1088/0957-0233/12/9/301.
- De Kat R and van Oudheusden BW (2010) Instantaneous planar pressure from PIV: analytic and experimental test-cases, *15<sup>th</sup> Int. Symp. on application of laser techniques to fluid mechanics*, Lisbon, Portugal.
- Di Florio D, Di Felice F and Romano GP (2002) Windowing, re-shaping and re-orientation interrogation windows in particle image velocimetry for the investigation of shear flows, *Meas. Sci. Technol.*, **13**:953-962.
- Discetti S and Astarita T (2012a), A fast multi-resolution approach to tomographic PIV, *Exp. Fluids*, **52**:765-777.
- Discetti S and Astarita T (2012b) Fast 3D PIV with direct sparse cross-correlation, *Exp. Fluids*, DOI 10.1007/s00348-012-1370-9.
- Discetti S, Ianiro A, Astarita T and Cardone G (2012) On the development of a novel low cost high accuracy experimental setup for Tomographic Particle Image Velocimetry, *16th Int Symp on Applications of Laser Techniques to Fluid Mechanics*, Lisbon, Portugal, 09-12 July, 2012.
- Eckart C and Young G (1939) A principal axis transformation for non-hermitian matrices, *Bull. Amer. Math. Soc.*, 45:933-947.
- Elsinga GE and Westerweel J (2011) The point-spread-function and the spatial resolution of PIV cross-correlation methods, *9<sup>th</sup> Int. Symp. On Particle Image Velocimetry PIV'11*, Tsukuba, Japan, 21-23 July.
- Elsinga GE, Scarano F, Wieneke B and van Oudheusden BW (2005), Tomographic particle image velocimetry, *6th Int. Symp. PIV*, Pasadena, USA.
- Elsinga GE, van Oudheusden BW and Scarano F (2006) Experimental assessment of Tomographic-PIV accuracy, *13th Int. Symp. Appl. Laser Tech. Fluid Mech.*, Lisbon, Portugal.
- Elsinga GE, Westerweel J, Scarano F and Novara M (2011) On the velocity of *ghost particles* and the bias error in Tomographic PIV, *Exp. Fluids*, **50**:825-838.
- Elsinga GE, Wieneke B, Scarano F and van Oudheusden BW (2006), Tomographic particle image velocimetry, *Exp. Fluids*, **41**:933-947.
- Enrich RJ (1981) Methods of experimental physics, part 1, p. 6 *Fluid Dynamics Academic*, New York.

- Gesemann S, Schanz D, Schröder, Petra S and Schnörr C (2010) Recasting Tomo-PIV reconstruction as constrained and L1-regularized non-linear least squares problem, *15th Int. Symp. Appl. Laser Tech. Fluid Mech.*, Lisbon, Portugal.
- Ghaemi S and Scarano F (2010), Multi-pass light amplification for tomographic particle image velocimetry applications, *Meas. Sci. Technol.*, **21**:127002.
- Ghaemi S and Scarano F (2011), Counter-hairpin vortices in the turbulent wake of a sharp trailing-edge, *J. Fluid Mech.*, **689**:317-356.
- Ghaemi S, Ragni D and Scarano F (2012) PIV-based pressure fluctuation in the turbulent boundary layer, *Exp. Fluids*, DOI 10.1007/s00348-012-1391-4.
- Golub GH and Van Loan CF (1996) Matrix Computations, *Johns Hopkins*, ISBN 878-0-8018-5414-9.
- Goodman JW (2004) Introduction to Fourier optics, Roberts & Company Publishers, Greenwood village.
- Gordon R, Bender R and Herman GT (1970) Algebraic reconstruction techniques (art) for three-dimensional electron microscopy and x-ray photography, *J. Theor. Biol.*, **29**:471.
- Gurka R, Liberzon A, Hefetz D, Rubinstein D and Shavit U (1999) Computation of pressure distribution using PIV velocity data, *PIV'99*, Santa Barbara, California.
- Haigermoser C (2009) Application of an acoustic analogy to PIV data from rectangular cavity flow, *Exp. Fluids*, **47**:145-157.
- Hain R, Kähler CJ and Michaelis D (2008), Tomographic and time resolved PIV measurements on a finite cylinder mounted on a flat plate, *Exp. Fluids*, **45**:715-724.
- Herman GT and Lent A (1976) Iterative Reconstruction Algorithms, *Computers in Biology and Medicine*, **6**:273-294.
- Hinsch KD (2002) Holographic particle image velocimetry, *Meas. Sci. Technol.*, **13**:R61-R72.
- Hori T and Sakakibara J (2004) High-speed scanning stereoscopic PIV for 3D vorticity measurements in liquids, *Meas. Sci. Technol.*, **15**:1067-1078.
- Huang HT, Fielder HF and Wang JJ (1993) Limitation and improvement of PIV, part II. Particle image distortion. A novel technique, *Exp. Fluids*, **15**:263-273.
- Humble RA, Elsinga GE, Scarano F and van Oudheusden BW (2009), Three-dimensional instantaneous structure of a shock wave/turbulent boundary layer interaction, *J. Fluid Mech.*, **622**:33-62.
- Hunt JCR, Wray AA, and Moin P (1988) Eddies, stream, and convergence zones in turbulent flows, Tech. rep., *Center for Turbulence Research*.
- Jambunathan K, Ju XY, Dobbins BN and Ashfort-Frost S (1995) An improved cross correlation technique for particle image velocimetry, *Meas. Sci. Technol.*, **6**:507-514.
- Kähler CJ, Scharnowski S and Cierpka C (2012) On the resolution limit of digital particle image velocimetry, *Exp. Fluids*, **52**:1629-1639.
- Keane RD and Adrian RJ (1992) Theory of cross-correlation analysis of PIV images, *Applied Scientific Research*, **49**:191-215.
- Koschätzky V, Moore PD, Westerweel J, Scarano F and Boersma BJ (2010) High speed PIV applied to aerodynamic noise investigation, *Exp. Fluids*, **50**:863-876.

- La Porta A, Voth GA, Crawford JA, Alexander J and Bodenschatz E (2000) Fluid particle accelerations in fully developed turbulence, *Nature*, **409**:1017-1019.
- Lin JC and Rockwell D (1996) Force identification by vorticity fields: techniques based on flow images, *J. Fluid. Struct.*, **10**:663-668.
- Liu X and Katz J (2006) Instantaneous pressure and material acceleration measurement using a four-exposure PIV system, *Exp. Fluids*, **41**:227-240.
- Liu Z, Zheng Y, Lufei J, Jao J and Zhang Q (2006) Stereoscopic PIV studies on the swirling flow structure in a gas cyclone, *Chem. Eng. Science*, **61**:4252-4261.
- Lorenzoni V, Tuinstra M, Moore P and Scarano F (2009) Aeroacoustic analysis of rod-airfoil flow by means of time resolved PIV, *15th AIAA/CEAS aeroacoustics conference*, Miami, USA.
- Maas HG, Gruen A and Papantoniou D (1993) Particle tracking velocimetry in three-dimensional flows, *Exp. Fluids*, **15**:133-146.
- Maas HG, Westfeld P, Putze T, Boetkjaer N, Kitzhofer J and Brücker C, (2009) Photogrammetric techniques in multi-camera tomographic PIV, *8th Int. Symp. PIV*, Melbourne, Australia.
- Meinhart CD, Wereley ST and Santiago JG (2000) A PIV algorithm for estimating time-average velocity fields, *J Fluids Eng.*, **122**:285-289.
- Michaelis D and Wolf CC (2011), Vibration compensation for tomographic PIV using single image volume self-calibration, *9th Int. Symp. PIV*, Kobe, Japan.
- Michaelis D, Novara M, Scarano F and Wieneke B (2010), Comparison of volume reconstruction techniques at different particle densities, *15th Int. Symp. Appl. Laser Tech. Fluid Mech.*, Lisbon, Portugal.
- Nogueira J, Lecuona A and Rodriguez PA (1999) Local field correction PIV: on the increase of accuracy of digital PIV systems, *Exp. Fluids*, **27**:107-116.
- Nogueira J, Lecuona A and Rodriguez PA (2005) Limits on the resolution of correlation PIV iterative methods, *Exp. Fluids*, **39**:305-313.
- Nogueira J, Lecuona A, Ruiz-Rivas U and Rodriguez PA (2002) Analysis and alternatives in two-dimensional multigrid particle image velocimetry methods: application of a dedicated weighting function and symmetric direct correlation, *Meas. Sci. Technol.*, **13**:963-974.
- Novara M and Scarano F (2012) Performances of motion tracking enhanced Tomo-PIV on turbulent shear flows, *Exp. Fluids*, **52**:1027-1041.
- Novara M, Batenburg KJ and Scarano F (2010), Motion tracking-enhanced MART for tomographic PIV, *Meas. Sci. Technol.*, **21**:035401.
- Novara M, Ianiro A and Scarano F (2012) Adaptive interrogation for 3D-PIV, *Meas. Sci. Technol.*, accepted for publication.
- Ortiz-Dueñas C, Kim J and Longmire EK (2009), Liquid-Liquid Drop Coalescence using Tomographic PIV, *8th Int. Symp. PIV*, Melbourne, Australia.
- Percin M, Hu Y, Van Oudheusden BW, Remes B and Scarano F (2012) Wing Flexibility Effects in Clap-and-Fling, *International Journal of Micro Air Vehicles*, **3**:217-228.
- Pereira F and Gharib M (2001) Defocusing digital particle image velocimetry and the three-dimensional characterization of two-phase flows, *Meas. Sci. Technol.*, **13**:683-694.

- Petra S, Schröder A, Wieneke B and Schnörr C (2008) On Sparsity Maximization in Tomographic Particle Image Reconstruction, *LNCS*, **5096**:294-303.
- Prasad AK (2000) Stereoscopic particle image velocimetry, *Exp. Fluids*, **29**:103-116.
- Proebsting S, Scarano F, Bernardini M and Pirozzoli S (2012) A comparative study of turbulent boundary layer wall pressure fluctuations obtained from high-speed tomographic PIV and DNS, *16<sup>th</sup> Int. Symp. on application of laser techniques to fluid mechanics*, Lisbon, Portugal.
- Raffel M, Willert CE, Wereley ST and Kompenhans J (1998) Particle image velocimetry: a practical guide, *Springer*.
- Ragni D, van Oudheusden BW and Scarano F (2012) 3D pressure imaging of a propeller blade tip region by phase-locked stereoscopic PIV, *Exp. Fluids*, **52**:463-477.
- Romano GP, Antonia RA and Zhou T (1999) Evaluation of LDA temporal and spatial velocity structure functions in a low Reynolds number turbulent channel flow, *Exp. Fluids*, **27**:368-377.
- Roth GI and Katz J (2001) Five techniques for increasing the speed and accuracy of PIV interrogation, *Meas. Sci. Technol.*, **12**:238:245.
- Scarano F (2000) Particle Image Velocimetry Development and Application, *PhD thesis*.
- Scarano F (2002) Iterative image deformation methods in PIV, *Meas. Sci. Technol.*, **13**:R1-R19.
- Scarano F (2013) Tomographic PIV: principles and practice, *Meas. Sci. Technol.*, to appear.
- Scarano F and Poelma C (2009) Three-dimensional vorticity patterns of cylinder wakes, *Exp. Fluids*, **47**:69-83.
- Scarano F and Riethmuller ML (2000) Advances in iterative multigrid PIV image processing, *Exp. Fluids*, suppl S51-60.
- Scarano F and Sciacchitano A (2011) Robust elimination of light reflections in PIV, *9th Int. Symp. PIV*, Kobe, Japan, July 21-23, 2011.
- Scarano F, Bryon K and Violato D (2010), Time-resolved analysis of circular and chevron jets transition by Tomo-PIV, *15th Int. Symp. Appl. Laser Tech. Fluid Mech.*, Lisbon, Portugal.
- Scarano F. (2003) Theory of non-isotropic spatial resolution in PIV, *Exp. Fluids*, **35**:268-277.
- Schanz D, Gesemann S, Schroder A, Wieneke B and Novara M (2012) Non-uniform optical transfer functions in particle imaging: calibration and application to Tomographic reconstruction, *Meas. Sci. Technol.*, accepted for publication.
- Schrijer FFJ and Scarano F (2008) Effect of predictor-corrector filtering on the stability and spatial resolution of iterative PIV interrogation, *Exp. Fluids*, **45**:927:941.
- Schröder A, Geisler R, Elsinga GE, Scarano F and Dierksheide U (2008b) Investigation of a turbulent spot and a tripped turbulent boundary layer flow using time-resolved tomographic PIV, *Exp. Fluids*, **44**:305-316.
- Schröder A, Geisler R, Staack K, Elsinga GE, Scarano F, Wieneke B, Henning A, Poelma C and Westerweel J (2011), Eulerian and Lagrangian views of a turbulent boundary layer flow using time-resolved tomographic PIV, *Exp. Fluids*, **50**:1071-1091.

- Schröder A, Geisler R, Staack K, Wieneke B, Elsinga GE, Scarano F and Henning A (2008a), Lagrangian and Eulerian views into a turbulent boundary layer flow using time-resolved tomographic PIV, *14th Int. Symp. Appl. Laser Tech. Fluid Mech.*, Lisbon, Portugal.
- Sciacchitano A, Scarano F and Wieneke B (2012) Multi-frame pyramid correlation for time-resolved PIV, *Exp. Fluids*, DOI 10.1007/s00348-012-1345-x.
- Solf KD (1986) *Fotografie: Grundlagen, Technik, Praxis*, Fisher Taschenbuch Verlag, Frankfurt.
- Soloff SM, Adrian RJ and Liu ZC (1997) Distortion compensation for generalized stereoscopic particle image velocimetry, *Meas. Sci. Technol.*, **8**:1441-1454.
- Tennekes H (1975) Eulerian and Lagrangian time microscales in isotropic turbulence, *J. Fluid Mech.*, **67**:561-567.
- Theunissen R, Scarano F and Riethmuller ML (2007) An adaptive sampling and windowing interrogation method in PIV, *Meas. Sci. Technol.*, **18**:275-285.
- Theunissen R, Scarano F and Riethmuller ML (2010) Spatially adaptive PIV interrogation based on data ensemble, *Exp. Fluids*, **48**:875-887.
- Thomas L, Grulier V, Braud P, Tremblais B, Germaneau A, Dupré JC, Doumalin P and David L (2009), Comparison of algebraic reconstruction and laser sheet scanning for tomography PIV, *8th Int. Symp. PIV*, Melbourne, Australia.
- Thomas L, Vernet R, Tremblais B and David L (2010), Influence of geometric parameters and image pre-processing on Tomo-PIV results, *15th Int. Symp. Appl. Laser Tech. Fluid Mech.*, Lisbon, Portugal.
- Van Oudheusden (2013) PIV-based pressure measurement, *Meas. Sci. Technol.* (to appear).
- Van Oudheusden BW, Scarano F, Roosenboom EWM, Casimiri EWF and Souverein LJ (2007) Evaluation of integral forces and pressure field from planar velocimetry data for incompressible and compressible flow, *Exp. Fluids*, **43**:153-162.
- Verhoeven D. (1993) Limited-data computed tomography for the physical sciences. *Applied Optics*, **32**:3736-3754.
- Violato D and Scarano F (2011) Three-dimensional evolution of flow structures in transitional circular and chevron jets, *Physics of Fluids*, **23**:124104.
- Violato D, Moore PD and Scarano F (2011) Lagrangian and Eulerian pressure field evaluation of rod-airfoil flow from time-resolved tomographic PIV, *Exp. Fluids*, **50**:1057-1070.
- Voth GA, Satyanarayan K and Bodenschatz E (1998) Lagrangian acceleration measurements at large Reynolds numbers, *Phys. of Fluids*, **10**:2268-2280.
- Westerweel J (2000) Theoretical analysis of the measurement precision in particle image velocimetry, *Exp. Fluids*, S3-S12.
- Westerweel J (1994) Efficient detection of spurious vectors in particle image velocimetry data sets, *Exp. Fluids*, **16**:236-247.
- Westerweel J and Scarano F (2005) Universal outlier detection for PIV data, *Exp. Fluids*, **39**:1096-1100.

- Wieneke B (2005) Stereo-PIV using self-calibration on particle images, *Exp. Fluids*, **2**:267-280.
- Wieneke B (2008) Volume self-calibration for 3D particle image velocimetry. *Exp. Fluids*, **45**:549-556.
- Wieneke B (2011) Iterative reconstruction of volumetric particle distribution, *9th Int. Symp. PIV*, Kobe, Japan.
- Wieneke B and Pfeiffer K (2010) Adaptive PIV with variable interrogation window size and shape, *15th Int. Symp. On Applications of Laser Techniques to Fluid Mechanics*, Lisbon, Portugal.
- Willert C (1997), Stereoscopic digital particle image velocimetry for application in wind tunnel flows, *Meas. Sci. Technol.*, **8**:1465-1479.
- Willert C, Stasicki B, Klinner J and Moessner S (2010), Pulsed operation of high-power light emitting diodes for imaging flow velocimetry, *Meas. Sci. Technol.*, **21**:075402.
- Willert CE and Gharib M (1991) Digital particle image velocimetry, *Exp. Fluids*, **10**:181:193.
- Worth NA and Nickels TB (2008), Acceleration of Tomo-PIV by estimating the initial volume intensity distribution, *Exp. Fluids*, **45**:847-856.
- Zhang J, Tao B and Katz J (1997) Turbulent flow measurement in a square duct with hybrid holographic PIV, *Exp. Fluids*, **3**:373-381.
- Zolotov DA, Buzmakov AV, Shiryaev AA and Asadchikov VE (2009) X-ray Computer Tomography of Natural Fibrous Diamonds and Ballas, *J. of Surface Investigation. X-ray Synchrotron and Neutron Techniques*, **3**:659-664.



## List of journal publications

- Elsinga GE, Westerweel J, Scarano F and Novara M (2010) On the velocity of *ghost particles* and the bias error in Tomographic PIV, *Exp. Fluids*, **50**:825–838.
- Haigermoser C, Vesely L, Novara M and Onorato M (2008) A time-resolved particle image velocimetry investigation of a cavity flow with a thick incoming turbulent boundary layer, *Physics of Fluids*, **20**:105101.
- Novara M and Scarano F (2012) Performances of motion tracking enhanced Tomo-PIV on turbulent shear flows, *Exp. Fluids*, **52**:1027-1041.
- Novara M, Batenburg KJ and Scarano F (2010), Motion tracking-enhanced MART for tomographic PIV, *Meas. Sci. Technol.*, **21**:035401.
- Novara M, Ianiro A and Scarano F (2013) Adaptive interrogation for 3D-PIV, *Meas. Sci. Technol.*, **24**:024012.
- Schanz D, Gesemann S, Schroder A, Wieneke B and Novara M (2013) Non-uniform optical transfer functions in particle imaging: calibration and application to Tomographic reconstruction, *Meas. Sci. Technol.*, **24**:024009.

## Conferences

- Haigermoser C, Vesely L, Novara M, Zuzio D and Onorato M (2007) Time-resolved PIV applied to cavity unsteady flows, *13th AIAA/CEAS Aeroacoustics Conference*, Rome, Italy.
- Michaelis D, Novara M, Scarano F and Wieneke B (2010) Comparison of volume reconstruction techniques at different particle densities, *15th Int. Symp. On Applications of Laser Techniques to Fluid Mechanics*, Lisbon, Portugal.
- Novara M and Scarano F (2009) *Ghost intensity* reduction by means of Motion Tracking Enhanced MART Tomography, *PIV'09*, Melbourne, Australia.
- Novara M and Scarano F (2010) Performances of motion tracking enhanced Tomo-PIV on turbulent shear flows, *15th Int. Symp. On Applications of Laser Techniques to Fluid Mechanics*, Lisbon, Portugal.
- Novara M and Scarano F (2012) Lagrangian acceleration evaluation for tomographic PIV: a particle-tracking based approach, *16th Int. Symp. On Applications of Laser Techniques to Fluid Mechanics*, Lisbon, Portugal.
- Novara M, Ianiro A and Scarano F (2011) Adaptive interrogation for 3D-PIV, *9th Int. Symp. PIV*, Kobe, Japan.



# Acknowledgements

This thesis, and the research that led to it, would not have been possible without the help of many people who supported and motivated me during these years.

I would like to thank my supervisor Prof. Dr. Fulvio Scarano for the opportunity he gave me to carry out this PhD research. I am grateful for the number of ideas brought up and for his availability to meet for discussion and advice.

I am thankful to Prof. Joost Batenburg for his contribution on the development of the Motion Tracking Enhancement technique.

I would like to thank Bernd Wieneke and Dirk Michaelis for their suggestions and their work on the implementation of the MTE technique into DaVis.

I would like to thank Dr. Gerrit Elsinga for giving me the opportunity to collaborate in the study on the behavior of *ghost particles*.

I am grateful to Dr. Daniel Shanz; it has been a pleasure to work with him on the experiment for the OTF study.

Thanks to Dr. Andrea Ianiro who, with his enthusiasm and competence, motivated me to engage the research on adaptive correlation. His contribution has been essential throughout the whole process; from the very first idea to the drafting of the paper.

The application of the processing algorithms to experimental data represented an important part of my work; thanks to Daniele Violato and Sina Ghaemi for providing the experimental database.

I would also like to thank Andrea Sciacchitano and Kyle Lynch for the productive discussions and Rogier Giepmans and Ferdinand Schrijer for their help with the Dutch versions of the summary and the propositions.

Thanks to Matteo Enrici for the amazing work on the cover image and to the *3MaStudio* for offering me company, desk and coffee when I was working in Cuneo.

I would like to thank Colette Russo for her help, efficiency, understanding and patience and the technical staff, namely Eric de Keizer, Frits Donker Duyvis, Peter Duyndam and Nico van Beek, for their help.

This work has been conducted as part of the FLOVIST project (funded by the European Research Council, ERC, grant n° 202887) and of the AFDAR project (funded by the European Community's Seventh Framework program, grant n° 265695).

A special thanks goes to my friends for being always there for me, for the conversations, the phone calls, for the jokes and the dinners, the parties and everything else.

I do not have enough, and good enough, words to express my gratitude for my family. Their love, support and understanding have been source of strength and motivation for my entire life.

This work is dedicated to my father Silvio, my mother Aurora and my sister Roberta.



# Curriculum vitae

Matteo Novara was born on December 30, 1982 in Cuneo, Italy. He obtained his Aerospace Engineering Master of Science degree with Honors at Politecnico di Torino in May 2007. The Master thesis work concerned the investigation of cavity flows by means of particle image velocimetry. From July 2007 to June 2008 he worked as a researcher at Politecnico di Torino on innovative unsteady methods for DNS and LES simulation of turbulent flows on aircraft surfaces. On September 2008 he started the PhD under the supervision of Dr. Fulvio Scarano in the Aerodynamics group at “Delft University of Technology”. The PhD research concerned the development of advanced algorithms for processing of tomographic PIV data. The results of this research are described in the present thesis. During his PhD he collaborated with Prof. Joost Batenburg (Centrum Wiskunde & Informatica Scientific Computing group, Amsterdam, The Netherlands), with LaVision GmbH (Göttingen, Germany), with the German Aerospace Center (DLR), with Dr. Gerrit Elsinga and Prof. Jerry Westerweel (Process and Energy department, Delft University of Technology) and with Dr. Andrea Ianiro (Aerospace Engineering department, University of Naples). He also acted as responsible for advanced algorithms for Tomo-PIV data processing within the FLOVIST project (Flow Visualization Inspired Aeroacoustics with time-resolved tomographic PIV, funded by the European Research Council) and as responsible for the TU Delft contribution to the experimental database for the AFDAR project (Advanced Flow Diagnostics for Aeronautical Research, within the Seventh Framework program of the European Community).